

# **Design and Application of a High Temporal Resolution Radiation Beam Analyser**

Thesis submitted for the degree of

Doctor of Philosophy

at the University of Leicester

By

Stephen G Hunt

Department of Cardiovascular Sciences

University of Leicester

November 2011

# Design and Application of a High Temporal Resolution Radiation Beam Analyser

By

Stephen G Hunt

## Abstract

The introduction of dynamic radiotherapy has resulted in the development of medical linear accelerators capable of high dosimetric accuracy. A novel test instrument has been developed that is capable of simultaneously measuring the radiation profile and four associated accelerator control signals in a single pulse of radiation, fully synchronised to the beam generation system of the accelerator. The system was constructed, validated and tested to investigate its ability to provide a greater insight into and deeper understanding of the behaviour of accelerator beam transport and generation control systems during dynamic operating conditions pertinent to Intensity Modulated Radiotherapy (IMRT) beam delivery. The performance of the electron gun filament and its associated servo control system was investigated in relation to the lower limit of small Monitor Unit (MU) segments for 'step and shoot' IMRT. Accelerator electron beam current control, using the electron gun filament current as the controlling element, and its significance to small segment doses is presented.

The behaviour and characteristics of the radial steering system during gantry rotation were also measured. First, the fundamental properties were characterised to explore the use of the instrument for engineering development, and then the accelerator performance during gantry rotation was investigated. Low frequency periodic oscillations found in the radiation beam during rotation were considered from an engineering standpoint, and the consequences for patient dose were evaluated.

The instrument has the ability to observe the relationship between radiation beam profile and control system events concurrently with the radiation pulses, at high temporal resolution, which was crucial in identifying the source of and possible cure for unexpected system behaviour in the work presented in the thesis. This was demonstrated by identifying the processes involved that set the lower limit for small MU segments and by the characterisation of the radial control system during gantry rotation on the Elekta SLi series accelerator. The multi-input analogue capability proved useful in understanding the interactions between the different control system elements involved in beam production. The instrument should prove to be of particular benefit for improving the accuracy and reliability of patient treatment in the context of dynamic radiotherapy.

## Acknowledgements

This thesis is dedicated to my wife Chris and all my family, who have encouraged and supported me, during my period of study. I could not have done this without your patience, sacrifice, help and love.

Especially, I would like to thank my supervisor, Dr. Mark Horsfield for his constant guidance, assistance and encouragement throughout this research project. Also a special thanks to Dr. Ruth McLauchlan for her constant support, boundless energy and enthusiasm for everything in science, you are a great inspiration. Many thanks to Professor David Evans for making it all possible and also for your unwavering confidence in my ability to succeed.

Also, thanks to Mark Norton for his help in escaping the ‘Madness’ of funding applications and financial paraphernalia, also for your endless encouragement. Also thanks to Ghislaine Boyd and Elekta Oncology Systems Ltd. for funding support.

Finally, thank you, all my friends and colleagues, Glen Bush, John Sage (including all the Radiation Physics team, too many to mention), Mike Dunn, Dr. Andrew Glendinning, Dr. David Bonnett and anyone I may have overlooked, for all your help and support. Thanks to Sunil, Vaughan, Naresh, Mike, Milan and Tim for the ‘day to day’ smooth running of the Clinical Engineering team during my period of study. Thanks to Mike Squires and the mechanical workshop team for all their support, with special thanks to Naushad Mangia for his hard work in fabricating of the ionisation chamber array hardware.

Abstract .....	<i>i</i>
Acknowledgements .....	<i>ii</i>
Table of Contents .....	<i>iii</i>
List of Abbreviations .....	<i>viii</i>

## Table of Contents

<b>Chapter 1. Introduction.....</b>	<b>1</b>
1.1 Brief History of X-ray Generation .....	1
1.2 Overview of Therapeutic Radiation Production Using a Linear Accelerator .	2
1.2.1 Beam Generation .....	2
1.2.2 Accelerating Waveguides .....	5
1.2.3 Beam Bending, X-ray Target, Filtration and Collimation .....	7
1.2.4 System Control and Monitoring.....	9
1.3 Radiotherapy: Aiming to Improve the Therapeutic Ratio.....	10
1.3.1 Intensity Modulated Radiotherapy.....	11
1.3.2 Supplementary Developments .....	12
1.4 The Development of Linear Accelerator Systems .....	13
1.4.1 Conception .....	14
1.4.2 Early Accelerators.....	15
1.4.3 Later Developments .....	15
1.5 The Modern Medical Linear Accelerator.....	20
1.5.1 Control Systems .....	20
1.6 Quality Assurance, Test and Measurement.....	24
1.6.1 Measurement Axis .....	25
1.7 Dynamic Therapy .....	26
1.7.1 The Production of Intensity Modulated Beams .....	26
1.7.2 Small Segment Exposures.....	28
1.7.3 Radiation Symmetry During Gantry Rotation .....	30
1.8 Aims of this Thesis.....	31

<b>Chapter 2. Review of Radiation Technologies .....</b>	<b>34</b>
2.1 Radiation Beam Measurement Methods .....	34
2.1.1 Commercial Systems .....	36
2.2 Beam Production and Measurement Equipment Development .....	40
2.2.1 Application to Dynamic Therapy.....	43
2.2.2 Beam Energy and Delivery Concerns.....	44
2.3 Conclusion.....	49
<b>Chapter 3. Measurement Equipment .....</b>	<b>51</b>
3.1 Introduction .....	51
3.2 Development Strategy and Specification .....	52
3.2.1 Review of a Previous Project.....	52
3.2.2 Remit for New Data Acquisition System.....	55
3.3 Design Considerations for Radiation Measurement.....	56
3.3.1 Beam Energy Effects .....	57
3.3.2 Beam Trajectory Effects .....	59
3.3.3 Accelerator Pulse Rate .....	61
3.3.4 Diode Detectors .....	62
3.3.5 Ionisation Chambers .....	63
3.3.6 Discussion .....	65
3.4 Design of the Air Spaced Ionisation Chamber.....	67
3.4.1 Collecting Plate Area .....	67
3.4.2 Plate Separation .....	69
3.4.3 High Tension Supply to Satisfy Ion Transit time .....	73
3.4.4 Design Detail and Construction .....	73
3.4.5 Assembly.....	78
3.4.6 Completed Array.....	79
3.5 Design - Integrating Electrometer .....	81
3.5.1 Evaluation and Description.....	81
3.5.2 Electrometer Construction .....	83
3.5.3 Ion Chamber Simulator.....	85
3.5.4 Initial Testing .....	85
3.5.5 Discussion .....	95
3.5.6 Conclusions Drawn from Initial Tests .....	96
3.6 Design – Data Acquisition System.....	97
3.6.1 Design Plan .....	97
3.6.2 Core Microcontroller .....	99
3.6.3 Interface to Host PC.....	99

3.6.4	Analogue Input.....	102
3.6.5	Analogue Output.....	105
3.6.6	Electrometer Auto Zero .....	106
3.6.7	Synchronisation.....	107
3.7	Construction – Data Acquisition System .....	110
3.7.1	Electromagnetic Interference .....	110
3.7.2	Functional Tests .....	111
3.8	Ion Chamber Connecting Cable .....	113
3.9	Completed Measurement System.....	113
3.9.1	External Data Input Pod.....	113
3.9.2	Treatment Room Control Box .....	114
3.9.3	External Interface Box .....	115
3.10	Conclusion .....	115

## **Chapter 4. System Characterisation and Validation ..... 117**

4.1	Introduction .....	117
4.2	Bench Tests .....	119
4.2.1	Baseline Noise and EMI Suppression.....	119
4.2.2	Collected Charge per Sample.....	120
4.2.3	Ion Chamber Connecting Cable Capacitance .....	121
4.2.4	Electrometer Drift .....	125
4.2.5	Data Pod Channel ‘Cross Talk’ .....	127
4.3	Accelerator Tests .....	127
4.3.1	Extraneous Noise Tests.....	127
4.3.2	Initial Signal Levels .....	128
4.3.3	Ion Transit Time .....	130
4.3.4	Charge Build Up .....	133
4.3.5	Saturation Curve .....	136
4.3.6	Calibration.....	137
4.3.7	Electric Field Distortion.....	146
4.4	Analysis of Initialisation Confidence Test Data .....	148
4.4.1	Acquisition Reference Voltage Test .....	149
4.4.2	Electrometer Offset.....	151
4.5	Conclusion.....	153

## **Chapter 5. Initial Measurements..... 154**

5.1	Measurement .....	154
5.1.1	Analogue Calibration .....	155
5.1.2	Dosimetric Calibration.....	156
5.1.3	Reference Data.....	157
5.1.4	Beam Status Detection.....	157
5.2	Data Pre-processing.....	162
5.3	Analysis.....	162
5.3.1	Data Filtration .....	163
5.4	Conclusion.....	172

## **Chapter 6. Electron Gun Behaviour at Beam Start ..... 173**

6.1	Introduction .....	173
6.1.1	Electron Gun Filament ‘Aging’ .....	174
6.2	Prerequisite.....	174
6.3	Beam Start-up (Experiment 1) .....	175
6.3.1	Materials and Methods.....	175
6.3.2	Results.....	180
6.3.3	Discussion .....	183
6.4	Further Investigation into Beam Start-up Effects .....	184
6.4.1	Materials and Methods – Overshoot Effect .....	184
6.4.2	Results – Overshoot Effect .....	184
6.4.3	Discussion – Overshoot effect .....	184
6.4.4	Materials and Methods - Delay Effect .....	185
6.4.5	Results – Delay Effect .....	186
6.4.6	Discussion – Delay Effect.....	187
6.4.7	Summary .....	188
6.5	Dosimetric Evaluation (Experiment 2) .....	188
6.5.1	Materials and Methods.....	188
6.5.2	Results.....	189
6.5.3	Discussion .....	194
6.6	Conclusions .....	195

## **Chapter 7. Secondary Radial Steering During Rotation ..... 197**

7.1	Introduction .....	197
7.1.1	Measurement Conventions.....	198
7.2	Technical Overview .....	198

7.3	Fundamental Operation (Experiments 1 and 2)	199
7.3.1	Materials and Methods	199
7.3.2	Results and Discussion	200
7.4	Measuring the Radial Lookup Table (Experiment 3)	204
7.4.1	Materials and Methods	204
7.4.2	Results	205
7.4.3	Discussion	205
7.5	Results Summary for Initial Measurements	208
7.6	Rotation under Servo Control (Experiment 4)	208
7.6.1	Material and Methods	209
7.6.2	Results and Discussion	209
7.7	Measurement of Radial Displacement (Experiment 5)	212
7.7.1	Materials and Methods	212
7.7.2	Results and Discussion	215
7.8	Radial Symmetry	216
7.8.1	Materials and Methods	216
7.8.2	Results and Discussion	217
7.8.3	Conclusion for Error in CW Rotation	221
7.9	Conclusion	221

## **Chapter 8. Consequences for Patient Dose..... 223**

8.1	Introduction	223
8.1.1	Quality Control	223
8.2	Materials and Methods	228
8.2.1	Processing to produce the 3D Dose Map	230
8.3	Results	231
8.3.1	Confirmation of Under-damping	231
8.3.2	Dosimetric Effect on Whole Rotations	232
8.3.3	Dosimetric Effects of Segments of Rotation	237
8.4	Discussion	239
8.5	Conclusions	241

<b>Chapter 9. Conclusions and Further Work .....</b>	<b>243</b>
9.1 Conclusions .....	243
9.2 Future Developments .....	246
<b>Chapter 10. Appendices.....</b>	<b>248</b>
10.1 Appendix 1 - Standard Array Configuration .....	248
10.2 Appendix 2 – Details of the Test Ionisation Chamber Array .....	249
10.3 Appendix 3 – Dose Simulator.....	254
10.3.1 Conception .....	254
10.3.2 Design .....	257
10.3.3 Construction .....	261
10.3.4 Conclusion .....	262
10.4 Appendix 4 - System Specification .....	263
<b>Chapter 11. References.....</b>	<b>264</b>

## List of Abbreviations

AC Alternating Current
ADC Analogue to Digital Convertor
AFC Automatic Frequency Control
ASCII American Standard Codes for Information Interchange
ASU Automatic Set-Up
BNC Bayonet Neill Concelman (BNC connector)
CAX Central Axis
CNC Computer Numerical Control
CMOS Complementary Metal Oxide Semiconductor
CSV Comma Separated Variable
CT Computerised Tomography
DAC Digital to Analogue Convertor
DAO Direct Aperture Optimisation
DC Direct Current
DMLC Dynamic Multi-Leaf Collimation
DPO Digital Phosphor Oscilloscope
DSP Digital Signal Processor
DVM Digital Volt Meter
EMC Electro-Magnetic Compliance
EMI Electromagnetic Interference
EPID Electronic Portal Imaging Device

FET Field Effect Transistor  
FIR Finite Impulse Response  
HT High Tension  
IGRT Image Guided Radio Therapy  
IIR Infinite Impulse Response  
IMAT Intensity Modulated Arc Therapy  
IMB Intensity Modulated Beams  
IMRT Intensity Modulated Radio Therapy  
LCD Liquid Crystal Display  
LSB Least Signification Bit  
LT Low Tension  
LVDT Linear Differential Voltage Transformer  
MIPS Million Instructions Per Second  
MLC Multi-Leaf Collimator  
MFA Multi File Analysis  
MU Monitor Unit  
NTCP Normal Tissue Complication Probability  
PC Personal Computer  
PCB Printed Circuit Board  
PD Prescribed Dose  
PFN Pulse Forming Network  
PIC Peripheral Interface Controller  
PID Proportional Integral Derivative  
PRF Pulse Repetition Frequency  
PPM Planned Preventative Maintenance  
PPS Pulses Per Second  
PTFE Polytetrafluoroethylen  
PTV Planning Tumour Volume  
QA Quality Assurance  
RISC Reduced Instruction Set Computer  
RF Radio Frequency  
SD Standard Deviation  
SDD Source Detector Distance  
SME Synchronised Multi-channel Electrometer  
TCP Tumour Control Probability  
UART Universal Asynchronous Receiver Transmitter  
VMAT Volumetric Modulated Arc Therapy  
Vmos V-groove Metal Oxide Silicon

## Chapter 1. Introduction

Since the discovery of the curative effects of X-rays, scientists and engineers have continually strived to develop radiotherapy treatment delivery systems to improve the therapeutic ratio. Currently, the linear accelerator is the technology of choice for conventional external beam radiotherapy employing X-ray energies in the range of 4-25 MV. Ongoing development aims to improve the delivery of a tumouricidal dose to the target volume whilst sparing normal tissue and organs at risk. This is the aim of Conformal Radiotherapy, where the treatment delivery is shaped to conform to the tumour volume. Thus, regions of high dose conform closely to the target volume while normal tissue is spared. Modulation of the beam fluence has further enhanced conformity, making it possible to achieve 3 dimensional dose distributions that conform closely to irregularly shaped volumes.

To implement these techniques, linear accelerator manufacturers have developed new features and improved the stability and precision of the beam delivery systems on their machines. This has resulted in more stringent operating tolerances in both mechanical and electronic engineering terms, placing a greater importance on the maintenance and setting up of the equipment for these advanced treatment regimes. In the experimental work in this thesis, the SL15i linear accelerator (Elekta Oncology Systems Ltd., Crawley, UK) is used for the delivery of treatment beams.

### 1.1 Brief History of X-ray Generation

In the early years of X-ray generation, development involved the acceleration of particles to higher energies with greater stability and delivery accuracy. Early machines in the 1930's employed high voltage Direct Current (DC) generators such as the voltage multiplier invented by Cockcroft and Walton (Cockcroft J D & Walton E T S, 1930). Using this technique, energies up to 1 MV were achieved, but electrical

insulation breakdown was the limiting factor in the generation of high accelerating voltages.

The first accelerator of this type was installed at St. Bartholomew's Hospital in 1936 (Allibone T E *et al*, 1939). The invention and subsequent development of the linear accelerator enabled the 1 MV barrier to be surpassed with ease, leading to compact treatment machines using relatively low voltages in the beam generation process. An important factor in improving delivery accuracy was the ability to mount the accelerator and associated systems on a rotating gantry, thus enabling isocentric treatment delivery (Lennox A J, 2001). Continuing engineering development has made the modern medical linear accelerator into a highly sophisticated, versatile and stable treatment delivery platform.

## **1.2 Overview of Therapeutic Radiation Production Using a Linear Accelerator**

The components in the beam generation systems of a generic linear accelerator are shown in Figure 1-1. This overview will only discuss the production of X-ray beams. Although most current machines will also produce electron beams for treatment, this is beyond the scope of this thesis.

### **1.2.1 Beam Generation**

The fundamental purpose of a microwave based linear accelerator in a radiotherapy treatment unit is to produce high energy beams without the need for a generating voltage of the same magnitude as the required energy. This eliminates the need for extremely high electrical potentials with the concomitant risk of insulation failure. The high beam energy is achieved by accelerating electrons, launched from an electron gun (Figure 1-1e), into a high power microwave Radio Frequency (RF) field in a tuned accelerating structure (Figure 1-1f).

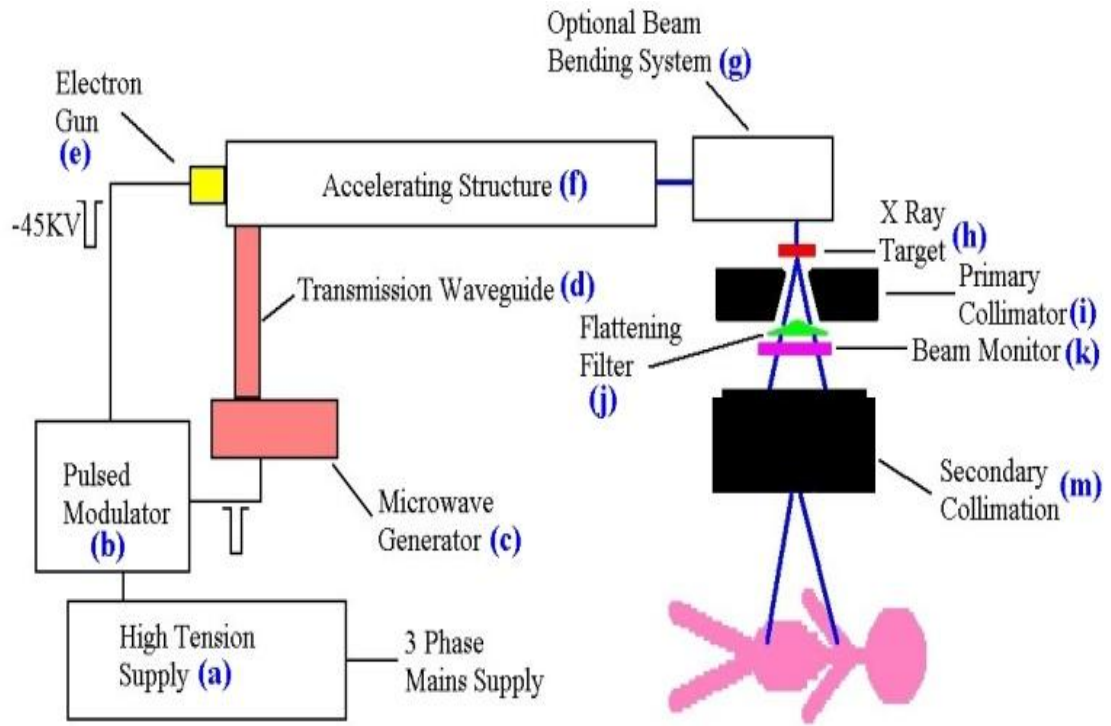


**Figure 1-1: Block diagram of the beam generation systems in a typical medical linear accelerator.**

The electrons gain energy from the electromagnetic wave as they pass through the accelerating structure, and exit at a speed approaching the speed of light. The beam is positioned and focused during its transit through the accelerator by magnetic fields created by sets of fixed coils set along the length of the accelerator. The final energy is determined by the RF power level and frequency, the electron beam current and injection energy in the accelerating waveguide and by the waveguide design. Generally, for X-ray beams, nominal RF power and injection voltage levels are preset for the required beam energy and then electron beam current is adjusted to fine-tune the required energy by setting the emission of the electron gun. The RF frequency is set to the resonant frequency of the accelerating waveguide and is servo controlled to maintain it, since the accelerator operating frequency is temperature dependent.

A high power microwave generator (Figure 1-1c), such as a magnetron or klystron (Karzmark C J *et al*, 1993h, Loverock L, 2007), coupled to the accelerator by a rectangular transmission waveguide (Figure 1-1d) is used to produce the high power RF field. Operation of these devices in medical linear accelerators is described

in Karzmark C J *et al*, 1993e, Karzmark C J & Pering N C, 1973, Loverock L, 2007, Greene D. & Williams P C, 1985d, Karzmark C J, 1984. The nominal wavelength of the RF is 10 cm (3 GHz), and accelerator power levels are in the order of 2-5 MW.

### 1.2.1.1 Pulsed Operation

It would be impractical to produce the high RF power level required in a continuous mode, since the mains input power to the machine would be of the same order. In fact, after accounting for the inefficiency of the RF power device, the input power levels would need to be significantly greater. The RF power source is therefore pulsed, to reduce the mean power level and accelerator output to a practicable value. A typical Pulse Repetition Frequency (PRF) range is 50 to 400 Pulses Per Second (PPS), with the RF active for a period of 3.2  $\mu\text{s}$  (where specific examples are given, they are for the Elekta SL 15i accelerator). The PRF signal is derived from a master pulse generator in combination with other signals which are used to synchronise the accelerator beam generation and control systems.

As an example, using the SL 15i accelerator to deliver a standard unmodulated therapy beam, the nominal PRF is 400 PPS. The RF power device used in the machine is a magnetron. Typical magnetron current and voltage levels for a 6 MV X-Ray beam are 133 Amperes and 37 kV respectively. This results in a peak input power of 4.92 MW to the magnetron. With a nominal PRF of 400 PPS and an RF 'on' time of 3.2  $\mu\text{s}$ , a duty cycle of 1:781 is produced. Thus, the mean input power is only 6.3 kW. The absolute maximum rating for the magnetron used in SLi 15 accelerator is 7 kW mean power and 14 MW peak input power as specified in the MG 6028 magnetron datasheet (e2v Technologies Ltd, 2002b).

This high peak power required by the RF generator is produced using a 'Pulsed Modulator' (Figure 1-1b) as described in Karzmark C J *et al*, 1993g. Energy is stored in a Pulse Forming Network (PFN) which consists of a bank of capacitors

connected together by inductors as shown in Figure 1-2 to form a network with a nominal  $3.2 \mu\text{s}$  time constant. The PFN is charged from the high tension power supply (Figure 1-1a) during the 'off' phase of the PRF cycle. The charging path is shown in Figure 1-2 by the red arrows and is controlled to enable the final pulse energy to be set. The PRF signal triggers a high power switch, typically a thyatron (Marconi Applied Technologies Ltd, 2007, Pirrie C A & Menown H, 2000), to discharge the PFN as shown in Figure 1-2 by the blue arrows.

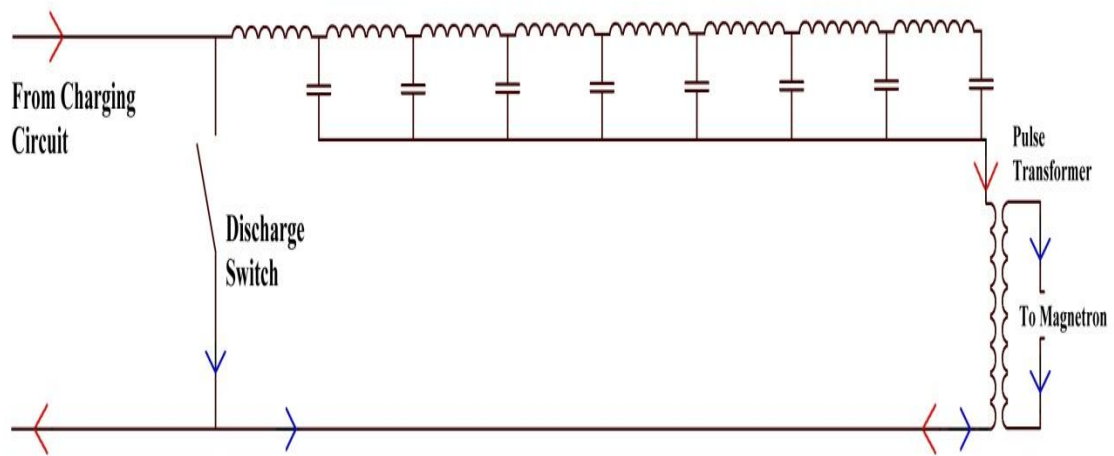


**Figure 1-2:** Typical pulse forming network (PFN) configuration consisting of 8 pairs of capacitors and inductors.

The pulse transformer, which is inactive during the charging phase due to the small number of turns on the primary coils with respect to the charging frequency, couples the narrow PFN discharge pulse to the microwave generator (Magnetron or Klystron).

### 1.2.2 Accelerating Waveguides

The acceleration of electrons in a medical linear accelerator uses a high power RF wave to replace the high electrical potentials used in early devices (Section 1.4), to overcome the problem of insulation failure (Section 1.1). An RF wave can be propagated through hollow tubes (Roddy D, 1986) allowing acceleration of electrons by means of the electric field plane of the transverse electromagnetic RF wave. However, the wave is travelling at a phase velocity greater than the speed of light (where

'phase velocity' is the velocity at which a point of fixed phase propagates in space) (Greene D. & Williams P C, 1985a, Karzmark C J, 1984). At the electron gun end of the accelerator, the wave velocity is reduced by loading the accelerating waveguide structure with disks, with a hole in the centre to allow the electron beam to pass. This synchronises the RF wave and electron velocities, and electrons are 'bunched' and gain energy from the RF wave by modifying the disk geometry along the length of the accelerating waveguide accordingly (Greene D. & Williams P C, 1985a).

### 1.2.2.1 RF Power Transport

Two approaches to RF propagation have been developed for accelerating waveguides using standing or travelling waves (Fry D W & Walkinshaw W, 1949). The key difference between these two methods is the accelerating waveguide termination impedance. A travelling wave type, is terminated at each end by a matched microwave mode transformer, resulting in a 'reflectionless' match (Roddy D, 1986). The RF signal is injected into the accelerating waveguide at the electron gun end, propagates the length of waveguide, and exits via the output mode transformer to be recycled (Saxon G, 1954) or 'dumped' into a microwave load. Depending on the design of the waveguide, energy is gained by the electron bunch in 1 in every 3 or 1 in every 4 of the accelerating waveguide cavities (Karzmark C J, 1984, Podgorsak E B, 2005). The standing wave type is unterminated at the ends, with the RF signal connected at some point along the length of the waveguide; consequently a standing wave is setup along the length of accelerator cavities. The reflected RF power due to the unterminated accelerating waveguide exits from the same point as injected, and is routed to a microwave load via a multi-port microwave circulator (Karzmark C J *et al*, 1993e). In this standing wave design, energy is gained by the electron bunch in alternate cavities along the length of the accelerating waveguide.

### 1.2.3 Beam Bending, X-ray Target, Filtration and Collimation

On exiting the accelerator, the beam enters the bending system (Figure 1-1g) to turn the beam into the treatment axis (Karzmark C J *et al*, 1993b). This is optional, since some machines used in the low energy range frequently have the accelerating waveguide mounted in-line thus obviating the need for the beam bending system shown in (Figure 1-1g.). This option though, requires the use of the 'standing wave' type of accelerating structure compared the 'travelling wave', since alternate cells in the wave not contributing to beam acceleration are placed outside the beam line and only form part of the RF circuit producing the standing wave (Karzmark C J *et al*, 1993d, Karzmark C J & Pering N C, 1973). This reduces gantry weight and eliminates any associated shortcomings in the beam bending process, but requires the gantry to be raised to allow for extra floor clearance during rotation of the in-line waveguide. This increase in gantry height results in an increase in the iso-centric height. Since the target volume to be treated is placed at the iso-centre, this is a disadvantage to the machine operator.

The electron beam then encounters the target (Figure 1-1h) where X-rays are produced by Bremsstrahlung or 'Braking Radiation'. At mega-voltage energies, most of the X-rays produced are forward projected, this effect increasing with beam energy.

Next, primary collimation (Figure 1-1i) results in a circular beam with a diameter suitable for producing a field of maximum size 40 cm x 40 cm at the isocentre after secondary collimation. Precise restriction of the field boundary by primary collimation also limits the scatter in the radiation head of the machine and defines the maximum dimensions of the remaining components in the beam path.

To produce a radiation field of uniform intensity, a flattening filter is required (Figure 1-1j) (Karzmark C J *et al*, 1993i). A typical beam profile in the Gun-Target (GT) axis, as defined in Figure 1-11, for 6 MV X-rays taken with the flattening filter removed is shown in Figure 1-3. The peak of the profile is coincident with the

Central Axis (CAX) of the primary collimator and the profile is symmetrical about it, which is a fundamental requirement for the filter to produce a uniform field. Since the field profile and the attenuation of the filter material are energy dependent, a series of filters or combination of filters is required to produce a set range of X-ray energies. This is achieved by arranging the filters in a mechanised tray or carousel. The beam energy, lateral/radial position and angle of incidence with the filter will affect the geometry of the flattened clinical beam, and it is therefore essential that these parameters are precisely monitored and controlled.

The ionisation chamber or beam monitor (Figure 1-1k) is the next component in the beam path. Its function is to monitor the dose and geometry of the beam. Since patient dosimetry is critical, the dose monitoring plates are duplicated. Two electrically separate channels process the dose signals to generate a value of dose rate and integrated dose for each channel.

A set of segmented plates monitors the beam geometry to produce signals to identify deviations in beam position and energy (Karzmark C J *et al*, 1993c). These signals are fed back to the machine control systems to correct errors and are also used to generate interlocks to terminate a treatment exposure if the beam is out of tolerance (Karzmark C J *et al*, 1993a).

Finally, secondary collimation (Figure 1-1m) allows the beam to be shaped to the prescription. All modern machines allow complex beam shapes to be produced by a combination of diaphragms and individual leaves in the form of a Multi-Leaf Collimator (MLC), (Section 1.3).

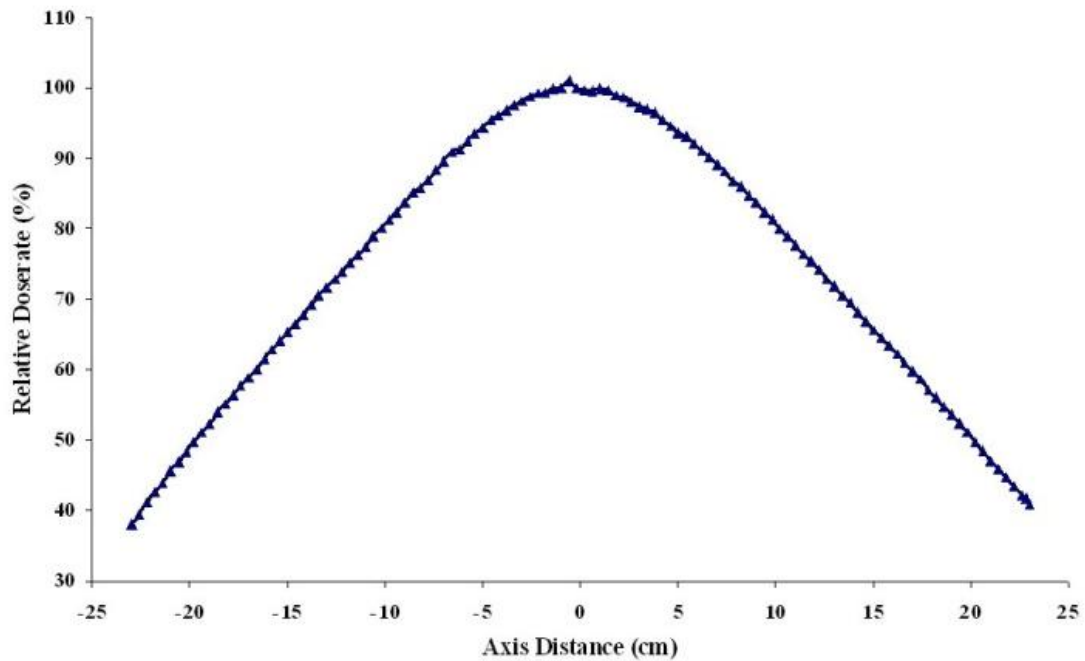


**Figure 1-3:** Raw beam profile measured at the isocentre with the flattening filter removed. Radiotherapy Department Leicester Royal Infirmary (Elekta SL15i Serial No. 5455 May 2001).

#### 1.2.4 System Control and Monitoring

The machine control and instrumentation systems allow the automation of many accelerator control functions with virtually no human intervention (Greene D. & Williams P C, 1985b, Karzmark C J *et al*, 1993a). Parameters such as set points, gains, offsets and trip limits for control elements are derived from a combination of preset potentiometers in analogue systems or software values in digital/computer controlled systems. These are set during commissioning, maintenance and quality assurance. Operating parameters and limits are checked and adjusted as part of a planned schedule and linked to a regular on-going dosimetric quality control of the clinical beams (Thwaites D I *et al*, 2005).

A high level of confidence is required in control system reliability and the ability to detect the onset of scenarios that may compromise safety. Backup and duplication of critical control systems are key elements of the safe operation of the machine. Machine control systems will be presented in more detail later in the chapter.

### 1.3 Radiotherapy: Aiming to Improve the Therapeutic Ratio

Radiotherapy is the field of clinical medicine which treats cancers by the application of ionising radiation. The aim is to deliver a homogeneous radiation dose to the tumour whilst minimising dose to surrounding normal tissues. To achieve this, a tumouricidal radiation dose is delivered in a fractionated regime, which progressively kills the cancerous cells but allows time for normal cell repopulation. This maximises loss of cancerous tissue with the least complication to healthy tissue. The probability of tumour control and sparing of healthy tissue is characterised by two sigmoid curves (Mayles P & Thwaites D I, 2007, Ford J C, 2001) shown in Figure 1-4.

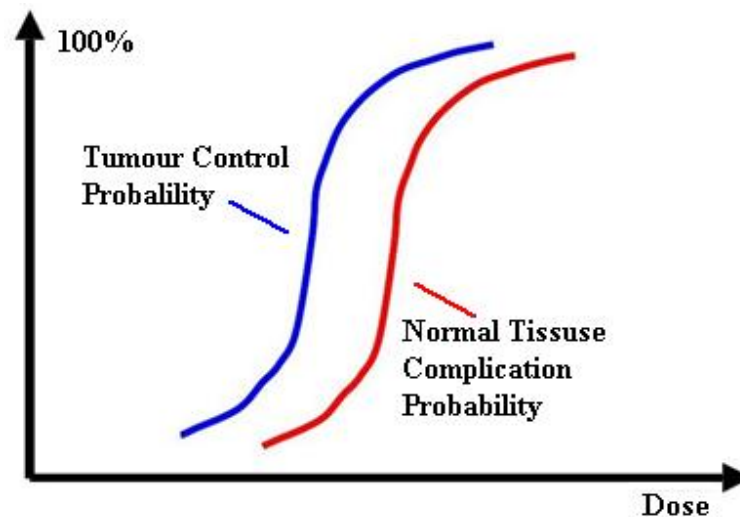


*Figure 1-4: Dose response curves for tumor control probability and tissue complication (Based on Ford J C, 2001).*

The total dose and fractionation regime are designed to achieve a high point on the Tumour Control Probability (TCP) curve with a low point on the Normal Tissue Complication Probability (NTCP) curve. The therapeutic ratio is thus the distance between the curves along the dose axis. The greater the distance, the greater is the probability of tumour control for a fixed level of normal tissue complication, assuming that the same dose is delivered to both target volume and surrounding tissues (Section 8.1.1). The goal of conformal therapy is to produce a regime that results in a much lower dose to the surrounding tissues compared with the target, which increases the distance between the curves (Webb S, 1993). Conformal therapy

can be achieved using shaped shielding blocks, which are unique to each patient, or by the use of an MLC which comprises small leaves that intercept the beam to shape the radiation field to conform to the tumour (Jordan T J & Williams P C, 1994.)

### 1.3.1 Intensity Modulated Radiotherapy

Radiotherapy has traditionally been accomplished with radiation beams of uniform radiation intensity across the field. IMRT is a relatively recent novel approach to conformal therapy that allows the delivery of highly complex dose distributions (Guerrero Urbano M & Nutting C, 2004a, Guerrero Urbano M & Nutting C, 2004b, Nutting C M *et al*, 2000, Webb S, 2005b). There are a number of ways of delivering Intensity Modulated Beams (IMB) for radiotherapy. Kijewski P K. *et al*, 1978 produced a wedge-shaped dose distribution by moving a secondary collimating diaphragm across the radiation field. Extending this concept further by using an MLC, it is possible to produce complex dose distributions using two methods (Williams P C, 2003). The first is to deliver a succession of static beams through different MLC shapes, known as ‘Step and Shoot’ IMRT. The second uses the MLC to move a dynamically shaped aperture across the field. This is called Dynamic Multi-leaf Collimation (DMLC). Furthermore, the accelerator can be rotated during DMLC to enhance conformation of the target volume, tissue sparing and the sparing of organs at risk. This is known as Intensity Modulated Arc Therapy (IMAT) or Volumetric Modulated Arc Therapy (VMAT). These techniques will now be described in further detail, and the technical aspects discussed in Section 1.7.

#### 1.3.1.1 Step and Shoot IMRT

A step and shoot sequence consists of a number of sub-fields or segments with differing MLC shape for each segment. The MLC is stationary during beam on, when the segment is delivered. The accelerator is paused in-between each segment, allowing the MLC to be driven to the next field shape. Segments are stacked together to

produce the required distribution (Yu C et al, 1995) for each field. A method was developed to optimise the number of segments and total dose known as Direct Aperture Optimisation (DAO) (Bedford J & Webb S, 2007, Jiang Z *et al*, 2005, Shepard D *et al*, 2001). Shepard D *et al*, 2001 states that in comparison with traditional optimisation techniques, DAO can result in a significant reduction in both the number of segments and monitor units (MU). Where an MU is an arbitrary unit used by the accelerator dosimetry system for dose measurement and it is the responsibility of the radiation physicist to calculate the number of MU necessary to give the required dose in Gy (See Section 3.4.2.2, Pages 70 and 71).

### **1.3.1.2 DMLC**

This method uses opposing MLC leaves to produce a moving aperture across the treatment field whilst the radiation is on. Each opposing leaf pair moves with a different speed as a function of time, and aperture opening, to create a window that results in a variable intensity fluence being delivered across the field (Convery D & Rosenbloom M E, 1992, Kallman P. *et al*, 1988).

### **1.3.1.3 IMAT and VMAT**

IMAT is a delivery technique where the field shape changes during accelerator gantry rotation, and in later implementations, the dose rate is also changed. The intended dose distribution builds up using multiple superimposing gantry arcs. It was first proposed by Yu C, 1995 and patented as an invention by Yu C, 1998 for implementation on the Philips SL25 series of accelerators. Later, VMAT was proposed as a single arc approach to delivering rotation IMRT by Otto K, 2008.

## **1.3.2 Supplementary Developments**

Accurate targeting of the tumour volume has been enhanced by the introduction of imaging systems attached to the accelerator gantry to evaluate geometric and geographic error. The 'Electronic Portal Imaging Device' (EPID)

(Althof V *et al*, 1996) acquires an image directly from the treatment beam using a small number of monitor units on a active matrix flat-panel imager (Kirby M & Glendinning A G, 2006) for patient geometric verification. Image quality is limited, though, in the megavoltage energy range. Alternatively, a kilo-voltage X-ray system and flat panel imager are mounted on the treatment machine gantry orthogonal to be treatment head. As well as planar images, it is also possible to produce 3D images using cone beam Computerised Tomography (CT) by rotating the imaging system around the patient. The patient is setup on the accelerator table ready for treatment. An image of the setup is acquired prior to treatment and compared with a reference image, usually obtained from the patient's planning CT. Using anatomical, or in some cases fiducial markers, the displacement between the target and the reference is measured and the patient repositioned accordingly. This development is known as Image Guided Radio Therapy (IGRT). Further consideration of IGRT systems is beyond the scope of this thesis

Radiotherapy has traditionally been delivered using beams of X-rays and electrons. As technology has developed, other particles such as protons and neutrons have been used clinically and currently the use of more exotic particles is under development (Lennox A J, 2001). Further discussion of these technologies is beyond the scope of this thesis.

#### **1.4 The Development of Linear Accelerator Systems**

A considerable amount of pioneering research was undertaken to establish machines capable of energies of 1 MV and above for use in clinical radiotherapy (Thwaites D I & Tuohy J B, 2006, Meredith W J., 1984, McGinty G K, 1962, Miller C W, 1962). In the 1950's, the move to megavoltage therapy, initially using Cobalt-60 and then the linear accelerator, led to greater penetration and skin sparing (Halnan K E, 1999). Due to the high level of technology required for accelerators to deliver

standard therapy beams, Cobalt-60 machines are still used in many developing countries (Lennox A J, 2001).

### 1.4.1 Conception

In 1928 a Norwegian physicist named Rolf Wideröe (Wideroe R, 1928 cited in Voss G A, 1997) conceived a radio frequency (RF) based accelerator built on a concept developed in 1925 by Swedish physicist Gustav Ising (Ising G, 1924 cited in Karzmark C J & Pering N C, 1973). The apparatus was based on a series of co-linear drift tubes contained in an evacuated glass cylindrical vessel (Figure 1-5). Each drift tube was alternately connected to a high-frequency voltage source. The drift tubes were of increasing length so that the accelerating particle bunch arrived at the end of each tube in phase with the peak accelerating voltage occurring between successive tubes.

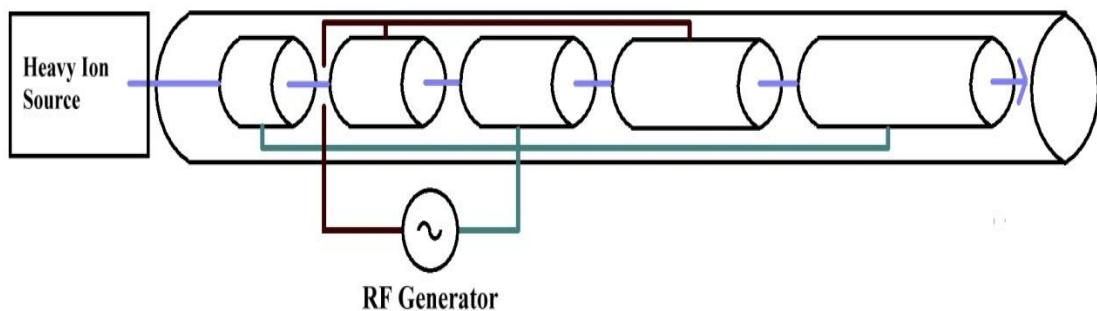


**Figure 1-5: Early linear accelerator design. Rolf Wideröe type for heavy ions (Adapted from Karzmark C J & Pering N C 1973).**

The system was only suited to the acceleration of heavy ions, since the comparatively low mass of electrons would cause a rapid increase in velocity between the gaps and therefore require such inordinately long drift tubes as to make the system unusable as described by (Karzmark C J & Pering N C, 1973). This meant that the apparatus was not suitable for the production of high energy X-rays and so was of no use in the medical field at that time.

### 1.4.2 Early Accelerators

In the mid-1930s, William Hansen in Stanford USA conceived an electron accelerator based on the resonant microwave cavity (Dupen W D, 2007). The device was known as a rhumbatron. A high energy beam was produced by repeatedly passing electrons through the cavity, gaining energy on each successive pass. The problem with the system was the inadequate RF power sources available at the time which made the system impracticable. The demands of World War II accelerated the development of microwave power devices for their use in radar (Karzmark C J & Pering N C, 1973). The magnetron (Boot H & Randall J, 1976, Collins G B *et al*, 1948) in England and the Klystron power amplifier (Varian R H. & Varian S F., 1939, Meddaugh G E, 1994) in the USA were both suitable devices for generating megawatts of 'S' Band pulsed RF power at 3 GHz and therefore ideal as microwave power sources for linear accelerators.

After the end of World War II, the development of the microwave powered linear accelerator continued under William Hansen at Stanford University, California USA and at the Atomic Energy Research Establishment (AERE) Great Malvern, England led by D W Fry (Fry D W & Walkinshaw W, 1949). Both groups produced accelerating structures based on the travelling wave principle (Mullett L B & Loach R G, 1948).

The first clinical machine was installed at the Hammersmith hospital London in 1952, manufactured by Metropolitan-Vickers Electrical Ltd. Utilising a corrugated accelerating waveguide of length 3 m, a beam energy of 8 MV was achieved using a 2 MW magnetron (Miller C W, 1953).

### 1.4.3 Later Developments

In the 1960's, improvements were made in the construction of accelerating waveguides by electro-forming. This reduced the number of components in the

assembly process. Also, the ‘sputter ion pump’ replaced the traditional ‘oil diffusion pump’ for maintaining the high vacuum required in the accelerating structure (Loverock L, 2007). This was a significant development because the ‘oil diffusion pump’ suffered from ‘back migration’ of oil from the pump assembly, causing contamination of the accelerator’s vacuum system.

In 1986, Varian Medical Systems in the USA filed a patent (Whitham K, 1986) on the design of a machine based on the standing wave principle using side coupled waveguide cavities (Knapp E A *et al*, 1968). Using this design, waveguide shunt impedances in excess of  $100 \text{ M}\Omega \text{ m}^{-1}$  could be achieved, greatly reducing the length of the accelerating structure to only 30–35 cm for 6 MV acceleration (Knapp E A *et al*, 1968). This enabled low energy machines to be constructed with the waveguide in line with the target, thus obviating the need for a beam bending system. However, high energy designs where a longer accelerating structure was required to achieve the beam energy still needed the waveguide to be horizontally mounted and consequently required a beam bending system. Even so, the standing wave accelerating structure would always be considerably shorter than its travelling-wave counterpart for a given beam energy.

Accelerators using horizontally-mounted waveguides require a beam bending system to project the beam into the treatment plane. Early machines used a transverse magnetic field to produce a  $90^\circ$  bend. It was common on single energy machines to use a fixed magnet (Figure 1-6).

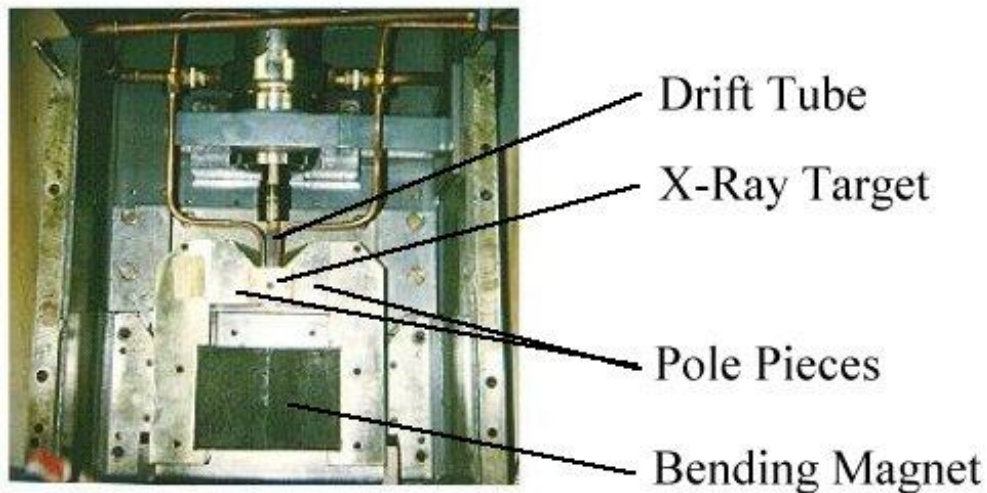


**Figure 1-6:** *Picture of a fixed magnet 90° beam bending system (plan view with gantry at 180°). Radiotherapy Department Leicester Royal infirmary (Philips SL75/5 Serial No. 351. August 1996.) (Printed by kind permission of Elekta Limited).*

Although simple in concept, this system produced errors in the trajectory of the beam due to the change in beam angle with beam energy. An increase in the energy caused the beam to under-bend and conversely a decrease in beam energy caused an over-bend (Figure 1-7).

This undesirable effect caused major problems, since an incorrect beam trajectory entering the field flattening filter produced a tilt in the final treatment beam. This effect was very pronounced in the machine illustrated in Figure 1-6 and required regular adjustment to the beam control system servos to maintain a clinically acceptable beam. This was also reported by Blad B *et al*, 1998.

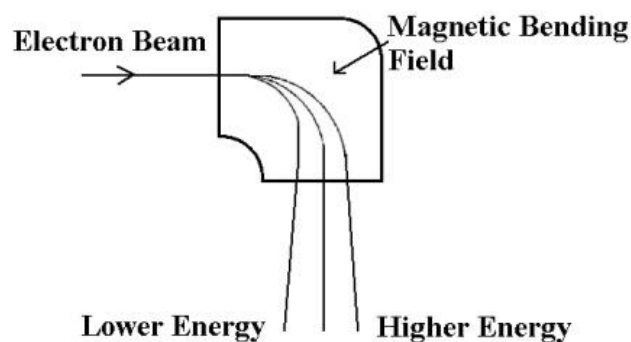


**Figure 1-7:** *Spectrometer effect of a 90° beam bending system (Taken from Thwaites D I & Tuohy J B 2006 with permission).*

To overcome this problem, the ideal bending magnet would focus the electron beam to a common point and trajectory. Known as a ‘doubly achromatic’ or  $270^\circ$  bending system, the first system was designed and patented by Enge H A, 1968. Its operation depended on the increasing magnetic field gradient as shown in Figure 1-8. The system was inherently more stable than its  $90^\circ$  counterpart, although any spatial deviation of input beam trajectory would be translated to the output. Using a servo controlled beam steering system, this was easily overcome.

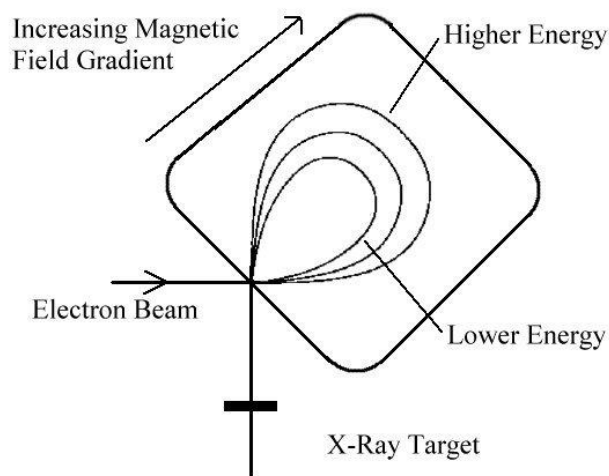


**Figure 1-8: Enge's doubly achromatic bending (Taken from Thwaites D I & Tuohy J B 2006 with permission).**

One operational drawback with the  $270^\circ$  bending system is that extra clearance above the accelerating waveguide is required to accommodate the magnet assembly. Thus, iso-centric height needs to be raised to allow clearance to rotate the machine under the treatment table.

To overcome this problem, a novel design by Philips Medical Systems Crawley UK (Allen D, 1986), now Elekta Oncology Systems Ltd., was to split the  $270^\circ$  bend into three segments. This is now standard on their ‘SL series’ machines (Botman J *et al*, 1985). To accommodate the system, the accelerating structure is inclined by  $22.5^\circ$  with the electron gun located at the same level as the iso-centre. With reference to Figure 1-10 magnets M1 and M2 have a  $45^\circ$  bending angle and M3 a  $112.5^\circ$  bending angle to bring the beam into the treatment plane. This arrangement is

known as an achromatic triple or slalom beam bending system (Figure 1-9). A summary of beam bending systems can be found in Greene D. & Williams P C, 1985c, Karzmark C J, 1984, Karzmark C J *et al*, 1993b, Loverock L, 2007.

The scene was set for machines currently in use today. No major developments have taken place in beam generation systems since the triple bending system, but work has focused on improving stability and extending the operating life of components, including the development of the fast tuning magnetron (Budgell G *et al*, 2001, e2v Technologies Ltd, 2002b), also see Chapter 2, Section 2.2.2.2, Page 45.

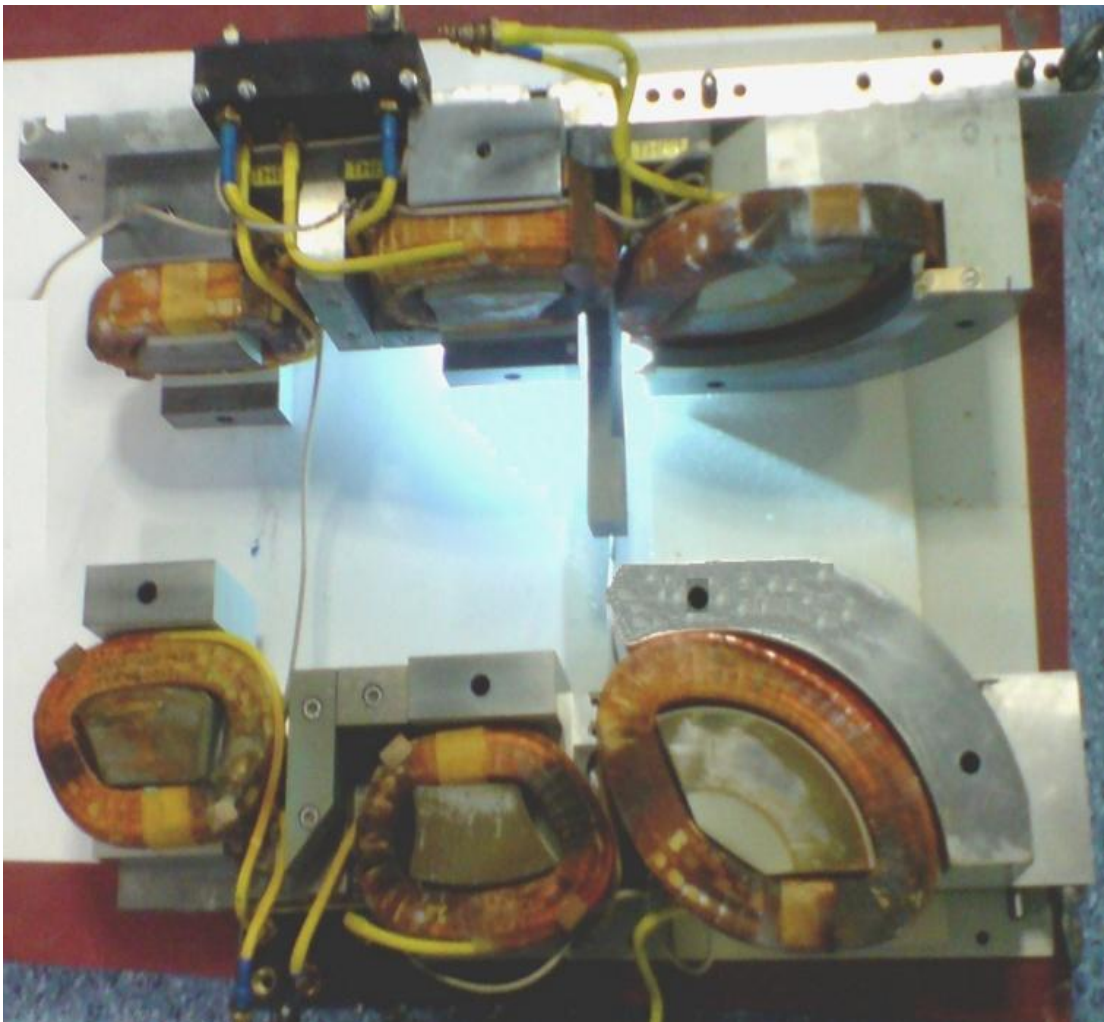


***Figure 1-9 : Picture of the bending magnet assembly used on the Elekta ‘SL series’ machines. The assembly is shown removed from the machine and split open during repair (Radiotherapy Department Leicester Royal infirmary, Elekta SL15i Serial No. 1188), (Printed by kind permission of Elekta Limited).***

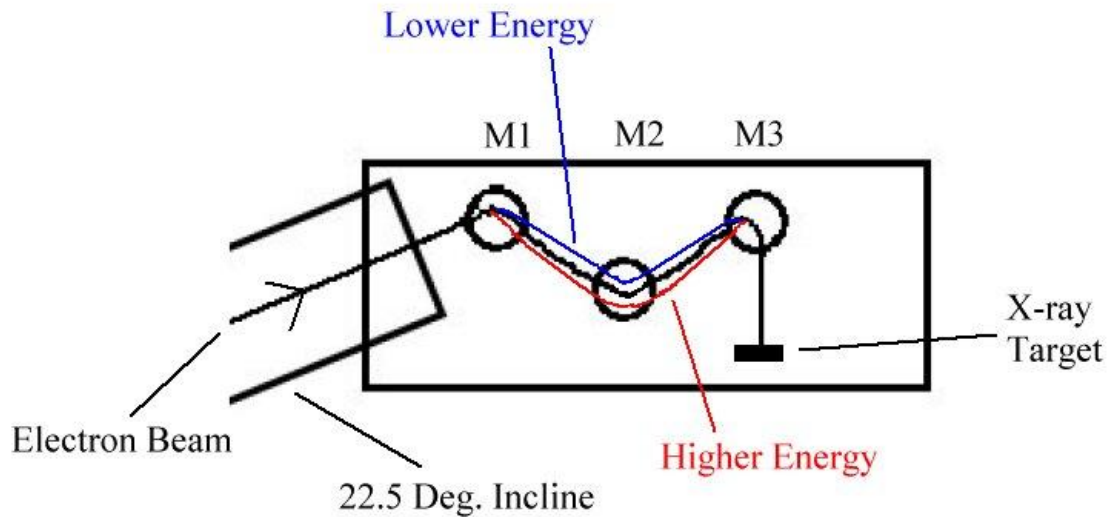


*Figure 1-10: Achromatic triple magnet system used on the Elekta SL Series accelerators (Adapted from Botman J et al, 1985).*

## 1.5 The Modern Medical Linear Accelerator

The modern medical linear accelerator is a highly sophisticated, versatile and stable machine, with improvements coming from new technologies in engineering and materials science. In the author's experience of 25 years, significant advances have been made in magnetron reliability, particularly in the mid 90's when links were forged between magnetron and accelerator manufacturers (Bates A *et al*, 1996). Solid-state design has brought about major advances in control systems, resulting in more compact and stable electronics hardware, but digital technology and computing have been the chief driving forces in the implementation of new treatment regimes (Greene D. & Williams P C, 1985b).

### 1.5.1 Control Systems

Although there are many control systems, such as for machine movements, power supply systems for beam control and temperature controllers, on a medical linear accelerator, only those relating to beam generation and transport will be discussed here.

### 1.5.1.1 Electron Beam Focusing and Steering

Since electrons are negatively charged particles, mutual repulsion will occur during the course of acceleration, resulting in beam divergence. A focusing electrode is thus used in the electron gun assembly, and solenoidal focusing coils are placed along the length of the accelerating waveguide to provide correction. Generally, the electrostatic focusing in the gun is fixed, but the electromagnetic focusing of the accelerating waveguide is adjustable. Furthermore, static and dynamic (mainly during gantry rotation) mechanical misalignments of components along the length of the accelerating structure and external magnetic field effects, result in beam trajectory errors to the required beam line (Karzmark C J, 1984). These are known as ‘steering’ or ‘centring’ errors and are corrected by using sets of Helmholtz coils, placed in orthogonal pairs, along the beam line (Loverock L, 2007). The purpose of the focusing and steering systems is to produce a finely focused electron beam, which strikes the X-ray target with the correct trajectory, resulting in a uniform and correctly positioned radiation profile at the isocentre.

Values for the focusing currents for the accelerating waveguide are fixed and usually determined during commissioning of the beam energy by the manufacturer at the factory, and are generally fixed for the life of the machine. Steering current values though, are of more interest to the engineer in the field, since these need to be reconfigured when components in the machine are replaced. They may be static in setting or dynamically controlled by a servo control system. The Elekta system is described in Section 7.2, and other manufacturers’ systems are similar, depending on the type of beam transport, accelerating waveguide and beam bending systems employed (Karzmark C J, 1984, Podgorsak E B, 2005).

### 1.5.1.2 RF Generation

Control of the RF generator should not be overlooked, since energy transfer to the electron beam from the RF wave in the accelerator is dependent upon RF power and frequency. In the main, for most manufacturers' designs, the accelerating waveguide operates at resonant frequency and this is dependent on the dimensions of the accelerating cavities. Ambient temperature level and temperature rise from power dissipation due to copper losses during 'beam on', affect the resonant frequency. Additionally, if a magnetron is used as the RF power generator, where the resonance occurs in cavities in the anode block, temperature rise due to anode power dissipation has a pronounced effect on the output frequency of the device. The frequency at any tuner setting will typically increase by around 630 kHz per Kw reduction in mean input power (English Electric Valve Company Ltd, 1974). This is not the case for a klystron, where the device is only a microwave amplifier, and frequency is controlled by an isolated low power RF driver and is thus unaffected by changes in the klystron operating temperature. A precise, Automatic Frequency Control (AFC) system is required to match the RF generator operating frequency to the changing resonant frequency of the waveguide to maintain optimum power transfer to the electron beam (Karzmark C J et al, 1993e). This is particularly the case at radiation start-up and after any change in PRF during radiation during the delivery of dynamic beam sequences.

At radiation start up there an initial rise in temperature in the waveguide as power is dissipated into the walls of the cavities due to losses: a value of 16 KW dissipation for a 4.5 MeV standing wave, 'S' band accelerator is quoted by Nepal N *et al*, 2001. During dynamic power conditions the AFC system must 'track' the output frequency of the RF generator to match the waveguide resonant frequency, since this may affect the electron beam energy (Casebow M & Mayles P, 1999a), and in the case of a magnetron also compensate for the change in frequency due to the anode power dissipation. Should the PRF change during 'beam on' then the mean power

dissipation, and therefore resonant frequency, of the accelerating waveguide will change. The AFC system must then adjust the frequency of the RF generator to compensate. It's now common design practice to ascertain the accelerating waveguide's resonant frequency by measuring the phase difference between the RF input and output of the accelerating waveguide. There is a direct relationship between the phase difference and the resonant frequency, and a microwave phase discriminator is used to produce an error signal; this is the case for both travelling and standing waveguides.

A pulsed modulator, as mentioned earlier in the chapter, provides a stable pulse of electrical energy to the RF power generator, and also on some designs to the electron gun cathode to launch the electron cloud into accelerating waveguide. Other designs use a fixed DC power supply. To maintain stable beam generation, precise control of this and all electrical services to the RF generation systems is important in the control of RF power and frequency.

### 1.5.1.3 Generic Requirements

The generic requirements for beam control systems on all but the most simple of medical linear accelerator designs are to provide control functions with selectable references, thus allowing the optimal configuration of parameters for the delivery of multi-mode (X-ray or electron), multi-energy and dynamic therapy beams (Karzmark C J *et al*, 1993f, Purdy J A. & Goer, D A, 1985, Tanabe, E & Hamm, Robert W., 1985).

These are fabricated using sophisticated hardware and/or software to configure control parameters such as gains, operating limits, safety interlock trips levels and time constants for the various operating modes of the machine. In order to set most of these parameters, the machine needs to be radiating, and thus the setting facility must be provided in the machine control area outside the radiation bunker. This was achieved in earlier designs by routing the accelerator control signals and readouts to

and from a cabinet situated outside the treatment room containing the control electronics, and then adjusting potentiometers to configure the various operating modes. The trend now is to keep the control hardware in the accelerator gantry or stand, limiting the cabling to and from the control area. This results in a neater cabling structure, but more importantly, helps to reduce system noise. Setting values are then programmed from the control area using a remote digital link. Furthermore, this reduction in cabling allows the designer to consider more parameters for selection. A further advantage of this method is that the setting parameters are stored numerically, for each operating mode, by a control computer, and are thus easier to backup, recover and log.

## 1.6 Quality Assurance, Test and Measurement

Accuracy and precision in radiotherapy, as described in Section 8.1.1.1, and the clinical consequences, Section 8.1.1.2, where a quality assurance program aims to optimise tumour control and sparing to healthy tissue (Section 1.3) are critical to a successful outcome, and safe delivery of radiotherapy. An small degree of variation of specific parameters is allowed within a quality control process, as determined by quality standards (Mayles P & Thwaites D I, 2007, Thwaites D I, 1999, Thwaites D I *et al*, 2005). This is achieved by limiting systematic and random errors in all stages of treatment to attain doses as close to the ‘target value’ as possible.

The introduction of new technologies often requires new test and measurement capabilities. Advancement in medical accelerator technology to meet clinical need and the subsequent requirement for test and measurement equipment for quality assurance and machine development are reviewed concurrently in the next chapter.

Measurement is the process by which parameters and variables involved in the operation of a system are acquired. These may be measured and displayed in ‘real time’, where repetitive events are overlaid based a sample rate or known trigger point,

or digitally stored as ‘single events’ for analysis ‘off-line’ (Tektronix Inc, 1989), where there is the need to collect information faster than the human eye can interpret. Faithful extraction of the underlying process, without misrepresentation, requires the frequency of measured events and the bandwidth of the measuring system to be considered, if the properties of process are to be meaningfully measured.

**1.6.1 Measurement Axis**

The radiation profile measurement convention for the thesis is shown in Figure 1-11, where the view is from the X-ray source (beams eye view) with the gantry at zero degrees rotation. The point of reference is the accelerating waveguide; therefore the transverse axis moves with the gantry rotation.

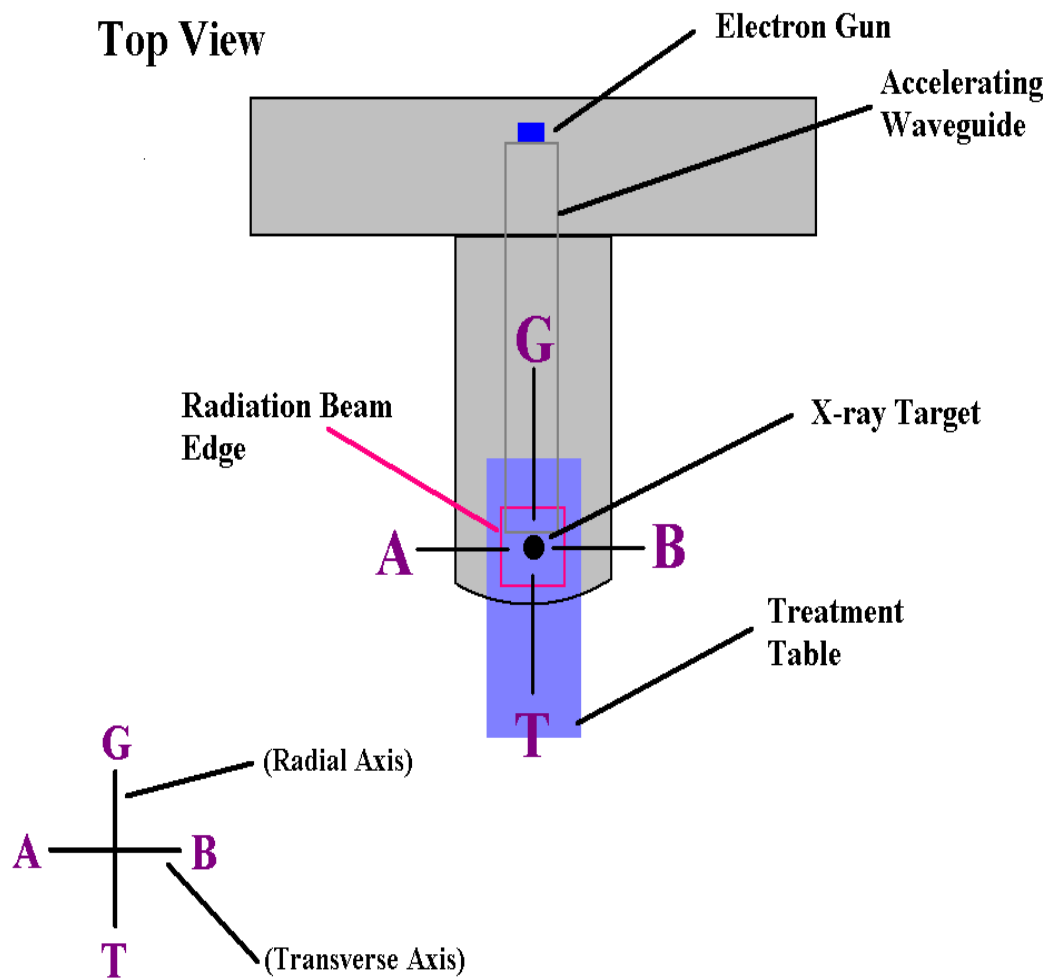


*Figure 1-11: Diagram of the measurement axis used in the thesis, radial or ‘GT’ and transverse or ‘AB’. The accelerator gantry is at zero degree rotation.*

## 1.7 Dynamic Therapy

It is important to consider that during the development cycle of dynamic therapy methods, successive implementations have been based on control system upgrades in hardware and software to existing medical linear accelerators technologies. Where the original system design specifications were for less demanding treatment regimes, even after extensive upgrading, there may still be shortfalls in the basic technology. The high demands of the AFC system for step and shoot IMRT were discussed in section 1.5.1.2. The fast tune magnetron was introduced to overcome the inadequacies of the gearbox tuned magnetron design (Budgell G *et al*, 2001, e2v Technologies Ltd, 2002b). The focus in this section will be to establish the pertinent engineering issues in the generation of radiation beams for the dynamic therapy techniques discussed in Section 1.3.1.

### 1.7.1 The Production of Intensity Modulated Beams

The aspects of beam generation relating to the production of dynamic beams will be discussed next. It would be inappropriate not to mention the MLC (Section 1.3) at this point, since this is the fundamental element in beam shaping for dynamic therapy and is also a major topic of research. Matters such as MLC leaf positional and speed accuracy, leaf transmission, leaf-end leakage, and inter-leaf leakage have been extensively investigated (Chui, Chen Shou *et al*, 1996, LoSasso, Thomas *et al*, 1998, LoSasso, Thomas *et al*, 2001, Mayles P, 1999). Further discussion of the MLC is beyond the scope of this thesis, since radiation beams will all be measured with the MLC leaves fully retracted to a 40 x 40 cm field size, unless otherwise stated.

#### 1.7.1.1 Step and Shoot IMRT

The advantage of this method is that the MLC leaves are stationary during radiation beam delivery (Yu C *et al*, 1995); therefore it is straightforward to verify the

leaf positions in the event of a failure of the MLC during treatment. The disadvantage through, is the increased number of beam start-up transitions.

Stabilisation of microwave RF power at ‘beam on’ results in changes in operating conditions in the RF power generation systems, particularly for magnetron powered machines (Section 1.5.1.2), and also for the accelerating waveguide, due to temperature changes. This results in a high workload for the AFC control system. Furthermore, the servo control of beam transport parameters is not operating under steady state conditions during the startup phase. This is particularly the case in accelerators that use the electron gun filament current to control electron beam energy, since thermal lag in the filament delays stabilisation of the electron beam current and therefore beam energy. This will be explored later in Chapter 6.

Control system inaccuracies may result in inferior beam radiation profiles and dosimetric errors. Additionally, errors may be exacerbated if the servo controlled elements are not configured for operation at their optimum values. Linac performance for the delivery of ‘small MU per segment’ can be an issue in IMRT dose delivery accuracy.

### **1.7.1.2 Dynamic Multi-leaf Collimation**

This method does not suffer from the problem of multiple start-ups, but is more risky from a dosimetry point of view if the machine malfunctions during an IMRT treatment, where the exact point in the treatment sequence would need to be known in order for the treatment to be completed at a later time. Some mechanical backlash in the MLC leaves and has been observed as the gantry rotates.

### **1.7.1.3 Rotational Therapy (IMAT)**

IMAT treatments deliver an improved dose distribution by rotating the radiation beam around the patient with modulation of field geometry and doserate. Beam control system work load is increased since the doserate, beam energy and

beam profile are susceptible to changes induced by rotating the accelerating structure (Karzmark C J, 1984). Where the RF power device is a magnetron, and is gantry mounted, there can be a particular problem with sag in the cathode assembly (Greene D. & Williams P C, 1985d) resulting in modulation of the RF output power and frequency with gantry rotation. This was effect was noted by the author on an older magnetron type M5125, then with the development on the M5028 though to the fast tune version (e2v Technologies Ltd, 2002b, Budgell G *et al*, 2001) , the effect was minimal but still measureable. To keep the ‘beam on’ time to a minimum, it is desirable to make the doserate as high as possible to limit the exposure time to the patient, but this is limited by the maximum rotation speed of the gantry.

### 1.7.2 Small Segment Exposures

Accelerator performance during start-up was first presented in the 1980’s. Dosimetric performance at low monitor unit settings was evaluated for a range of machines (Barish R *et al*, 1987, Das I J. *et al*, 1991). An error exceeding 20 % was reported for some accelerators during the first few monitor units, but less than 5 % when more than 10 monitor units were delivered. Rajapakshe R & Shalev S, 1996 used a camera-based electronic portal imaging device (EPID) to evaluate beam characteristics during the first few monitor units. Hansen V N *et al*, 1998 performed a comprehensive study of the start-up characteristics of the Philips SL25 series accelerator across three radiotherapy centres. Measurement over a range of PRF’s and electron gun aiming levels were included in the study but only on a single machine. The term ‘optimal value’ was used for the electron gun aiming level, but there was no clarification regarding the electron gun control system calibration. In addition, the start-up performance of the Elekta SL Series was compared to a Siemens Mevatron (Buchgeistera M & Nusslin F, 1998) to evaluate the new Elekta ‘slitless’ flight tube design. The scheme also involved replacing the software controlled electron gun servo with discrete hardware. Comparable performance was reported compared with the

Siemens machine. However, Ravikumar, Manickam *et al*, 2005 concluded that the accuracy at low monitor unit settings should be confirmed for the Mevatron accelerator before implementing IMRT treatments.

Errors in the delivery of small segments (between 2 and 4 MU) for the Elekta SLi series machine have been reported. Sharpe M B *et al*, 2000 stated that relative to the dose delivered at 100 MU, +/-2% for exposures larger than 4 MU, flatness and symmetry met quality assurance standards. The relative dose per MU was measured and found to be constant within about 1 % down to fields with only 2 MU (Martens C *et al*, 2001a); however, there was no mention of whether the machine used the new type 'slitless' flight tube (Section 2.2.2.1). For the Siemens Primus accelerator for both 6 and 15 MV X-rays, dose linearity was reported as being stable for beam segments above 5 MU (Reena P *et al*, 2006, Aspradakis M *et al*, 2002, Cheng C W & Das I J., 2002). A Siemens Primus linear accelerator was also investigated by Saw C *et al*, 2003 at 6 and 23 MV beam energies, similar results were obtained for both energies, the dose linearity was within 2% above 2 MU and better than 1% for monitor units greater than 5 MU.

A study performed in 2007, where the relative dose per MU was measured on an Elekta machine (Mohr P *et al*, 2007), found it to be constant within about 1% with exposures down to 2 MU and deviations of 2% at 1 MU, and in fact never exceeding 2% at 1 MU which is an encouraging result. However, this differs from mainstream publications in this review, where values lower than 2 MU are all greater than 2% for Elekta Machines. Also, field flatness and symmetry were not measured, though other research work was referenced (Hansen V N *et al*, 1998, Ravikumar, Manickam *et al*, 2005). However, the more recent of the two references was based on the field flatness and symmetry performance for the Siemens Mevatron KDS machine, not the Elekta.

Publications emphasise that it is important to characterise the dose delivered per MU, the beam flatness, and the beam symmetry as a function of the number of

MU delivered (Kang, Sei Kwon et al, 2008, Sharpe M B et al, 2000, Williams P C, 2003), but there is minimal discussion about the source of errors present during the first few MU's of a beam. Li J et al, 2012 investigated dose accuracy on a Varian C-series Trilogy, using the 'C-series MLC controller' and a Varian TrueBeam machine, using a single integrated controller. They found a significant improvement in the TrueBeam machine for all combinations of small MU's per segment (1 to 10) and doserates in the range of 200 to 600 MU/min, concluding that this was due to a faster sampling rate, and the improved integration of the controller. Li J et al, 2003 compared the fractional MU delivered by two Varian machines in the step-and-shoot mode as recorded in the MLC logfiles to those measured using a commercial two-dimensional diode array. Large discrepancies were found between, that intended and those delivered. These were larger for small MU segments at higher doserates and some of the small MU segments were completely undelivered.

### 1.7.3 Radiation Symmetry During Gantry Rotation

Rotational symmetry with gantry angle has been measured on an Elekta SL20 and compared to Varian Clinac 6/100 and Clinac 4/100 machines (Loyd M D. *et al*, 1989). A greater variation in the Elekta machine at 6 MV in both radial (2%) and transverse axis (1.2%) compared to the Varian, where radial was < 0.8% and transverse was <1.5%. There was no origin of rotation quoted. A smaller value would be expected, since the Varian Clinac 6/100 and Clinac 4/100 machines used inline waveguides (Section 1.2.3). Bedford J & Warrington A, 2009, using an Elekta SL series machine, established similar results for the GT axis, but found that the AB axis (AB axis is defined in Figure 1-11) deteriorated with lowering doserate, since this axis is not servo controlled. In the author's experience, symmetry errors can be present in both axes, even though the GT axis is under servo control, and are also dependent on the direction of rotation. This effect has been observed on 3 machines during creation of the steering look-up tables and will be explored in Chapter 7.

## 1.8 Aims of this Thesis

Instrumentation for the measurement of radiation beam profiles is essential for the radiation physicist performing quality assurance of radiotherapy treatment beams. Furthermore, sophisticated test and measurement equipment is vital to the linac engineer, if the performance of linac control systems is to be validated and then optimised. This is important in both the equipment ‘service and maintenance’ role and in machine development environments. Apparatus for both situations is available, and commonly used in the practical situation. However, both of these generally measure data in ‘real time’ in a repetitive or triggered mode (Section 1.6).

Instruments have been developed to record single radiation sequences for dosimetric verification at high temporal and spatial resolutions; these will be discussed in the next chapter. High bandwidth and high capacity data logging systems are also available to the linac engineer. However, from the engineer’s perspective, if a source of artifact or error in a radiation beam profile is linked to a beam generation or transport problem, and is to be accurately assessed, then there may be a need to record both radiation beam profile and instrumentation control signals simultaneously, and at high temporal resolution. Furthermore, since linac radiation is delivered in pulses, the acquisition of such data must be in synchrony with the accelerator beam generation systems.

Having reviewed the literature, particularly for the delivery of small segment exposures (Section 1.7.2), where the problems surrounding dose per MU are well documented from a radiation physics perspective, the engineering challenges involved are generally not presented in the literature. There are two aspects to this: first, the dosimetric consequences are the main concern in the delivery of dynamic therapies, but also the engineering characteristics may be more difficult to quantify with current test and measurement equipment. Moreover, the specialist equipment required may not exist.

The engineering aspects of therapy beam production are addressed in this thesis, with reference to the following questions. Is there a niche for a specialised radiation beam analyser which integrates radiation beam profile measurements with linac control parameter monitoring at high temporal resolution? Furthermore, does this provide a greater insight into machine performance?

This thesis describes the development of a novel ‘radiation beam analyser system’ named ‘Beam Scope’. Fundamental design, construction, characterisation and validation are documented. Also, the value of such an instrument is tested with respect to the engineering mechanisms involved in small segment exposures for step and shoot IMRT, specifically during the beam startup phase (Chapter 6), and with periodic oscillations and errors in radiation symmetry during gantry rotation (Chapter 7). It is anticipated that the system will provide a deeper understanding of the dynamic behaviour of accelerator beam transport and generation control systems during IMRT beam delivery and insights into the dosimetric consequences of beam imperfections for patient treatments (Chapter 8).

Radiation beam measurement methods, commercially available measurement systems and beam production for conventional and dynamic radiotherapy are discussed in chapter 2. Two commercial devices specifically suited to the engineering assessment of radiation beam profiles at high temporal are identified, opening discussion for the designs options in the next chapter.

Initial prototyping and testing of the critical components in the design, construction and final functional tests of the ‘Beam Scope’ are presented in Chapter 3. The instrument is characterised and validated in Chapter 4, then a test data set is measured in Chapter 5 to ascertain what is required for analysis and visual presentation of results. The instrument is used to investigate and characterise one facet of the radiation beam delivery system pertinent to ‘step and shoot’ IMRT in Chapter 6 and then IMAT Chapter 7, on the Elekta accelerator. The use of the system for

dosimetric assessment is then considered in Chapter 8. The thesis is concluded in the final chapter and future work is discussed.

## Chapter 2. Review of Radiation Technologies

Since the first clinical linear accelerators were installed, there has been steady development towards machines capable of high dosimetric and mechanical accuracy for the delivery of radiotherapy. Measurements systems for radiation beam profile measurement and analysis have also developed in tandem with accelerator technology, as the need for greater spatial and temporal resolution grows with advancing treatment modalities.

### 2.1 Radiation Beam Measurement Methods

Several methods are available for the measurement of radiation beam profiles. In one technique, the beam is scanned by a single detector fixed to a carriage driven by a motorised position servo system, either in 'air', nominally in 1 axis or in a 'water tank', with 3 axis movement. Any variation in accelerator dose rate is measured and compensated for by a further fixed detector within the active field.

A 1D beam profile measuring device named the '585 field flatness scanner' (Multivolt Ltd) used at the Leicester Radiotherapy Centre, consisted of a thimble ionisation chamber in a block of Perspex on a mechanical carriage fixed to the accessory ring of the machine, which was scanned across the radiation field. The profile was plotted on a 'flatbed' analogue XY plotter in synchrony with the carriage position. This type of system produced poor resolution in the time domain, since a single sweep of the plotter carriage took of the order of 10 seconds. Since these devices were fitted to the accessory ring, they could be used to make profile measurements at gantry angles other than the standard zero degrees.

Scanning in air has now been largely superseded by diode or ionisation chamber arrays. However, it is still current practice to scan using a single detector in a 'water tank', since water closely approximates the composition of the human body. This allows measurements with interchangeable detector types with traceable

calibrations, and is therefore used to measure definitive data. Furthermore, due to the potential for high precision, determined by the mechanical resolution of the scanner mechanisms, results in high spatial resolution measurements.

Waterproof array based systems are available to measure radiation beam profiles in water. This allows faster acquisition of data, which is paramount in the characterisation of acceleration treatment beams based on the measurement of many parameters during machine commissioning. Likewise, some systems also allow the array to simultaneously scan in the orthogonal axis using the carriage, whilst acquiring data from the array, thus allowing beam profiles in the water tank to be measured in 2 dimensions. This leads though, to an important concern regarding frequency response.

Aliasing in the measurement will occur if periodic oscillations in the radiation beam are faster than the whole scan time. This would be a significant problem in the scenario above where a 2 dimensional profile map is generated at two different sample rates, where aliasing in the axis with the slowest acquisition time would result in data error. Consequently, this method is only valid if the intensity of the beam profile to be measured is virtually static with time.

A similar effect was noted by the author during a quality assurance session using a water tank configured to measure GT axis profiles, where multiple plots of the same axis looked entirely different. Since the scan took around 20 seconds to complete, slow periodic oscillations of significant amplitude in the profile resulted in substantial aliasing of the data. Further measurement of the same axis, using a linear array, confirmed that the gain of the steering servo controlling the axis was too high.

Therefore, a major shortcoming of mechanically scanned devices is their inability to measure dynamic conditions where the beam profile changes with time. This is resolved by using an array of detectors in a 1 or 2 dimensional configuration, where each detector produces an output signal proportional to radiation intensity at its

location in the array. Only systems based on multi-detector arrays will be considered from this point with reference to the design of the proposed measurement system.

There are two import factors to consider when specifying the temporal resolution of the system (Section 3.3.3.1). Firstly, there is the time taken for a valid electrical signal to be established from the detector, for a given radiation intensity. Secondly, there is the time allocated in the design for the signal to be measured, digitised and stored by the data acquisition hardware and software. These will be explored in detail in the next chapter. Before deciding on a final design specification for the measurement, commercial systems available in the field were reviewed.

### **2.1.1 Commercial Systems**

Manufacturers' pamphlets and data sheets were studied for a range of radiation beam measurement arrays. Since these are aimed at sales promotion, cautious interpretation of the specifications presented is required and with this in mind, an overview of systems is presented in Table 2-1 for 'diode based' devices and Table 2-2. for those based on ionisation chambers.

#### **2.1.1.1 Discussion**

With reference to Tables 2-1 and 2-2, it would be expected that the specified sample times in the table include the detector and instrumentation acquisitions times as discussed in Section 2.1. The spatial axis data is defined as follows: devices labeled as '1D' or '1', measure a single axis only, with the exception of device reference 'D4' which has a carriage/slide arrangement for measuring a second axis (Section 2.1 regarding differing sample rates applies to this device).

Ref	Manufacturer	Name	Spatial Axis	Detector Type	Points	Sample Time (ms)	Detector Details	Volume (cm <sup>3</sup> )
D1	Sun Nuclear	Profiler 2	2	Sum Point Diodes	139	100	X Axis: 57 Y Axis: 83 4 mm spacing width 0.8 mm Z: 21 Detectors in a 10 cm x 10 cm field spaced 7.07 mm and then 14.14 mm in the rest of the field area 22 cm X 22 cm Total field size (0.8mm x 0.8 mm active detector area)	0.00019
D2	IBA Dosimetry	Elbe Phantom Array	1	Diodes	198	3000	Centre Array (10 cm x 10 cm) 7.07 Diag and 1 cm Vert/Horz Outer Array (6 cm wide surrounding the centre array) 14.4 mm Diag and 2 cm Vert/Horz	Not specified
D3	Sun Nuclear	MAP Check	2D	Radiation Hardened Diodes	445	Not specified	Second Axis is by Mechanical Slide 5 mm spaced, 2.5 x 2.5 mm	Not specified
D4	Schuster GmbH, Forchheim, Germany	EMS 96	1 (Z)	Diodes	88	12	Detection area per plane 20 x 20 cm Distance between detectors Central area (60x60cm) 5 mm Outer area (20x20cm) 10 mm	Not specified
D5	ScandDos AB	Delta 4	2D (3D)	p-Si Diodes	1069	Not specified	Helical Grid (HelGrid) 1 cm offset	Not specified
D6	Sun Nuclear	ArcCHECK	2D (3D)	Sum Point Diodes	1386	50		0.00019

Table 2-1: Commercial diode based systems.

Devices with the 'spatial axis' labeled '2', simultaneously measure in the GT and AB axes, whereas, '2D' measures a 2 dimensional plane. Four axis devices take simultaneous measurements in the GT, AB and the two diagonals axes.

Ref	Manufacturer	Name	Spatial Axis	Detector Type	Points	Sample Time (ms)	Detector Details	Volume (cm <sup>3</sup> )	Bias (V)
I1	Fluke Biomedical	Thebes II (7020)	1D	Ion Chambers	47		Detector Spacing 0.5 cm, Ion Chamber Dimensions 0.42 (w) x 0.95 (d) x 0.50 cm (h)	0.17	
I2	Fluke Biomedical	Thebes II (7040)	1D	Ion Chambers	47	1.1	Detector Spacing 1 cm, Ion Chamber Dimensions 0.88 (w) x 0.88 (d) x 0.50 cm (h)	0.36	-300
I3	PTW Freiburg GmbH	StarCheck	4	Chambers (Liquid)	527	200	Detector intervals: 3 mm along the profile and diagonals (centre to centre), 5 mm for the MLC chambers Chamber arrangement: 83 measurement points per main axis, 109 measurement points per diagonal axis, 2 x 53 measurement points for MLC check and 40 measurement points for checking the radiation field size	0.08	1000
I4	Emplex-Medizintechnik	Model 90100 TRACKER	2	Ion Chambers (Vented)	5	Not specified	Four orthogonally-placed ion chambers on a 10cm radius from a fifth isocentrally-located ion chamber	Not specified	300
I5	PTW Freiburg GmbH	LA 48 Fast	1	Ion Chamber (Liquid)	48	10	4 cm x 4cm x 0.5 cm 8 mm spaced	0.008	1000
I6	Sun Nuclear	IC Profiler	4	Ion Chambers	251	125	X, Y, diagonals X Axis: 63 / Y Axis: 65 -Diagonal: 63 / +Diagonal: 63 5 mm Spacing, Width 2.9 mm	0.046	Not Specified
I7	Standard Imaging	Beam Checker Double Check® Pro Daily Check Device (7600)	2	Ion Chambers	8	Not specified	One centre detector Four quadrant detectors (7.5 cm from centre) Three energy identification chambers One central axis; four 4 cm off axis; four 8 cm off axis; energy constancy chamber for external fibers @ 9 cm off-axis	0.46	Not Specified
I8	Fluke Biomedical	Victoreen 7200 Double Check	2	Ion Chamber (Vented)	10	Not specified	Not Specified	0.65	300
I9	Emplex-Medizintechnik	Victoreen 7200 Double Check	2	Ion Chambers	10	Not specified	Not Specified	Not specified	Not Specified
I10	PTW Freiburg GmbH	Octavus 1000	2D (3D)	Chambers (Liquid)	977	200 - 1000	Centre (5.5 cm x 5.5 cm): 2.5 mm center-to-center, Outer area (11 cm x 11 cm): 5 mm center-to-center	0.003	Not Specified
I11	PTW Freiburg GmbH	Seven29	2D	Ion chambers (Vented) Pixel Ion Chambers (Vented)	729	Not specified	2D 27 x 27 Spaced 10 mm	0.125	400
I12	IBA Dosimetry	Matrix	2D	Pixel Ion Chambers (Vented)	1020	20	Spacing 7.62 mm, Active Area 24.4 x 24.4 mm	0.08	Not Specified
I13	PTW Freiburg GmbH	LA 48	1	Ion Chamber (Liquid)	48	1000	4 cm x 4cm x 0.5 cm 8 mm spaced	0.008	Not Specified

Table 2-2: Commercial ionisation chamber based systems.

There are three devices identified as ‘3D (2D)’ in the review sample. Device reference D5 (ScaniDos Delta 4), utilises two perpendicular 2D diode arrays that intersect at the isocentre, thus covering the cross-section of a radiation beam in any direction. Device reference D6 (Sun Nuclear ArcCHECK), is a cylindrical detector array with 1386 diodes. Finally, the ‘PTW Octavius’ is actually a measurement ‘phantom’ with the device reference I10 as the detector array consisting of 977 liquid filled ionisation chambers. This is a development of the original design using device reference I11 consisting of only 729 liquid filled ionisation chambers. The detector array measures in a 2 dimensional plane, but when inserted into the phantom it is rotated by an electric motor. The phantom is kept perpendicular to the central ray-line of the beam using an inclinometer that measures gantry angle (Section 2.1 regarding differing sample rates applies to this device).

#### 2.1.1.2 Conclusion

There is a compromise in the design of radiation measurement systems between high spatial resolution, and high temporal resolution. An essential factor in this is the time required for acquisition of the radiation signal and its processing. Both diode and ionisation chamber based systems noted in this review would be suited to the radiation measurement requirements for the thesis. Device I2 (Thebes II) claims an ‘array scan time’ of 1.1 ms, although looking deeper into the data sheet a ‘frame rate’ of 5 frames/s is stated. There is some conflict here, since a time between samples (frames) of 200 ms, which may be the display rate, with the array updating at a much rate. Diode based Device D4 (BMS 96) claims to acquire a profile in just 12 ms. Modification of these devices to meet the requirement for radiation beam profile measurements along with linac control parameters at high temporal resolution is problematic, since this would require access to the device hardware and software at a low level. This would not be possible on a commercial system and, since the market is competitive, any design details would not be available, due to commercial

confidentiality. In fact, commercial confidentiality by manufacturers is one issue that restricts engineering development from reaching the public domain.

Although this review is not exhaustive, it provides an insight into commercial systems in the field and some of their specifications.

## 2.2 Beam Production and Measurement Equipment Development

Many of the technical concerns associated with beam generation for dynamic therapy (Webb S, 2005a) consolidate the engineering themes and form the link to primary literature in this section.

During the 1960's and early 70's, interest intensified in beam control issues, such as radiation symmetry and 'Ears' or 'Horns' on the periphery of the un-collimated beam. Koschel K & Clarke H., 1963 used 5 Philips ORP61 cadmium sulphide detectors, one fixed, for measurement at the CAX and four at the cardinal points, driven by a single motor, allowing the distance from the CAX detector to be remotely adjusted, to measure radiation beam flatness and symmetry.

An enhancement of this design was presented by Procter N, 1969 using five small ionisation chambers. The four mobile chambers were mounted on four orthogonal, motor driven lead-screws. The author claimed that enhanced performance using ionisation chambers overcame shortcomings in the cadmium sulphide detectors, with respect to dose linearity and response time. However, the design detail specifies thermionic valves in the signal processing stages, requiring negative feedback to compensate for input cable capacitance. Field Effect Transistor (FET) operational amplifiers are suggested, but with a cost implication. Also, a similar system using a pair of matched 0.6 cc ionisation chambers was presented by Naylor G P & Williams P C, 1971.

A single axis profile scanner was presented by Boyer A, 1980 and addresses the need for the detector to be within a phantom to allow for buildup and back-scatter. Furthermore, the detector system is mounted on to the radiation head of the

accelerator to facilitate measurement at gantry angles other than zero degrees. A polystyrene block formed the phantom; with a male dovetail cut into the base of the block fitting into a fixed female dovetail slide in the scanner base frame. The phantom was driven by a motorised chain system, with the ionisation chamber detector buried in the block.

Schmidt W *et al*, 1990 produced a 2 axis diode array with 10 silicon diodes, four in each orthogonal axis, one in a corner and one at the CAX. The system was designed to provide information on relative distribution of dose in patient treatments, beam energy and absolute dose.

An impressive design for an array of ionisation chambers is presented by Johns H *et al*, 1974, consisting of 49 points in a 7 x 7 matrix. The purpose of the work was to investigate radiation profile non-uniformity during gantry rotation. In the design, each ionisation chamber in the matrix was connected to a capacitor and reed switch. The charge on each capacitor was proportioned to the radiation intensity at the point in the matrix. The other connection on the reed switches made a common connection to a charge measuring circuit. The array was read sequentially, and the measured value printed on a teletype printer. The time taken to read and print the whole data matrix was approximately 40 seconds.

Such systems allowed measurement of radiation beam profiles, thus enabling engineering issues relating to beam generation to be evaluated in the hospital environment. This was reflected in published work that considered the performance of machines in clinical service (Horsley R J *et al*, 1968, Naylor G P & Chiveralls K, 1970, Gillin M & Quillin R, 1976, ) where the operating condition and performance of components such as the electron gun, magnetron, and beam transport system were examined. Conclusions recommended regular checks of machine beam transport system performance. A review of the development up to the early 1970's can be found in Karzmark C J & Pering N C, 1973.

Literature sources have highlighted topics of interest, including beam flatness and symmetry, stability with gantry rotation and magnetron power conditions. Naylor G P & Chiveralls K, 1970 investigated the change in field flatness with gantry rotation over one year on a Phillips SL75/5 series accelerator, concluding that due to the complex nature of the machine, routine measurement and adjustment of the beam profile was necessary. The authors commented on the lack of published data for comparison.

A novel approach to the measurement of field symmetry with gantry angle was presented by Padikal T N *et al*, 1981. Two radiation detectors were connected to a commercial electrometer (RFA3 Therados Ltd. USA) configured in ratiometric mode and the gantry read-out signals were connected to an X-Y recorder. The accelerator was rotated with the beam on and the ratiometric signal was plotted as a function of gantry angle. The author suggested that, should the gantry read-out be unavailable, a ramp generator synchronised to the gantry rotation speed could be used as an alternative. This would lead to systematic errors in the data should the gantry speed change during the measurement.

Blad B *et al*, 1998 further investigated rotation and its effects on field flatness, concluding that steering servo setup should be optimised to gain maximum performance over all gantry angles.

Gillin M & Quillin R, 1976 investigated the dosimetric calibration in response to magnetron operating conditions on a Varian accelerator. The authors measured field flatness over a range of 70 to 90 Amperes of magnetron anode operating current. A criticism of this paper is that the field flatness part of the measurement is a valid assessment of the radiation field, but there is no mention of the magnetron magnetic field conditions during the experiment. The magnetron operating conditions are set by the correct magnetron modulator impedance matching (English Electric Valve Company Ltd, 1974): both the electric and magnetic field components in the

interaction space within the magnetron must be matched to produce stable RF output. Therefore, to change the RF power conditions within the accelerator, both magnetron parameters need to be adjusted, using the impedance matching as guidance. A further paper by Constantinou C & Sternick E S, 1984 presents effects of magnetron power where both the electric and magnetic field potentials are correctly addressed.

A comprehensive analysis of the beam bending system on a Radiation Dynamics 'Dynaray 4' was presented by Sutherland W H, 1976. Performance measured over a two year period showed that flatness remained within +/-1 %. The paper describes the 270° achromatic magnet design and its configuration to produce a clinical beam. Useful comments on the adjustments required after service/breakdown events, such as gun cathode replacement and vacuum faults, are described.

### 2.2.1 Application to Dynamic Therapy

Accelerator performance concerns for small segment beams were highlighted in the previous chapter (Section 1.7.2). Beam measurement concerning radiation start-up (Buchgeistera M & Nusslin F, 1998) used a Schuster BMS96 (device 'D4' in Table 2-1), configured for a simultaneously array read out every 50 ms. Martens C *et al*, 2001b investigated the use of the PTW LA48 (device 'I5 in Table 2-2) for the characterisation of intensity modulated beams and concluded that it's a valuable high-precision device for the relative dosimetry of intensity modulated beams.

Le'tourneau D *et al*, 2004, used a MapCHECK (device 'D3' in Table 2-1) and concluded that the device offered the dosimetric characteristics required for performing both relative and absolute dose measurements. The same device was compared to an IBA MatriXX (device I12 in Table 2-2) by Li J *et al*, 2009 for their use in the quality assurance of patient-specific IMRT treatment. This is an interesting comparison since MapCHECK is diode-based and the MatriXX is ion chamber-based. The study found that a warm-up time greater than that recommended by the manufacturer appeared to be necessary in order to achieve accuracy for the MatriXX

array, but both devices were found to perform well. Further discussion of this device is can be found in Saminathan S *et al*, 2010 and Wagner D & Vorwerk H, 2011.

These is a considerable amount of literature for array based systems for use in treatment plan verification, some of these have been included in this review to assess the technical aspects of the instrumentation involved with respect to number of elements and sample time. In fact these devices are referred to as 4D, where the extra dimension is time. Therefore, this has some relevance, since the ‘Beam Scope’ device will measure accelerator parameters over time in the same way (Section 1.6) for off-line analysis. However, since the purpose of the thesis is to consider an engineering based tool, then from this point on, these 4D devices will not be considered further.

### 2.2.2 Beam Energy and Delivery Concerns

The two major technical advances presented in Webb S, 2005a will be discussed in this section.

#### 2.2.2.1 Flight Tubes in Elekta Machines

The flight tube in the Elekta machine was upgraded from a ‘slitted’ to a ‘slitless’ design, circa 1998.

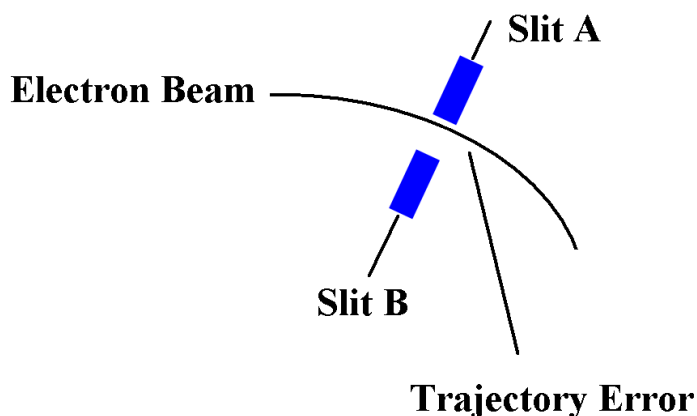


*Figure 2-1: Illustration of the function of energy slits in the flight tube (the electron beam in the figure is under the influence of a bend magnet field; this has not been shown for clarity).*

This is a common design used for accelerator energy control, where the electron beam path through the slits is determined by the beam energy, due to the bending magnet field (Figure 2-1). In Varian accelerators, the beam is actually clipped by the slits, should the energy be outside of the specified operating range, thereby preventing its passage to the X-ray target. In the Elekta concept, each slit has an electrical connection, and therefore some of the electron beam current flows into each slit, dependent on beam position. This produces a differential signal, which was used in the original design for electron gun control.

Especially when using the lower X-ray beam energies, where the electron beam current is higher, the slits would heat up, due to the constant flow of beam current, resulting in overheating and consequential failure of the vacuum seals that allow the external electrical connectivity. This was a significant problem if the electron gun filament servo was incorrectly configured, resulting in the electron beam consistently passing close to one of the slits at the nominal operating beam energy.

In the slitless design, the two slits were removed, thus eliminating the problem with the vacuum seals. Energy discrimination was then provided by an extra set of plates located in the beam monitor ionisation chamber situated in the radiation head of the machine (Section 6.4.6). Budgell G *et al*, 2001 in their investigation into the fast tune magnetron, present data on a machine before and after a flight tube upgrade, with a considerable improvement in beam start-up dose per MU from 4-5% down to a 2% error.

#### **2.2.2.2 'Fast Tune' Magnetron**

The EEV Ltd (Now e2v Ltd), fast tuning magnetron (Figure 2-2) design was used by Elekta to improve start-up characteristics of their SL Series accelerators, as discussed in Section 1.7.1.1. Stabilisation of microwave RF power at 'beam on' is a particularly a concern for these magnetron powered machines, in comparison to those using a klystron RF power source (Section 1.5.1.2).



***Figure 2-2: The ‘Fast Tune Magnetron’. The power connector to the tuner coil can be seen (in black). This is in the same position that the input shaft is situated in the gearbox tuned design. (Printed by kind permission of e2v technologies Ltd, Chelmsford UK).***

In the original EEV magnetron design, tuning is accomplished by a motorised drive system, coupled to the magnetron body via a constant velocity coupling, to allow for positional mismatch between the two assemblies. The drive speed is reduced within the device by a gearbox to provide precise movement to a set of tuning plungers located within the resonant cavities of the magnetron.

The gearbox design was totally reworked by the manufacturer in 1996 to overcome problems with the gear chain jamming, during high speed tuning, at radiation beam start-up (Bates A *et al*, 1996). To achieve the required operating frequency range of 10 MHz (see note 1, e2v Technologies Ltd, 2002a data sheet)

using the mechanical gearbox, required 347 turns of the input shaft, resulting in 30 kHz/turn sensitivity (Bates A *et al*, 1996).

An investigation by the author into a tuning problem on an Elekta SL Series accelerator at the Leicester radiotherapy centre resulted in a sensitivity value of 25 kHz/turn, measured using a precision microwave pulse counter with oven stabilisation (Hewlett Packard HP 5361b). Furthermore, the doserate for the accelerator was in the order of 550 MU/min with 4 turns of the magnetron tuner between the 95% doserate points. Bates A *et al*, 1996 states that the resolution of mechanical control required for the tuner is  $\pm 0.025$  mm to meet the device specification. To achieve this level of precision requires a high reduction ratio in the gearbox taking a long time to adjust, compared to the rest of the accelerator control systems, to settle to steady state operation at radiation beam start-up. On the machine used in the investigation, this was of the order of 9 seconds.

It should be noted that the 'beam on' criterion for the Elekta accelerator is based on the AFC/phase control servo system error being lower than a set threshold. When this point is reached, the electron gun filament current is raised from the stand-by level to the aiming level (Section 6.3.2.3) and in conjunction with the configured and active beam generation and transport systems; this meets the conditions for X-ray production.

A new approach to magnetron tuning (e2v Technologies Ltd, 2002b, Budgell G *et al*, 2001, Martens C *et al*, 2001a) uses a design similar to the arrangement employed to drive a loudspeaker cone. An Alternating Current (AC) would result in spatial modulation of the speaker cone and DC would produce a fixed deflection (although DC current in the voice coil is not a remit of loudspeaker design). Consequently, a coil arrangement comparable to the voice coil in the loudspeaker was used to move the tuning plungers, where an increase in current results in an increase in magnetron output frequency with a sensitivity of 1.0 - 1.4 MHz/A. To eliminate

overheating when the maximum current of  $\pm 5$  A (for 10 MHz tuning range) is applied, the coil was water cooled (e2v Technologies Ltd, 2002b).

This was a major improvement on the original tuner design based on a mechanical gearbox (e2v Technologies Ltd, 2002a) reducing the time for the tuner to reach steady state by around half. However, Budgell G *et al*, 2001 states that there was little effect on dose per MU and flatness before and after upgrade to the fast tune device. Some improvement though, is shown on paper in some machines, after the upgrade. This is of interest, since an Elekta accelerator at the Leicester radiotherapy centre, using a gearbox tuned magnetron, was investigated for flatness and symmetry at beam start-up by the author in support of a PhD project (Glendinning A G, 2001) for Step and shoot IMRT delivery. It was found that, with the mechanical gearbox there was dynamic instability in the form of oscillations in the tuner drive at beam start-up, resulting in flatness and symmetry errors, since the configuration of the AFC/Phase control system settings were optimised for conventional radiotherapy treatments in this machine. This configuration resulted in a beam start-up time of around 6 seconds. Decreasing the tuner gain in the machine software increased the start-up time to around 11 seconds. However, by allowing a greater time for the AFC/phase control servo to reach steady state operation, there was a noticeable improvement in the flatness and symmetry profiles at start-up. Although this was only tested on a single machine, it may be concluded that there is little improvement in flatness and symmetry using the fast tune magnetron compared to the gearbox tuned magnetron, if the control system performance is optimised for each device.

The accelerator used for investigation in this thesis is fitted with a fast tune magnetron and achieves a start-up time of around 4 seconds, which is in agreement with Budgell G *et al*, 2001. The advantages gained, are an improved efficiency in step and shoot IMRT delivery, because of the reduction in treatment delivery time. This is

an advantage, even with technologies like DAO (Section 1.3.1.1) which reduces the number of segments in a sequence.

## 2.3 Conclusion

The review of the delivery of small segment beams for step and shoot IMRT presented in chapter 1 (Section 1.7.2) highlights the variations in the MUs per segment. Webb S, 2005a also concludes that machine performance varies by manufacturer, specific accelerator, segment size and version of hardware. Furthermore, that some inconsistencies are present in the reports from different groups using similar machines.

It is recognised that complex processes are involved in the generation and transport systems of the accelerator, where certain aspects of the variations reported in Webb S, 2005a may be hidden and difficult to measure. Random and systematic errors produced in the beam generation and transport systems of the accelerator during high work load periods, such as beam start-up, are of current interest. In this situation, more sophisticated novel engineering test and measurement equipment might help to provide an insight to beam control system behavior.

The Quality Assurance (QA) for treatment delivery (IPEM Report 81, Thwaites D I, 1999) and the QA process for machines is paramount in the safe delivery of radiotherapy. Furthermore, Planned Preventative Maintenance (PPM) procedures must be in place to ensure the machine operating specifications are within tolerances. Having said this, optimising beam generation and transport control system configuration parameters may be beneficial in maintaining machine operation within the specified QA tolerances, especially for IMRT.

Understanding of control system behaviour would be a useful asset. This will be explored in detail for the electron gun filament system control system at beam start-up in Chapter 6 and for the radial steering control system during gantry rotation in Chapter 7.

From the review of commercial devices specifically suited to the engineering assessment of radiation beam profiles at high temporal resolution, two devices were found to be potentially useful: the ion chamber based Thebes II (Device I2 in Table 2-2) and the diode based BMS 96 (Device D4 in Table 2-1). Ultimately, neither of these devices was used for the work in this thesis, but their designs formed the basis of design discussions in the next chapter.

## Chapter 3. Measurement Equipment

### 3.1 Introduction

A novel test instrument has been developed, constructed and validated. The instrument was used to investigate the effect that accelerator control systems hardware and software have on radiation beam profiles, specifically during beam start for small segment beams and gantry rotation during rotational therapy. The 'Beam Scope' was conceived as an engineering test tool to simultaneously record radiation beam profiles and external analogue data at high temporal resolution over a range of user settable sample times synchronised to the accelerator PRF (Section 1.2.1.1).

The principal components of the prototype measurement system are shown in Figure 3-1. The design, construction and fundamental testing of the instrument are described in this chapter.

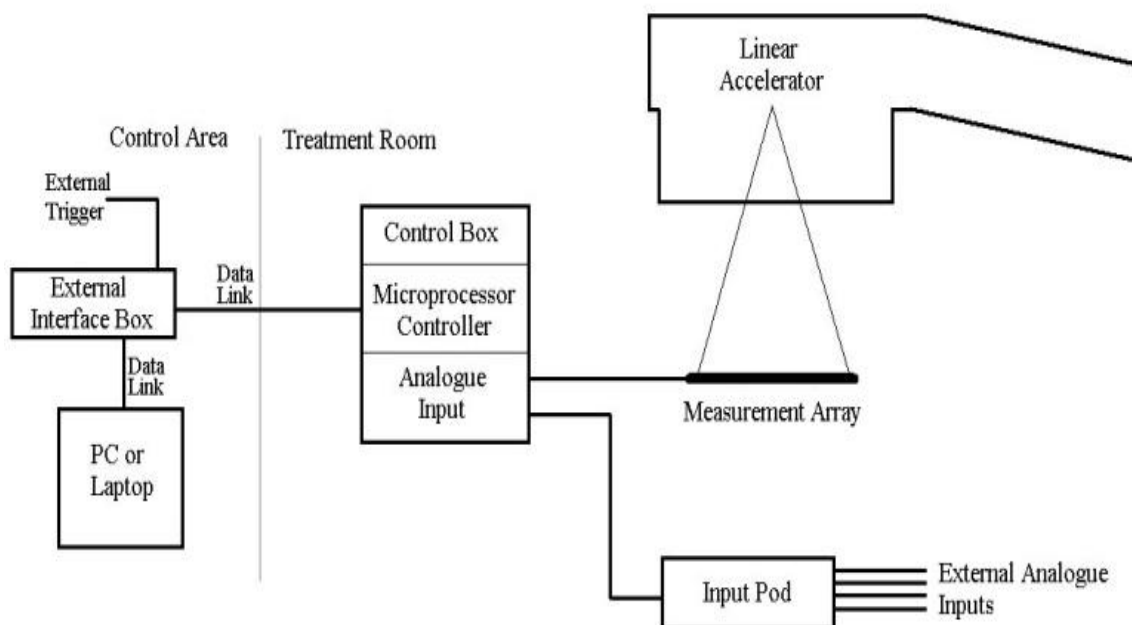


**Figure 3-1: Block diagram of the 'Beam Scope' measurement system. The physical location of the component parts is shown.**

**The main features of the final ‘Beam Scope’ design (detailed specification presented in Appendix 4) are:**

- 1D linear ionisation chamber measurement array, 36 cm between the centres of the end detectors, overall length 40 cm and width 15 cm. Consisting of 19 vented, air filled chambers with 2 cm between centres, 10 mm wide by 20 mm deep and 5 mm separation between collecting and high tension plates, resulting in a total collecting volume of 1 cc per chamber.
- Low noise acquisition with high immunity to Electro Magnetic Interference (EMI).
- High stability over time.
- High temporal resolution, measuring a radiation beam profile at a maximum PRF of 500 PPS (a profile measured and stored every 2 ms).
- A maximum of 16 ms of data can be integrated at the maximum PRF of 500 PPS (8 radiation pulses).
- ‘Y’ Axis resolution of 12 bits (4096 levels).
- Synchronised to the accelerator PRF with a range of options inducing a ‘free run mode’ to allow continuous acquisition in-between ‘step and shoot’ IMRT segments if required.
- Electrometer ‘auto zero’ function.
- 4 analogue data channels. Electrically the same as oscilloscope inputs, allowing the use of standard oscilloscope 10:1 probes for connection to test signals.
- Additional electrometer channel.
- Fully configurable acquisition timing including electrometer reset pulse width.
- Off line data analysis tools.
- On-board self-tests and log file generation.

## **3.2 Development Strategy and Specification**

### **3.2.1 Review of a Previous Project**

A Synchronised Multi-channel Electrometer (SME) was previously developed by the author to measure linear accelerator performance related to IMRT treatment verification. This work was undertaken to support a PhD project (Glendinning A G,

2001) and associated publications (Glendinning A G *et al*, 2001a, Glendinning A G *et al*, 2001b, Glendinning A G *et al*, 2001c). Design limitations of the authors' original SME were addressed in the early phase of the development cycle of the new measurement system, enabling a more flexible system to be built. The limitations were mainly:-

1.) The acquisition of the electrometer signal was synchronised by an external input from a test output on the linear accelerator. As this interface is machine specific, various input designs would be required to collect data from other manufacturer's equipment. However, since the machines available during this project development were Elekta SL15i linear accelerators, the hardware development and testing of other interfaces would prove difficult. Also, the measurement of data at other hospital sites may be an issue, as a hardware trigger connection of a prototype instrument to their linear accelerators may cause concern. This has been addressed by the inclusion of a comprehensive trigger system comprising:-

- a) A 'free run' acquisition mode to allow continuous capture of data during the intersegment/start-up phase of a radiation beam where the PRF is inhibited and acquisition trigger is lost. This allows intersegment times to be considered for 'step and shoot' beams and also enables the continuous recording of external analogue data channels during the intersegment phase.
- b) An 'internal' trigger mode based on the rate of change of integrator output to determine the point at which to acquire a radiation pulse, or group of radiation pulse samples. This is achieved by differentiating the electrometer outputs to produce a trigger pulse. A trigger level would be

user set manually, using a peak detector to display the maximum pulse height, to then allow a trigger threshold to be set.

- c) An 'isolated external trigger' input as used in the original SME. This would still enable custom modules to be developed for specific linear accelerators as required. It would also be useful to test the new 'auto trigger system' against a known benchmark.

- 2.) The communication with the host Personal Computer (PC) was originally ASCII (American Standard Codes for Information Interchange) with a baud rate of 9600 bit/s using an RS232 connection. This resulted in a 10 minute wait to unload the entire SME memory to the host computer. This was substantially improved by increasing the baud rate to 115200 bit/s and using a check summed binary transfer mode. The link was updated to RS423 which uses a twisted pair connection, thus improving the noise immunity of the communications link.

The design aims of the new system were that it should:

- a) Be able to record data from a range of linear accelerator manufacturer's.
- b) Capable of operating in a standalone trigger mode.
- c) Equipped with 4 extra channels to record analogue data from the linear accelerator control system.
- d) Use a more integrated microcontroller as the core component.
- e) Provide a faster serial data link.
- f) Use a new detector based on a one dimensional linear array.

A complete redesign of the acquisition, control and communication resulted in a more flexible instrument. The new design is based around a core microcontroller to manage the local processes, timing and control within a single integrated circuit. This reduced the discrete hardware required to collect, store and relay data back to the host

computer. The core controller orchestrates the communication and timing functions of the onboard hardware as requested by the host computer application.

For research purposes, the measurement system was developed as a prototype. A Peripheral Interface Controller (PIC) was chosen as the core device. The PIC18 microcontroller family (Microchip Technology Inc Arizona USA, 2002, Microchip Technology Inc Arizona USA, 2005) was selected as this range of PIC devices easily fulfils the criteria for the measurement system specification as compared with the Z80 (Zilog Semiconductors Inc.) chip set used in the SME.

The PIC18 range of microcontrollers includes:

- a) Large scale integration of peripheral devices.
- b) A high speed serial link.
- c) High noise immunity.

These enhancements linked with a redesign of the analogue input circuitry to include the 4 extra inputs and a new triggering system met the requirements of the new design.

### **3.2.2 Remit for New Data Acquisition System**

The measurement of pulsed radiation beam data at a high sample rate is pivotal to this research work and requires a high level of confidence in the equipment used. It was therefore decided to start from first principles on the front end electronics of the 'Beam Scope' system to identify any possible measurement errors that could be introduced. With circuit diagrams, design and component datasheets to hand, it was a straightforward task to extensively test the data acquisition part of the design. This would not be possible on a commercial system.

Later in this chapter, the application of an electrometer to process the radiation detector signal is explored in detail, as this presents the most challenging and demanding part of the electronics design. Any deficiencies here would result in

inferior signal quality due to sampling errors, DC drift, induced noise and extraneous pickup.

Consideration of the design requirements for the engineering test tool was undertaken. External limitations imposed on development time and funding were important factors that were considered in the hardware design phase of the working prototype system including the radiation detector, as well as the technical requirements.

### 3.3 Design Considerations for Radiation Measurement

Both, ionisation chambers (air or liquid filled) and diode detectors are suitable for linear array technology (Das I J *et al*, 2008) and various configurations of these are considered later in this chapter for use as the radiation detector for the 'Beam Scope' design.

The properties of the detector element used in the array should be carefully considered, since a critical factor in the design specification is the requirement for high temporal resolution. Specifically, if a beam profile for every radiation pulse is required at the maximum design PRF of 500 PPS, then the level, and the acquisition time of the electrical signal produced in a specific measurement volume of the detector element by a single radiation pulse, is of significance. Furthermore, since the 'Beam Scope' is intended as an engineering test tool, then the parameters to be evaluated from a radiation beam profile should be considered in context. Since dynamic therapy is concerned with small segments of beam, then the behavior of the radiation profile the beam startup phase should also be considered.

The main mechanisms that cause deviation from the normal expected radiation profile, are changes in beam energy and trajectory (Karzmark C J *et al*, 1993b, Karzmark C J *et al*, 1993c). Machine design to control these, results in either precision regulation of beam transport parameters, or by servo control (Karzmark C J, 1984). Therefore, beam energy and trajectory effects were investigated in detail, to decide a

practical number of measurement channels required for the prototype 'Beam Scope' system to measure these parameters.

### 3.3.1 Beam Energy Effects

A deviation in beam energy results in 'horns or ears' in the radiation flatness profile due to the effect of the flattening filter in the radiation head (Casebow M & Mayles P, 1999a). Flatness is defined in Casebow M & Mayles P, 1999b as the ratio of the maximum dose in the profile, to the minimum dose, expressed as a percentage within the flattened area of the profile. It is usual to measure the corresponding point on the other side of the beam axis and take the mean, to account for any asymmetry error; this method was adopted in the analysis of data measured by the 'Beam Scope' to measure energy effects.

The effect of changing the beam energy is demonstrated in Figure 3-2, measured in a water tank using an X-ray beam of energy 6 MV, 5 cm deep and 40 x 40 cm field size. The electron gun servo system was set to manual and GT axis profiles measured, firstly at the nominal electron gun filament current of 8.17 Amperes, normalised to the CAX, and then 10 mA either side, likewise normalised to the CAX (Figure 3-2). This action changes the accelerated beam energy (Section 6.5.3). The measured data was also saved with the 'normalisation' function set to 'inactive' in the water tank control software in order to access the raw data from the measurement (Figure 3-3).

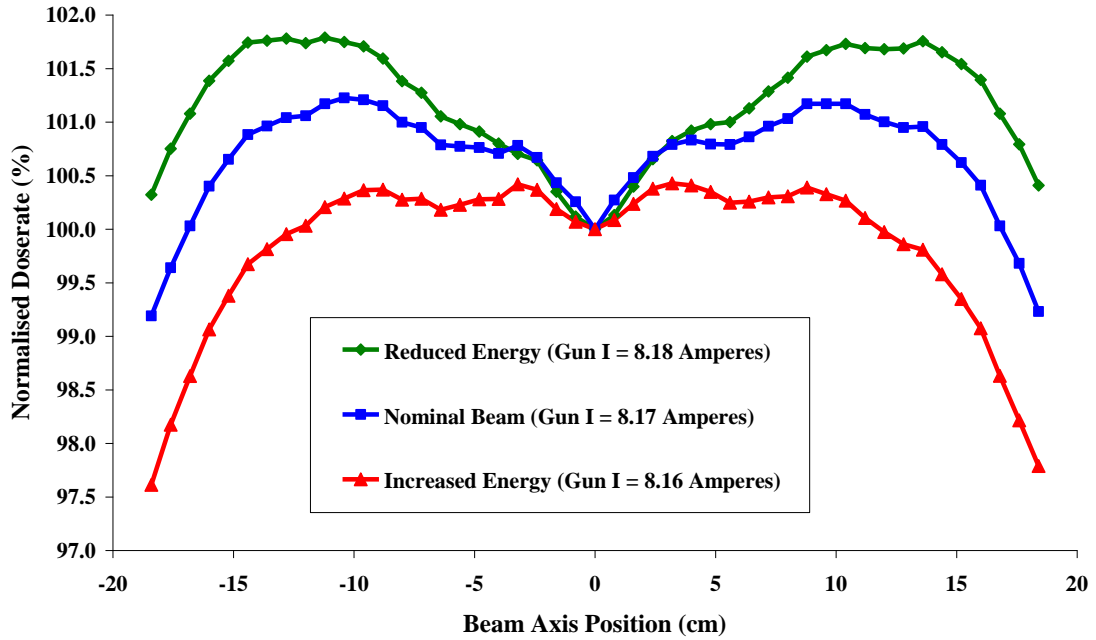


*Figure 3-2: Profiles measured in a water tank on the accelerator under test in this thesis, normalised to the CAX. The beam energy was changed by adjusting the electron gun filament current with the servo control system switched to ‘manual’ mode. The filament current was changed by +/-10 mA from the nominal value of 8.17 Amperes. The values shown in the plot legend are the actual electron gun filament currents as displayed by the accelerator.*

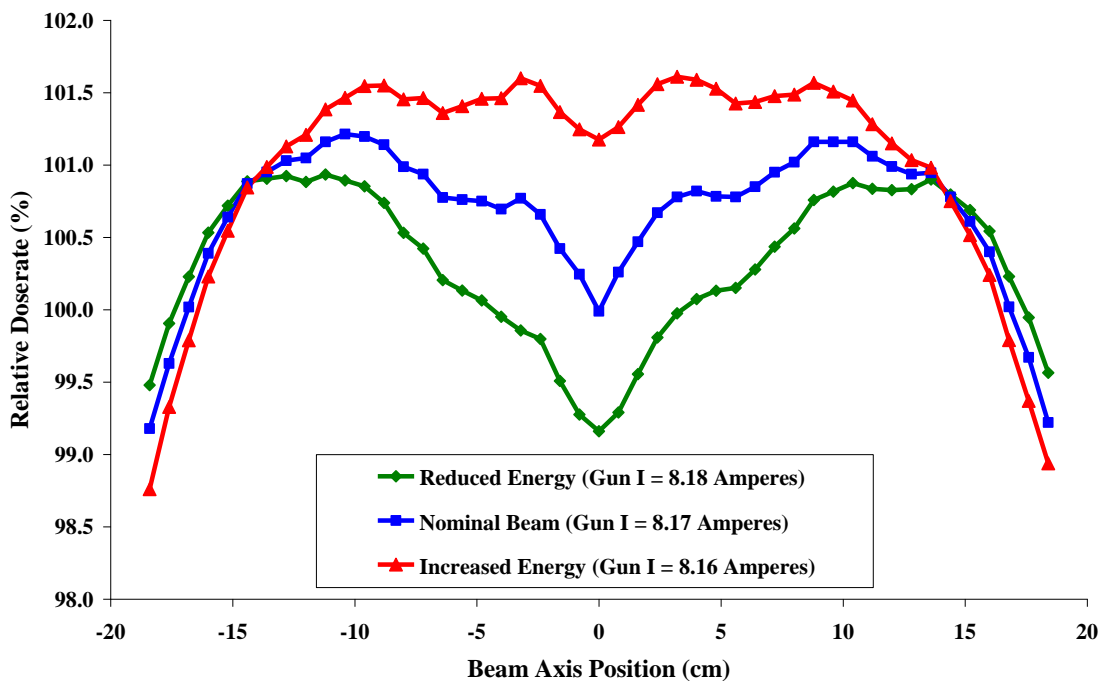


*Figure 3-3: The same profile data as in Figure 3-2 saved with the normalisation setting inactive in the plotting tank controller. The values shown in the plot legend are the actual electron gun filament currents as displayed by the accelerator.*

Generally, beam profiles are measured, and then normalised to the CAX to allow comparison, since the dose rate at the central axis may vary between measurements. This however, is not representative of the real situation as depicted in Figure 3-3, where the difference in the profile is maximal at the central axis with change in beam energy for the profiles saved with the normalisation option disabled. This is expected, since the CAX of the profile is at the thickest point of the flattening filter, and therefore most sensitive to energy change (Section 6.5.3).

The small change in current used, demonstrates the sensitivity of the beam profile to variations in electron gun filament current. Since the instrumentation on the machine used in the experiment displays electron gun filament current to 2 decimal places for both setting and monitoring,  $\pm 10$  mA was the smallest change that could be made for the experiment, and still resulted in a  $\pm 1$  % change in dose rate at the CAX. The small magnitude of current change was also chosen to circumvent loss of dose rate or symmetry error, should the energy produced by the experimental values be close to, or outside of the beam bending magnet operating range.

In Figure 3-2 and Figure 3-3 two suitable points, 12 cm either side of the CAX with low dose rate gradient and away from the penumbra at the field edge of the profiles were considered to be suitable for the measurement of beam energy effects. Furthermore, data sets will not be normalised by default, for veracity. Therefore, only 3 measurement points of sufficient profile area to produce a suitable signal level for high temporal resolution are required for the assessment of energy effects, one at the CAX and one 12 cm either side.

### **3.3.2 Beam Trajectory Effects**

An error in beam trajectory results in asymmetry in the radiation profile due to the effect of the flattening filter. Error in symmetry is defined in Casebow M & Mayles P, 1999b as the absolute maximum value of the ratio of dose at two

equi-distant points either side of the central axis, where the maximum symmetry may be at any point within the flattened area.

The shape and the asymmetry of the radiation profile about the CAX is dependent on the nature of the trajectory error, either an angular divergence, radial shift or a combination of both (Karzmark C J *et al*, 1993b Karzmark C J, 1984, Karzmark C J *et al*, 1993c, Loverock L, 2007). An example from the commissioning data, measured by the author, for the same accelerator used in Figure 3-2 is presented in Figure 3-4. Observing the same points 12 cm either side of the central axis as described for energy effects (3.3.1) there is a tilt in the radiation profile of  $\pm 4.6\%$  for a  $\pm 50$  mA deviation in radial steering current either side of the nominal 100 mA value. Again these are on a low gradient portion of the symmetry profiles in the example.

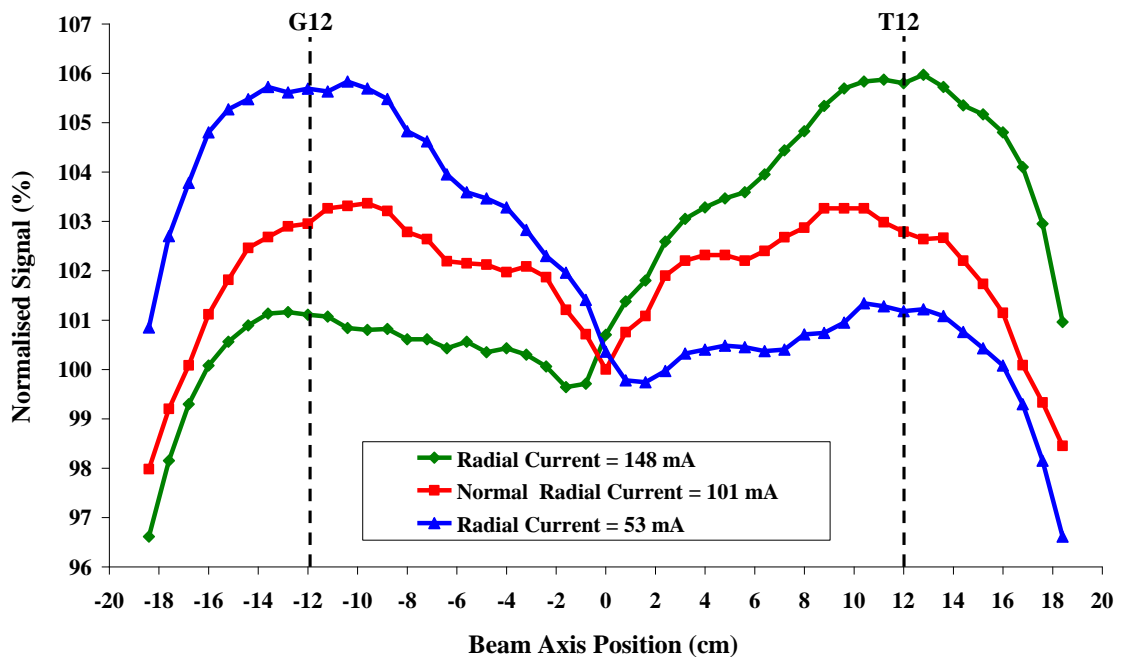


**Figure 3-4:** The result of correct and mis-steered radial beam trajectories on radiation profile for a change of  $\pm 50$  mA in the radial steering coils. The plots were taken from the commissioning data set for the same machine as used in Figure 3-2. The values shown in the plot legend are the actual radial steering coil currents as displayed by the accelerator.

It is clear though from the figure, that the profiles are not symmetrical about the CAX point. Consequently, it is possible to ascertain the type of error, symmetric

or asymmetric and its magnitude, should this be required, by measuring the same set of points as described in Section 3.3.1.

### **3.3.3 Accelerator Pulse Rate**

As described in Section 1.2.1.1, linac radiation is delivered in pulses. The accelerator used for measurements in this thesis has a maximum PRF of 400 PPS; other machines available in the department for future measurements, by ‘Varian Oncology Systems Ltd.’ operate at nominal PRF of 360 PPS. Since these are the two major medical accelerator manufacturer’s and the maximum design acquisition PRF for the ‘Beam Scope’ design is 500 PPS (2 ms), see Section 3.1, then this provides some level of redundancy should measurements at marginally higher PRF be required in future.

All the charge produced by a single radiation pulse needs to be transferred from the radiation detector in the array to the electrometer integrating capacitor in the measurement system within the design specification 2 ms period. The electrometer output then needs to be digitised, stored and the electrometer reset ready for the next radiation pulse. It is apparent therefore, that acquisition timing is critical in the design of the measurement system and that any aspect of the design which influences timing needs to be carefully considered. This includes the type of radiation detector element used in the array.

#### **3.3.3.1 Initial System Timing Constraints**

To realise an acquisition every 2 ms (Section 3.1) time slots was equally allocated to the radiation detector, to account for ion mobility in ionisation chamber based detectors (Section 3.4.2.2), and for the reading and storage of the integrating electrometer signal levels (Section 3.6.4.5).

### 3.3.4 Diode Detectors

Semiconductor detectors are used for the detection of radiation (Dearnaley G, 1966, Jones A, 1963). Their sensitivity relative to the ionisation volume is high compared to an ionisation chamber, about 18000 times greater (Rosenfeld A, 2008). The sensitive volume is therefore small and well defined. The effective measuring point may be less than 1 mm below the surface of the detector resulting in good spatial response (Rikner G & Grusell E, 1978). Devices are manufactured with p-type and n-type doping (Knoll G, 2000b), and the characteristics of both types for radiation therapy are well documented (Dam J & Merinello G, 2006, McKerracher C & Thwaites D I, 1999, McKerracher C & Thwaites D I, 2006, Rosenfeld A, 2008, Yin Z *et al*, 2004). Doserate and Source Detector Distance (SDD) dependence (Saini A & Zhu T, 2004), temperature effects (Grusell E & Rikner G, 1986) and radiation damage (Rikner G & Grusell E, 1983) are highlighted in the literature.

There are two operating modes (Ramírez-Jiménez F *et al*, 2006): photovoltaic and photoconductive (requiring a reverse bias voltage). In the photoconductive mode, single radiation events can be recorded, and since the charge produced by the detector is directly proportional to the energy of the radiation, this mode is used for spectrometric measurements. An example of this mode in relation to the applied reverse bias operating conditions is presented in Houdayer A *et al*, 2002.

The photovoltaic mode, where a current is produced from the mean of the radiation interactions within the detector, is the method employed for radiation therapy beam measurements. A diagram of the typical electronic interfaces required for pre-amplification for both modes is shown in Figure 3-5

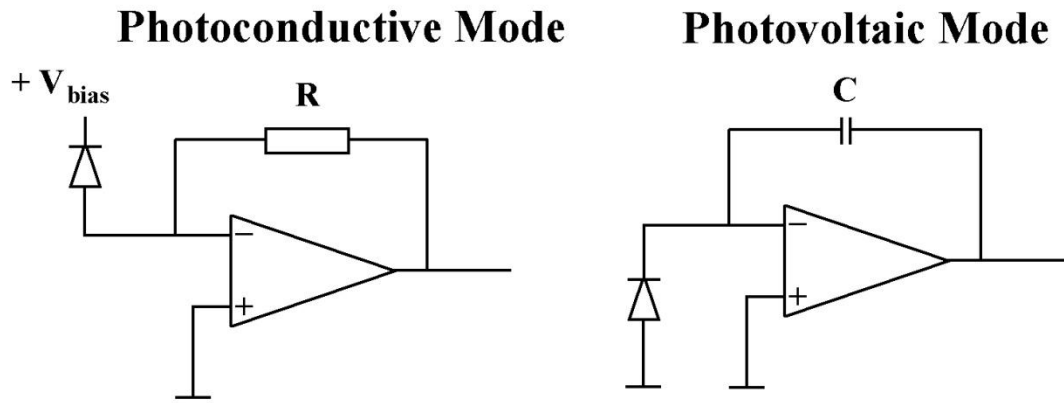


*Figure 3-5: Preamplifier configurations for the photoconductive mode using a current to voltage electrometer, and the photovoltaic operating mode using an integrating electrometer.*

### 3.3.5 Ionisation Chambers

An ionisation chamber is a gas or liquid filled radiation detector consisting of two plates to which an electrical potential is applied. Charge is collected from ion pairs formed between the plates by direct ionisation. Positive ions migrate towards the negative plate and free electrons towards to the positive plate resulting in an electrical current, which can be measured using an electrometer (Andreo P *et al*, 2007, Boag J, 1966, Knoll G, 2000a). Special consideration to the design of ionisation cavities with respect to ion mobility would be required for the 'Beam Scope' system, since the array would be used at high sample rates.

#### 3.3.5.1 Electron Charge Mobility

Electron charge mobility is a quantity describing the drift velocity of electrons in an applied electric field across a medium and must be considered when establishing the acquisition timing for the measurement of pulsed radiation beams (Boag J, 1950, Boag J & Wilson, T., 1952). The ability to clear the collecting volume of charge is dependent on the ion chamber plate separation, collecting medium (liquid or gas) and high tension supply voltage, this time period is known as the ion transit time. Boag J, 1966 presents the formula for ion transit time (Equation 1).

$$Ti = \frac{d^2}{V k}$$

Equation 1

where  $k$  is the ion mobility in the collecting medium,  $V$  is the applied voltage and  $d$  is the distance between the plates.

### 3.3.5.2 Liquid Filled Ionisation Chambers

Due to the higher ion production density (Johansson B & Wickman G, 1997) of dielectric liquids, these chambers produce a high yield compared to air for the same collecting volume (Wickman G & Nystrom H, 1992). Liquid isooctane and tetramethylsilane as the collecting medium are frequently described in the literature for use as detectors for radiotherapy applications. The properties of dielectric liquids are highly dependent on their purity, since leakage and general recombination depend on trace impurities (Wickman G & Nystrom H, 1992). Experiments using liquid isooctane and tetramethylsilane performed on a Varian model 2300 C/D linear accelerator, delivering a 20 MV X-ray beam with a PRF of 30 PPS and radiation pulse length of 3.5  $\mu$ s by Wickman G & Nystrom H, 1992 found that the ion transit time was never shorter than 5 ms. This was sufficient for the low pulse repetition rate used, providing the applied polarising voltage exceeded 1000 V for isooctane and 500 V for tetramethylsilane. However, this would result in pulse overlap at rates higher than 200 pulses per second.

### 3.3.5.3 Commercial Detector Array

The use of a commercial detector array available in the department consisting of 47 liquid filled ionisation chambers 8 mm spaced, 4 mm x 4 mm and a plate separation of 0.5 mm, total collecting volume of 0.008 cc (PTW Freiburg GmbH, 1997) was an option for consideration. The array (named LA48) uses isooctane as the dielectric in the collecting volume and a high tension supply of 1000 V (Martens C *et*

*al*, 2001b). Ion mobility for isooctane is quoted as  $3.5 \times 10^{-8} \text{ m}^2 \text{ atm/V/s}$  by Wickman G & Nystrom H, 1992 and  $2.9 \times 10^{-8} \text{ m}^2 \text{ atm/V/s}$  by Johansson B *et al*, 1997 (presumably the difference found in the values is due to differing purity in the liquids, as described in Section 3.3.5.2.). Taking the mean of the two ion mobility values, a plate separation of 0.5 mm and 1000 V supply, as stated above, results in an estimated ion transit time 7.8 ms (from Equation 1). Even though the purity of the liquid is unknown for the LA48 device in question, the calculated value is several times the maximum design acquisition period of 2 ms, so rendering the device unsuitable for the project in its current form. Increasing the high tension supply voltage would be the only option to improve the ion transit time on this commercial array. This would not be viable, since this would necessitate the high tension supply voltage to be raised to around 4000 V (based Equation 1) to yield a transit time of 2 ms. This would result in a high probability of electrical breakdown in the chamber and consequently this option was not considered further.

### 3.3.6 Discussion

#### 3.3.6.1 Radiation Detector Type

A diode array operating in the photovoltaic mode would be most suited for use in the 'Beam Scope' design, since the drift velocity for charge carriers is very high (Knoll G, 2000b) compared to that of a ionisation chamber. This would be appropriate for high temporal measurements as required by the acquisition timing specification (Section 3.3.3.1). However, on the grounds, that a previous detector based on an ionisation chamber array had been successfully used by the author (Section 3.5.4.4) for high temporal resolution radiation beam profile measurement, with some constraints, and the high cost of suitable diodes, funding was not made available. Furthermore, since the objective of the project was to measure beam profile data, synchronised to machine control signals, the detector choice was not a critical element in the design of a prototype system, as long as the implementation fulfilled the design

criteria. An ionisation chamber design built in-house was the final choice. A gas fill was used as the charge collecting medium, liquid having been rejected due to the excessive ion transit delay (Section 3.3.5.2) in a commercial device (Section 3.3.5.3). Since the array would be built in-house, air was chosen as the fill gas, as this would be the simplest option to implement.

### 3.3.6.2 Number of Channels

Based on Sections 3.3.1 and 3.3.2 where only 3 points would have sufficed to measure most errors in electron beam transport, a design was formulated using a 19 channel ionisation chamber array to allow the overall shape of the beam profile to be determined, and a microprocessor based data acquisition system to acquire the beam data. This would also permit some expansion capability, but with reduced spatial resolution, to allow simultaneous measurement in both the radial and transverse beam planes, for later development of the system. This would enable measurement of beam energy effects in both planes, where asymmetry in the ‘ears’ or ‘horns’ might be explored in relation the electron beam shape presented at the X-ray target. Clearly, the more channels available, the more planes can be measured and with greater spatial resolution; however the influence that variation in beam transport parameters has on the radiation profile can effectively be measured with a small number of points, as described above.

It is standard practice in commercial beam measurement systems to multiplex electrometers to save space and cost, whilst still providing high spatial resolution. Multiplexing results in a reduction in the data sampling rate thus rendering most commercial systems unsuitable for high temporal resolution measurements. To avoid this, each of the detector elements in the measurement array was allocated its own integrating electrometer. A total of 19 signal channels was considered to be a realistic number to construct for a prototype instrument. An odd number of channels were chosen so as to position a measurement point at the CAX of the radiation beam. With



### 3.4.1.1 Guard Rings

The space between the chambers should include a guard ring around the collecting plate (Boag J, 1966). Boag J, 1963 states that to create consistency in the collecting volume, the ionised gas should form the border to the active volume and that this should be achieved using a wide extension to the collecting plate. To maintain the collecting volume it is important to create an equi-potential plane over the whole collecting area of the array, since a difference in potential between collecting plate and the grounded guard ring would cause electric field distortion (Boag J, 1964). This effect was noted in the design of a strip ionisation chamber array (Glendinning A G, 2001) devised to investigate real-time verification of DMLC on a linear accelerator. The strip collecting plates were 80.0 x 3.0 mm arranged in two opposing arrays with ten plates either side of central axis separated from the high tension supply by 0.83 mm. Each collecting plate was separated by a 3 mm grounded guard. When measuring the signal on plate 5 of one bank with adjacent collecting plates disconnected from their respective electrometers and allowed to 'float', changes in collected charge found were as tabulated in Table 3-1. The text suggests no further effect was observed when grounding plates beyond two adjacent plates on either side of the test plate. Although the dimensions were different from the proposed design, especially the high tension plate separation of only 0.84 mm compared to the 5 mm for the proposed design, Table 3-1 demonstrates significant field distortion due to the disconnected plates.

To avoid this situation in a multi-plate array, it is therefore essential to use a virtual earth input electrometer and electrically grounded guard ring to maintain an equi-potential plane across the collecting plates and thus obtain minimal distortion of the electric field.

Collecting Plate Measured	Irradiation Conditions	Adjacent Plates	Change in charge collected (%) on grounding surrounding plates ( $\pm 2$ SD)
5	6 MV 1.0 Gy  Isocentre (5.5 Gy min <sup>-1</sup> )	4,6	-6.4 $\pm$ 0.2
		3,4,6,7	-7.6 $\pm$ 0.2
		2-4,6-8	-8.9 $\pm$ 0.2
		1-4,6-9	-8.7 $\pm$ 0.2

Table 3-1: Change in collected charge for the example strip ion chamber as adjacent plates are grounded (Taken from Glendinning A G, 2001 with permission).

### 3.4.2 Plate Separation

The ion chamber plate separation is a critical factor for the design specification for a maximum PRF of 500 PPS (Section 3.1). The exposure for a given set of collecting volume dimensions and charge can be calculated using Equation 3 (Page 72 Section 3.4.2.4).

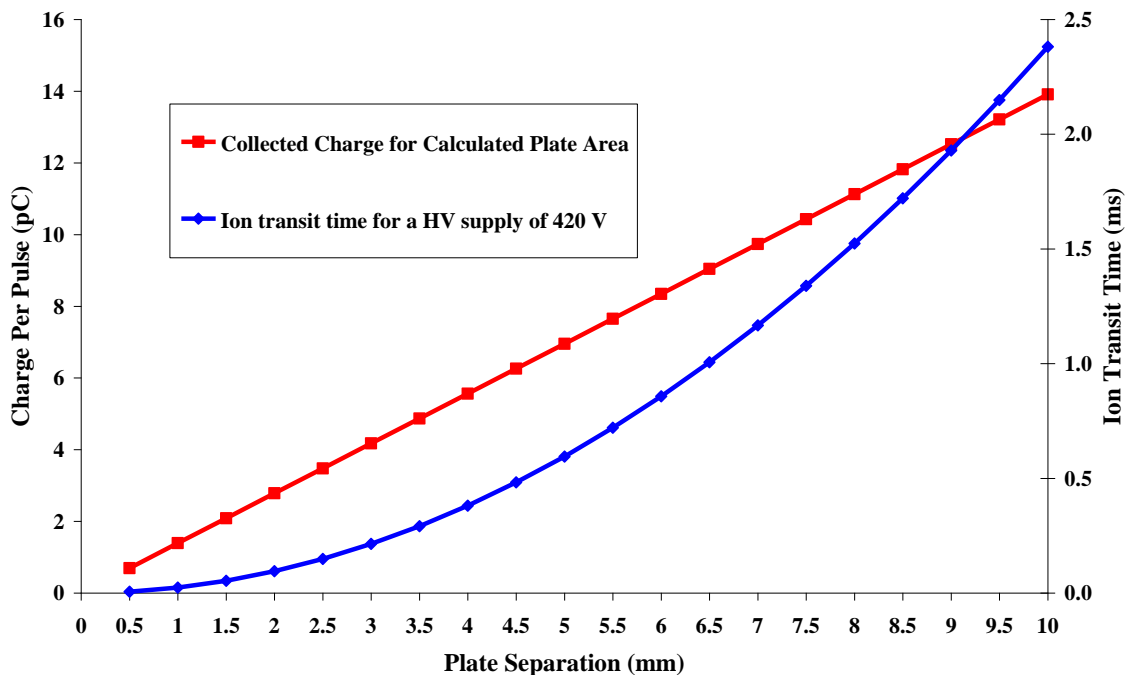


Figure 3-7: Charge collection per pulse and ion transit time for the design collecting plate area and high tension supply.

For a given exposure, fixed plate area and air density, then the charge collected is proportional to plate separation (L). However, for a fixed ion mobility and high tension supply, then ion transit time in Equation 1 (Page 70) is proportional to the square of the plate separation (d); these are plotted in Figure 3-7. It is therefore important to select the lowest plate separation possible that meets the minimum specified charge (Section 3.4.2.1) in the required ion transit time. The final value will be calculated further in the chapter.

#### 3.4.2.1 Minimum Charge per Radiation Pulse

An electrometer output of 150 mV per radiation pulse is required to utilise the full range of the Analogue to Digital Convertor (ADC). Furthermore, a minimum value of 47 pF integrating capacitance is also a prerequisite for the electrometer to function within specification (Section 3.5.1).

Applying these values to Equation 5 (Section 3.6.1 Page 97) a minimum collected charge of 7 pC per pulse is necessary to satisfy an electrometer output of 150 mV per radiation pulse. In order to specify the plate separation required to yield a 7 pC charge in a single radiation pulse, the dose per pulse must first be ascertained at the physical radiation detector location.

#### 3.4.2.2 Dose per Radiation Pulse

An experiment was setup on an accelerator to ascertain the dose per pulse. Based on a standard output beam of 100 cGy per 100 MU (6 X-rays, 5 cm deep in Perspex), a timer/counter (HP 5315a Hewlett Packard) was connected to the oscilloscope test output on the accelerator 'test patch bay' to count pulses from the High Tension (HT) modulator and thus radiation pulses. The timer/counter measurement input was gated with a signal from a device that was developed by the author for detecting the initiation of radiation (Glendinning A G *et al*, 2001a) by detecting light emitted from the electron gun of the accelerator during active exposure

(Figure 3-8). Using this apparatus it was possible to count the number of radiation pulses present during the measurement.

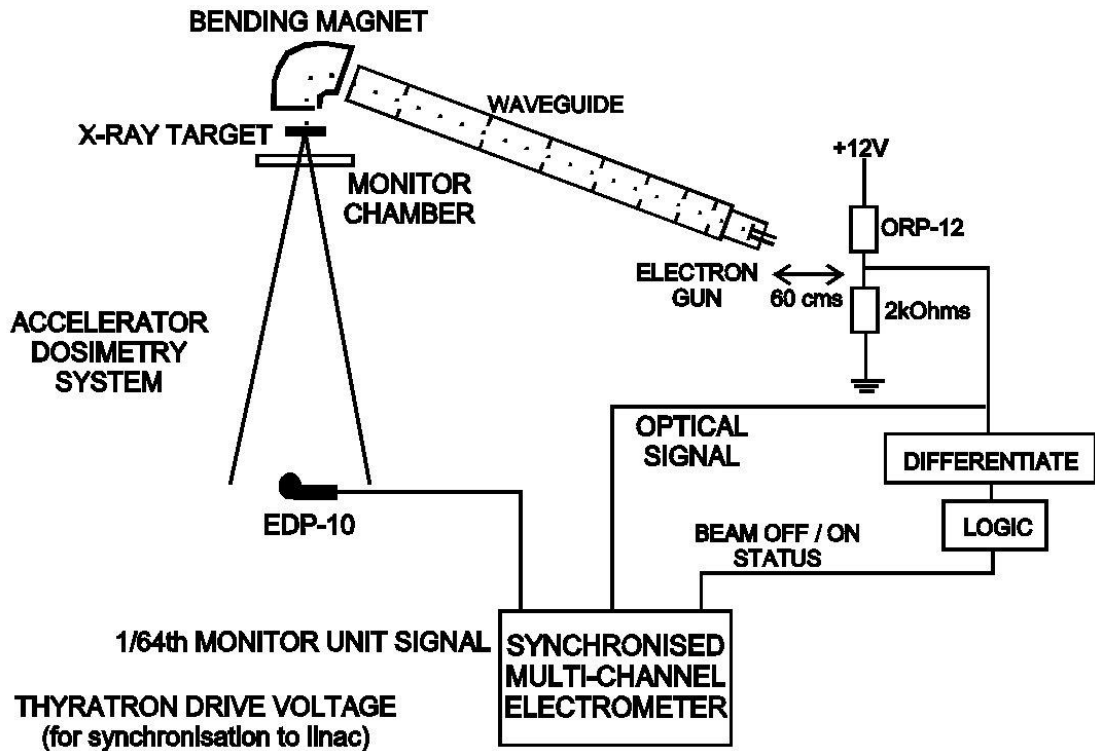


*Figure 3-8: Schematic of the device used to detect radiation (Taken from Glendinning A G et al, 2001a with permission).*

The timer/counter was reset and a beam of 100 Monitor Units (MU) was delivered. This was repeated 5 times resulting in a mean count of 4439 (2 SD = 11.9) radiation pulses per 100 MU beam. The accelerator was in clinical service and calibrated to deliver 100 cGy/100 MU to the isocentre 5cm deep in a 10 cm x 10 cm field size (Leicester department protocol); therefore the dose in each pulse was equal to the total dose delivered divided by the number of pulses in the beam, which equates to 0.0225 cGy per pulse. A value of 0.022 cGy per pulse was obtained from the secondary standard calibration data for the accelerator used for the experiment (Leicester Royal Infirmary Radiation Physics Data, August 2008).

### 3.4.2.3 Exposure per Radiation Pulse

In order to calculate the plate separation, we first need to convert the dose to exposure. Dose in air is obtained from exposure using Equation 2. As  $(W/e)$  and the dose are known it is possible to calculate the exposure.

$$D = X \left( \frac{W}{e} \right)$$

Equation 2

where  $W/e$  is the mean energy required to produce an ion pair in dry air and is equal to 33.97 J/C,  $X$  is the exposure in C/kg and  $D$  is the dose in Gy.

This yielded an exposure per pulse of  $6.632 \times 10^{-6}$  C/kg.

### 3.4.2.4 Plate Separation to Satisfy ADC Range

The exposure for a given set of collecting volume dimensions and charge can then be calculated using the following equation:

$$X = \frac{Q}{\rho \cdot A \cdot L}$$

Equation 3

where  $\rho$  is the air density ( $1.05 \text{ kg/m}^3$  nominal value),  $A$  is the cross-sectional area,  $L$  is the length of the collecting volume and  $Q$  is the charge.

Rearranging Equation 3 for the length of the collecting volume ( $L$ ), then applying the exposure per pulse of  $6.632 \times 10^{-6}$  C/kg (Section 3.4.2.3), the required charge per pulse of 7 pC (Section 3.4.2.1), air density of  $1.05 \text{ kg/m}^3$  and collecting plate area  $2 \text{ cm}^2$  from Section 3.4.1 to the formula, results in a collecting volume length of 5.03 mm.

Plate separation to meet design criterion = 5.03 mm

### 3.4.3 High Tension Supply to Satisfy Ion Transit time

The next step is to establish the high tension supply voltage that is required to produce an ion transit time that satisfies the 1 ms acquisition period allocated for the radiation detector (Section 3.4.2.1) for a plate separation of 5 mm.

#### 3.4.3.1 Ion Mobility

Knoll G, 2000a states that charge mobility is of the order of 1 m/s at 1 atmosphere for an electric field strength of  $10^4$  V/m. Using a nominal 5 mm spacer width, a high tension supply of 50 volts would produce this field strength in the 5 mm spacing. Therefore at 1 m/s it would take a maximum of 5 ms to clear all of the charge from the gap.

Using the above data the mean ion mobility for positive and negative ions in air can be calculated by rearranging Equation 1 for  $K$ . The result is  $1 \times 10^{-4}$  m<sup>2</sup> atm/V/s. Knowing the value of  $K$  it is then possible to calculate the ionisation chamber high tension supply value for the plate spacing of 5 mm using the same formula rearranged for  $V$ . A value of 250 volts would yield the required ion transit of 1 ms. However, since a 420 volt stabilised power supply was available, it was decided to use this to establish a safe margin, resulting an ion transit time of around 600  $\mu$ s.

### 3.4.4 Design Detail and Construction

The array was designed to be assembled in layers, secured together by plastic screws around the edge. There are 4 large holes, one in each corner, to insert plastic studs to facilitate the fixing of the external buildup layers to allow the array to be rotated to measure radiation beams at all gantry angles. A latch-clip at each end of the array is provided for fixing to a commercial holder (Section 8.2). A pixel segmented array was successfully produced using fibre-glass circuit board (Pardo J *et al*, 2005); thus the same material was adopted for this design. Double-sided copper clad fibre-glass circuit board was used for the signal and high tension layers, with lands

and tracks formed by CNC milling. Perspex sheet sprayed with electrically conductive paint was used for the chamber spacer and plain Perspex for the backscatter, integral and external build-up layers. Since the measuring system is sensitive to very small currents, the electrically conductive paint was used to provide an electrical shield. The location of the component layers and collecting plate layout is shown in Figure 3-9 and the dimensions in Figure 3-10.

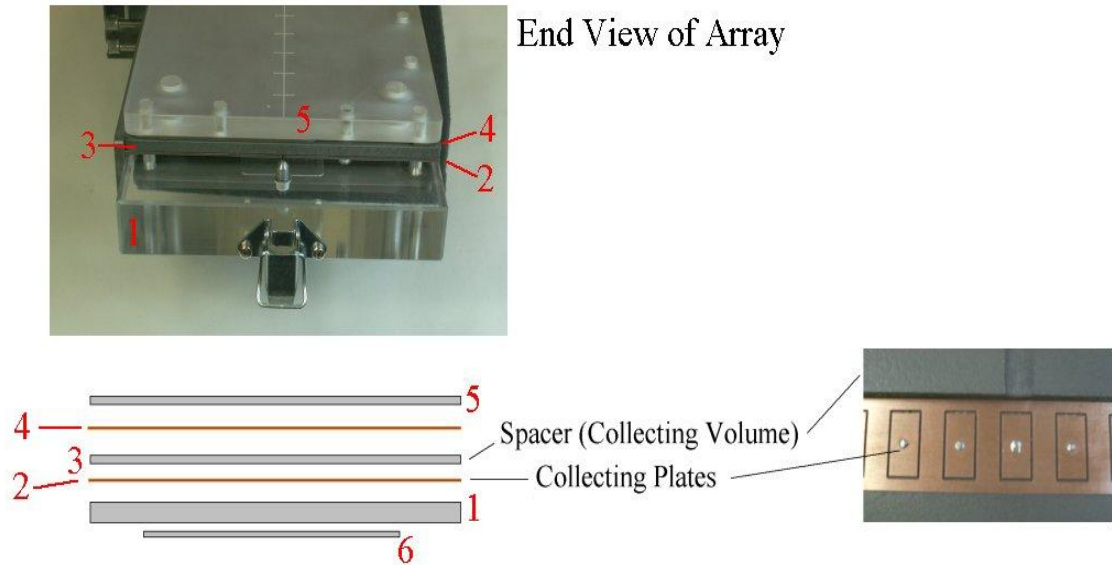


Figure 3-9: End view of the component parts in the completed the ionisation array

- 1.) Perspex backscatter plate.
- 2.) Double-sided copper-clad board incorporating the collecting plate on top and the signal tracks underneath.
- 3.) Perspex spacer with a cut-out to establish the collecting volume.
- 4.) Double-sided copper-clad board incorporating the high tension plate and electrical screen for the top of the array.
- 5.) Perspex integral buildup plate.
- 6.) Perspex plate sprayed with electrically conductive paint to form the electrical screen for the underside of the array.

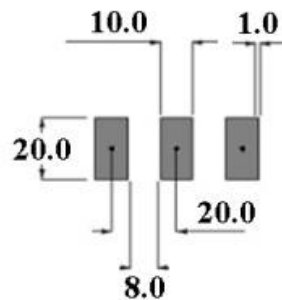
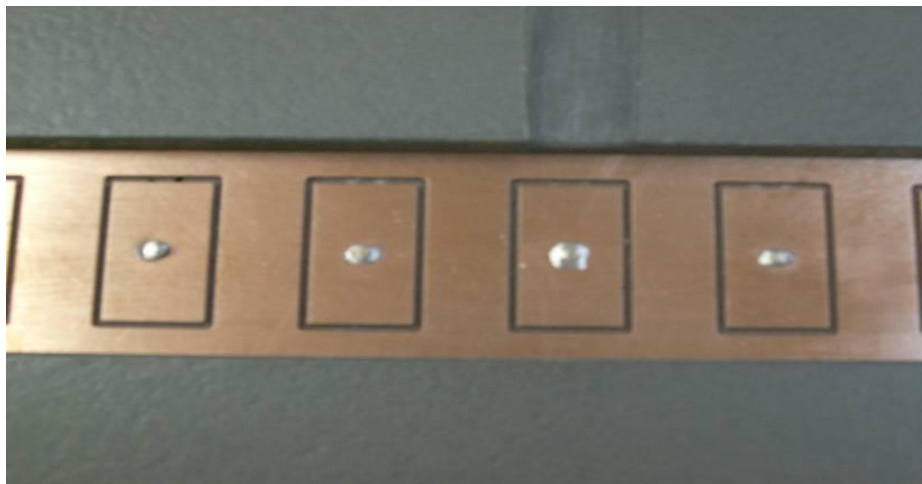


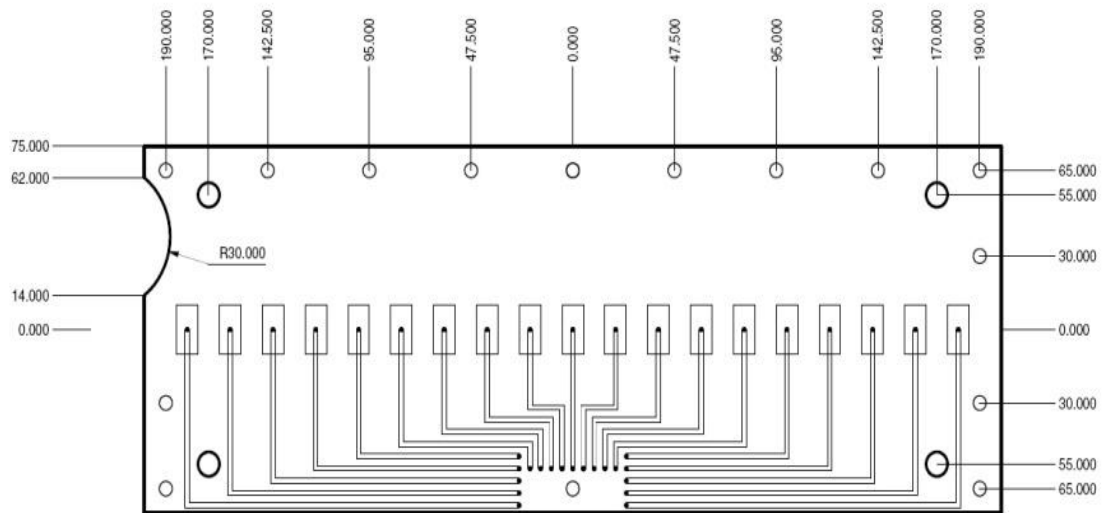
Figure 3-10: Engineering drawing showing the collecting plate detail (dimensions are in mm).

The lands for the 19 collecting plates are laid out as shown in Figure 3-6; these were CNC milled into the fibre-glass board using a 1 mm cutter to form an insulating gap, thus leaving 8 mm of grounded copper between plates to form a guard (Figure 3-10). A hole was drilled in the centre to create a signal path to the underside on the board via a soldered pin (Figure 3-11).



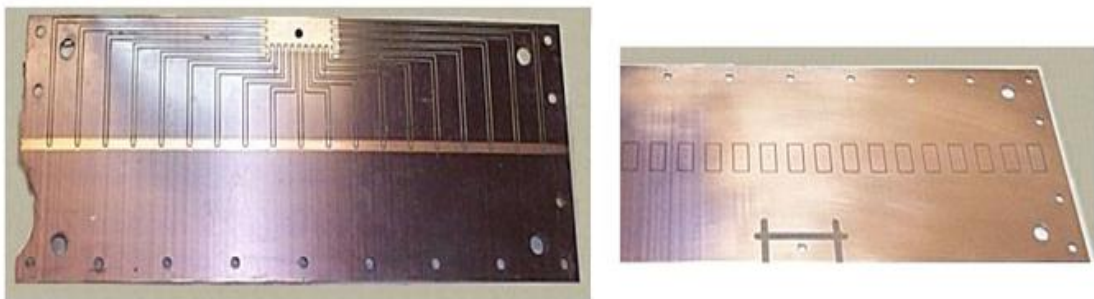
*Figure 3-11: A solder pin in a hole drilled through the substrate connects the centre of the collecting plates to the signal tracks on the underside of the board.*

Figure 3-12 shows the underside of the copper board track designed to carry the signal away from the plates to a common connection point located at the edge of the copper sheet. Note that all the copper that is not part of the signal path is left in place and connected to signal 0 volts, to act as a ground plane and signal guard (Figure 3-13). This is of particular importance on the collecting plate side, since the grounded copper promotes a uniform termination of the electric field with minimal fringing effect and thus defines the active collecting volume of the chamber (Section 3.4.1.1).



**Figure 3-12:** Engineering drawing showing the underside of the collecting plate printed circuit board layer. (The outline of the collecting plates on the top of the layer is shown for clarity) The signal tracks that connect the collecting plates to the edge connector are illustrated (dimensions are in mm).

The grounded zero volt planes in conjunction with the spacers sprayed with electrically conductive paint form a fully enclosed shield, guarding the collecting volume and signal paths from extraneous interference.



**Figure 3-13:** The right hand picture shows the collecting plates milled into the top of the sheet. The signal tracks on the underside can be seen in the left hand picture terminating at the edge of the board. The remaining copper on both sides is connected to signal ground.

A 5mm spacer with an aperture cutout to form an open volume for the 19 chambers and further cutout to allow for the high tension connection and the high tension connecting land is shown in Figure 3-14.

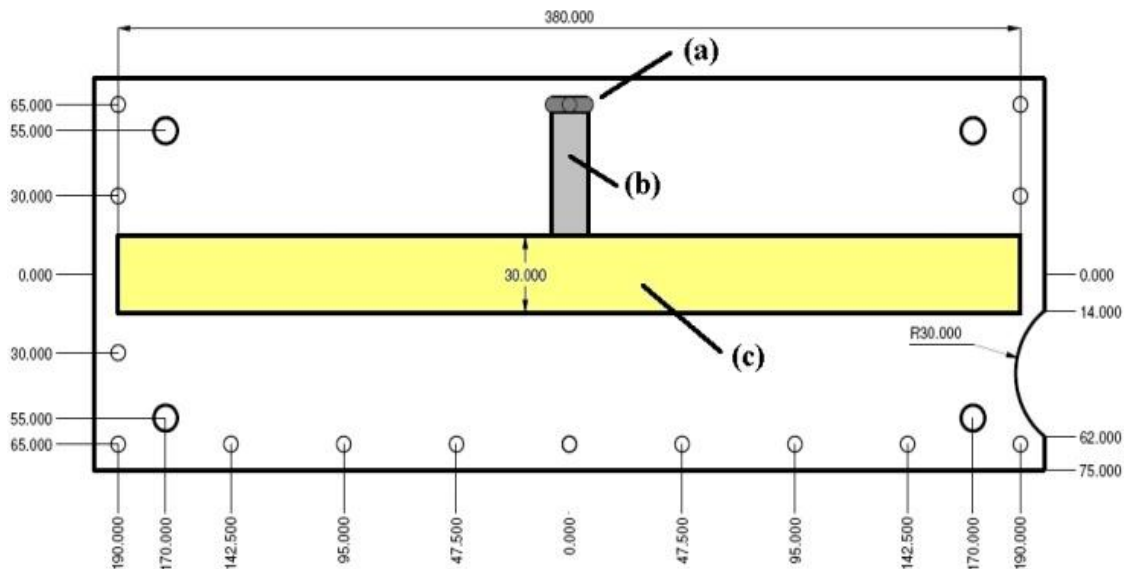


**Figure 3-14:** Engineering drawing showing the Perspex spacer forming the collecting volume. The physical cut-out is shown in (c). The hole allowing the high tension supply to pass through the spacer (a) and the channel to clear the high tension connection from the painted zero volt coating (b), are also shown. (All dimensions are in mm).

The high tension plate area was also defined by a grounded guard to limit the boundary of the field to the collecting volume (Figure 3-15). This kept the electric field away from the internal grounded edge of the spacer, to avoid the formation of a fringe field and also to prevent electrical breakdown to the painted spacer.

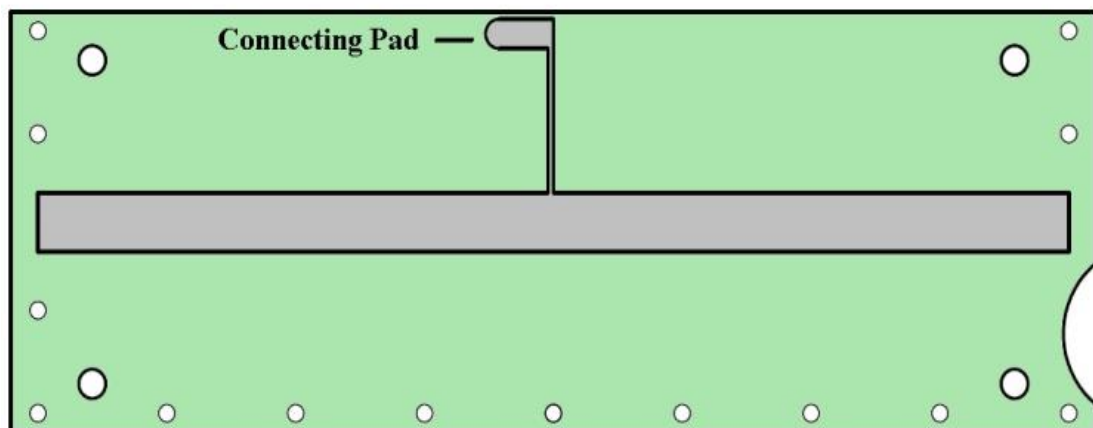


**Figure 3-15:** The high tension plate (grey) and its connection to a pad that lines up with the spacer cut-out to facilitate the high tension supply connection. The green area is connection to signal ground.

The high tension plate, 5 mm spacer and collecting plates are shown prior to final assembly in Figure 3-16. The wiring to from the high tension connection can be seen and also the cutouts that allow continuity to the high tension plate.



*Figure 3-16: The high tension plate, 5mm spacer and collecting plate ready for final assembly. The electrically conductive paint can be clearly seen on the spacer.*

### 3.4.5 Assembly

Both boards were cleaned with solvent to remove grease deposits and solder flux contamination and dried in an oven for 3 hours at 80 °C. From then on, gloves were used when handling the boards. The array was then assembled and tested for electrical grounding.

All of the outer covers were painted with electrically conductive paint. The covers, guard tracks and internal ground planes were all connected to a common point to facilitate a star grounding regime. Connectivity to the star point was confirmed using a Digital Volt Meter (DVM).

The 19 collecting plates, star ground and high tension supply were all terminated to a 'D type' connector. The connector shell was of the 25 way pin-out size, but with a coaxial insert in the centre. The high tension supply was connected through the centre pin of the coaxial connection and the ground connected via the sleeve. The 19 collecting plates were connected to the 'D type' pins. This arrangement meant that the high tension supply was shielded from the sensitive signal connections by the coaxial shroud to avoid leakage currents across the surface on the connector substrate. The outer metal body of the 'D type' connector was also connected to the

star ground point. Polytetrafluoroethylene (PTFE) sleeved instrument wire was used throughout, including the high tension supply, to avoid leakage currents (Figure 10-7).



*Figure 10-7: External connector wiring (PTFE insulated) showing the signal tracks connected to the pins and the central coax connection in place ready to connect the star ground point and high tension supply.*

### 3.4.6 Completed Array

Based on the limiting values for the ADC and electrometer (Section 3.4.2.1), a nominal spacer thickness of 5 mm was chosen for the plate separation. Using a 420 V supply for the high tension (Section 3.4.3) more than fulfills the ion transit time requirement of 1 ms to meeting the system timing specification (Section 3.3.3.1).

Although a diode array was excluded on funding grounds, and may have been a less challenging technique and easier to produce, the design and construction of an in-house array was a valuable and instructive solution to the design requirement. The completed radiation detector assembly is shown in Figure 3-17.

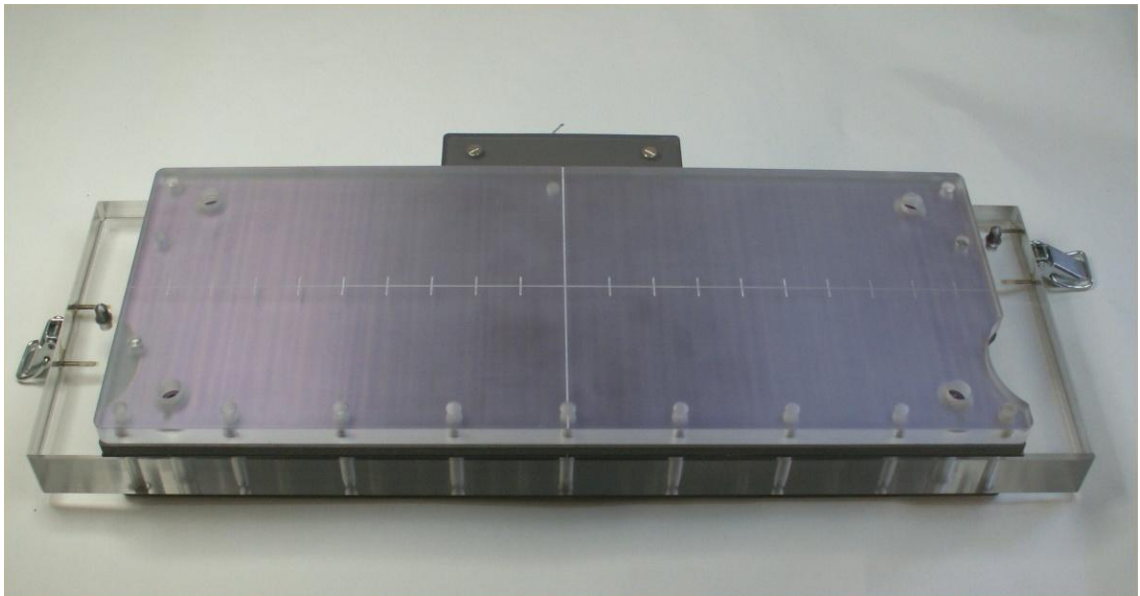


*Figure 3-17: Photograph of the completed linear array: consisting of 19 equally spaced ionisation chambers. The fixing clips enabling the array to be attached to the holding frame can be seen at either end.*

The array is designed to fit a commercial holding frame that attaches to the accelerator radiation head accessory ring (Figure 3-18). This facilitates the study of radiation beam profiles during gantry rotation. The collecting plate centres are marked on the top face to facilitate alignment with the accelerator axis to be measured.



*Figure 3-18: The completed array fitted the accelerator radiation head accessory ring using the commercial holding device, with the required build up secured by 2 of the 4 threaded studs, ready to measure rotational beams.*

### 3.5 Design - Integrating Electrometer

To process the small current pulses from the ion chamber array, an electrometer amplifier is required to produce a signal of usable amplitude (Clayton G & Winder S, 2003, Khan F M, 2003). Also, to avoid the need to detect the peak amplitude of the pulse, an electrometer can be configured as an integrator. Thus, the area under the pulse is equal to the collected charge, and is used to represent the level of the radiation collected by the ionisation chamber plate.

#### 3.5.1 Evaluation and Description

An integrating electrometer circuit previously designed by the author in support of a PhD project (Glendinning A G, 2001) was evaluated for its suitability for meeting the required specification. Utilising the AD549 integrated circuit (Analog Devices Ltd, 2007) the original design was carefully conceived for low drift and low leakage (Analog Devices Ltd, 1971, Andreo P *et al*, 2007, Rich A, 1983).

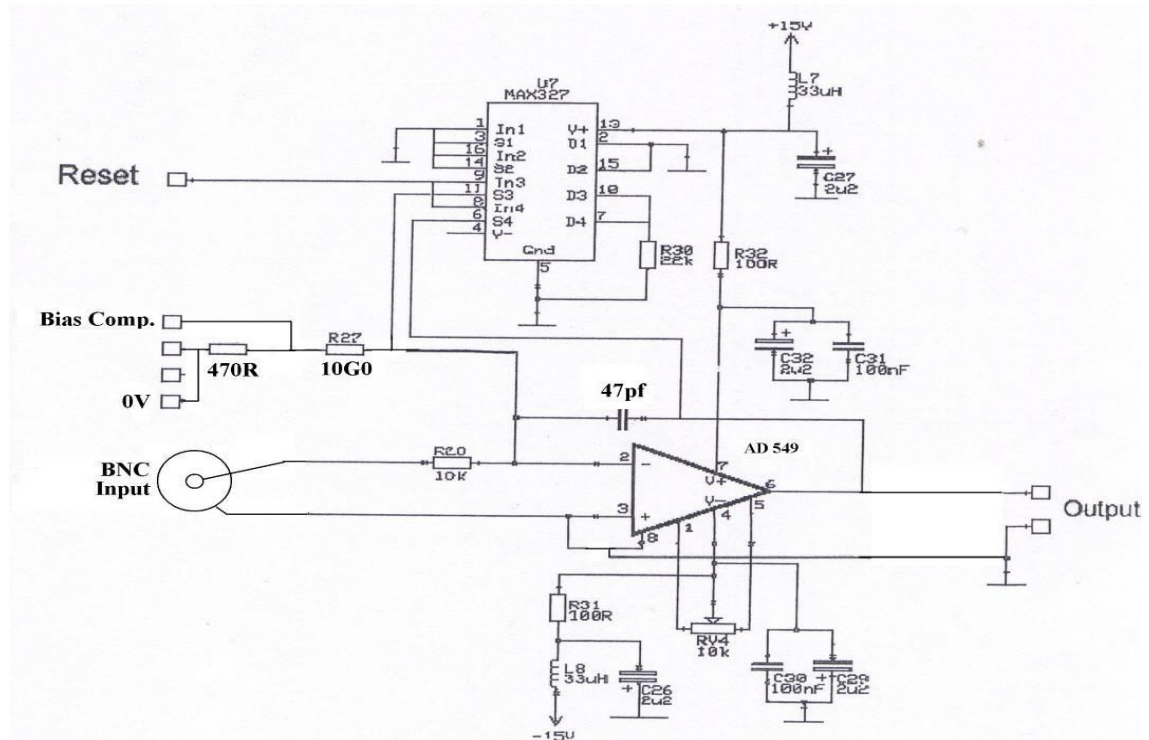
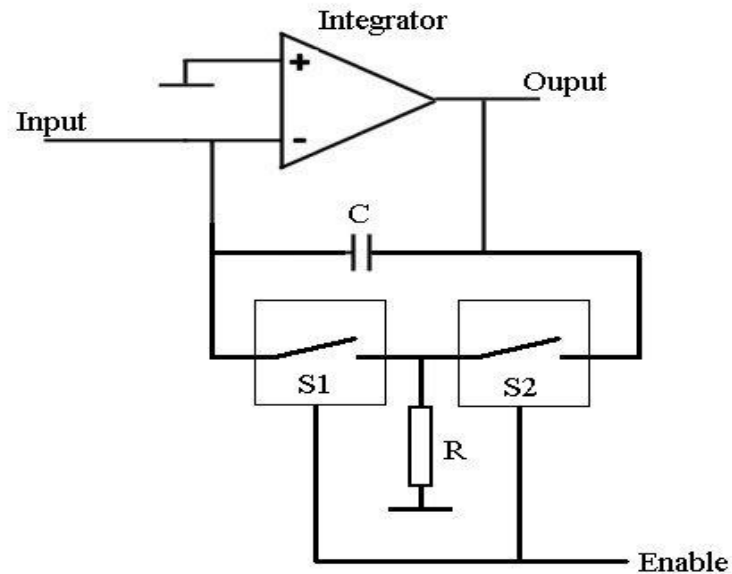


Figure 3-19: One integrating electrometer channel.

The AD549 integrated circuit was configured as a current integrating electrometer (Figure 3-19) using a 47 pF capacitor, producing an output voltage proportional to the integral, with respect to time, of the input signal current. This was the smallest value of integrating capacitance that could be used for the design, since values less than 25 pF resulted in low frequency instability in the form of oscillations superimposed on the output signal.

Bias current offset compensation adjustment was provided by a preset potentiometer connected to pin 4 of the AD549. A 10 G $\Omega$  (Welwyn Ltd, 2004) resistor was incorporated into the circuit allowing an offset compensation current to be injected in to the input summing junction to null out any external leakage. This feature was added since the ionisation chamber array was not yet constructed, and therefore the leakage current was unknown and may have required leakage compensation. Also, it would be possible to use the offset compensation system for diagnostic testing and performance evaluation each time the measuring system was turned on.

To avoid the leakage problem of a single switch, integrator reset was achieved using two Complementary Metal Oxide Semiconductor (CMOS) bi-lateral switches type MAX 327 (Maxim Semiconductors Ltd, 1996) in series with a common enable (S1 and S2 in Figure 3-20) (Clayton G & Winder S, 2003). When the switches S1 and S2 are in the 'off' state, the integrator output ramps up at a rate set by capacitor C and the input current. The voltage at the junction S1, S2 and R is zero as S1 and S2 are off and the point is pulled down to 0 Volts by resistor R.



**Figure 3-20: Integrator reset circuit.**

Since there is no volt drop across S1, no current can flow into the integrator summing input other than any internal leakage within the device. This arrangement leads to superior input offset performance. When both S1 and S2 are set to the ‘on’ state then capacitor C is discharged and the integrator reset. With no input connected to the circuit and a total ‘on’ resistance per switch of 3.5 k $\Omega$  at a temperature of 25 °C (Maxim Semiconductors Ltd, 1996) and an integrating capacitor of 47 pF, a reset time constant of around 330 ns is realised.

### 3.5.2 Electrometer Construction

Great care was taken in the construction of the electrometer hardware. During the Printed Circuit Board (PCB) artwork phase, caution was taken in the isolation of signal paths by the use of grounded guard tracks (Clayton G & Winder S, 2003). All unused areas of the PCB were left with the copper in place and connected to ground potential to produce a ground plain. Attention was paid to position power supply decoupling components as physically close to the electrometer integrated circuit as possible. This would limit the inductive effects of the printed circuit board track on high frequency instability due to the high gain of the circuit. Care was taken to prevent

parasitic currents at the input summing junction of the integrator from producing systematic errors in the measured signal. This was achieved using the PTFE spaced pillar (Figure 3-21) with an integral solder post as a common connection point (Analog Devices Ltd, 1967, Williams T, 2005). Terminating the input components to this point resulted in superior isolation of the signal path from parasitic currents flowing in the PCB substrate. Surface residues on the circuit board were removed by cleaning with a proprietary PCB solvent spray and then drying in an oven at 50 °C for 4 hours. After cleaning, the PCBs were handled using gloves.

The input signal was connected to the circuit using a PCB mounted Bayonet Neill–Concelman (BNC) connector. In this type of connector the outer shield is commonly connected to ground potential with the threaded mounting. In this case, a connector was chosen with its mounting isolated from the shield to eliminate common ground connection at the electrometer inputs, as the whole electrometer array would finally be encapsulated in a screened metal box. Ground loop currents would thus be avoided, as all the electrometers would be connected to a common ‘star’ ground potential at the analogue input (Clayton G & Winder S, 2003, Williams T, 2005). The signal pin of the BNC was soldered directly to a 10 kΩ resistor which was connected to the input summing point on the PTFE spacer, thus avoiding any connection with the PCB. This prevents any parasitic currents in the PCB substrate from entering the signal path.

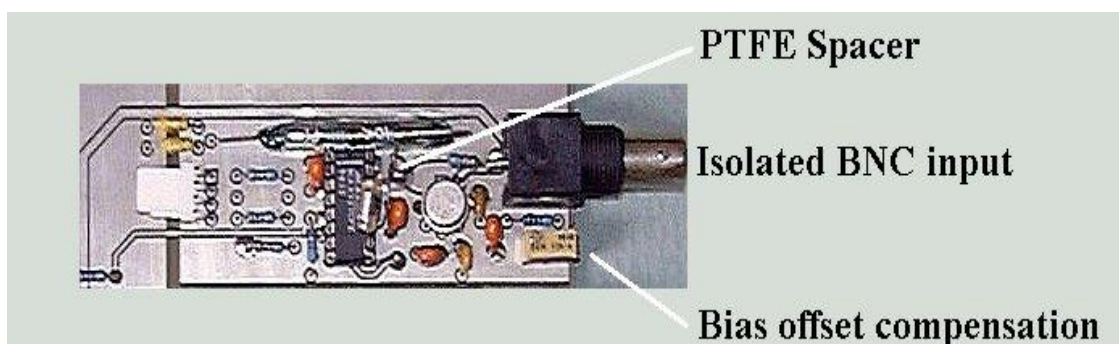


*Figure 3-21: Single electrometer channel. The PTFE spacer to isolate the input summing point, isolated BNC connector and bias offset are illustrated.*

### 3.5.3 Ion Chamber Simulator

Moving delicate prototyped electronic circuits from the bench to a linear accelerator for development and testing is not ideal. The possibility of the circuit becoming damaged in transit is high. Also, access to a treatment machine is limited by clinical need. As revealed in the initial electrometer development, the circuit under test must be in the treatment room to avoid the problems with the ion chamber connecting cable capacitance (Section 3.5.6). Thus the use of test equipment would be very limited, as it is not possible to be in the treatment room with the radiation beam on. Remote control of equipment is an option, but is prohibitively costly for this project. Some work could be done using extension leads, but this would be limited by cable effects which could misrepresent a measured parameter or ‘load’ the circuit under test. It was therefore decided to construct a device dedicated to producing a signal similar to that from an ion chamber array in a linear accelerator radiation beam to aid system testing, fault diagnosis and operational validation in the laboratory environment. This was named ‘Dose Simulator’ and is detailed in Appendix 3. It was decided to use the same core microcontroller as the proposed measurement system to provide insight into its use in the final measurement system, in hardware and software terms.

### 3.5.4 Initial Testing

As described in Section 1.2.1, linear accelerator radiation is delivered in pulses, and the integrating electrometer circuitry has been designed with this in mind. Initially, though, fundamental tests were implemented on the bench by introducing DC current into the circuit to confirm basic functionality. Performance was then assessed under pulsed operation on a linear accelerator.

### 3.5.4.1 Test Setup for Direct Current

The circuit was connected to an array of test equipment to allow basic functional performance to be evaluated in both the DC and pulsed modes (Figure 3-22). System timing was established using a pulse generator (Philips Test and Measure Ltd. PM 5712) connected to the electrometer reset. The required pulse intervals were set by monitoring the signal with a counter/timer (HP 5315a Hewlett Packard) and channel 1 input of a Digital Phosphor Oscilloscope (DPO) (Tektronix DPO 4034). Since the pulse generator was limited to 20  $\mu\text{s}$  minimum pulse width, 25  $\mu\text{s}$  was chosen as the reset pulse width, which is more than 75 times the calculated time constant of 330 ns (Section 3.5.1). The acquisition duty cycle was carefully set to 25  $\mu\text{s}$  reset period, 5, 10 and 20 ms sampling intervals as required, to generate simulated timing for 2, 4 and 8 radiation pulses respectively, of width 2.5 ms (PRF = 400 PPS).

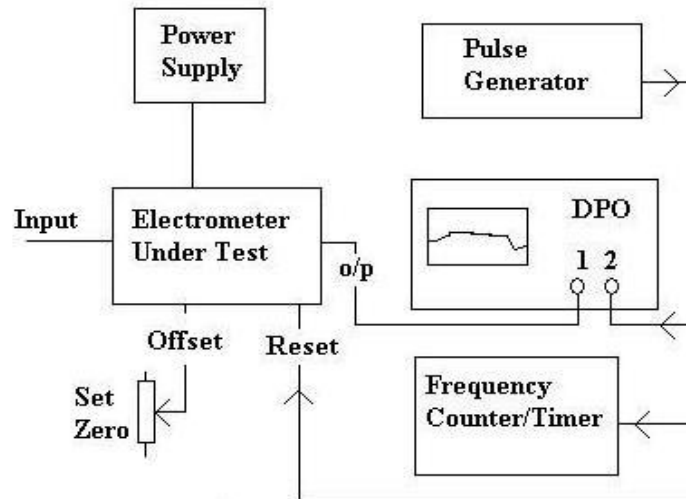


**Figure 3-22: Test fixture of prototype integrating electrometer circuit. Arrangement of test equipment to evaluate performance in DC and pulsed modes.**

The equipment was powered on for longer than the 15 min warm-up period required for the AD549 electrometer, specified in the datasheet (Analog Devices Ltd, 2007) to allow the integrated circuit to reach thermal equilibrium. The pulse generator was turned off and the 'set zero' potentiometer disconnected from the electrometer.

The bias offset potentiometer, on the circuit board (Figure 3-21), was then adjusted for zero volts at the electrometer output. The 'set zero' was then reconnected and the electrometer output set to zero volts by adjusting the potentiometer; the pulse generator was then switched on again. The output of the electrometer was connected to the channel 2 input of the DPO ready to view the integrated samples. The circuit was then ready for testing.

### 3.5.4.2 Direct Current Test

The output of a stabilised DC power supply (Farnell Electronics Ltd) was connected to a digital voltmeter (DVM) to provide an adjustable DC voltage source (Figure 3-22). This was connected to a 10 G $\Omega$  precision resistor (Welwyn Ltd, 2004) screened in a metal box as a voltage to current converter to the electrometer test fixture input (Figure 3-23).

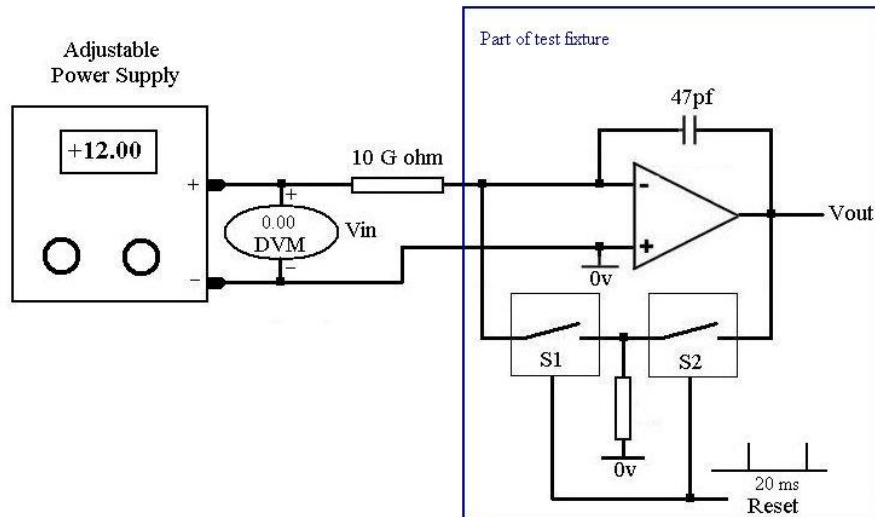


**Figure 3-23: Test configuration for DC input to the test fixture in Figure 3-22.**

With a 47 pF integrating capacitor and a 10 G $\Omega$  input resistor, the input voltage was adjusted using the DVM from -12 volts to +12 volts in 0.5 volt steps (an input current range of +/-1.2 nA) and the output voltage recorded using a precision voltage measuring function within the DPO. The whole experiment was repeated 4 times for samples rates of 5, 10 and 20 ms. The results are plotted in Figure 3-24.

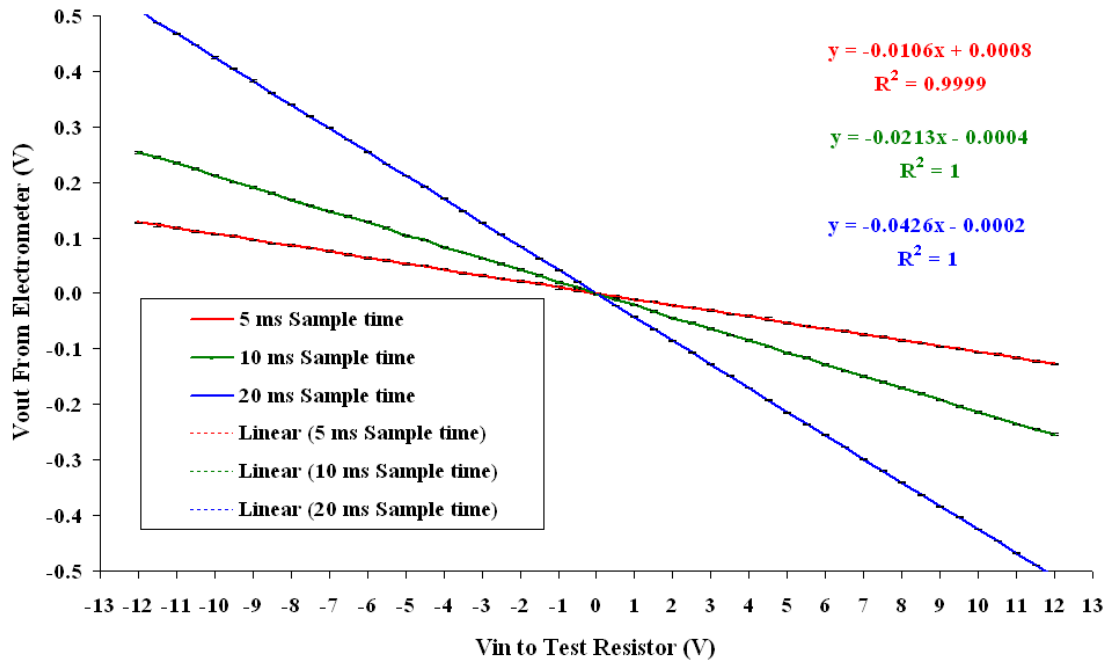


**Figure 3-24:** Measured electrometer output for sample times 5, 10 and 20 ms over the test range -12 to +12 volts.

The expected output of the test integrator circuit was calculated using Equation 4.

$$V_o(t) = \frac{-1}{RC} \int_0^t V_{in}(\tau) d\tau$$

**Equation 4**

where  $V_o(t)$  is the output voltage at time  $t$ .  $R$  is the input resistance,  $C$  is the integrating capacitance and  $V_{in}$  is the input voltage ( $R$  and  $C$  determine the time constant).

The expected output voltages for input currents generated using a 10 G $\Omega$  input resistor and power supply as configured in Figure 3-23 from -12 volts to +12 volts in 0.5 volt steps for the 3 samples rates were calculated. The calculated output values were compared with the mean of the 4 measured samples; the results are presented in Table 3-2.

The main purpose of this fundamental test was to prove the circuit design for use in a sampled mode, by demonstrating a linear transfer function of expected values for the 3 sample rates tested (5, 10 and 20 ms).

Sample Time (ms)	Max error (mV)	Min error (mV)	Error Over Test Range (+/-12 volts)	
5	0.27	-2.13	+0.001%	-0.009%
10	2.13	-1.27	+0.009%	-0.005%
20	1.61	-1.26	+0.007%	-0.005%

**Table 3-2: Summary of the worst case deviations from the calculated values for the sample times used in the test.**

Exceptional linearity is demonstrated by the  $R^2$  values in Figure 3-24 and minimal deviation from the expected calculated values as shown in Table 3-2.

### 3.5.4.3 Electrometer Reset

Using the same test setup as in Sections 3.5.4.1 and 3.5.4.2, the expected electrometer reset behaviour was confirmed. The stabilised DC power supply connected to the 10 G $\Omega$  input resistor was adjusted to produce a 1 V peak to peak ‘saw-tooth ramp’ from the electrometer output on the DPO; this was captured and transferred from the DPO memory to a computer for processing as high resolution numerical data, to enable small segments of the signal to be examined in detail. The whole data set from the DPO is plotted in Figure 3-25.

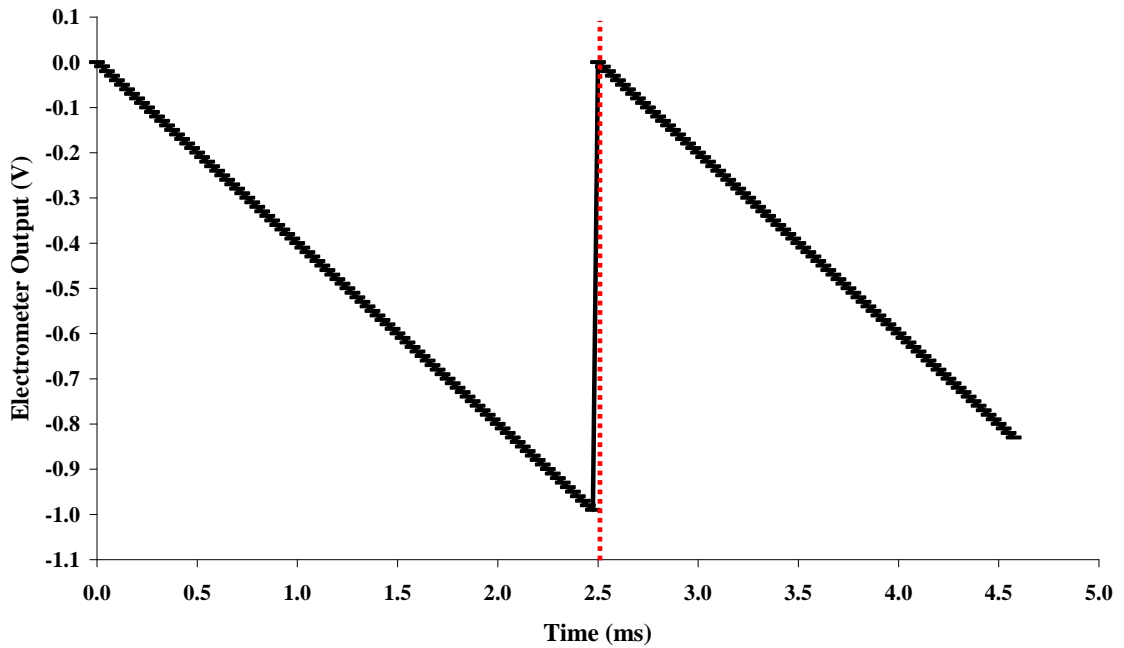


**Figure 3-25:** *Electrometer output for reset confirmation. The red dotted line depicts a reference marker at which the electrometer signal approaches zero volts, after the electrometer reset pulse terminates.*

A small segment of the same DPO data set is expanded and plotted in Figure 3-26 where the discharge time constant of 330 ns (Section 3.5.1) is approximated between the blue markers in the figure. An electrometer reset to zero volts is confirmed in Figure 3-27 where the mean of all the points from the 4 to 20  $\mu\text{s}$  time period is 0.03 mV (2 SD = 2.27 mV).

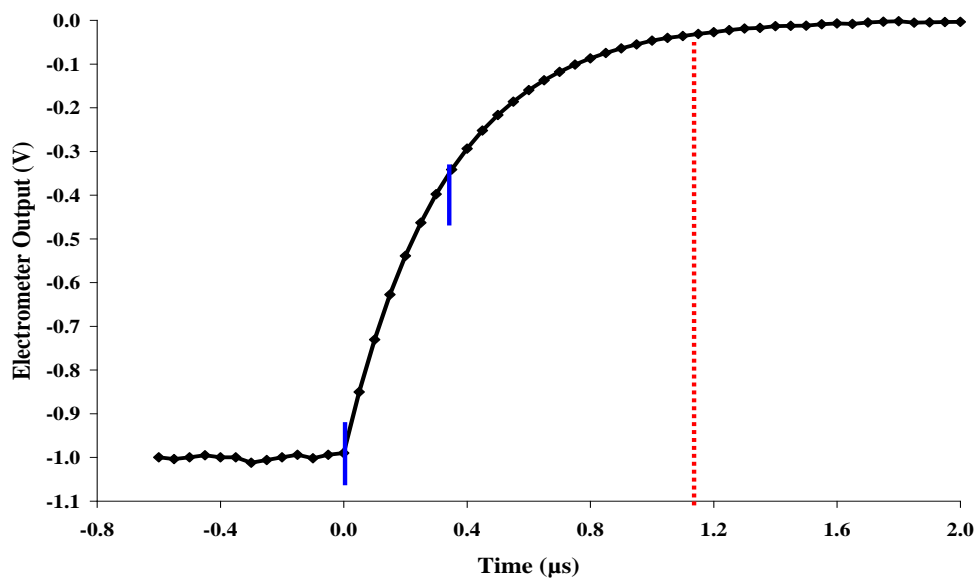


**Figure 3-26:** *Data from Figure 3-25 expanded to show the point of integrator reset. The blue markers show approximately 1 time constant (330 ns, Page 83), the data marker in red aligns with the marker in Figure 3-25.*

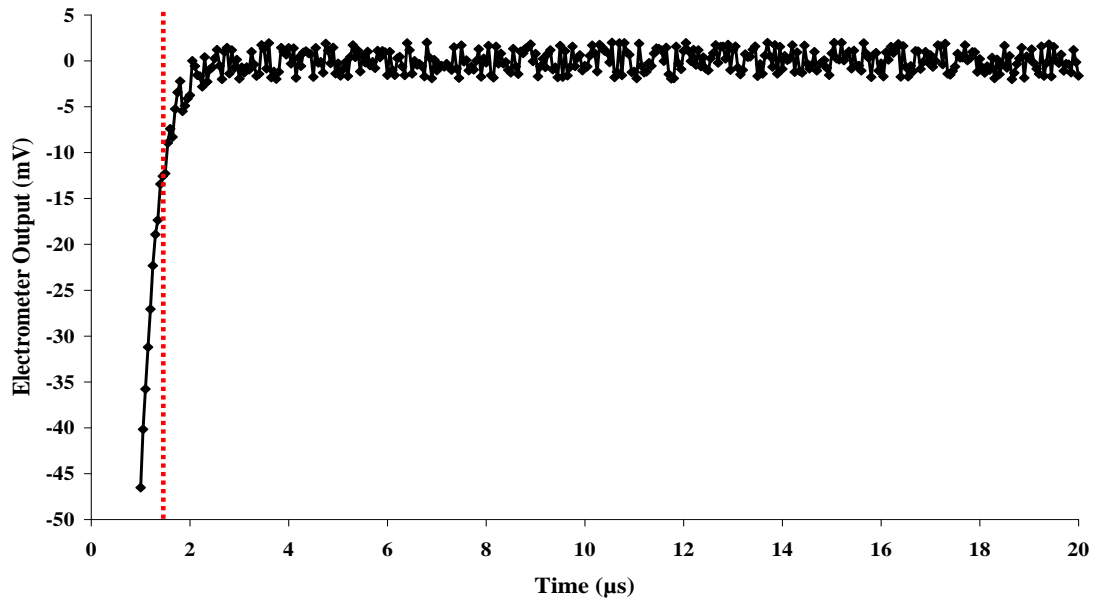


*Figure 3-27: Data from Figure 3-25 expanded to the point of integrator reset to demonstrate that the electrometer is reset to zero volts. The data marker in red aligns with the marker in Figure 3-25.*

#### 3.5.4.4 Prototype Ionisation Chamber for Preliminary Testing

A 20 channel linear ionisation chamber array (Figure 3-28) previously constructed by the author was used to evaluate the electrometer hardware on the Elekta linear accelerator (See Appendix 2 for specification).

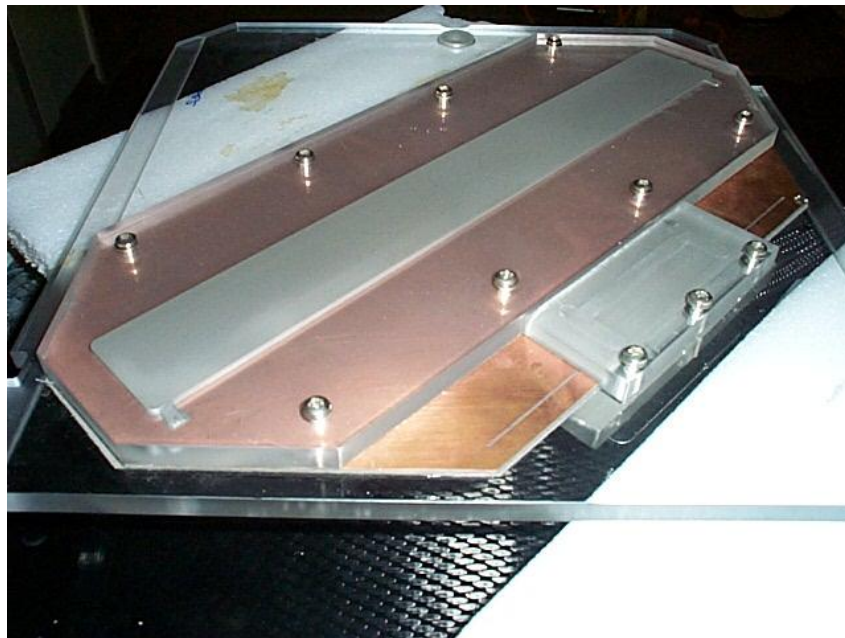


*Figure 3-28: Ionisation chamber used to produce a test signal from a linear accelerator (See Appendix 2 for specification).*

The array was only useful as a test signal source, since design defects had been noted previously, making this array unsuitable for the proposed research work:

1) The array was designed to fit in to the ‘shadow tray’ of the accelerator, measuring beam data 63 cm from the source to the midpoint of the collecting volume. Radiation beam quality assurance measurements are performed at the isocentre, so to measure beam data at a non-standard SDD would deviate from standard practice.

2) During the initial calibration of the chambers, the factors required to calibrate the outer chambers were substantially different from the rest of the chambers. This was attributed to scatter due to insufficient clearance with the end of the collecting cavity (Figure 3-29).

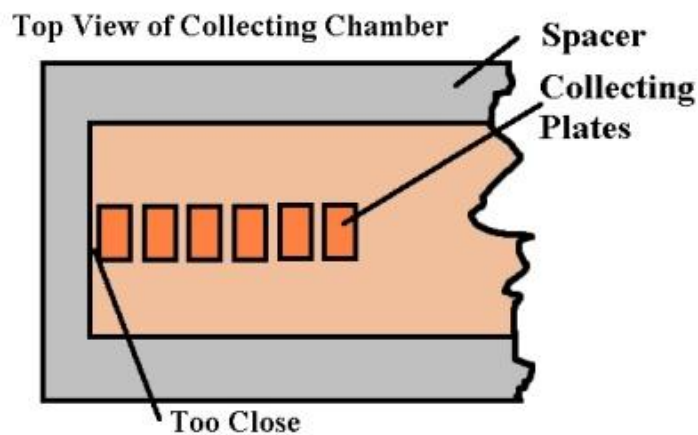


*Figure 3-29: Diagram of one end of the collecting chamber of the test ionisation chamber array, illustrating the suspected error.*

To have confidence in the validity of the measured data, the effect of such a large discrepancy in the calibration factors of the end chambers and the concern regarding the SDD would need to be investigated. Other lessons had been learnt in the construction of the array. For example the complexity of the mechanical assembly made it difficult to maintain cleanliness during construction. All the lessons learned were incorporated into the design and construction of a new array.

### 3.5.4.5 Electrometer Performance on an Linear Accelerator

A signal from the prototype ion chamber array described above was taken by cable down the treatment room maze of a linear accelerator to the control area outside the radiation bunker to the same test fixture used in the DC current tests (Figure 3-30).

The linear accelerator was set to 6 MV X-rays and the test ionisation chamber array to 63 cm SDD in the radiation head shadow tray with 5 cm of Perspex build up. A supply of -420 volts DC was applied to the polarising plate of the array.

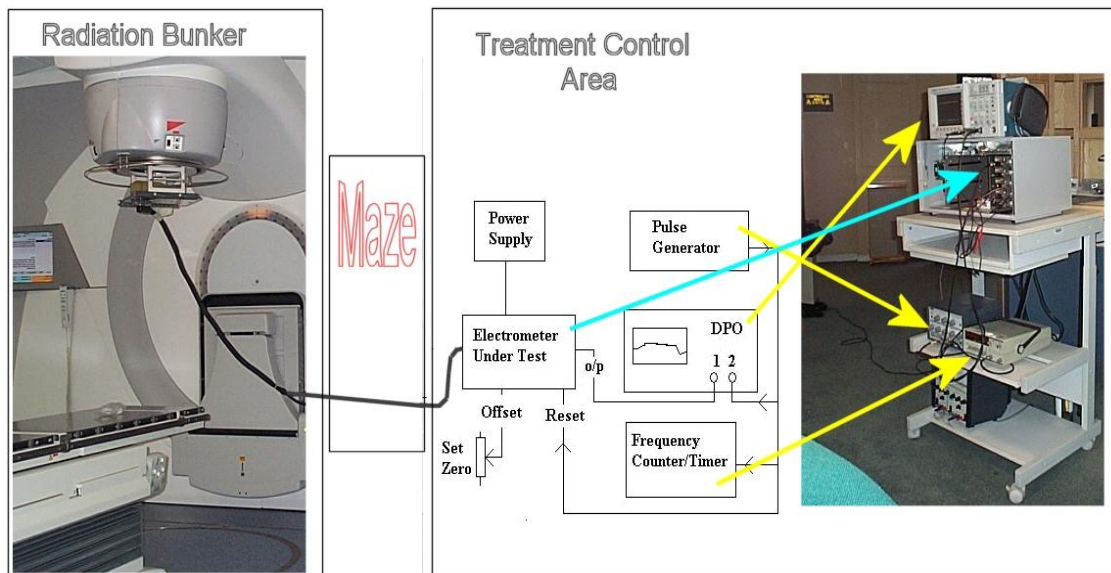


**Figure 3-30** Initial testing of electrometer hardware.

The radiation beam was switched on and the electrometer output signal levels were monitored on the DPO channel 2 display. The DPO display was stored (Figure 3-31) and the signal levels examined. The results were not as expected since the reset did not restore the output of the circuit to zero volts (Section 3.5.4.3).

The data was analysed as follows. With reference to Figure 3-31, after the reset pulse marked 'C' in the figure, the next sample starts from a positive plateau, voltage level 'B' at point 'G' instead of zero volts 'D' at point 'F'. The voltage 'A' would be sampled by the proposed measurement system at point 'E', the end of the sample. This voltage should represent the integrated value of the sample of radiation pulses.

This overshoot voltage ‘B’ at point ‘G’ was clearly incorrect, as the design specifies the electrometers should reset to zero volts, as confirmed in Section 3.5.4.3, where the acquisition system read would the voltage ‘A’ at point ‘E’. Should the integration of the next radiation pulse not start from a known reference, in this case zero volts, then the value of the measured signal is unreliable.

Test parameters were changed to find which would affect the overshoot level. It quickly became apparent that reset pulse width was the key. The reset pulse had to be at least 120  $\mu\text{s}$  long to produce no overshoot. The experiment was then concluded.

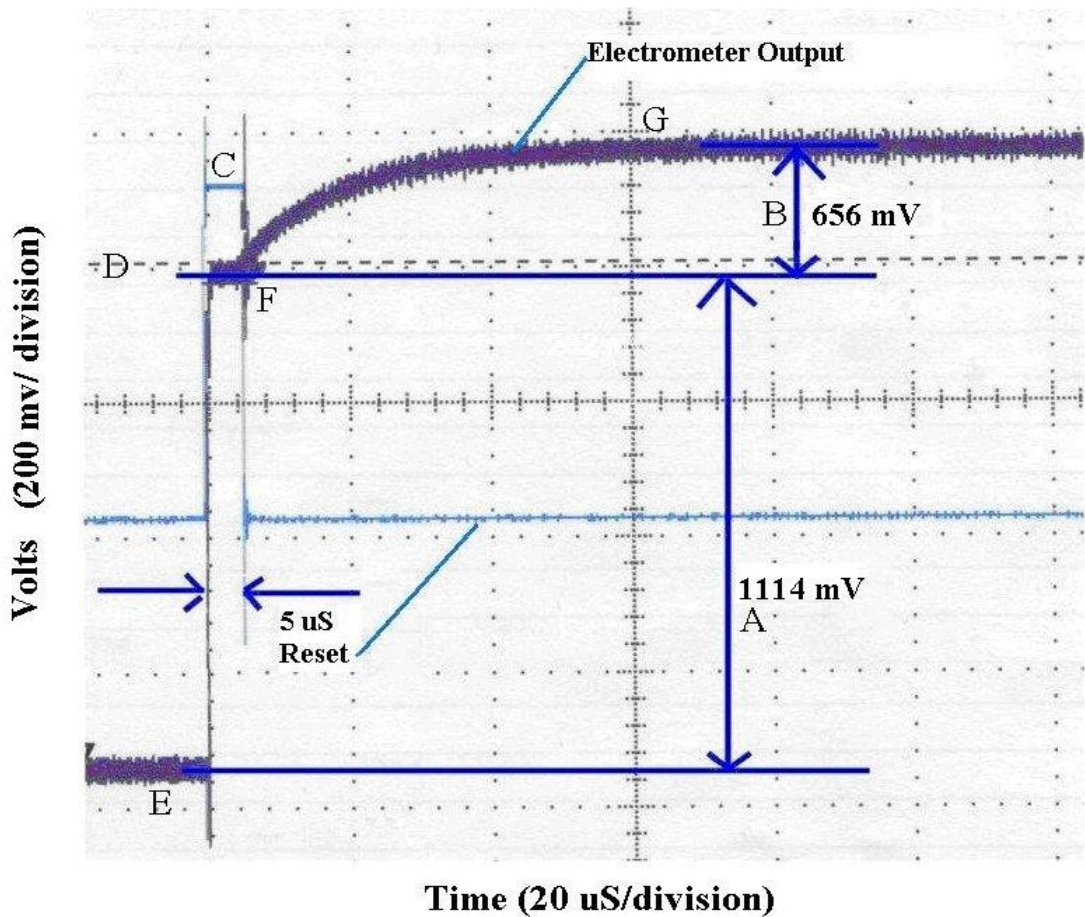


Figure 3-31: Electrometer output waveform on DPO channel 1.

Key to measurement references in Figure 3-31	
A	Voltage to be sampled by acquisition system
B	Unexpected output overshoot
C	Electrometer reset pulse
D	Zero volt reference
E	Final integrated sample on electrometer output
F	Start of unexpected output overshoot
G	End point of overshoot

### 3.5.5 Discussion

A reset pulse width of 120  $\mu\text{s}$  required to produce no overshoot was different from the 25  $\mu\text{s}$  reset period of the test setup, which was based on a value many times greater than 5 time constants of 330 ns (the internal time constant of the reset circuit in Section 3.5.1). The anomaly was attributed to an unexplained phenomenon in the test experiment. In Figure 3-31 the rise to the overshoot between F and G looks exponential and is an order of magnitude longer than the 5  $\mu\text{s}$  reset pulse used in the experiment. This pointed to a capacitive effect somewhere in the circuit, which was verified when the circuit was tested on the bench in the electronics laboratory using a simulated current source from a pulse generator. The ‘overshoot’ was not evident until the long maze extension cable was introduced into the circuit. The observed effect appeared to be due to the line capacitance of the extension cable. The cable type G 02330 HT tri-axial cable has a quoted capacitance of 115 pF/m (Hubner and Suhner Ltd, 2007). Using a 20 meter length, approximately 2300 pF capacitance would be presented to the input circuit of the electrometer. The quoted internal capacitance of the 10 G $\Omega$  offset compensation resistor is less than 1 pF, which is negligible compared with that of the cable. The cable capacitance would produce an input time constant of approximately 22  $\mu\text{s}$  for an input resistor of 10 k $\Omega$ . Within 110  $\mu\text{s}$  (5 time constants), the extension cable would be fully discharged. No overshoot was evident in the experiment at reset pulse widths greater than 120  $\mu\text{s}$ , at which point the extension cable would be fully discharged.

The electrometer circuit was analysed and the conclusion drawn was that during reset, the front edge of the electrometer output signal is presented to the input cable as a step change. This charges the cable capacitance, which then discharges into the electrometer at a rate set by its own time constant. The reset pulse must be asserted for longer than 5 time constants of the input circuit capacitance to fully discharge the input capacitance and hence realise no significant error in the collected charge.

In the case above, at reset, the negative signal on the output of the electrometer, (voltage 'A') charges the extension cable negatively. The reset pulse 'C' terminates too early and charge stored on the cable is transferred into the electrometer summing input causing it to ramp up exponentially in a positive direction 'F' to 'G'. When most of the charge is transferred at point 'G', the electrometer will hold its output until the next radiation pulse.

If the overshoot voltage 'B' (Figure 3-31) was included in the acquisition, the electrometer charge could be correctly measured, but since the system design specifies the acquisition point after the last pulse of a sample, the measurement would be in error. The voltages A + B represent the actual signal to be recorded. Acquiring all the 19 channels twice to yield the electrometer charge and overshoot would be impractical due to the tight timing constraints of the design. This would also throw doubt on the reliability of the data since the cable capacitance would influence the measurement.

### 3.5.6 Conclusions Drawn from Initial Tests

Basic functionality was demonstrated by presenting a DC current to the test fixture at 3 sample times. The same test fixture used for the DC tests was moved to the linear accelerator control area and the test ionisation chamber array was installed on the machine. During testing, a problem was encountered with signal loss at short reset pulse widths. An investigation produced a hypothesis that there was a capacitive effect in the connecting cable between the ionisation chamber array and electrometer. A similar effect was noted in a design by Iida T *et al*, 1978 that measured data from a nuclear reactor core at high temporal resolution using an ionisation chamber. The long cable described in the text required a 'driven' screen in the connecting cable to limit the cable's capacitive effect.

Although the electrometer hardware was to be in the treatment room in the final design, resulting in a much shorter connecting cable, the effect had to be considered. A reasonable length of cable would be required to allow sufficient clearance with the

control box when the array is used in the holding device for rotational beam measurements. It was therefore concluded that the same test should be repeated after construction of the acquisition system hardware with the new ionisation chamber array/cable assembly, as part of the validation testing to establish the correct minimal value for the reset pulse width.

## 3.6 Design – Data Acquisition System

### 3.6.1 Design Plan

A design for an ionisation chamber array and the collection of charge using an integrating electrometer has been explored in detail. Based on a predicted charge of 7 pC per pulse and a 47 pF integrating capacitor the electrometer output can be calculated using Equation 5, yielding a value of 0.148 V.

$$V = \frac{Q}{C}$$

**Equation 5**

where **Q** is the charge on the capacitor, **C** is the capacitance and **V** is the applied voltage.

On the basis of the points discussed in Section 3.2 and an electrometer design in Section 3.5 a microcontroller-based data acquisition system was conceived using a single ADC for analogue inputs utilising multiplexing to expand the number of input channels to accommodate electrometer and external analogue signal channels. A 12 bit resolution ADC with 2.4 mV per step was chosen (type MAX 176 Maxim Semiconductors Ltd, 1998). A resolution of 1 mV was chosen for the data acquisition design; therefore it was necessary to amplify the signal by 2.4 times after multiplexing. This figure results in close mapping for the calibration of the external analogue inputs to 1 mV/bit for ease of calibration. The charge resolution at the

electrometer inputs can also be calculated from Equation 5, and is 45 fC. Using an ADC range of +/-5 Volts, 14 pulses would clip the ADC input. This would set the upper limit at the accelerator maximum PRF of 400 PPS to 35 ms per sample. For a high temporal resolution system this is not a problem since the nominal sample rate would be around 10 to 20 ms. Based on the data in this Section and discussion in Section 3.2, a block diagram of the data acquisition part of the measurement system was envisaged (Figure 3-32).

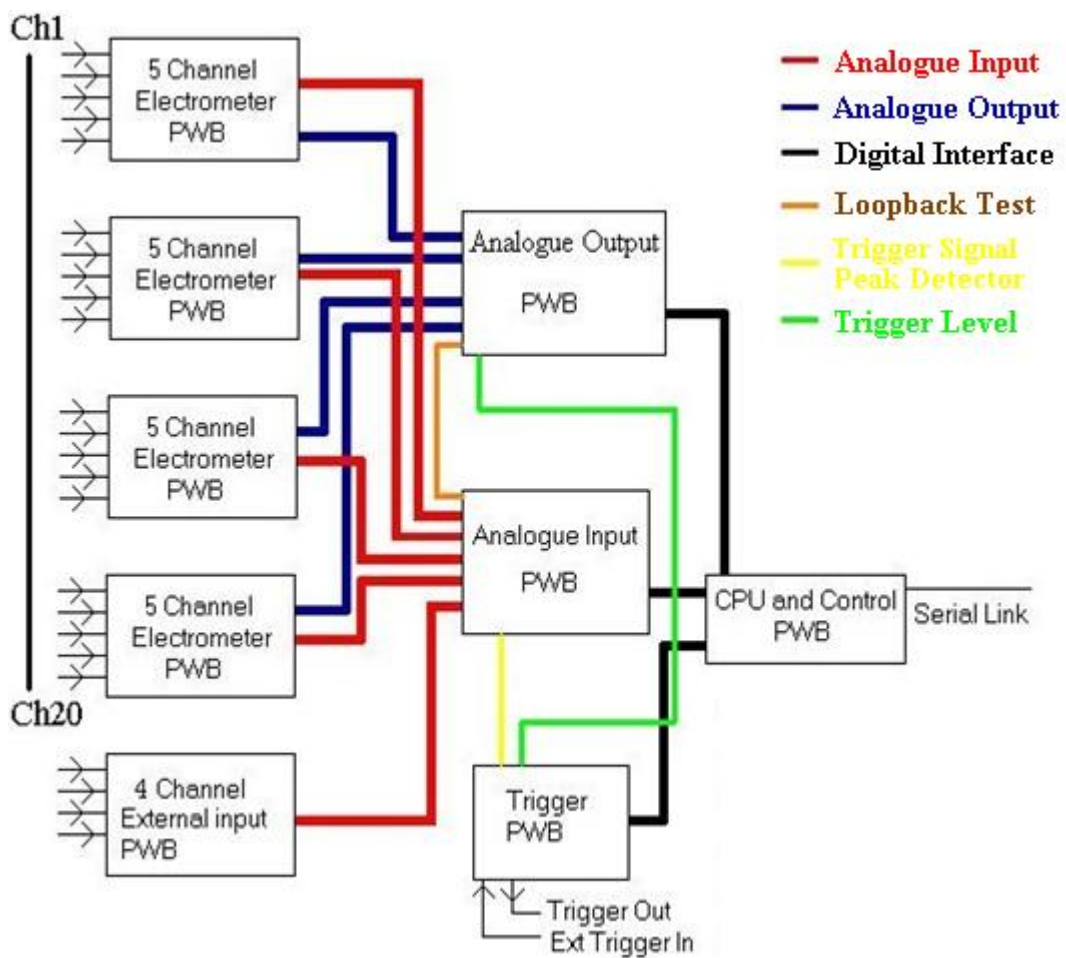


**Figure 3-32: Block diagram of 'Beam Scope' hardware.**

The design consists of a high speed serial analogue to digital converter with a pair of fast 16 channel multiplexers resulting in a 32 channel data acquisition system.

The channels were allocated as follows:

- a) 19 electrometers for the linear array.
- b) A spare electrometer for use with a single ionisation chamber as required.

- c) 4 dedicated analogue inputs with external signal processing in the analogue 'input pod'.
- d) A loopback test signal from the digital to analogue convertor section for functional testing.
- e) 2 voltage reference channels used for functional testing.
- f) Trigger peak level signal.
- g) Temperature sensor.

A 32 channel Digital to Analogue Convertor (DAC) provides the electrometer offset compensation and also other signals that are used for diagnostic testing. Three voltage references, one connected to analogue ground and the other two configured as +1.2 and -1.2 volts derived from two 'Zref1v2' (Zetex Semiconductors Ltd, 2005) band-gap devices for stability confidence testing. The data acquisition system is managed by a microcontroller which also communicates with the host PC.

### 3.6.2 Core Microcontroller

Data acquisition is managed by a microcontroller based on the 18F4520 PIC as used in the 'Dose Simulator' (See Appendix 3). The device is operated with the system clock at its maximum of 40 MHz. A prototype system was developed to ascertain its suitability for the project with an RS232 serial interface at a baud rate of 9.6 Kb/s and 512 Kb of external memory. After initial testing, the serial interface was up-rated to RS423 twisted pair at a baud rate of 115 Kb/s to improve the data transfer rate. Once the serial interface was operational, code was written and transferred to the PIC to extensively test the external memory for construction and design errors by writing and reading back blocks of test data.

### 3.6.3 Interface to Host PC

#### 3.6.3.1 RS423 Data Link

A full duplex RS423 communication link was adopted using two sets of twisted pair cores for receive and transmit, adopting 'low voltage differential signaling'

technique. Both are contained within a single multi-core cable with a separate grounded woven outer screen. Both ends of the data link share a common ground.

Handshaking was established in software. The link serves 3 functions:

- 1) It enables acquired data to be transferred to the host PC in the accelerator control area.
- 2) It allows the host PC to control the functionality of the microcontroller in the treatment room control box using a 'command processor' software routine running on the PIC microcontroller. The command processor operates in two modes, these being 'terminal' and 'string'.  
On reset, the system always initialises in the terminal mode.
- 3) To upload the target code during system development.

Using terminal mode, a standard 'terminal' can be connected to the serial interface. A prompt character is issued by 'Beam Scope' and displayed on the terminal screen. A command line can be typed in, including any command arguments, followed by a carriage return. On receipt of the carriage return, the command line is executed by the command processor. Any response from the command will be returned to the terminal followed by a further prompt, ready for the next command line. This mode allows the user to execute low level fault finding and diagnosis commands on the system. A specific command can be sent from the host to change the mode from terminal to string. In this mode, the complication of using prompt and control characters, as required by terminal mode, is eliminated. The command structure is thus simplified into a command with a set of arguments and a terminating character. This structure is far more suitable for fabricating commands in high level programming languages such as Microsoft Visual Basic™.

The command processor in both terminal and string modes responds to a programmed set of 'macro' commands which are sent by the host computer via the

high speed serial data link. These commands perform fundamental tasks such as ‘Set sample rate’, ‘Return a block of data’, ‘Test memory’ etc. Grouped together these commands form system functions such as ‘Zero electrometers’, ‘Test DAC/ADC’.

### **3.6.3.2 Data Acquisition Protocol**

Other than during acquisition of beam data, the host PC has total control over which commands are executed by the command processor. Since timing is critical during radiation beam measurement, the host PC can send sub-commands to the ‘Beam Scope’ which are accepted and put into a queue by the acquisition routine and only executed when timing permits. These include sub-commands to set trigger levels and gains, which need to be configured during active data acquisition. There is also a special sub-command which terminates acquisition and returns control to the ‘command processor’. Acquisition can also be terminated by an error handler if a fatal error occurs during data capture; again control is handed back to the command processor.

### **3.6.3.3 Data Upload**

During acquisition mode, data is stored in 512 Kb of static random access memory (SRAM) situated on the ‘Beam Scope’ processor PCB. On termination of data acquisition, the total amount of memory used, as blocks of data, is stored. Control is then returned to the command processor. To transfer the data to the host PC, one of the command processor calls is used to return the number of data blocks acquired. Based on this value, the host PC then repeatedly executes a command to recall a block of data and store it on the host PC hard disk drive until all the blocks have been transferred. The completed data set is formatted with a header containing all the information relating to the acquisition and then the actual data. Each item of data is separated by a comma to form a file which is readable into a spreadsheet program such as Microsoft Excel™.

### 3.6.3.4 Data Memory

A data block consists of 25 fields (Table 3-3). Each item of data is a word (2 bytes) and therefore each block uses a total of 50 bytes of memory. With a total storage capacity of 535288 Bytes (512 Kb), 10485 blocks of data can be stored. The maximum measurement period available is dependent on the sample time.

Data word	Function
1 – 19	Samples from ionisation chamber array
20	External electrometer input
21 – 24	External analogue channels
25	Trigger signal level

*Table 3-3: Format of a block of 'Beam Scope' data.*

## 3.6.4 Analogue Input

### 3.6.4.1 Acquisition Hardware

The ADC employs internal track and hold, resulting in an accurate conversion, even if the input signal level changes while the conversion is in progress. When conversion commences, the ADC changes from track to hold, returning to track mode on the 13<sup>th</sup> clock cycle of the internal clock. The internal successive approximation register calculates one digital 'bit' of the result on each clock cycle and simultaneously shifts this out to the serial interface. Thus, even though the device utilises a serial interface, the result is being output as the conversion is progressing. If the device used a parallel interface, it would be necessary to wait for the conversion to be complete before the data could be transferred over a parallel data bus. Accounting for the conversion time, address setup for the multiplexer and input/output transfer time, a channel can be addressed and converted in better than 25  $\mu$ s.

### 3.6.4.2 Electrometer Inputs

The first 20 multiplexer channels are connected to the 20 electrometers. An example of the electrometer acquisition timing for 6 radiation pulses is shown in Figure 3-33.

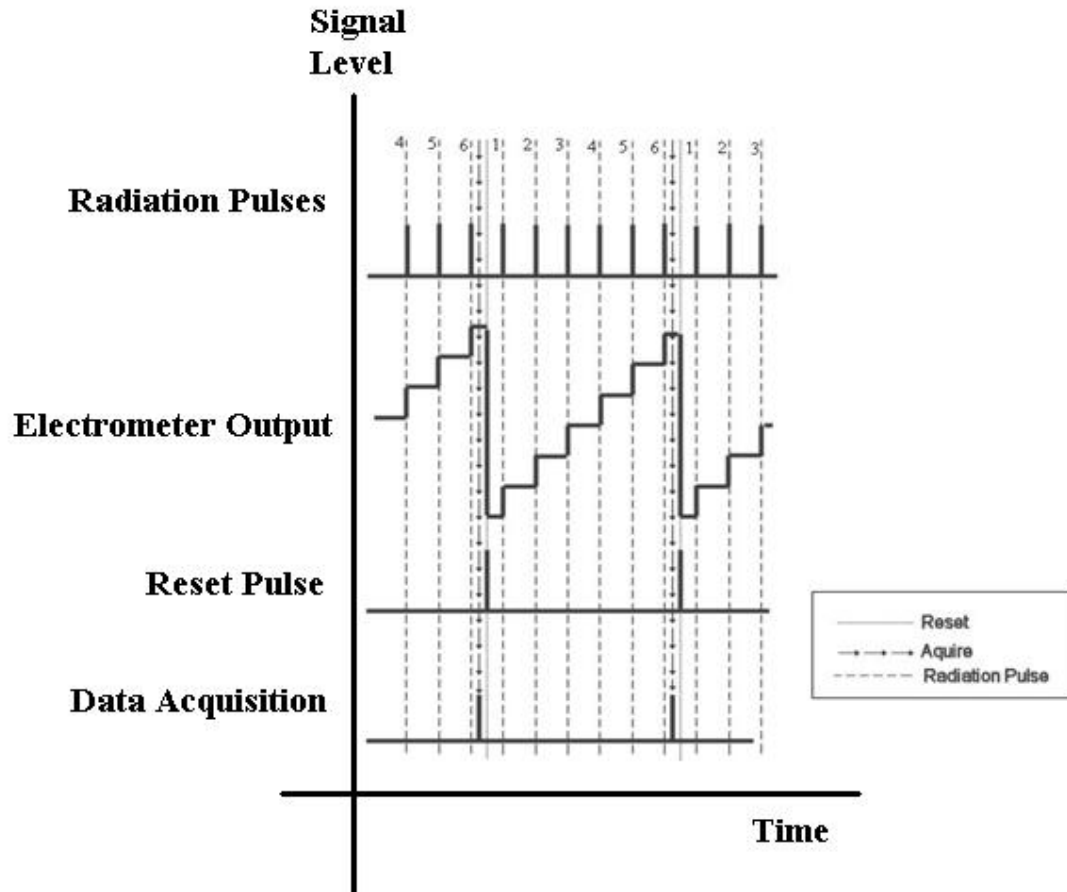


*Figure 3-33: Acquisition timing diagram for 6 radiation pulses per sample.*

After a time delay to account for the ion transit time, the electrometer output is digitised on the final radiation pulse in the sample. A reset pulse is then asserted to clear the charge from all the electrometer channels for the acquired sample. The system is then ready for the first pulse in the next sample.

### 3.6.4.3 System Test References

To measure the analogue acquisition system stability over time, two analogue input channels were dedicated to reading a pair of 2.5 volt precision band-gap references to produce a 2 point reference system of  $\pm 2.5$  volts referred to the reference star ground point, with one channel having the device configured to produce

a negative voltage. Also, since the acquisition system is referenced to 0 volts, an input channel was configured to make a measurement at the star ground point to measure the multiplexer and ADC input offset. The reference voltage is acquired 5 times and the mean calculated; the final value is then stored to the initialisation confidence test log file.

The precision band-gap references type Zref25 has a temperature coefficient of typically 30 ppm/°C (Zetex Semiconductors Ltd, 2005), which equates to approximately 75  $\mu\text{V}/^\circ\text{C}$  in the operating range 20 °C to 30 °C. If the system were used in this temperature range then maximum error would be 750  $\mu\text{V}$ .

#### 3.6.4.4 External Data Pod Inputs

The pod consists of 4 analogue inputs with associated hardware to allow the user to set scale and offset to match the dynamic range of the acquisition system. The signal is also filtered at this point reduce noise from the modulator PRF, 50 Hz mains pickup and to satisfy the Nyquist Criterion for the data acquisition system using a 4 stage analogue Salen key filter with a 30 Hz cut-off frequency.

#### 3.6.4.5 Acquisition Software

To complement the high speed hardware design described in Section 3.6.4.1, the software for the control of the multiplexer, ADC timing and the conversion of the serial data stream from the ADC were written in assembly language to realise maximum execution speed.

If 25 channels are read, stored and the electrometers reset, using a 150  $\mu\text{s}$  pulse, a complete acquisition cycle can be achieved in approximately 775  $\mu\text{s}$ . At the end of each cycle, one of the channels and a status word is returned to the host PC to form a user display of current activity. Even though the temporal resolution of this display is low compared to the stored data, since it takes 26 acquisitions to return a whole data block, it is useful as a guide to signal levels and acquisition status.

### 3.6.5 Analogue Output

#### 3.6.5.1 Analogue Output Hardware

Analogue output is accomplished using the same multiplexer device as for the analogue input. The multiplexer is formed using analogue switches, which are bi-directional; therefore the device can also be used as a de-multiplexer. A 16 bit serial DAC with on chip reference (type MAX 542, Maxim Semiconductors Ltd, 1999) was used in conjunction with the de-multiplexer to produce a compact multi-output solution. Each de-multiplexer channel uses a 'hold' capacitor and buffer which is constantly re-charged by the de-multiplexer as it polls each channel.

The first 20 analogue output channels are used for the electrometer 'auto zero' function and are very sensitive to noise and ripple currents. To address this problem, the value of the 'hold' capacitors was increased to greater than 50 time constants of the re-charge period, resulting in a very stable Direct Current (DC) reference. Utilising this method requires careful design of the system timing, since it takes a number of cycles to obtain the final voltage on each 'hold' capacitor. Once this has been achieved, the de-multiplexer is used to maintain the value. Since the voltage required for each channel is known and is a constant, the capacitors are first primed under software control to the correct value over an extended number of update cycles. The remaining channels are used for 'loop back' testing and setting trigger levels.

#### 3.6.5.2 Analogue Output Software

The software requirements for analogue output are straightforward, even during the priming of the hold capacitors. A serial output directive built into the PIC programming language was used to write data to the DAC. This accomplished the task in approximately 70  $\mu\text{s}$  per channel.

### 3.6.6 Electrometer Auto Zero

To null out any offset currents at the electrometer summing junctions, an ‘auto zero’ feature was incorporated into the design, employing the analogue output discussed in Section 3.6.5.1.

This is activated by the user at the beginning of a measurement session. ‘Auto’ meaning that the null is calculated and set automatically, not performed by the user adjusting a potentiometer for each channel. Some commercial dosimeters use ‘auto zero’ to automatically ‘null’ out the offset at the end of each measurement, by subtracting it from the measured value. A problem with this technique has been reported for use in ‘step and shoot’ IMRT measurements (PTW Freiburg GmbH, 2005). The dosimeter would be actively engaged in zeroing the offset during each of the short beam inter-segments. Since the machine manufacturer’s aim to produce the shortest inter-segment times, it is clearly possible for the beam to have started the next segment before the dosimeter has completed the zero procedure.

An offset compensation current was generated using a 10 G $\Omega$  resistor connected to each electrometer channel input summing junction and to one of the analogue output channels (Section 3.5.1). After the expiry of the recommended warm-up period of 15 minutes, a 2 point zero calibration routine is run from the host PC. This calculates the required current for each channel. The stability of the design is such that the function needs only to be run once at the beginning of a measurement session, eliminating the problem described above.

A service tool in the host PC application allows the user to run a test program to determine the offset on all channels simultaneously. This is run prior to ‘auto zero’ and allows all the electrometer channels to continually ramp up. The result is displayed and constantly updated, enabling the user to evaluate and investigate out of tolerance leakage currents, since large signals will occur with time, on channels

presenting high input offset currents. During the 'auto zero' function, any channel with an out-of-range value will be displayed to the user as an error.

### 3.6.7 Synchronisation

The radiation from a linear accelerator is pulsed and for most applications the measurement of beam profile at low temporal resolution is not a problem since the sample time is many times that of the radiation pulse rate. A 1.5 second sample period is not uncommon, and at an accelerator PRF of 400 PPS there would be 600 pulses in a data sample. A single lost or gained pulse in a sample due non synchronism between the PRF and sample frequencies would be negligible. When measuring at high temporal resolution, this becomes a major issue as the sample frequency approaches that of the accelerator PRF. For a 10 ms sample of data taken at a PRF of 400 PPS, there are only 4 pulses per sample, so a missed or added pulse presents a significant error.

A synchronisation pulse available from the accelerator 'test patch bay' can be connected to the external interface box as described in Section 3.9.3. to provide the trigger signal. An internal triggering option is available. The electrometer output on each channel of the measurement system ramps up during each radiation pulse and holds during the inter-pulse period resulting in a 'staircase' waveform which is reset at the end of each sample period (Figure 3-34).

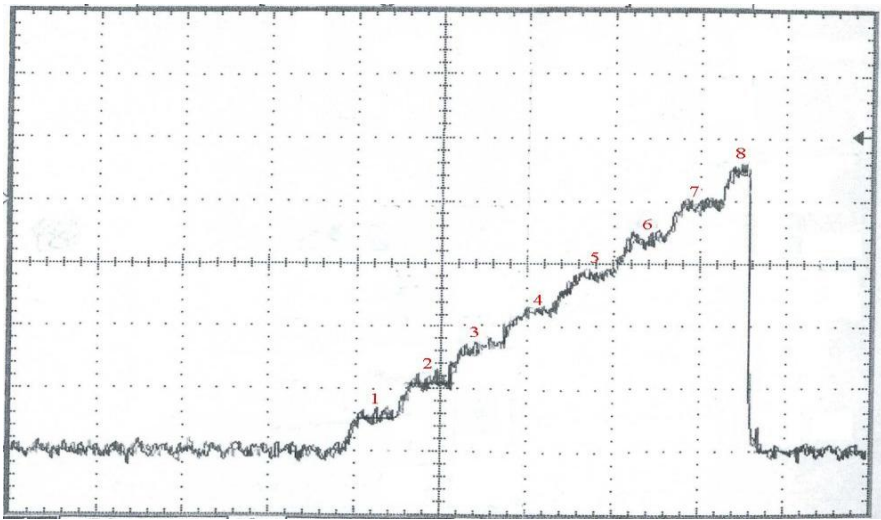


**Figure 3-34:** Staircase waveform at the electrometer output derived from 8 radiation pulses. The horizontal axis is 4.5 ms per division and the vertical axis is 100 mV per division.

A pulse representing each radiation event is generated by differentiating the summed electrometer outputs of the centre 5 electrometer channels (Figure 3-35).

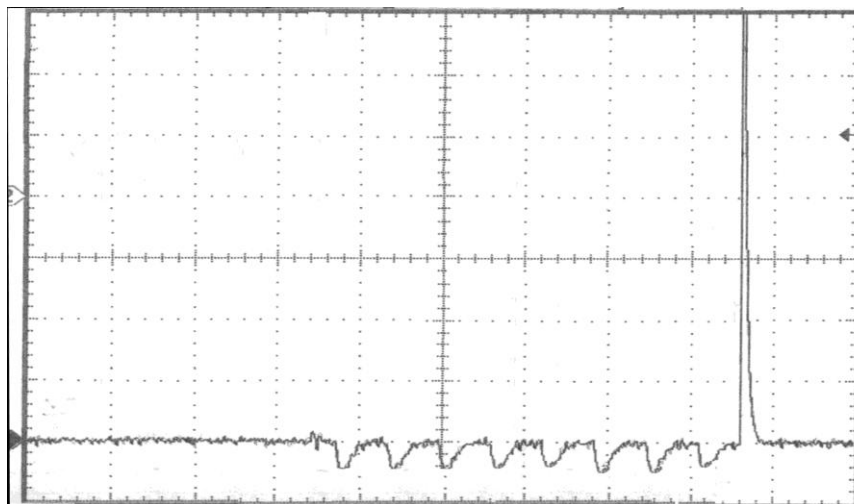


**Figure 3-35:** Result of differentiating the staircase waveform (the resulting derivative is negative, since an active differentiator circuit was used, resulting in an inversion of the signal polarity). The horizontal axis is 4.5 ms per division and the vertical axis is 200 mV per division.

After differentiation, the radiation events produce pulses which can be processed to generate triggers to time the acquisition hardware. The problem with the waveform in Figure 3-35 is that the differentiated electrometer reset pulse is large due to its large transition and high rate of change. The problem is exacerbated as the sample time is increased, since more samples are integrated and the staircase waveform increases in amplitude. This results in saturation of the signal amplifier

following the differentiator. However, the reset pulse timing is known, since it is generated by the acquisition program and it is straightforward to eliminate it. This was achieved by gating the output of the differentiator using the electrometer reset pulse as the gate control signal. The result is a usable trigger signal that can be amplified and processed (Figure 3-36)

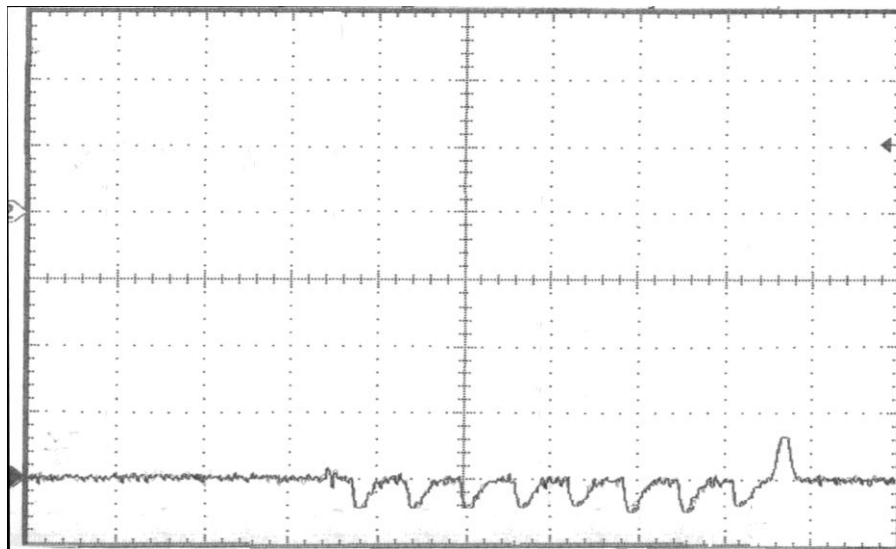


**Figure 3-36: Result of gating the differentiated pulses. The horizontal axis is 4.5 ms per division and the vertical axis is 200 mV per division.**

The small positive reset pulse left over following gating is ignored by the trigger processing electronics as it is of the opposite polarity to the valid radiation events. Signal amplification is applied using a low noise operation amplifier (Type OP 42, National semiconductors Ltd.) and software controllable potentiometer (Type X9313, Xicor Inc.) resulting in a variable gain of 10 to 20 times and basic RC filtering with a corner frequency of 700 Hz to remove high frequency noise, resulting in a clean waveform suitable for producing a trigger event.

The resulting signal from the internal or external trigger circuitry is connected to a peak detector, producing a DC level proportional to the trigger signal amplitude. This is digitised and returned to the user software application and displayed as 'trigger signal amplitude'. The signal is also connected to a fast comparator and compared with a 'trigger level' signal set by the user. When the trigger signal exceeds the trigger

level threshold, a digital trigger event is produced. This is read by the acquisition software routine in the PIC to correctly time the ADC control signals and electrometer reset.

### **3.7 Construction – Data Acquisition System**

A data logging system was constructed with digital and analogue inputs and outputs using the same microcontroller used in the ‘Dose Simulator’ (Appendix 3) as the core component for system timing, control and communications. The input signal processing was constructed on 4 circuit boards each with 5 integrating electrometers, based on the design evaluated in Section 3.2. A PC debug application was written to test the system at every stage of development and was kept resident in the final program as a test tool for development and fault finding. The test simulator was a very useful tool for fault diagnosis and operational validation during the construction and testing of both the hardware and software.

#### **3.7.1 Electromagnetic Interference**

Special consideration was made to manage EMI, since a linear accelerator produces a wide frequency band of electrical noise when radiating. The integrating electrometer inputs are also very sensitive to induced noise from power supplies. To achieve satisfactory suppression of EMI, a purpose designed, commercially manufactured screened instrument case was chosen. An EMI screen was fabricated to fit inside the case to isolate the electrometers from the rest of the digital circuitry to reduce noise pick up, and a remote mains power supply was used to eliminate stray pick up from inductors or transformers. A linear power supply was chosen to avoid high frequency interference which would radiate from ‘switch mode’ type supplies.

The transfer of data between the Host PC and the measurement system was based on the RS423 specification and provides good common mode rejection of EMI when the accelerator is radiating.

### 3.7.2 Functional Tests

To confirm the operation of the newly constructed data acquisition system, a number of basic tests were performed. A test current was applied to each electrometer channel using the ‘Dose Simulator’ to confirm that an equal known charge could be collected on each of the electrometer channels. A fundamental requirement of the system is that it should be able to acquire an analogue value with a high level of confidence. A single failed ADC acquisition in a data set would mean that the whole measurement in an experiment would be void. A worst case scenario would occur if the error in the data was not detected by the user. System timing was carefully designed to the manufacturer’s datasheet and care was taken in the Electro-Magnetic Compliance (EMC) of the instrument. Even so, a failed ADC read event could occur due to system induced noise on the analogue side or a timing artefact on the digital interface side of the ADC.

A test was thus devised to acquire a large volume of test data to validate the ADC read cycle. The acquisition software was modified to read only the positive voltage reference channel (Section 3.6.4.3) of the multiplexer during the acquisition cycle to use as a test value. Thus, this value was read 25 times instead of reading each individual channel once. This was achieved by changing a single machine code instruction in the software. Since the PIC is a Reduced Instruction Set Computer (RISC) device, each instruction has a fixed execution time and therefore the system timing was unaffected by the re-coding. Using a 10 ms sample time, the whole of the acquisition memory was filled with 90.17 seconds of data from the 25 channels, all reading the positive voltage reference, resulting in 9017 acquisitions. In total, the positive voltage reference channel was read 225,425 times. The overall maximum value read was 1.246 volts and the minimum 1.242 volts, resulting in a range of only 3 mV. The mean was 1.244 V (2 SD = 0.0005 V) demonstrating good spurious noise performance and reliable ADC interface timing.

With the software restored to read all the multiplexer channels, the 3 reference channels of +1.2, -1.2 and 0 volts were read from initial power up every 30 seconds over a period of 2 hours 20 minutes (Figure 3-37) using the debug application mentioned above. The +/-1.2 V reference channel results were referenced to 0 volts by subtracting the mean of the data sets so the y axis could be scaled appropriately on the graph, then all the references were normalised to the first point. During the measurement period there was a rise from 20 °C to 25 °C in the internal temperature of the system.

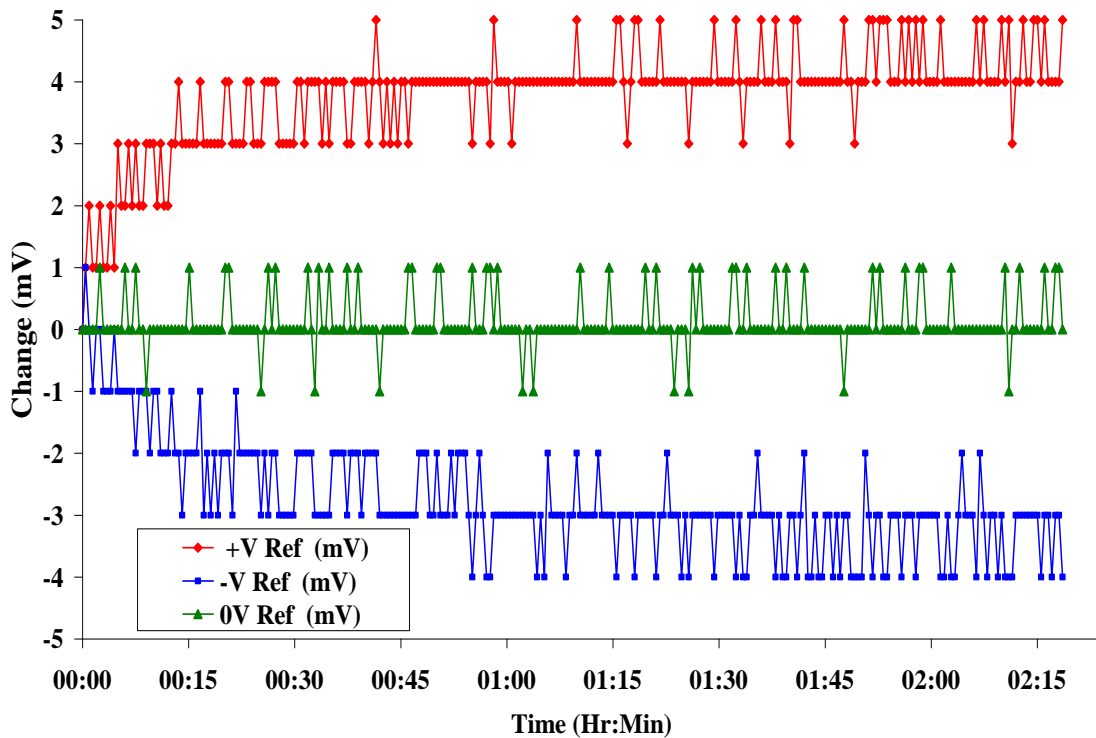


*Figure 3-37: System voltage references recorded every 30 seconds over a 2 hour 20 minutes period.*

The plot shows an initial warm-up period for both the +/- voltage references that is not apparent in the 0 volt reference. The error must be from the band-gap reference devices (Section 3.6.1) as the magnitude of the both the errors rises with time, whereas an offset in the acquisition system would cause both channels to change simultaneously, including the 0 volt reference. Although there is no suggestion of a warm-up period in the datasheet for the band-gap devices it is possible to measure the

change using a precision DVM. An error of 3 mV in 2.048 volts full scale represents an error of 0.15 % or 140 fC of collected electrometer charge. This is an acceptable limitation which will be taken into consideration in the confidence test limits set for the  $\pm 1.2$  V references. The limit could be tightened if the system were left to warm-up for 1 hour before use, but this would impose an unacceptable limit on the user when taking accelerator data. Since the  $\pm 1.2$  V references are only for diagnostic testing, excellent general overall stability is demonstrated by the 0v reference which shows no more than  $\pm 1$  least significant bit fluctuation in the converted value over the whole measurement period.

### 3.8 Ion Chamber Connecting Cable

A low-noise screened cable specifically designed for use in low-level signal circuits was chosen to connect the array to the treatment room control box containing the electrometers (RS Components Ltd, Type 367-280) based on the criteria suggested by Andreo P *et al*, 2007. The insulation to the centre conductor has a further layer of semiconducting polythene added to reduce tribo-electric noise generation if the cable is physically moved. This would be especially important during measurements taken with the accelerator gantry rotating, since the interface cables to the array would be in motion between the array and the treatment room control box. The ionisation chamber array was fitted into the holding frame and then mounted to the accelerator accessory ring on the radiation head. A cable of length 2 meters was chosen for the connection to the electrometer control box based on the discussion in Section 3.5.5. The functional validation of the cable is described in Section 4.2.3.

## 3.9 Completed Measurement System

### 3.9.1 External Data Input Pod

External transducers and signals from the accelerator control hardware can be connected to an 'Input Pod' to provide a local interface for analogue inputs to the

treatment room control box. Analogue preprocessing allows the user to calibrate signal levels to utilise the full dynamic range of the data acquisition system ( $\pm 2$  volts which maps to  $\pm 2048$  digital levels). Physical connection to the accelerator to measure control system signals was achieved using standard oscilloscope test probes with 10:1 attenuators. This avoids measurement perturbation by vastly reducing the impedance of the connecting cable and front end electronics of the 'input pod' to the signal being measured (Witte R A, 2006). A high level of confidence is required in the data pod interface to a fully clinical accelerator, so utilising standard test probes fulfills the requirement by achieving an 'industry standard' test connection.



*Figure 3-38: Photograph of the 'Input Pod'. The Potentiometers are used to calibrate the signal to be measured to fit the full scale range of the data acquisition system.*

### 3.9.2 Treatment Room Control Box

Signals from the ionisation chamber array and data pod are connected to the control box (Figure 3-39) located in the treatment room. The control box contains a microprocessor system which executes commands from a computer outside the treatment room via a high speed serial data link to orchestrate the acquisition of data. During data capture signals, from the ionisation array and external data pod are processed, digitised and stored locally for analysis 'off line'.



*Figure 3-39: Photograph of the treatment room control box.*

### 3.9.3 External Interface Box

A multi-core cable links the control box in the treatment room to an external interface box in the control area where the data link is connected to the computer. A BNC socket also allows connection to the ‘magnetron voltage test socket’ on the accelerator ‘test patch bay’ to facilitate external triggering. The connection is electrically isolated from ‘signal ground’ by the external interface box to eliminate ground loop currents forming when the input pod is used to record external signals. The input pod is thus the only ground connection between the ‘Beam Scope’ system and the accelerator under test.

### 3.10 Conclusion

The strategy for the development of a new measurement system was considered based on a previous project (SME). An ionisation chamber design was proposed to measure accelerator beam data.

A design for a beam data microcontroller based acquisition system has been considered and an integrating electrometer design was tested and validated on the bench and then on a linear accelerator based on the signal levels expected from the ionisation chamber design. This identified a problem with the capacitance of the connecting cable which will be revisited.

A 'Dose Simulator' (Appendix 3) was designed and constructed during the early phase of the design cycle. This proved invaluable in providing a range of test signals that were used for fault diagnosis and operational validation during the development, construction and testing of both hardware and software. A PC debug application was written during the development and construction cycle to test the system at every stage and kept resident in the final program for future use. The proposed ionisation array design was then fabricated.

The design and construction of the ionisation chamber array was the most challenging part of the design, having the most unknowns with respect to the behaviour and performance of the materials during use. Thus, a considerable amount of care was taken in the design, construction and fundamental testing phase of the measurement system electronics to help isolate any measurement artefacts that may be present in the ionisation chamber array. A range of experiments is described in the next chapter to validate the measurement system as a whole.

## Chapter 4. System Characterisation and Validation

### 4.1 Introduction

A test instrument named ‘Beam Scope’ has been developed and constructed to investigate the delivery of radiation beams for dynamic therapy on a medical linear accelerator. The electronics and software have been extensively tested during the design phase using a test simulator and prototype ionisation chamber from a previous project.

In this chapter the characterisation and validation of the project is described to ensure the design meets requirements. The characterisation process describes range, qualities and also highlights any peculiarities of the design. Validation confirms that the device reflects the requirements specified in the original design and that the resulting product will fulfill its intended purpose.

It was critical in this project to ensure that the experimental data to be measured was valid; therefore extensive functional testing was undertaken during the design, construction, characterisation, and validation stages. This will continue during use using an automated feature that stores initialisation confidence test data to a log file.

Once the prototype was finished and basic testing complete, the next phase was to characterise the design to verify its functionality and repeatability. This is of specific importance in the ionisation chamber array and electrometer components as their use in this project to acquire signals at high temporal resolution is atypical (Pardo J et al, 2005), since generally detector schemes used in radiation beam profiling arrays measure over many radiation pulses. The requirement for high temporal resolution for the measurement of IMRT beams and in the case of the ‘Beam Scope’ system, down to a single radiation pulse, results in a very small collected charge, which requires careful electrometer design and subsequent characterisation and validation.

Initially, the requirements and specifications which need to be validated against are determined. This step also serves to establish the means by which the requirements will be validated. A core design feature of the system to collect characterisation and validation data is the initialisation confidence tests. These are performed every time the measurement system is powered up, and the results of which are stored to a log file on the host PC hard disk drive to enable the long term stability of the system to be evaluated.

The system would mainly be used for relative dosimetry with some absolute measurements, accepting the limitations of an in-house developed ionisation chamber for absolute dosimetry. For any absolute measurement taken, a dose calibration factor would be generated for each session based on the fact that the accelerator was in clinical use and part of a comprehensive and strict QA regime. Therefore the need for long term absolute calibration would not be a requirement. A range of parameters was chosen for characterisation and validation based on published literature (Boag J, 1966, Khan F M, 2003, McCaffrey J P *et al*, 2005) and previous experience in the development of a system for multi-channel dosimetry using a strip ionisation chamber (Glendinning A G, 2001) and other types of radiation detection (Glendinning A G *et al*, 2001c, Glendinning A G, 2001). Initial testing was done in the laboratory and then the system was setup on a clinical machine for final characterisation and validation. The chosen specifications to be validated were:

**Laboratory Tests**

- a) Baseline system noise.
- b) Linearity of collected charge per sample.
- c) Input capacitance.
- d) Electrometer drift.

### Accelerator Tests

- a) Noise performance.
- b) Initial signal levels
- c) Ion transit time
- d) Charge build up
- e) Saturation curve
- f) Calibration

After a period of testing, the initialisation confidence test data was analysed to reveal performance data for the acquisition system electronics.

- a) Acquisition system volt reference data
- b) Electrometer offset
- c) Electrometer gain
- d) Analogue loop back

## 4.2 Bench Tests

Initial tests were performed in the laboratory to ascertain a baseline figure for noise. Collected charge was confirmed over a range of sample times. External data pod functionality was also validated at this stage. With the ionisation chamber array connecting cable length known (Section 3.8), the cable capacitance effect explored in Section 3.5.6 was also revisited.

### 4.2.1 Baseline Noise and EMI Suppression

This test was performed with the 'Beam Scope' hardware enclosed in its EMI screen case on the laboratory bench. The BNC inputs to the 20 electrometers were left disconnected. An earthed steel plate was placed in front of the 20 connectors to simulate the connection of screened BNC plugs. All sources of mains borne interference were minimised from the vicinity of the test. The electrometers were all

auto-zeroed and the baseline signal level measured over 1500 acquisitions, using a sample time of 15 ms. The mean for each channel is plotted in Figure 4-1.

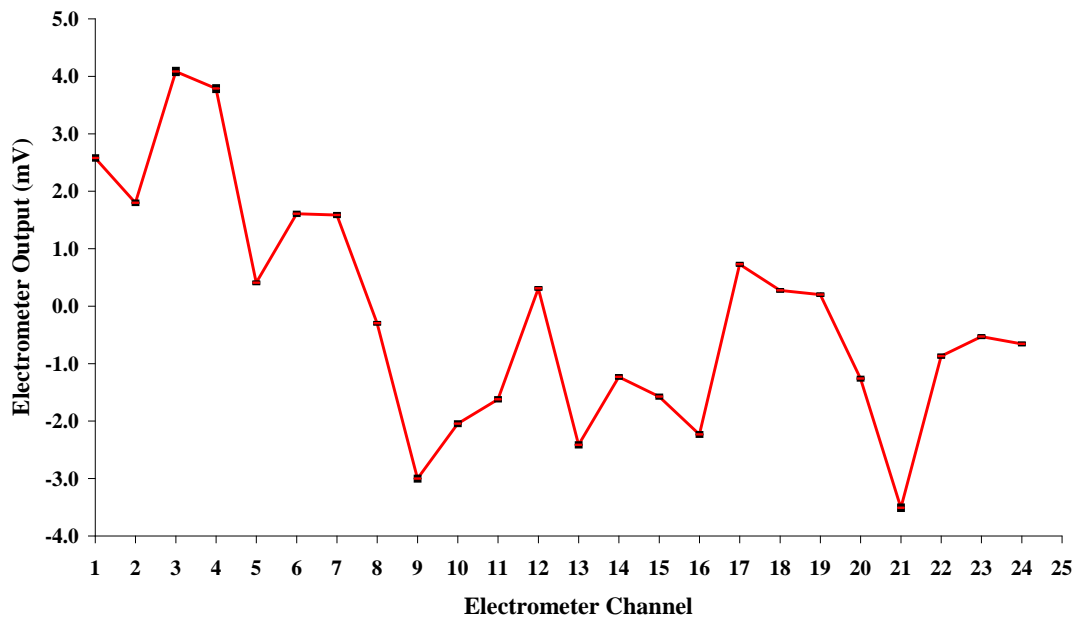


*Figure 4-1: Baseline noise for each channel with no input connected. The error bars show standard error based on 1513 samples. (The error bars show standard error based on 3 samples.)*

The worst case mean of 4.1 mV (standard error = 0.01 mV) was found for channel 3. The noise appears to be greater in the lower 5 channels, which may be attributed to a noise source closer to the top circuit board in the rack accommodating the first 5 electrometer channels. Even so, the value is within the Least Significant Bit (LSB) error of the ADC and is of no consequence to the performance of the instrument.

#### 4.2.2 Collected Charge per Sample

To ensure all of the charge per sample was collected, particularly in the final radiation pulse of the sample, a test was derived to measure the collected charge over a range of sample times. Using the ‘Dose Simulator’ (See Appendix 3), simulated radiation beams were configured at a PRF of 400 PPS (2.5 ms interval) and a DAC value (Figure 10-10) of 14000 units and run on the ‘Dose Simulator’. Five to 45 ms

sample times set on the measurement system resulted in 2 to 18 radiation pulses collected per sample (Figure 4-2).

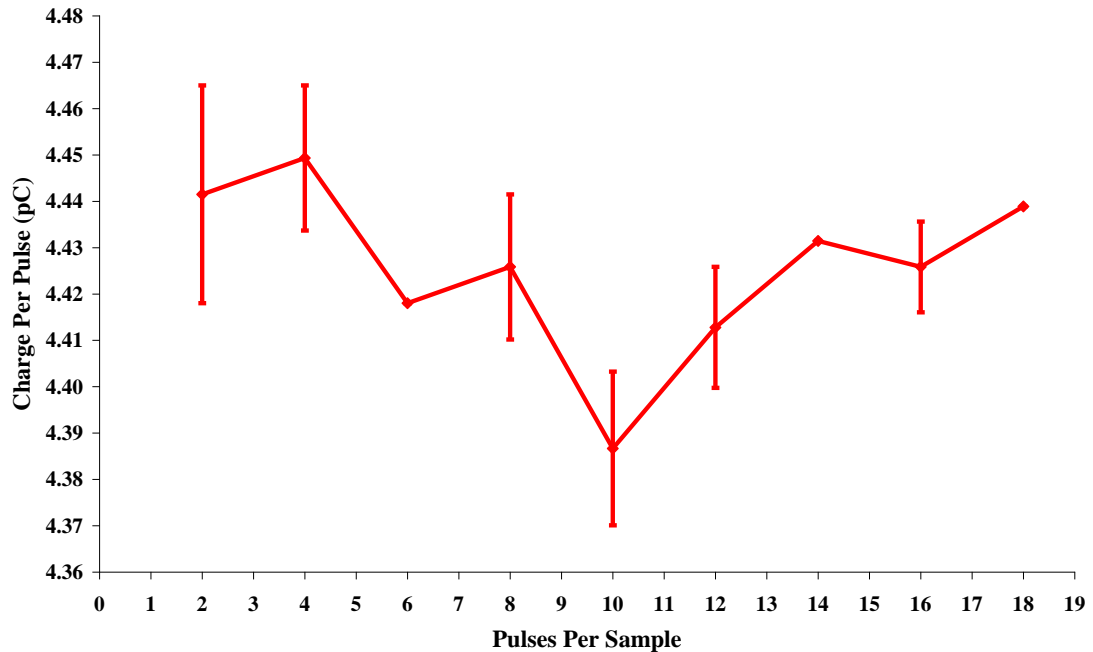


*Figure 4-2: Collected charges over a range of sample times. (The error bars show standard error based on 3 samples.)*

The mean charge collected was 4.43 pC per radiation pulse with an error of +0.54 % and -0.88 %. The result shows no trend towards lost signal on the last radiation pulse. This would occur if the acquisition of the sample occurred before the charge was fully collected on the last radiation pulse. This would be demonstrated on the graph by a consistent decrease in signal level as the number of radiation pulses per sample is reduced as the charge on the last pulse becomes more dominant. This may be of concern when the instrument is used with the ionisation chamber array, where the ion transit time, described in Section 3.3.5.1, is of significance. This test was repeated again later on in the validation process using the ionisation chamber array. A time delay in the software has been incorporated to accommodate ion drift effect.

### 4.2.3 Ion Chamber Connecting Cable Capacitance

The problem of the ionisation chamber connecting cable capacitance discussed in Section 3.5.5 was re-visited. Since the length of the array connecting cable was

known and thus the capacitance presented to the electrometer input circuit, the correct reset pulse width can be established based on a firm understanding of the events occurring during, and just after electrometer reset. The cable chosen is 2 m in length and has a capacitance of 103 pF/m, and therefore presents 206 pF to the electrometer input circuit.

#### 4.2.3.1 Testing the Simulated Cable Capacitance

To demonstrate the ‘recharge effect’, an experiment was setup using the ‘Dose Simulator’ (See Appendix 3) in the laboratory as a test source. A pulse configuration of PRF of 400 PPS was established using the ‘Dose Simulator’ to simulate radiation pulses as in Section 4.2.2. The current output of the ‘Dose Simulator’ was connected to the electrometer channel 10 input on the ‘Beam Scope’ to provide a trigger signal to synchronise the data capture. The voltage output of the ‘Dose Simulator’ was connected to a BNC tee piece via a 1 G $\Omega$  resistor in a screened box directly into electrometer channel 1 of the ‘Beam Scope’. The resistor was included as a voltage to current converter, using the same technique to produce the current output in the ‘Dose Simulator’.

The voltage output of the test source (labeled 1 in Figure 4-4) was specifically used in this experiment, so that no connecting cable was required between the voltage to current converter resistor output and the electrometer input (labeled 2 in Figure 4-4), thus avoiding measurement perturbation due to extraneous cable capacitance at the input terminals of the electrometer. This was achieved using a pair of air spaced wires, photographed in Figure 4-3, connected into the second input of the BNC tee piece. Extra capacitance was then added in the form of fixed capacitors (Figure 4-4), soldered on to the wires.

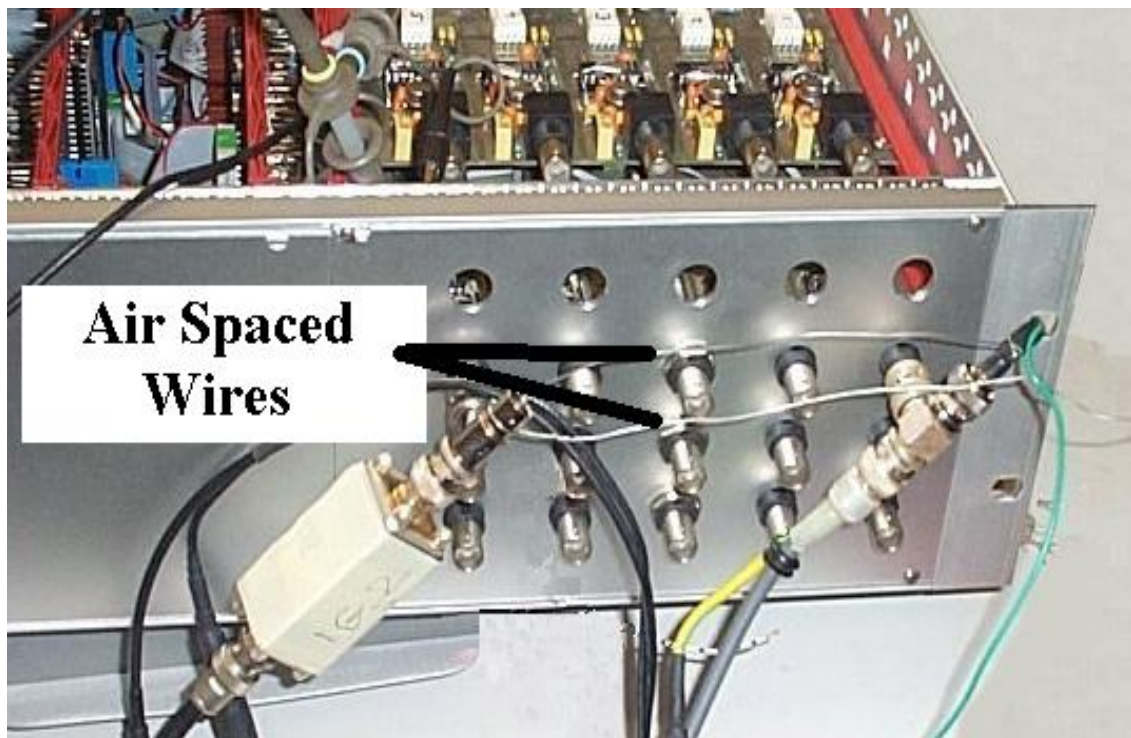


**Figure 4-3:** Photograph of the electrometer section of the 'Beam Scope' opened for testing the added extra input capacitance. The 'air spaced' wires used to eliminate extraneous circuit capacitance are identified.

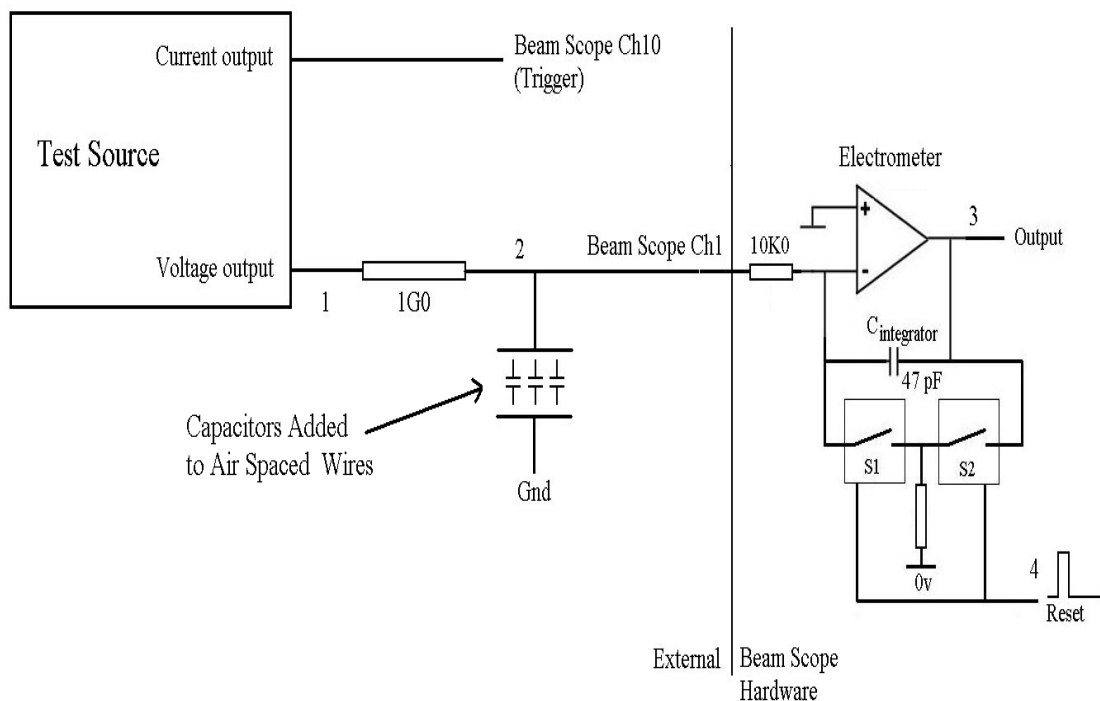


**Figure 4-4:** The test configuration to add a known capacitance to the input of electrometer CH1 using a BNC tee piece and a pair of air spaced wires. The 1 GΩ resistor was connected directly to the BNC tee to eliminate connecting cable capacitance. The current output was used to establish synchronisation.

Identical simulated test beams were run using the ‘Dose Simulator’, with the ‘Beam Scope’ acquisition configured for 5, 10, 40, 60, 80 and 100  $\mu\text{s}$  electrometer reset pulse widths. Each test beam was measured with 117, 235, 470, 705, 940, 1410 and 1880 pF capacitance, as multiples of 470 pF fixed capacitors connected in series/parallel arrangements, soldered to the pair of air spaced wires in electrometer channel 1. The resulting waveforms were recorded and stored on the DPO for analysis.

An example waveform is shown in Figure 4-5 using a reset pulse width of 5  $\mu\text{s}$  and 705 pF added capacitance.

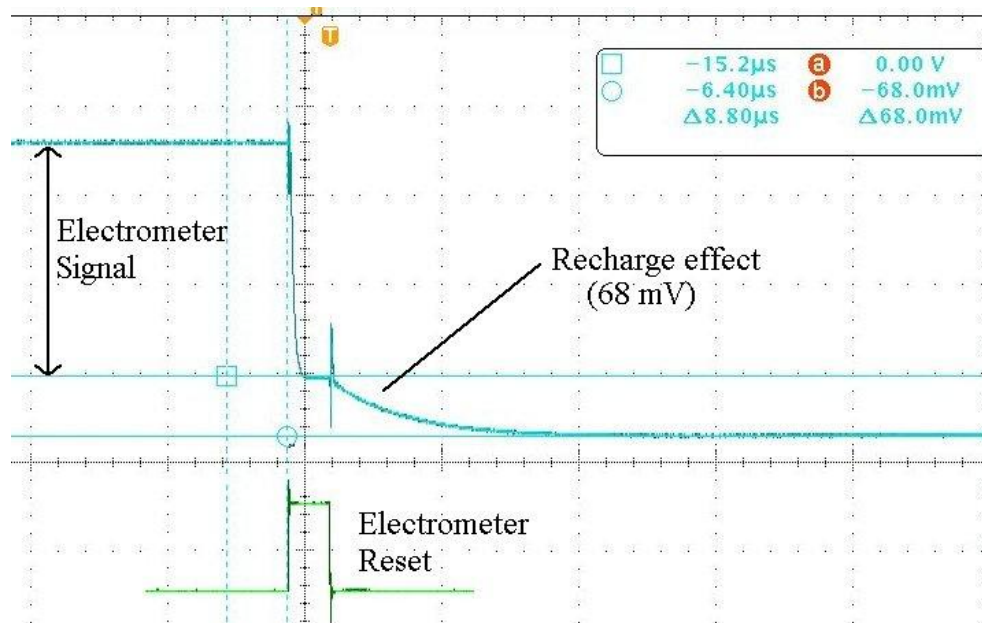


**Figure 4-5:** Example DPO waveform from electrometer Ch1 output showing 68 mV of recharge after the termination of reset with 705 pF added capacitance. The 5  $\mu\text{s}$  reset pulse has been included to clarify the reset timing. The horizontal axis is 20  $\mu\text{s}$  per division).

The waveform shows that the electrometer commences to charge immediately after the termination of the reset pulse, producing the recharge effect discussed in Section 3.5.5. The end point voltage results in a plateau is be added to the voltage from the charge collected in the next sample.

The recharge effect was measured on each of the waveforms and is plotted in Figure 4-6. The graph shows that a reset pulse width of  $> 50 \mu\text{s}$  would be adequate to eliminate the recharge effect for the 206 pF presented by the ion chamber cable (Section 4.2.3). Based on the time available after the ion transit delay of 1ms and data capture period of  $600 \mu\text{s}$  (Section 3.3.5.1) it was decided to exploit as much of the remaining period for reset as possible. An overestimated value of  $150 \mu\text{s}$  was used for the reset pulse width to guarantee electrometer reset and still leave a margin of protection to be sure all the software processes to capture and store the electrometer charge would be accomplished within the time period of 1 radiation pulse at a PRF of 400 PPS (2.5 ms).

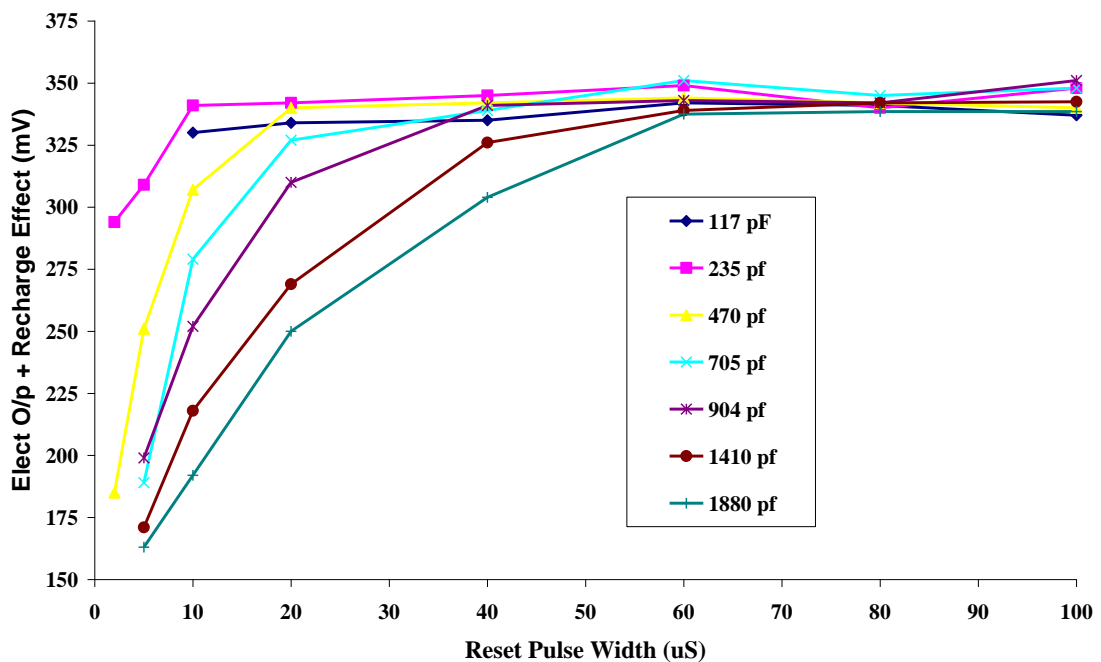


*Figure 4-6: Recharge effect plotted for a range of reset pulse widths for added input capacitance.*

#### 4.2.4 Electrometer Drift

##### 4.2.4.1 Input Bias Offset

The input bias offset was measured for all the 20 electrometer channels using a DVM connected to the output of each electrometer in turn. This was performed with the reset permanently asserted. The values were compared to those measured 6

months earlier when the electrometers were first commissioned; the worst case channel had 4 mV offset. This would be easily removed by the auto zero system without limiting its performance in zeroing ion chamber offset, so it was assumed that 4 mV was of no consequence. Therefore this value would be used as a test limit. All channels were then individually set for zero input bias offset using the DVM.

The input bias offset is measured by the ‘Beam Scope’ application during the initialisation confidence tests and any value exceeding the 4 mV test limit results in a failure of the test. This gives the user confidence in the electrometer performance, as any failure in the bias compensation of the electrometer integrated circuit will be detected.

#### **4.2.4.2 Electrometer Drift Rate**

The electrometer array is tested during the initialisation confidence tests. The test is to check for excess electrometer output drift due to PCB surface leakage from contamination inside the ‘Beam Scope’ electrometer electronics box and to also to confirm that the electrometer used in the design (AD549) is not producing excess drift due to an internal fault or if the warm up period is < 15 minutes (Section 3.5.4.1). A maximum limit (generated from data in the manufacturer’s datasheet, (Analog Devices Ltd, 2007) of 150 mV/s is used as the drift limit value. An error flag in the ‘Beam Scope’ software is set should this limit be exceeded and data measurements are inhibited.

The procedure first resets all of the channels and then allows the electrometers to ‘ramp up’ over a 100 ms period, at which all channels are read and stored. The electrometer drift rate for any channel is flagged up by the test if it exceeds 15 ADC steps in the 100 ms test period (150 mV/s) limit. So for one radiation pulse sample at a PRF of 400 PPS (2.5 ms interval), first converting the drift rate in to milliseconds, is 0.150 mV/ms and thus 0.375 mV in 2.5 ms (one radiation pulse period). This is a

17.6 fC charge per pulse limit, assuming a 47 pF integrating capacitor in the electrometer.

The percentage error for this limit as part of the total charge collected is evaluated in Section 4.3.2.1 when the array is tested on an accelerator, since the charge collected for a 100 cGy beam is known.

#### **4.2.5 Data Pod Channel ‘Cross Talk’**

To confirm the level of ‘cross talk’ between channels, a 0.2 Hz sine wave of approximately 4 volts peak to peak from a signal generator was connected to analogue input channels 1 and 3, the other two inputs being left disconnected. Approximately 5 seconds of signal were acquired and a single cycle of the sine wave analysed. The peak signal level was 728 raw ADC units, representing a 2.1 volts peak signal. The 0.5 Hz content of analogue channel 2 (disconnected input) was analysed using Matlab™ to generate a frequency spectrum of the signal. The 0.5 Hz content was found to be -70 dB of the random noise component and deemed to be of no significance to measurement ‘cross talk’.

### **4.3 Accelerator Tests**

In this section the measurement system was setup on a clinical accelerator using the ‘Standard Array Configuration’ as described in Appendix 1.

#### **4.3.1 Extraneous Noise Tests**

The experiment in Section 4.2.1 was repeated in the linear accelerator treatment room using the same test configuration. The first measurement was made with just the Low tension (LT) supplies turned on to the accelerator. To be sure that realistic parameters were set on the accelerator control system, a 6 MV X-ray prescription was loaded into the machine control console. This LT scenario would

expose the measurement system to EMI from high current circuits such as the beam bending system and associated thyristor power supplies.

The second test was carried out with the radiation on and the secondary collimation system closed with the electron gun set at standby current level. The measuring system was exposed to the EMI from the accelerator's modulator, which produces EMI over a very broad band of frequencies, as very high pulses powers with very short rise and fall times are present.

When the 3 data sets were examined there was no quantifiable difference between them. A great deal of care was taken in the control of EMI in the design (Section 3.7.1). This test result suggests the design has good EMI immunity with no greater than 2 raw ADC units of noise in the data.

#### **4.3.2 Initial Signal Levels**

Three, 100 cGy test beams (100 MU) were run on the accelerator at the nominal PRF of 400 PPS. The raw total ADC units and total number of beam samples for the central axis chamber (channel 10) for the each of the test beams were calculated. Taking the mean of these resulted in values of 1032760 for the raw ADC units and 809 for the beam samples (4845 radiation pulses).

The number of samples in the beam was based on a start-up threshold of 50 raw ADC units, and the end of the beam was simple to detect as the accelerator HT supply is switched off at beam termination and therefore the accelerator output falls to zero within 2 samples (based on a 15 ms sample rate). This is shown in Figure 4-7 where only a minimal amount of beam is lost below the start threshold, in this case 0.09 % and only one sample at beam off. Based on the noise data in Section 4.3.1 measured as 2 raw ADC units with the accelerator modulator running with the diaphragm system closed and the electron gun at standby level, the threshold figure of 50 raw units could easily be reduced to 10 units and still maintain a good overhead.

This would result in only 0.007 % of lost beam below the start-up threshold in the above case.

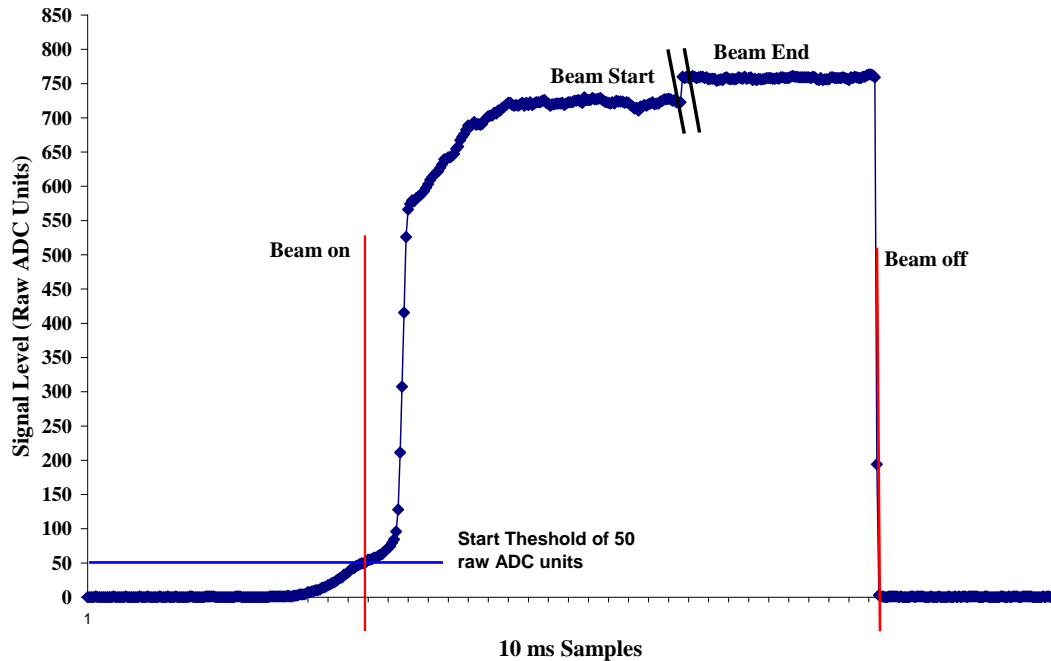


*Figure 4-7: Beam start and stop showing reference points used to analyze ‘Beam Scope’ data.*

The total value 1032760 raw ADC units is the equivalent of 1032.76 volts integrated by the electrometer over the whole beam and a collected charge 48.54 nC. Based on the measured 4845 pulses in the beam, the charge per pulse is the total charge collected divided by this value, which is 10 pC per pulse. The design specification in Section 3.4.2.1 was 7 pC per pulse, considering the effect the physical tolerances in the ionisation chamber spacer have on the collecting volume, this is in good agreement with the calculated value.

#### 4.3.2.1 Electrometer Drift Rate Limit

The electrometer drift rate test in Section 4.2.4.2 established an error limit of 17.6 fC drift per pulse in the initialisation confidence tests. In the 100 cGy beam used in the previous section (Section 4.3.2) there were 4845 radiation pulses in total, and therefore a total drift limit of 85.4 pC allowed in a 100 cGy beam. The percentage error as part of the total charge collected in 100 cGy can now be calculated, as this has

been measured as 48.54 nC and results in an electrometer drift error limit of 0.00175 %. This level of drift is of no significance and leaves a good overhead if the system is used to perform measurements at lower PRF's.

### 4.3.3 Ion Transit Time

To confirm the theoretical value chosen for the ion transit time in Section 3.3.5.1 an experiment was conceived to ensure that measured beam data was not influenced by ion transit time in the collecting volume of the ionisation chamber array.

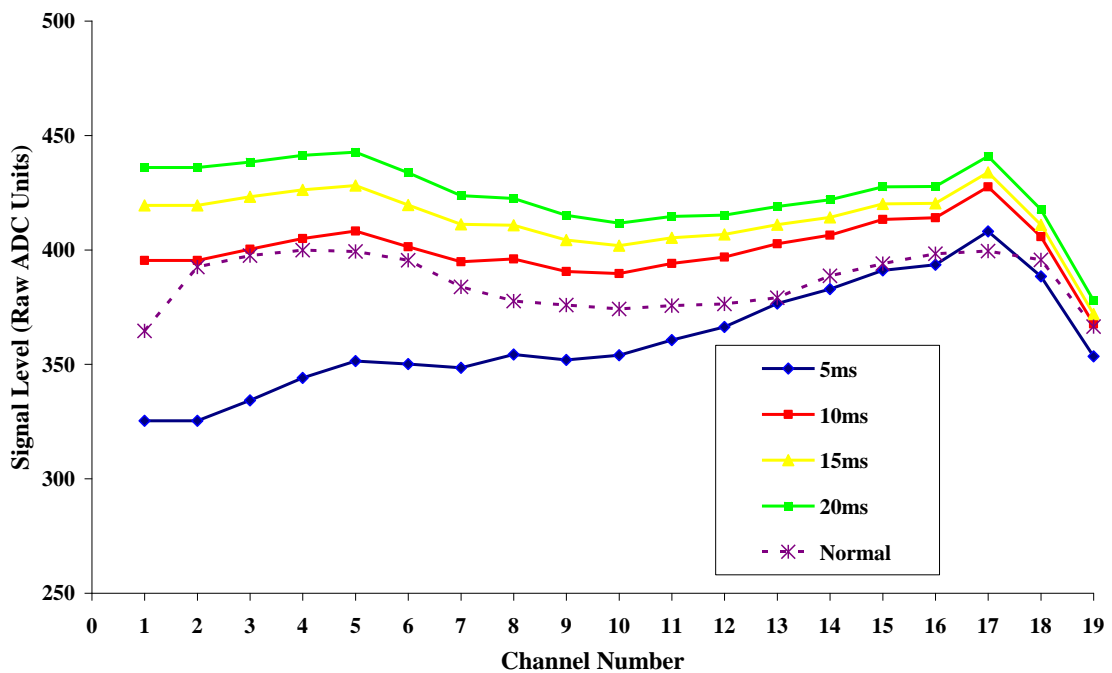


**Figure 4-8:** Tilt in radiation profile for 4 samples with the ion transit delay set to zero. The dashed line shows the contour of a normal profile for comparison.

With the ion transit delay in 'Beam Scope' set to zero, beams were taken for 4 sample times (Figure 4-8). The samples were normalised to the signal level of the 5 ms sample.

The acquisition code reads the electrometers sequentially, taking 31.6  $\mu$ s per channel, from channel 1 to channel 19 over a period of approximately 600  $\mu$ s. Since the charge collection in the ionisation chamber gap takes greater than 600  $\mu$ s (Section 3.3.5.1) and is on-going during the total acquisition period, the signal value stored at each channel acquisition is representative of the charge collected at that point

in time. Consequently, channel 1 signal is read first, and therefore has the lowest ion transit time of 31.6  $\mu\text{s}$ ; conversely channel 19 is read last, with the highest of 600  $\mu\text{s}$ .

This is evident in Figure 4-8 where the profiles more closely match the normal profile (Dotted line) in the higher channels as the transit time increases. Also, the effect is more pronounced for the shorter sample times, as the signal lost due to the effect occurs in the last pulse of a sample and is therefore more dominant in the shorter sample times. Since the instrument is designed for high temporal resolution the design solution must ensure that this effect is addressed.

The ‘Beam Scope’ acquisition was configured to a transit delay of 1 ms to include some extra overhead. A sample rate of 5 ms was used to measure the worst case scenario as described above. Six radiation beam profiles in the GT axis were taken: 3 normal and 3 with the acquisition code reconfigured to read the array in reverse sequence. The data acquisition software is coded to start at channel 1 then increment the channel address. For the experiment, the code was restructured to start at channel address 19 and decrement the channel address. The mean of each set of 3 profiles was taken and plotted (Figure 4-9).

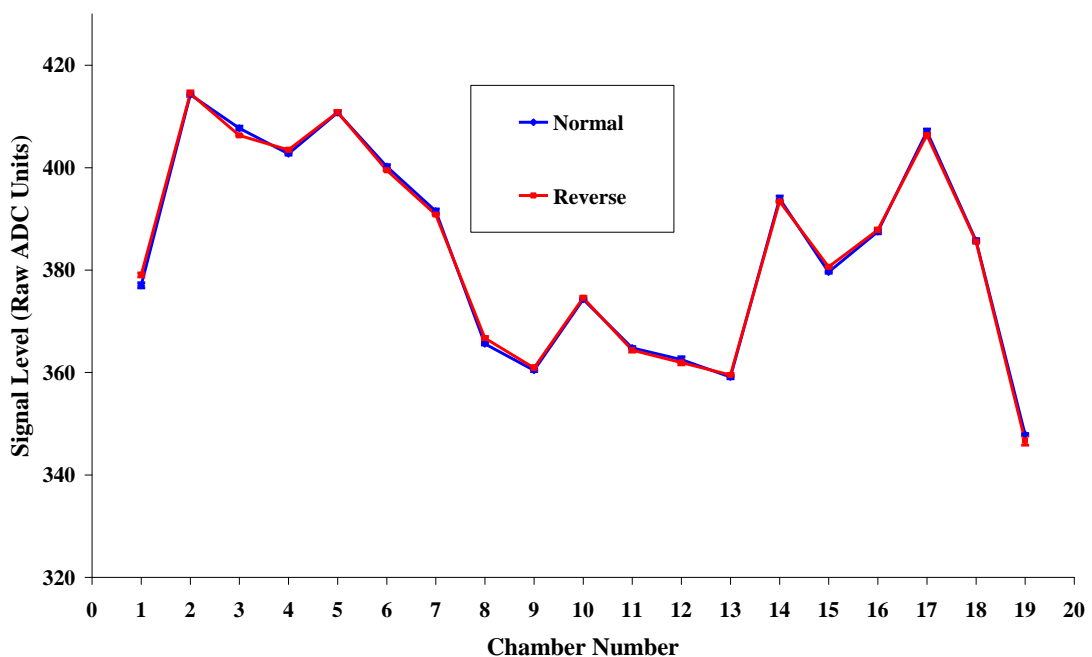


**Figure 4-9:** Profiles captured with the ionisation chamber array sequence normally (Ch1-19) and in reverse (19-1) (Error bars show 2 SD).

Should there be an issue with the transit delay time used in the experiment there would be a difference between the two plots. In the normal case the signal level would increase between chamber 1 and 19 during the ionisation chamber 1 to 19 read cycle, as more of signal from the last pulse in the sample was acquired. The signal level would fall in the reverse case, as chamber 19 would be the first channel to be read in the acquisition cycle and chamber 1 the last. Some overall tilt is evident in the data which must be a function of the ionisation chamber array and will be investigated further in the calibration section of the text.

As a final confirmation, 1 profile was measured using the ‘Standard Array Configuration’ for ion transit delays in steps of  $200\mu\text{s}$ . The data was taken immediately after a machine service where the flatness had been correctly set with  $<0.5\%$  difference between the 12 cm points in the GT axis.

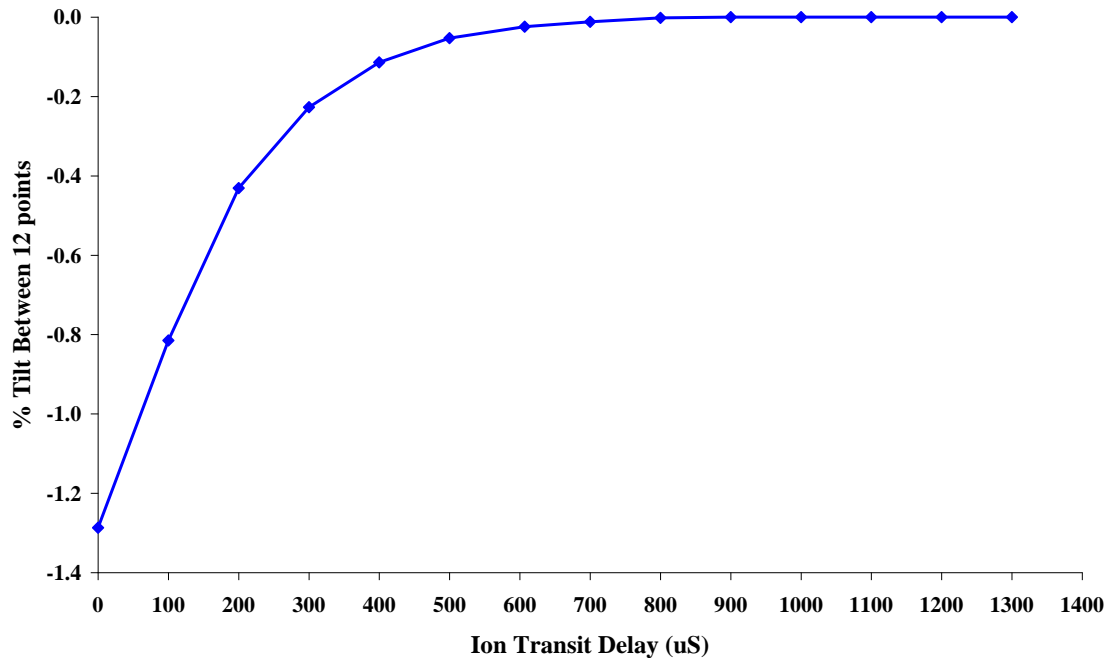


*Figure 4-10: The difference between the 12 cm points in a profile plotted for ion transit delays.*

With reference to Figure 4-10 it is clear from points leading up to the 1 ms ion transit delay value that the difference in the 12 cm points is negligible and therefore 1 ms was accepted as the final value for ion transit delay.

#### 4.3.4 Charge Build Up

When the array was first used in each measurement session it was noted that the mean signal level increased with beam on time until around 12 Gy was delivered, at which the signal then stabilised. This pre-irradiation effect is plotted in Figure 4-11.

Charge build up effects in parallel plate ionisation chamber arrays have been reported (Glendinning A G, 2001, McCaffrey J P *et al*, 2005) and the recovery from the discharged state (Fowler J F, 1959). Observed ratios of the initial reading to a settled final value of 1.5 % over 30 minutes of pre-irradiation or more were quoted with typical ratios of 0.5 % over 20 minutes. Internal spacers and insulators were reported to be the source of the effect for both parallel plate and thimble chamber types.

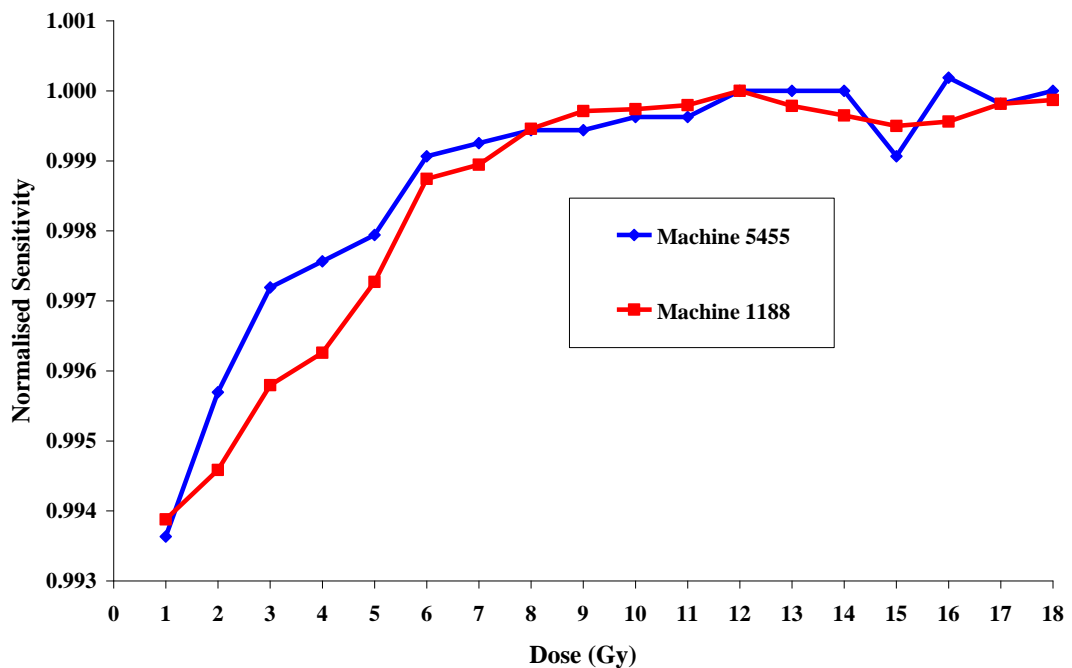


*Figure 4-11: Increasing signal with delivered dose during the pre-irradiation time at the beginning of a measurement session on two accelerators (Elekta SL Series numbers 1188 and 5455).*

The effect in the 'Beam Scope' array was established to be caused by the fibre-glass substrate contained in the space between the collecting plates and zero volt copper ground plain which produces the underside screen and top side guard (Section 3.4.4). The relatively large free space around the collecting volume may account for the short pre-irradiation time found in the 'Beam Scope' array (approximately 2.2 minutes at the nominal dose rate of 540 MU/min for the machine used), rather than the quoted >20 minute pre-irradiation period for measurement chambers, particularly thimble types (McCaffrey J P *et al*, 2005).

The same source also suggests that just maintaining the polarising voltage on the chamber will not suffice to stabilise the effect. Therefore, based on the result in Figure 4-11, the 'Beam Scope' array was pre-irradiated with 12 Gy before each measurement session commenced to allow the sensitivity to stabilise. This compares adequately to a value of 10 Gy quoted for a commercial device (MatriXX, Scanditronix Wellhofer) by Wagner D & Vorwerk H, 2011 and Herzen J. *et al*, 2007 and Li J *et al*, 2009. The MatriXX array consists of 1020 vented ionisation chamber detectors formatted as a  $32 \times 32$  grid (Saminathan S *et al*, 2010). Furthermore, a manufacturer's warm up time of 15 minutes before commencing pre-irradiation is quoted for the device (Wagner D & Vorwerk H, 2011, Herzen J. *et al*, 2007), which is presumably to allow for the electrometer electronics to stabilise (Section 3.5.4.1).

There must correspondingly be a time period for the 'Beam Scope' ion chamber array sensitivity to return to the 'rest' state, and this was also investigated.

#### 4.3.4.1 Materials and Methods

The 'Beam Scope' array was configured using the 'Standard Array Configuration' and pre-irradiated with 12 Gy as in Figure 4-11. Beams of 100 MU were run over the course of a day to measure the change in sensitivity of the CAX ionisation chamber in the array with time. The number of beams was limited to 16 in

total to avoid perturbation in the measurement, since making a measurement results in further pre-irradiation of the array.

#### 4.3.4.2 Results and Discussion

The CAX chamber data normalised to the first measurement is presented in Figure 4-12.

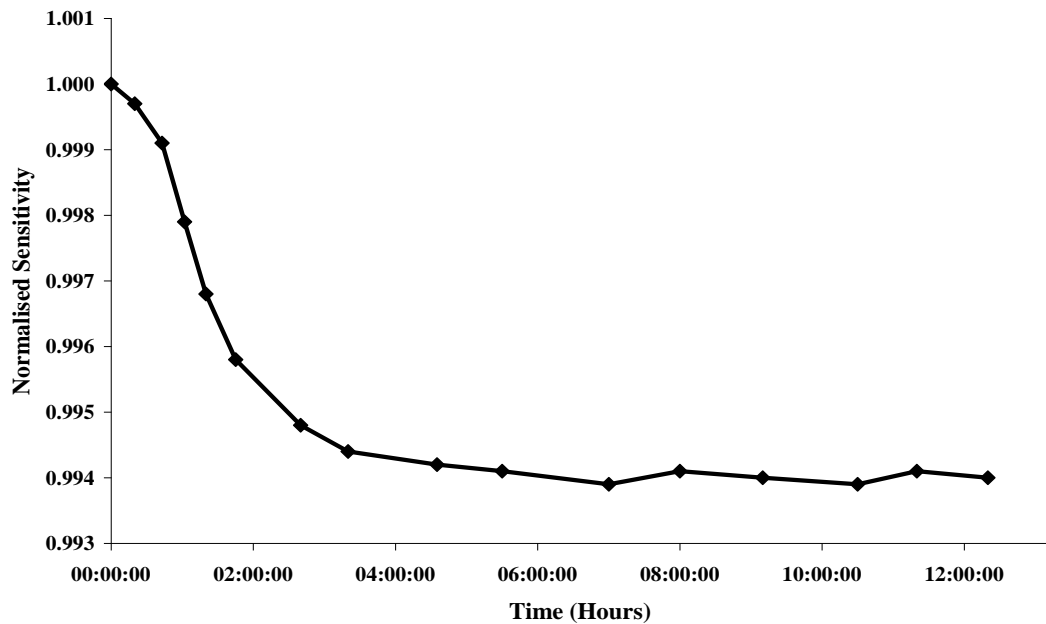


**Figure 4-12: Recovery to the ‘rest’ state sensitivity after an initial pre-irradiation of 12 Gy.**

The results of the measurements were compared to an assessment of an ionisation chamber array (MatriXX, Scanditronix Wellhofer) using 100 MU beams (Herzen J. et al, 2007). The normalised sensitivity of the MatriXX array prior to pre-irradiation was 0.965 compared to the ‘Beam Scope’ value of 0.994, resulting in change in sensitivity of 3.5 % and 0.6 % respectively. In fact the data in the evaluation shows that the sensitivity of the MatriXX decays to this point (0.994) after only 30 minutes of ‘beam off’ time and states that the array should be pre-irradiated before starting a measurement and after a break for reproducible measurement. The change in sensitivity is 5.8 times smaller for the ‘Beam Scope’ than for the MatriXX array. However, although the small change in 0.6% is of little significance, it would be beneficial to pre-irradiate the array after a break of 1 hour.

#### 4.3.4.3 Pre-irradiation effects on accelerator measurements

Since the purpose of the pre-irradiation dose is to stabilise the sensitivity of ‘Beam Scope’ array prior to investigative measurements, any change in accelerator performance due to this procedure would be an undesirable effect. The ‘Beam Scope’ array was configured using the ‘Standard Array Configuration’ and pre-irradiated with 14 Gy beam; GT axis profile data is presented (Figure 4-13). Good stability is demonstrated over the 14 Gy pre-irradiation period as would be expected for a modern machine design.

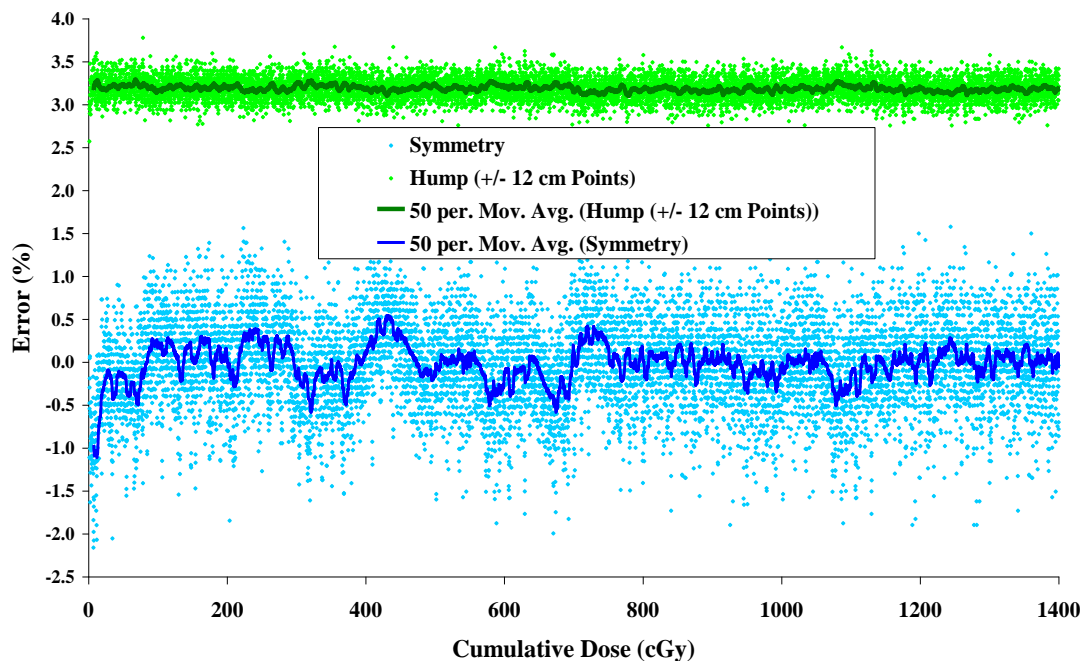


*Figure 4-13: Beam ‘symmetry’ and ‘hump’ measured over 14 Gy using the ‘Beam Scope’ array. A 50 point moving average was used to reduce noise in the plotted data.*

#### 4.3.5 Saturation Curve

The raw signal level for 100 MU was measured for a range of polarising voltages applied to the chamber for the design dose per pulse of 0.022 cGy. The current-voltage characteristic measured is shown in Figure 4-14 for the central axis collecting plate (channel 10) as described in Khan F M, 2003.

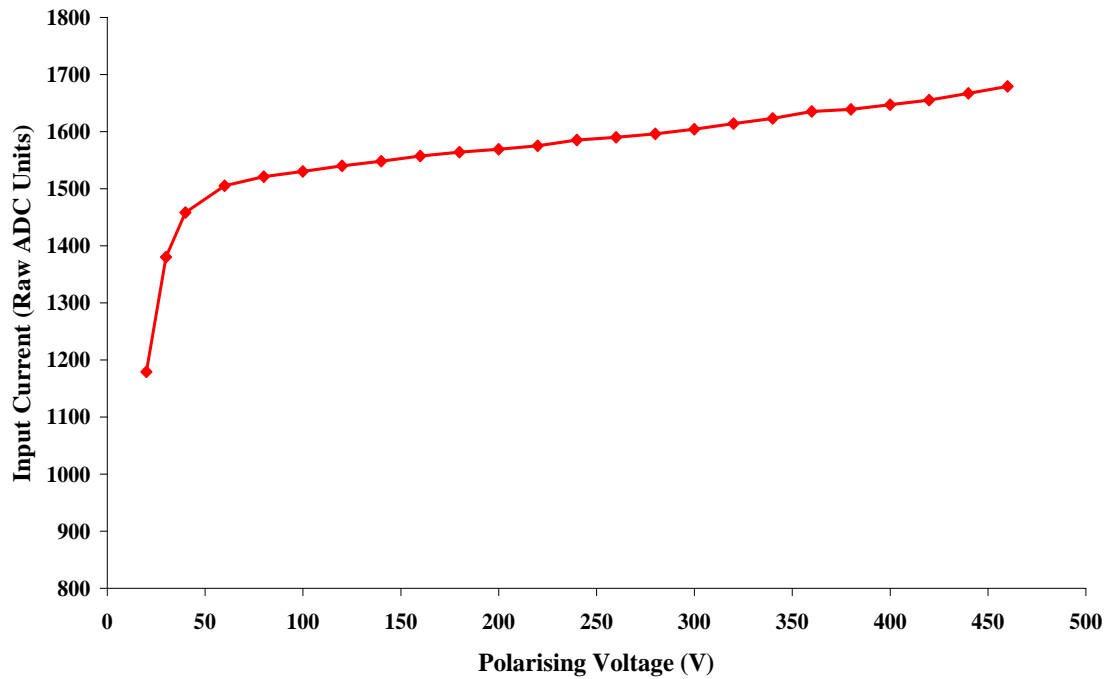


*Figure 4-14: Current-voltage characteristic for 100 MU beams from 20 to 460 volts. The nominal polarising voltage for the array is 420 volts.*

The chosen polarising voltage of 420 Volts, to satisfy the ion transit time, is in the saturated region of the characteristic away from the recombination region at the low end of the voltage spectrum, but not high enough for ionisation by collision to occur (Andreo P *et al*, 2007). To prevent inaccuracies in output current with variation in polarising voltage, due to the slope of the characteristic in the saturated region, the supply is stabilised.

#### 4.3.6 Calibration

To compensate for physical tolerances in the collecting volume of the chambers and electrometer sensitivities, a number of calibration methods were investigated. Throughout the calibration study, comparative profiles taken in a water tank were used as definitive data, the purpose of which was to pursue a method to confirm array calibration at any time without the necessity to setup a water tank.

### 4.3.6.1 Calibration Range

Initially a profile taken in the GT axis from the array was compared to a plot taken immediately after using a commercial 1D array (LA 48, PTW Freiburg Germany) to ascertain the magnitude of the errors to be calibrated out, as shown in Figure 4-15. The LA 48 device calibration had recently been certified by the manufacturer (Section 3.3.5.3). The random error in the ‘Beam Scope’ data demonstrates the un-calibrated elements in the array and electrometer components; however there is also a noticeable tilt in the profile.

The data was normalised to 100 % at the central axis (channel 10). The worst case difference between the LA 48 and ‘Beam Scope’ profiles were in Ch2 with 5.6 % and channel 19 with -6 %, both with respect to CAX (normalised to 100%), resulting in a difference of 11.6 %. To ascertain the tilt in the plot the difference between 12 cm points were taken. The actual ‘Beam Scope’ channels used were 4 and 5 for the ‘G side’ of the beam 15 and 16 for the ‘T side’, resulting in a tilt of 0.4 % on the LA 48 profile and 5.1 % on the ‘Beam Scope’ profile.

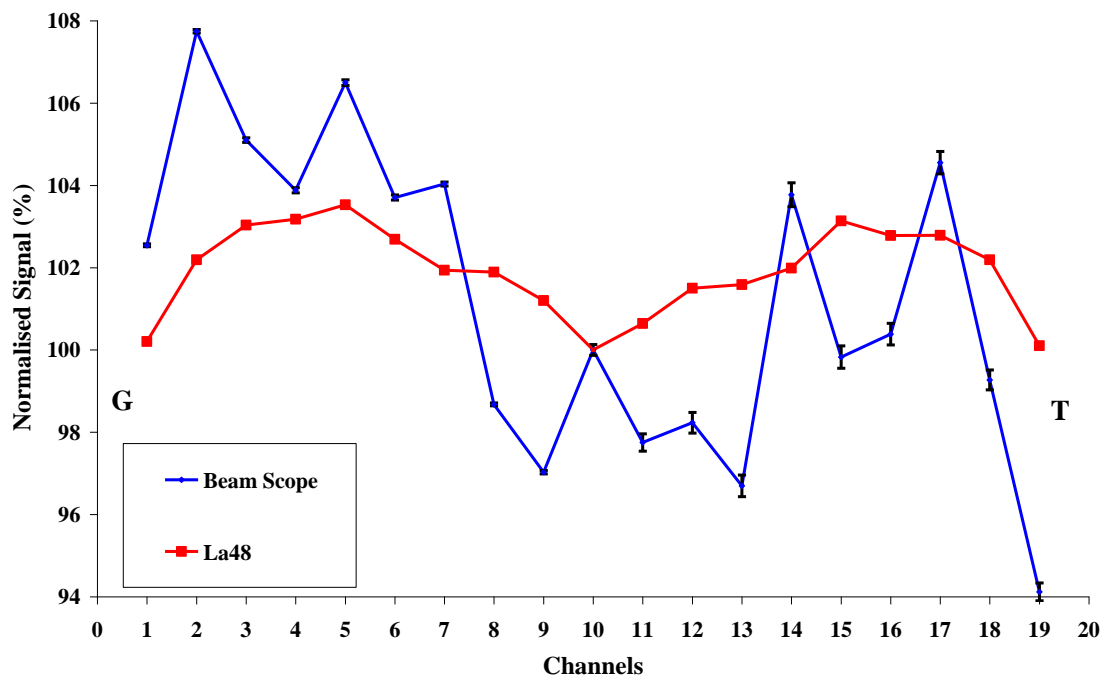


**Figure 4-15: Comparative plots in the GT axis between the ‘Beam Scope’ raw data and a PTW commercial 1D array. (Error bars show 2 SD)**

Having previously confirmed that the ion transit time was correctly set, the systematic tilt described must be a function of the array and electrometer sensitivities. To ensure there was no asymmetry in the accelerator profile, the beam was measured again with the array reversed, this time in the T-G axis. The plot in Figure 4-16 demonstrates that the tilt is still present across the array from channel 1-19 irrespective of the array orientation, whereas if the tilt was due to the accelerator the reverse plot would mirror the normal plot.

The same experiment was performed again, however this time only the order of the electrometer input channels from the array were reversed, instead of the array axis. Therefore, channel 1 with channel 19, channel 2 with channel 18 and so on, until the central channel 10 was reached. This time the plot described in Figure 4-15 was mirrored in the reversed condition, which finally confirms that the systematic tilt present was a function of the measurement array and not the accelerator or ‘Beam Scope’ acquisition instrumentation.

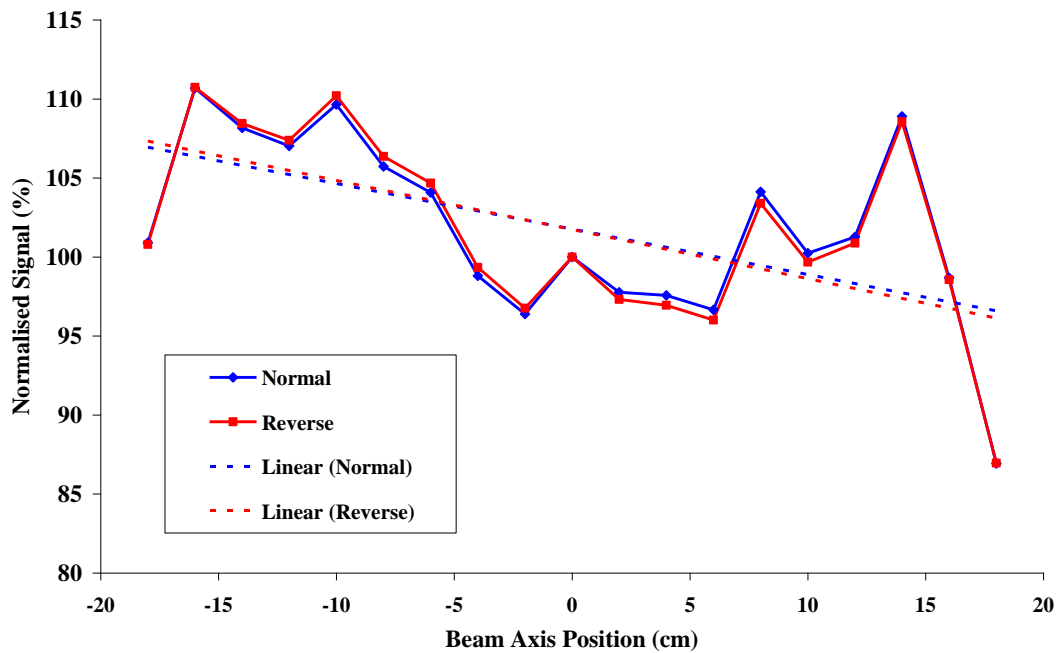


**Figure 4-16:** Beam profile in the ‘Normally’ plotted GT axis and then with the array reversed in the T-G axis. Linear regression is also plotted.

One possible explanation for the systematic tilt is the thickness tolerance of the spacer used in the ionisation chamber array to separate the plates. The supplier of the material quotes for extruded Perspex a manufacturing specification in accordance with ISO7823-2. The standard quotes ‘a thickness tolerance of +/-10 % for sheets below 3 mm thick and +/-5 % for sheets of 3 mm and above’. A 5 % tolerance of the 5 mm spacer in the array would have significant effect on the collecting volume and hence the calibration factors. This is acceptable, if calibration is correctly implemented and accounts for the error. However, the purpose of this chapter is to characterise the system to form a clear understanding of the behaviour of each sub-system in the design; therefore the thickness tolerance of the spacer was investigated. A data set created from the mean of three LA 48 and three ‘Beam Scope’ beams was used to derive a set of trial calibration factors for the ‘Beam Scope’ system. It would be expected that these would be randomly distributed; visual examination of the plot and regression suggests a tilt and some curvature in the data set (see the uncorrected series in Figure 4-17).

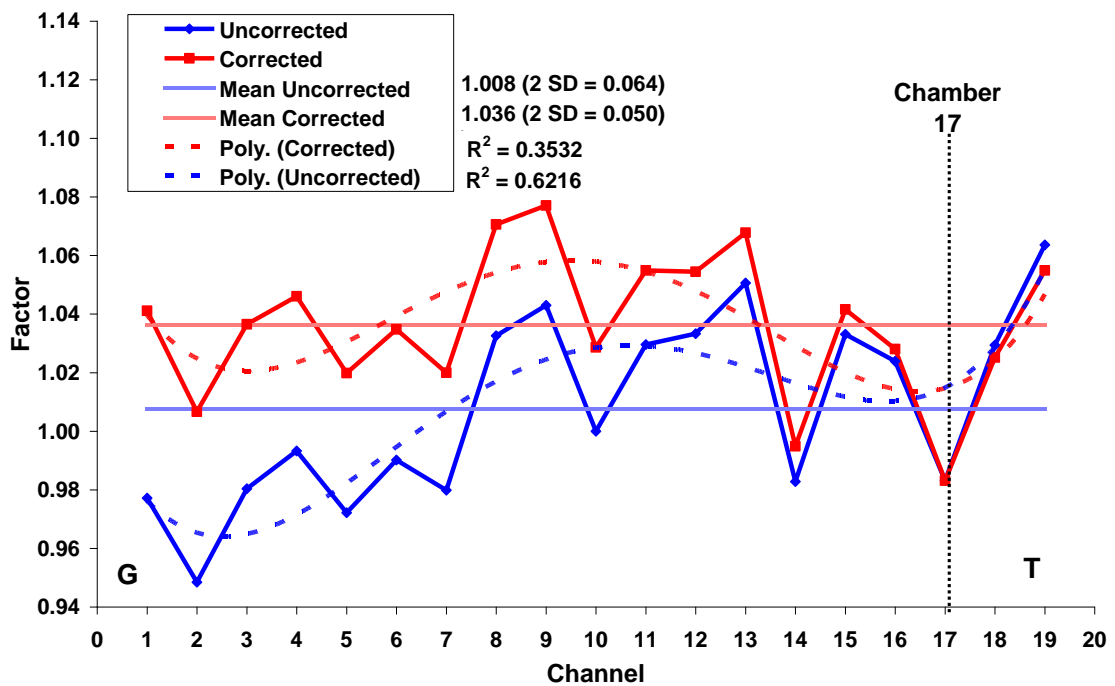


Figure 4-17: Calibration factors for the ‘Beam Scope’ array produced from the LA48 data set shown plotted in blue. The factors corrected for spacer thickness are in red. Regression and mean are plotted for both data sets.

Since the construction of the array was complete it was not possible to remove the spacer to confirm the tolerances in the thickness, but it was possible to measure the spacer at the 4 corners on a 'marking out table' using a height gauge.

An estimate of 0.41 mm for the overall thickness deviation across the array was calculated by taking the mean of the corner measurements at each end. Based on the 5 mm value used in the design calculation the tolerance in the array thickness is 8.2 % from end to end. This manufacturing tolerance was not considered at the design stage and in hindsight should have been resolved by machining the spacer thickness to a tighter tolerance before final assembly. Intermediate values were calculated assuming a linear change in slope; the key values are presented in Table 4-1.

A polynomial regression was chosen for the plots in Figure 4-17 as this produced the maximum best fit coefficient. As discussed earlier in this section the array could not be dismantled, so only the slope was investigated even though there may be other irregularities in the spacer thickness.

Location	Thickness (mm)	% error
Chamber 1 Edge	5.36	7.2
Chamber 1	5.34	6.8
Chamber 10 (CAX)	5.16	3.1
Chamber 17	5.01	0.2
Chamber 19	4.97	-0.6
Chamber 19 Edge	4.95	-1

**Table 4-1: Summary of spacer thickness across the array based on mean of the corner values measured at both ends. Note that the spacer is at the design thickness at Chamber 17.**

A set of correction coefficients was calculated based on the slope only and were normalised to Chamber 17, since this was the point where the spacer was actually the correct thickness. These are plotted in Figure 4-17. These were used to

correct the original ‘Beam Scope’ profile for spacer thickness error (linear only). The result was re-normalised to the central axis and is plotted in Figure 4-18.

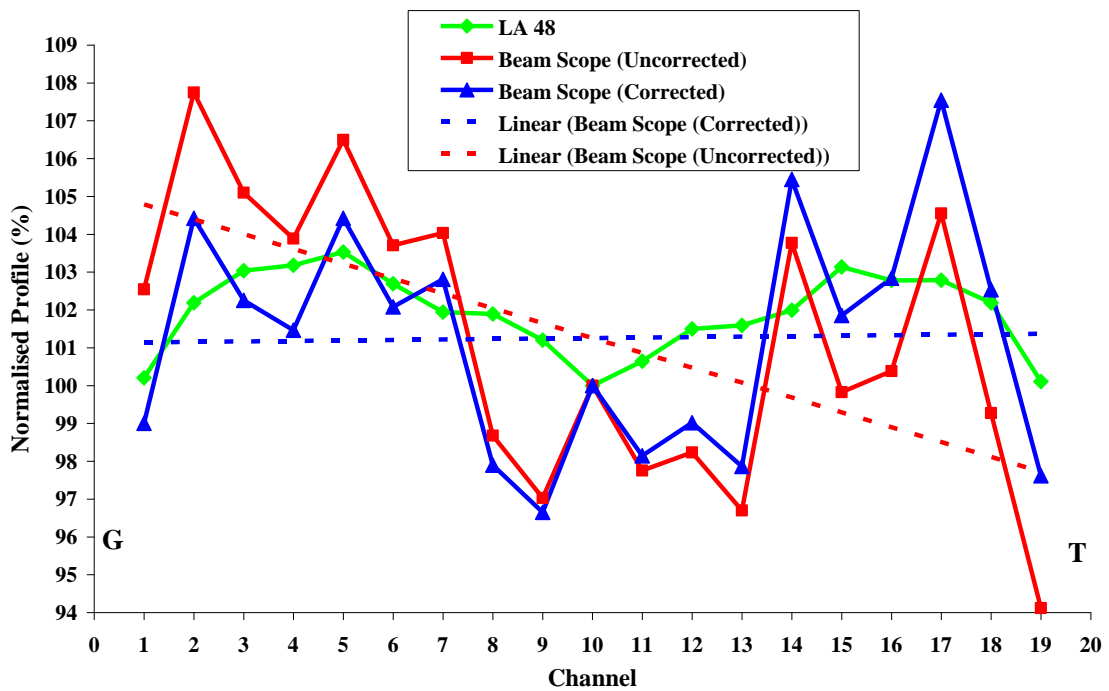


**Figure 4-18:** The ‘Beam Scope’ array profile corrected for the spacer slope shown plotted in blue. The original uncorrected ‘Beam Scope’ and the LA 48 plots from Figure 4-15 are included for comparison. Linear regression is plotted to show the trend in the profile.

Again the tilt was assessed using channels 4 and 5 for the ‘G side’ of the beam 15 and 16 for the ‘T side’. The resulting tilt of only 0.6 % compared to 5.1 % for the uncorrected profile demonstrates the coefficients produce correction in the right direction, and suggest a magnitude of the correct order. Since the contour of the data points has not changed, the mean error of the points is still the same value of 101.3 % shown in Figure 4-18; moreover the change in slope of the linear regression to near zero demonstrates that correcting the spacer thickness results in a randomly distributed profile.

The calibration should remain constant as long as the spacer dimensions remain stable and consequently the spacer thickness error is corrected in the final array calibration.

### 4.3.6.2 Calibration Methods

Three approaches were evaluated for the ‘Beam Scope’ array calibration and these are presented below:-

#### 4.3.6.2.1 Method 1-Transfer Calibration

Three calibration plots were taken from two machines to generate a transfer calibration. Two were taken from the same machine, one using the recently calibrated LA48 array and a further plot using a water tank. A single water tank plot was taken from the second machine. Since this is a rudimentary investigation into calibration methods, only a single data set was used from each of the calibration plots. Therefore the overall range has been used rather than the standard deviation to describe the data. A mean of the 3 calibration plots and the range of values are plotted in Figure 4-19.

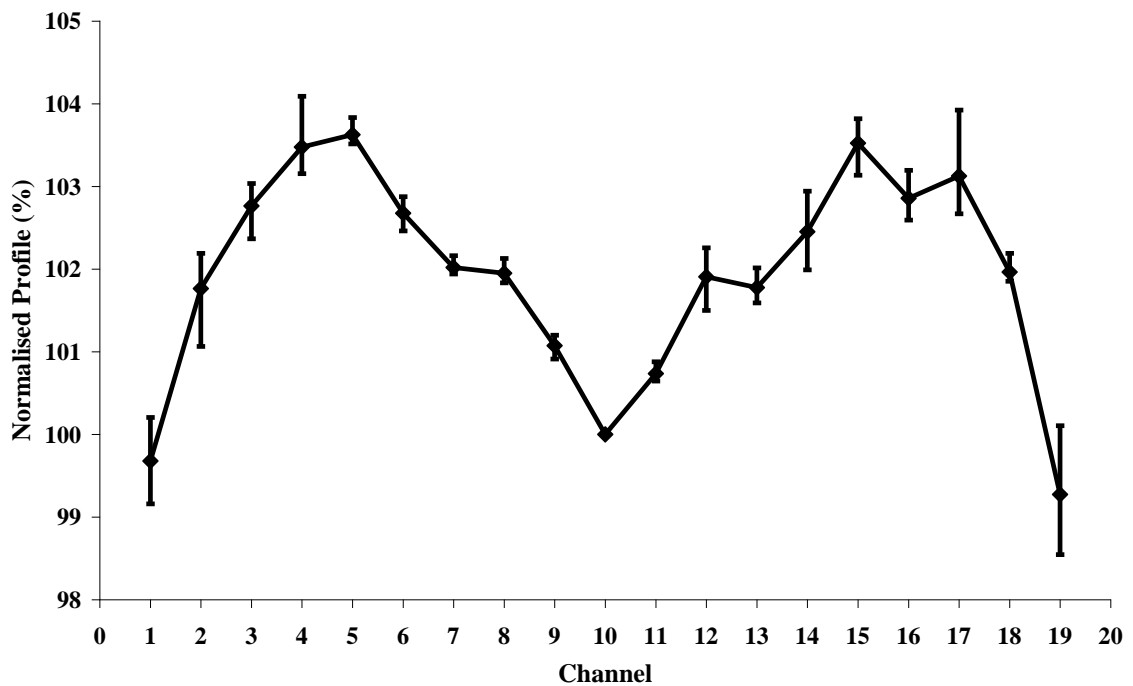


*Figure 4-19: The mean of the 3 calibration plots to be used to calculate the calibration factor. The error bars show the range of values in the 3 calibration data sets. (Error bars show 2 SD)*

Calibration factors were then calculated for each of the data sets (Figure 4-20), and a final calibration generated based the mean of these.

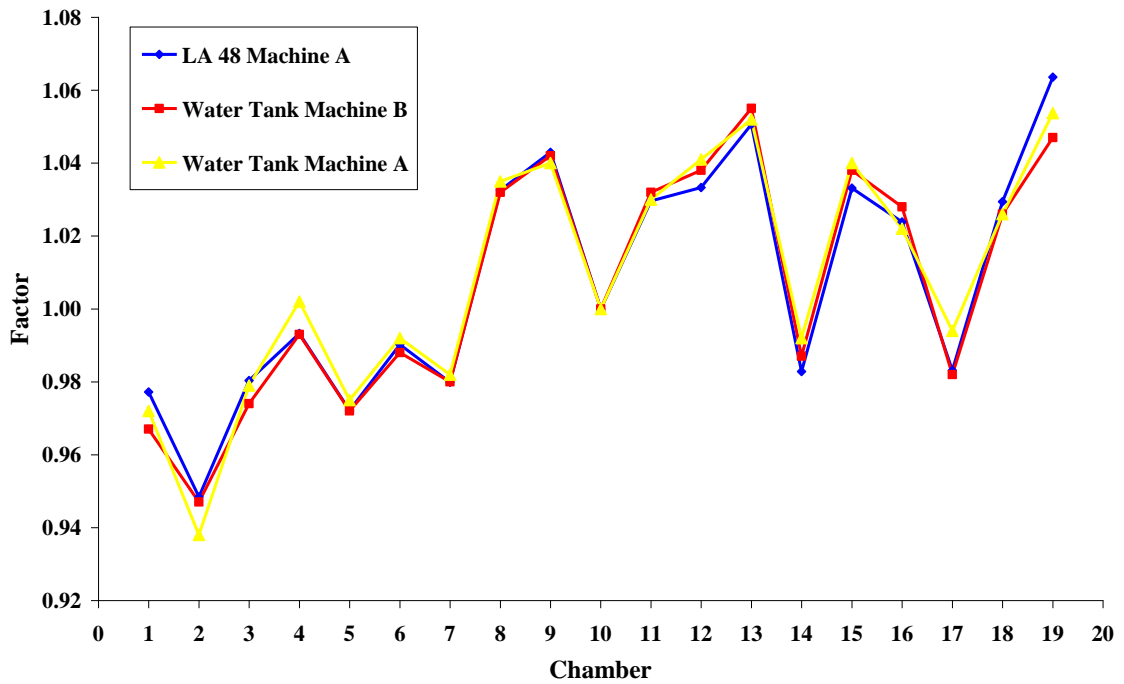


*Figure 4-20: 'Beam Scope' array calibration factors calculated from an LA 48, and 2 water tank plots (two machines were used for the water tank data).*

#### 4.3.6.2.2 Method 2- Shifting the array by one chamber either side of the CAX

A process where beam profile data is taken with the array nominally configured, then shifted by one chamber and then reversed to produce a calibration was evaluated (William S E. *et al*, 2000). Comparing the results of a calibration using this method with the LA 48 data showed discrepancies at the ends of the array. Extra Perspex was added to the ends of the array during the experiment to extend the buildup and back scatter regions. This improved the systematic error, but was not repeatable, as the added material was not integral to the array. The 2 cm spacing between chambers was also a concern compared with the much smaller value presented in the literature of 5 mm spacing (Profiler 2, Sun Nuclear Corp. USA). It was considered that this method would require a considerable amount of work to implement in this system, and was abandoned.

#### 4.3.6.2.3 Method 3- Shifting each chamber though the CAX

A calibration method by moving each chamber in the array though a 5 x 5 cm central axis field of 100 MU was tested.

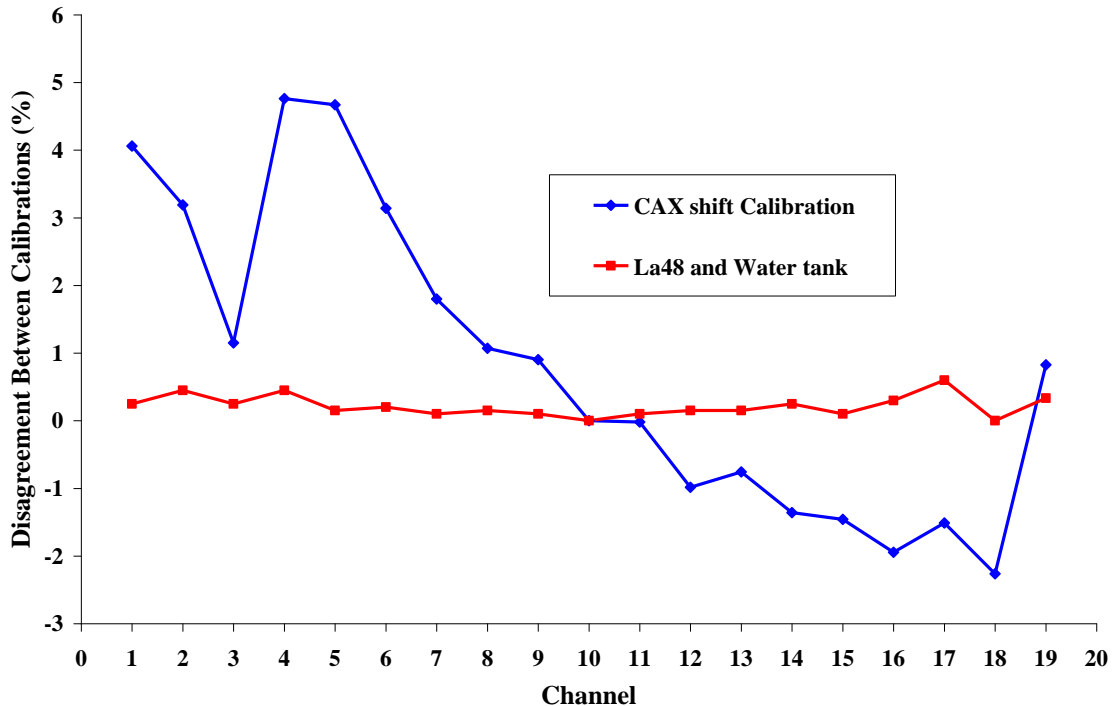


**Figure 4-21: The percentage disagreement between calibrations.**

The method was conducted on two occasions on the same accelerator. The mean error was 0.8% (2 SD = 4.6 %) with the worst case error in channel 4 of 4.7 %. This was compared with water tank and LA 48 plots in Figure 4-21.

This method also demonstrated discrepancies at the ends of the array as moving the chambers though the central axis for calibration would not account for off-axis effects due to field size and beam divergence.

#### 4.3.6.3 Conclusion

A number of calibration methods were investigated. The shift method (2) would have been a simple procedure, once mastered for this system, but needed time and a change of focus to implement. Both the shift (2) and CAX shift (3) methods required factors to correct for the chambers at the ends of the array. The LA 48 was the closest to the definitive water data and was part of the day to day departmental QA

process and therefore would be closely monitored for calibration. It was therefore decided to use the LA 48 as a cross calibration check, to be used as required to confirm the calibration of the system. Water tank data was used as a definitive reference to generate the array calibration factors (Figure 4-22) using the transfer calibration method (1).

**4.3.6.4 Final Array Calibration**

The mean of 3 beams in a water tank was taken, where the calibration reference point used was after the delivery of at least 100 cGy to ensure the beam was stable. The water tank was then moved away and replaced with the treatment table. The ‘Beam Scope’ array was then setup and pre irradiated as described in Section 4.3.4 to reduce charge build up effects. The mean of 3 beams of 100 MU was measured and used to calculate the final calibration factors for the array.

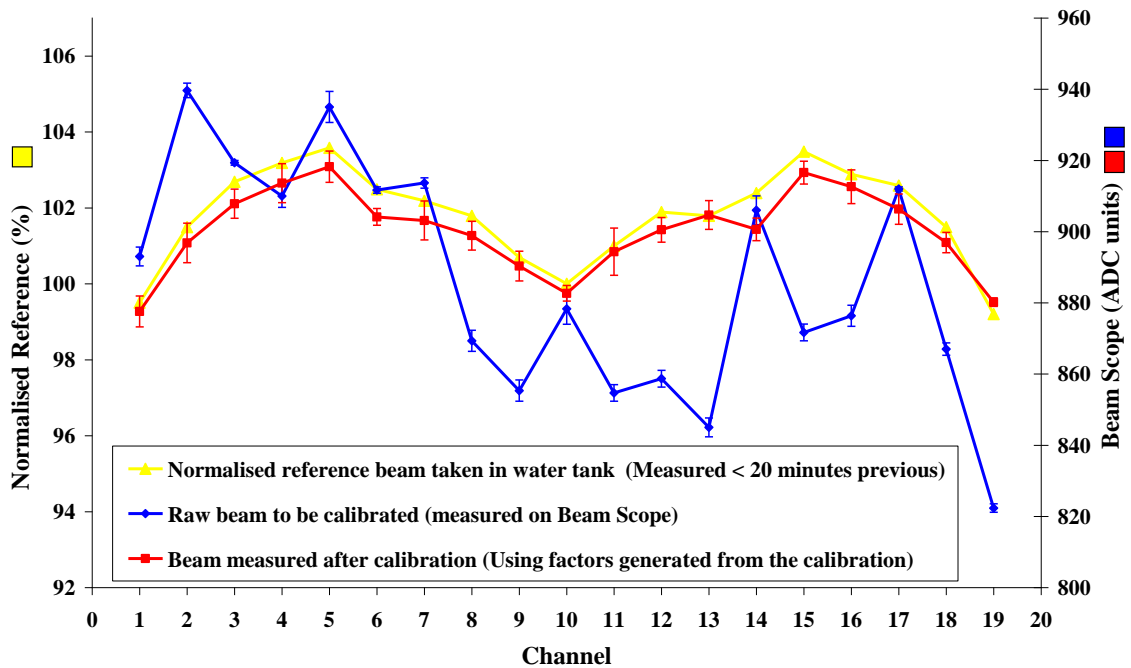
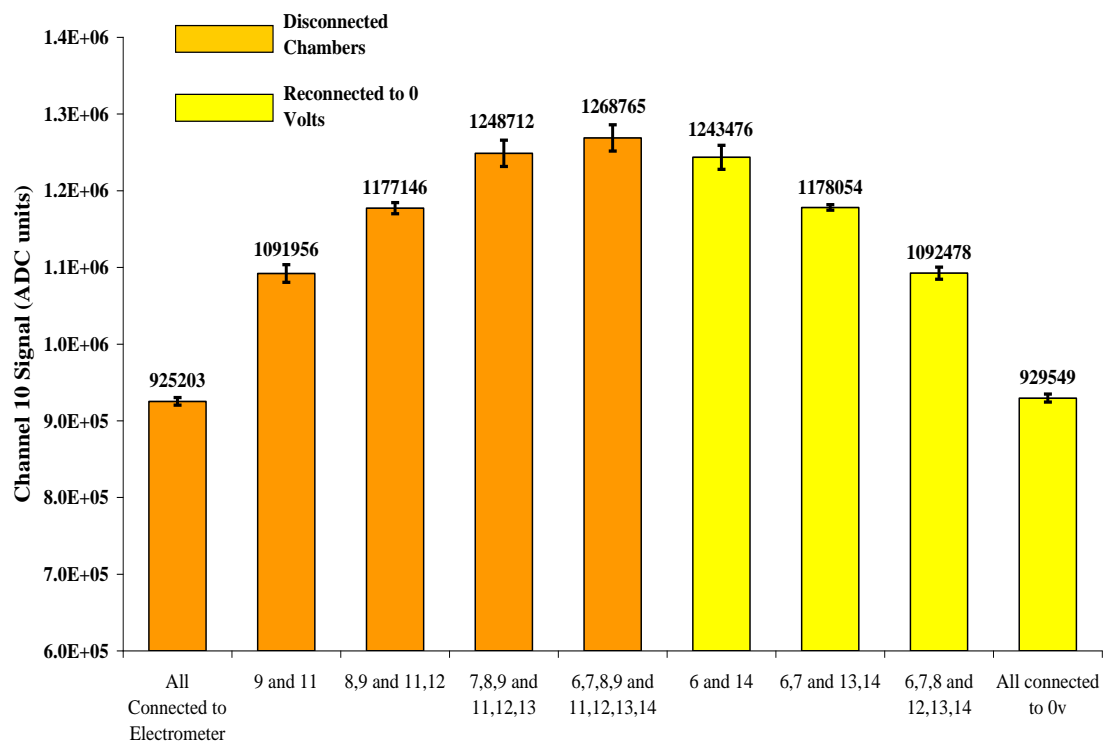


Figure 4-22: The final calibration of the system using data taken using a water tank. (Error bars show 2 standard deviations.)

**4.3.7 Electric Field Distortion**

The creation of an equi-potential plane over the collecting area of the array was discussed in Section 3.3.6. Since a difference in potential between the collecting

plates and the grounded guard ring would cause electric field distortion, it was necessary for the electrometer inputs to be at ‘virtual earth’ potential. To verify this, the investigation (Glendinning A G, 2001) described in Section 3.3.6 was repeated using channel 10 as a reference. Adjacent chambers were then disconnected in turn as far as chambers 6 and 14. The channel 10 reference signal was recorded at each stage. Chambers were then reconnected in turn to 0 volts; again the channel 10 reference signal was recorded as the chambers were reconnected. The results are plotted in Figure 4-23.



**Figure 4-23: Systematic disconnection of chambers from the electrometer and reconnection to 0 volts. The graph shows the signal level of the reference (channel 10) as connection configuration is changed. The signal was measured over a 100 MU beam using the default setup.**

As the adjacent chambers were disconnected they behaved similarly to un-terminated guards, increasing the collecting volume as described by Boag J, 1964. Consequently the signal from the reference chamber is larger as is observed in the central plot Figure 4-23 where 4 pairs of chambers were disconnected. The effect is demonstrated in an illustration from Boag J, 1964 reproduced in Figure 4-24 where an increase in potential of  $0.25 V_0$  ( $V_0$  being the high tension supply) of the guard ring

of a parallel plate chamber distorts the electric field, resulting in a field boundary QP instead of OO'. Since the field line QP terminates on the guard, no charge would be registered, but all ions collected to its right hand side would be swept towards the collecting plate. Thus the volume is increased and the signal from the collecting plate enhanced.

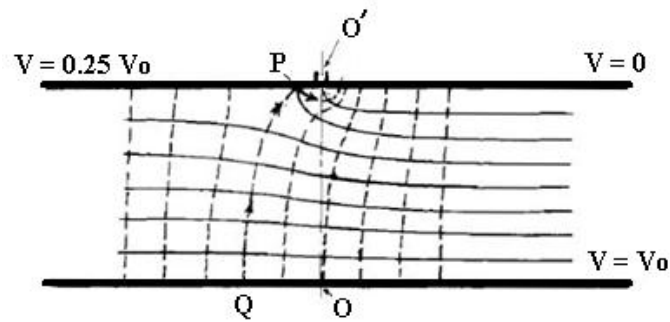


*Figure 4-24: Distortion of the electric field due to a potential difference of  $0.25V_0$  on the guard ring of parallel plate ionisation chamber (Based on Boag J, 1964).*

When all the chambers that were originally disconnected were reconnected to 0 volts there was better than -0.5 % difference in the channel 10 signal level. Comparing this with the 37% gross effect on the signal with adjacent plates left floating demonstrates that each ionisation chamber can be thought of in isolation when taking measurements with the 'Beam Scope' system, as the electrometer inputs are at virtual earth potential.

Considering that the effect is close to flattening out by the time 4 pairs of chambers are floating, this could represent a substantial measurement error if not accounted for, especially when the relatively large distance between the plates is considered.

#### 4.4 Analysis of Initialisation Confidence Test Data

Initialisation confidence tests are performed every time the measurement system is powered up. The results are stored to a log file on the host PC hard disk drive. The tests include electrometer functional tests, DAC/ADC loop back tests and the magnitude of 2 stable voltage references including the system zero voltage

reference. Also during the 'auto zero' process, which is required before any measurement session is initiated, values calculated for electrometer offset are recorded to the log file. All the log file data can then be analysed to profile the system performance over time.

#### **4.4.1 Acquisition Reference Voltage Test**

To measure the analogue acquisition system stability over time, measurements are taken from two 1.2 volt precision band-gap references, configured as a 2 point reference system, and also from the input star ground point (Section 3.6.4.3). Additionally, a temperature sensor was built into the acquisition system to log the temperature in the vicinity of the band-gap references. A mean of 5 acquisitions for each parameter are recorded into the confidence test log file during initialisation tests. Due to a software error the temperature value was not written into the log file. The value though, was manually checked at each measurement session and was always in range of 20 °C to 25 °C as would be found in the clinical environment. The data were then assessed for long term drift.

##### **4.4.1.1 Long Term Drift**

To ascertain the long term drift in the ADC and multiplexer the system test the reference readings in the log file were analysed. A daily value was calculated based on the mean of all the acquisitions in the log file entry for that day. Over an 8 month period, 14 samples of daily events were taken from the log file. These were processed and are plotted in Figure 4-25. To present the data on a universally scaled Y axis, the positive and negative voltage readings are referenced to zero volts by subtracting the mean value of the data sets. The number of readings taken per day is shown on the graph, and the mean value for that day and standard error are plotted. The warm-up error discussed in Section 3.7.2 can be clearly seen in the +/-1.2 voltage references as

the 2 plots are almost symmetrical along the x axis reflecting a systematic error with the daily ambient temperature.

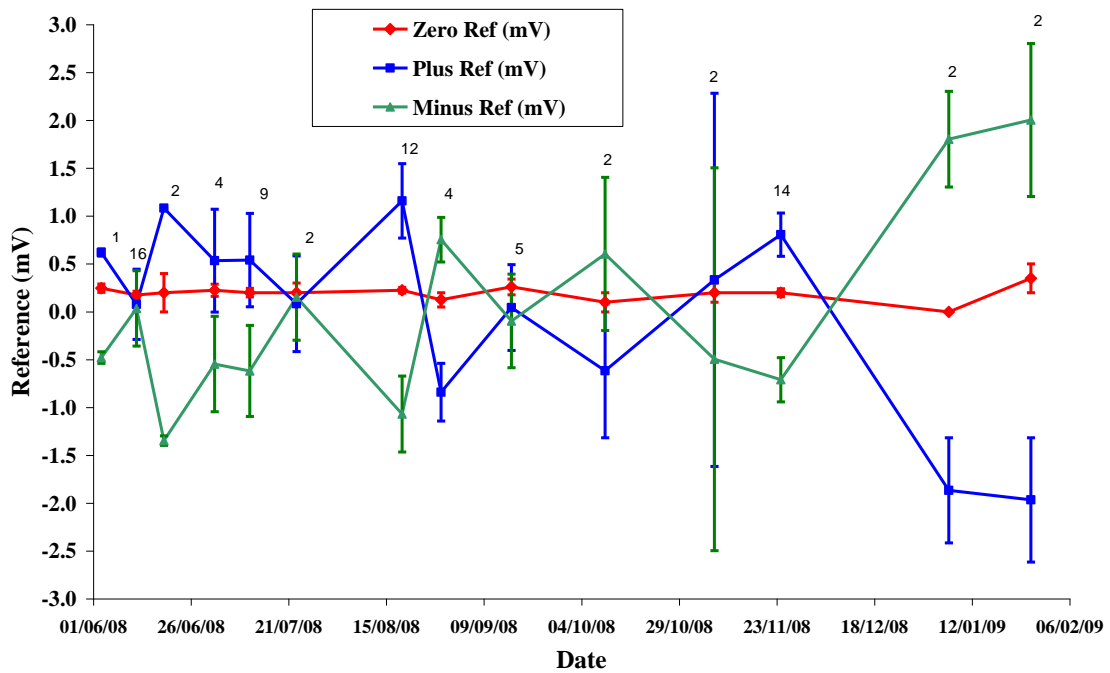


**Figure 4-25:** Error in the 2.5 V reference data over an 8 month period including the system 0V reference (The number of samples recorded for each date is shown on the plot).

Table 4-2 summarises the data presented in Figure 4-25. The worst case range of 3.35 mV was found in the negative reference. This is little more than the 3 mV error found over one measurement, which was attributed to the warm-up/ambient temperature in Section 3.7.2.

Reference (V)	Range (mV)	Std error	Mean (mV)	1 Std Deviation	% of full dynamic range (+/-5 Volts)
0	0.35	0.2	0.193	0.081	0.0007
Plus	3.125	1.95	0	0	0.063
Minus	3.35	1.95	0	0.35	0.07

**Table 4-2:** Summary of the voltage reference data taken from the log file over 8 months.

This is also reflected in the range of the 0 volt reference error value of 0.350 mV from Table 4-2. This channel is connected to the common star ground point and therefore any error is simply the combined offsets in the multiplexer,

amplifier and ADC components; again this is similar to that found in Section 3.7.2. These values obtained are insignificant and demonstrate excellent long term ADC/Multiplexer stability over the temperature range specified in both the confidence test log file (Section 4.4.1), and the functional testing data (Section 3.7.2) of 20 °C to 25 °C. Furthermore, any offset produced will be compensated for by the auto-zero function in the ‘Beam Scope’ software.

#### 4.4.2 Electrometer Offset

The internal offset along with any external offset presented by the transducer connected to the input is removed by the auto-zero function in the software. Even so it is reassuring to know that the mean internal electrometer offset is very small and stable over time.

To evaluate the electrometer performance, the spare electrometer channel was chosen (channel 20) as there was no transducer connected during the auto-zero function and therefore any offset present would be from the electrometer itself. The electrometer output with no zero compensation applied over an 8 month period is shown in Figure 4-26.

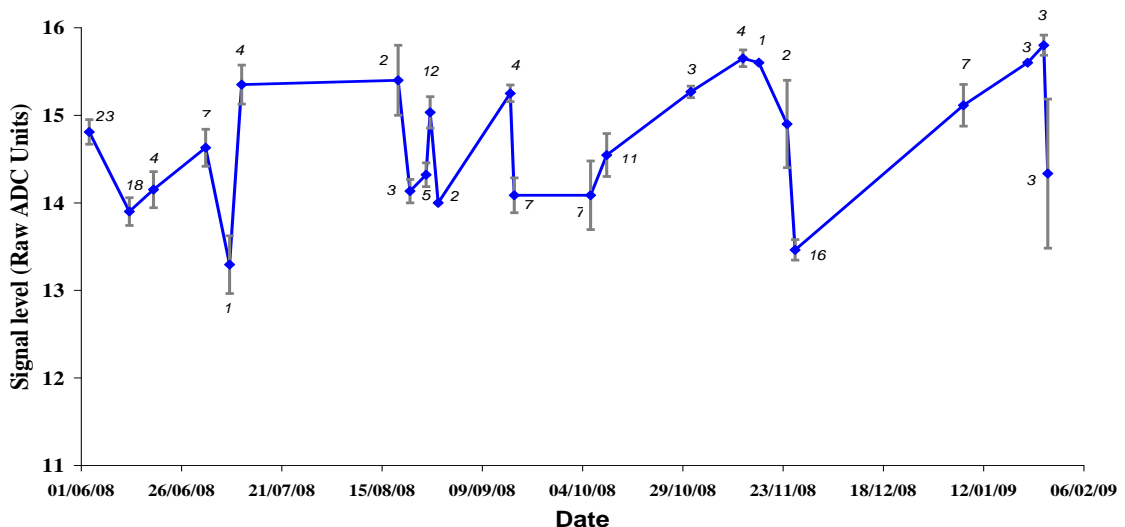


**Figure 4-26:** Un-compensated electrometer offset on channel 20 for an 8 month period. Error bars show 2 standard deviations.

A mean value of 14.7 (2 SD = 0.72) raw ADC units was calculated for the 8 month period; this value was typical for all the electrometer channels.

As stated in Section 4.2.4.1, electrometer offset with the reset asserted should be zero and is confirmed by the initialisation confidence test. The reason for the mean value of 15 raw ADC units with the reset inactive is not clear and may be due to input offset current. As this systematic error is stable with time and easily removed by the auto zero function it was not deemed to be a problem.

The compensation current injected in to channel 20 input is plotted in Figure 4-27 and shows no significant upward trend in the data. As this channel was not externally connected during the collection of the data, any increase in compensation current found would be due an internal source.

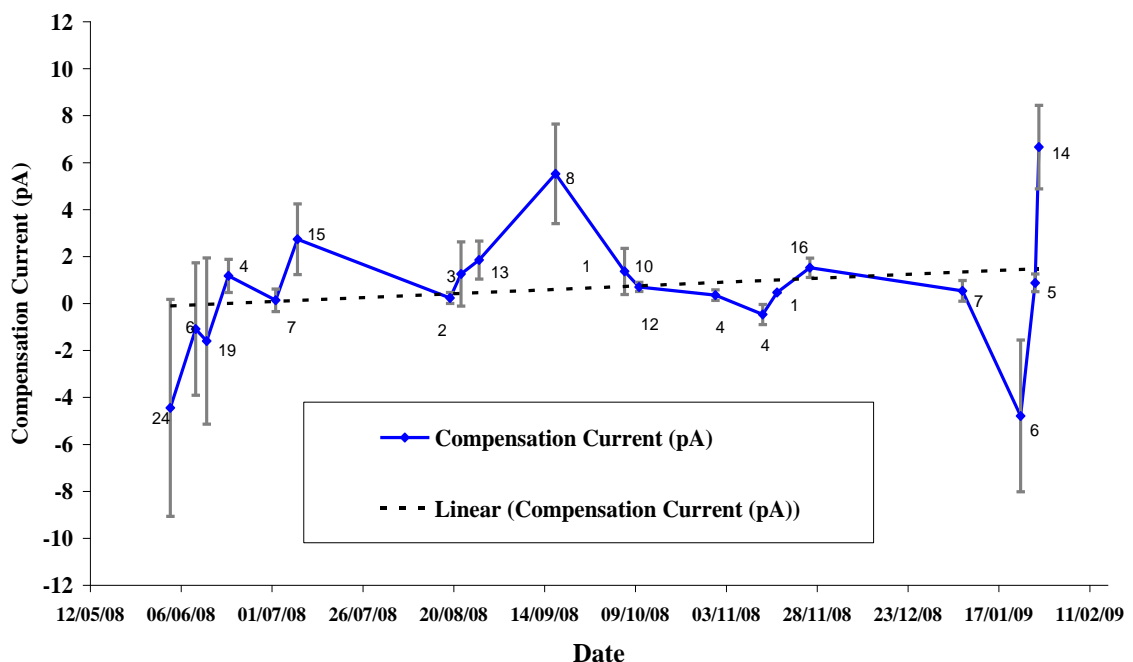


**Figure 4-27: Compensation current require for channel 20 over a 9 month period. Linear regression in plotted. Error bars show 2 standard deviations.**

The electrometer circuit boards were cleaned at commissioning and the screen enclosure holding the boards contains a number of silica gel bags to control the humidity. These measures have been sufficient to maintain offset to acceptable level.

**4.5 Conclusion**

The performance of the dosimetry and analogue data measurement hardware and software of the 'Beam Scope' system has been characterised and validated. Special consideration was given to ensure the integrity of measured data at high temporal resolution, specifically the system timing of data acquisition from the ionisation chamber. Final values for timing and calibration were chosen and tested in readiness for the measurement of the dynamic properties of radiation beams.

## Chapter 5. Initial Measurements

This chapter details how the first measurements and analysis were undertaken using the system. Firstly, calibration of the array for the measurement of analogue control system parameters and the calibration of the ion chamber array to the accelerator's dosimetry system are described. Reference data sets for use during analysis, are then discussed.

The method used by the 'Beam Scope' system to detect radiation start-up is investigated; including the measurement of a typical radiation start-up beam on an accelerator. This includes analogue control data, the 'magnetron tuner position', 'radial steering current' and 'electron gun filament current' which are recorded to illustrate the timing of control system signals during the radiation start-up phase. Correspondingly, the method for radiation 'end' detection is also examined.

Data processing and analysis are discussed, followed by the use of digital filters for the reduction of unwanted components or features in the analogue signals under investigation. A process for the analysis of multiple measurements is presented. Electron gun filament current signals measured during the radiation start-up investigation are low-pass filtered and processed using the multi-measurement process. These are then examined for shift invariance and artefacts in the digital filtration process.

Finally, the performance of the digital filtering that was used to process the electron gun filament current signals is investigated using 'chirp' signal characterisation.

### 5.1 Measurement

To produce useful data from the measurement of control system influence on linac performance, the 'Beam Scope' system is calibrated before each measurement session to present dosimetric data in units of cGy, and analogue inputs to the data pod

in the units appropriate to the signal being measured (e.g. electron gun filament current in Amperes). After analogue and dosimetric calibration have been completed, ion-transit time, trigger parameters, acquisition mode and sample rate are entered, data can then be acquired.

The machine configuration can also be entered and stored for future reference (e.g. collimator and gantry position, measurement axis, energy, SDD etc). The effect of changing a control parameter (e.g. electron gun filament current aim value) on the behaviour of the radiation field can then be investigated by analysing the results of radiation beams and analogue data taken as the chosen parameter is adjusted either side of its nominal value and compared to a reference profile. This results in a set of experimental data files one, for each value of the control parameter. An illustration of the measurement process is shown in Figure 5-1

### **5.1.1 Analogue Calibration**

The first step in the calibration of an analogue parameter to be measured is to adjust the gain and offset in the data pod pre-amplifier so that the range of the signal to be measured covers the full range of the 'Beam Scope' ADC. A simple program is provided in the 'Beam Scope' software suite to calculate the required values. The next step is to use the analogue calibration option in the 'Beam Scope' software to perform a 2 point calibration to present the analogue data in units appropriate to signal being measured, as described above. This option is only valid if there is a linear relationship between the parameter being measured and the resulting signal. The calibration is achieved by using the x and y values of the 2 points and solving these to find the slope and intercept values for a straight line law, where the slope is the system gain and intercept is the offset voltage. Should this method not be required then the analogue input may be calibrated in raw volts.

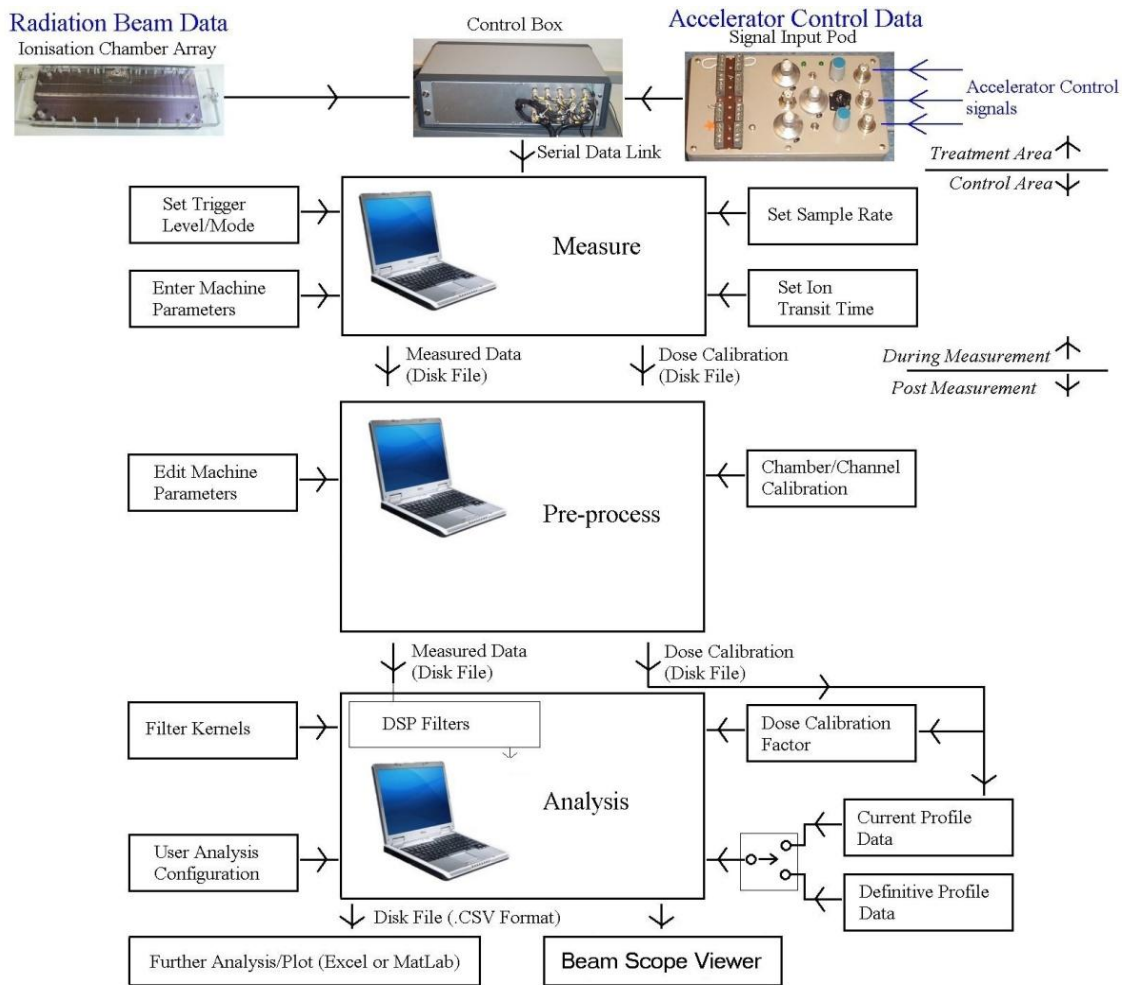


*Figure 5-1: Overview of the measurement process.*

### 5.1.2 Dosimetric Calibration

Beam profile measurements are based on a 40 cm x 40 cm field size to cover the maximum possible radiation field. All dosimetric calibration and dose measurements are based on this field size. After an initial pre-irradiation of 12 Gy to eliminate charge build up effects as described in Section 4.3.4, the system is calibrated to the accelerator's dosimetry system resulting in the 'Standard Array Configuration' (See Appendix 1). This eliminates the need for absolute dosimetric calibration of the 'Beam Scope' array and correction for local temperature and pressure before every measurement session. Three reference beams of 100 cGy each are measured in sequence and saved. These beams are assumed to be clinically in specification or from a post calibration session with a standard output measurement resulting in a transfer

calibration of 1 MU = 1 cGy on the machine. The dosimetric calibration factor for the ‘Beam Scope’ 1D array is then calculated as the mean of the summed central axis uncalibrated ADC signal of the three reference beams divided by the 100 cGy delivered dose.

The same calibration factor can be used for all channels since a calibration factor is applied to the other channels to match their sensitivity to the central axis channel (see Section 4.3.6).

### 5.1.3 Reference Data

Two types of data sets are required to analyse experimental data: beam profile and beam reference data. A mean of the 3 totalised reference beams, described above that were used for dosimetric calibration, are used to create a ‘normal’ profile. The individual reference beams are also saved and made available for inclusion during the data analysis phase. This is necessary since some oscillations and artefacts in both analogue parameters and beam data are unique to each beam and would be lost if the mean of the 3 data beams was used. Also, since the data sets are acquired in the time domain, any entity in the data that resulted from a cumulative dose event would also be lost, since the accelerator’s doserate is not fixed and therefore these events would occur at different times in the beam.

The effect of changing a control parameter on the behaviour of the radiation field is investigated by comparing experiment results against the reference data. Note that the control value used is also stored in each of the experiment data files.

### 5.1.4 Beam Status Detection

Beam data sets are recorded between the initiation and cessation of power supply/PRF to the accelerator’s modulator. Analysis can also use the same range or just the points between radiation start and finish. The ‘Beam Scope’ analysis names the radiation segment limits as the ‘Beam Start’ and ‘Beam End’ samples, as

illustrated in Figure 5-2. This approach was used to enable beam and analogue data events to be compared in the time domain if required by generating a synchronised start point for comparison. Also, for dose domain processing, data outside the bounds of ‘radiation on’ is ignored. Samples containing no useful dosimetric data are thus not analysed and therefore processing time is kept to a minimum.

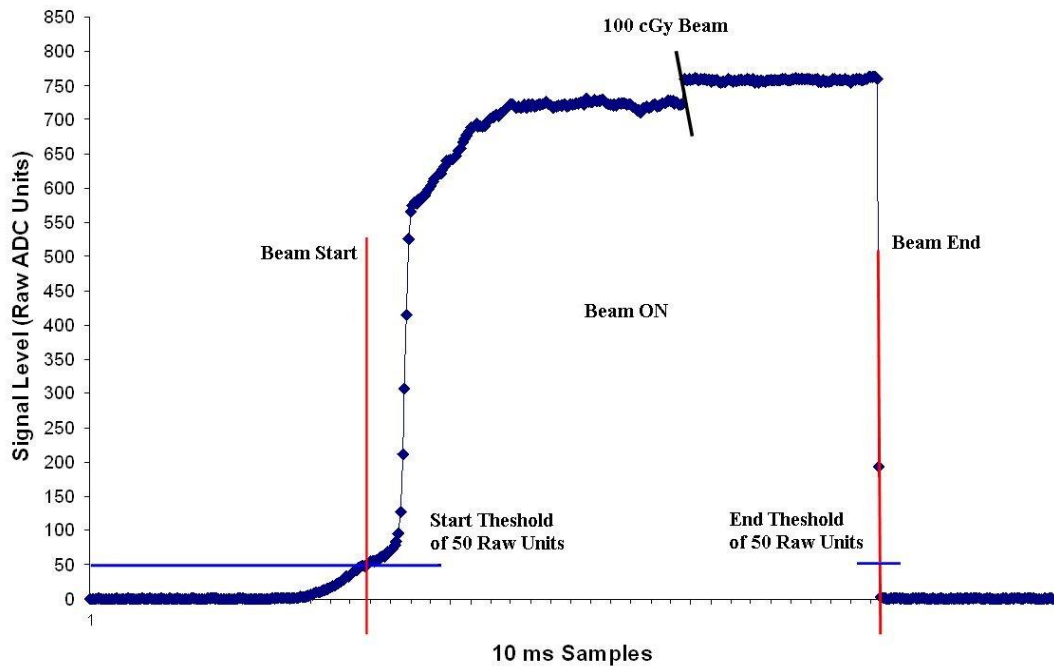


*Figure 5-2: Duplication of Figure 4-7 for ease of reference:- Example of the Beam Start/End events named ‘Beam Start’ and ‘Beam End’ sample in the ‘Beam Scope’ analysis and presentation applications. The raw signal from the central axis channel is shown.*

#### 5.1.4.1 Beam Start Detection

Analogue and dosimetric calibration was performed on the ‘Beam Scope’ system, as described above, with 3 of the analogue channels connected to the accelerator. These were configured to measure ‘magnetron tuner position’, ‘radial steering current’ and ‘electron gun filament current’ to facilitate the measurement of a typical radiation start-up sequence.

When a beam is captured, ‘Beam Scope’ data acquisition is always initiated before the ‘Start Button’ is pressed on the accelerator. This ensures that analogue signal activity that occurs before the commencement of radiation is recorded. This

sequence also guarantees that the ‘Beam Scope’ software is synchronised to the accelerator well before any useful signal data is present. With reference to Figure 5-2 a start threshold of 50 raw units is shown in the initial phase of the beam start-up.

A typical start-up sequence is shown in Figure 5-3, with detailed timing of the principal machine control signals. Acquisition is initiated at sample 0, where the ‘Beam Scope’ acquisition is in the ‘free run mode’, until sample 10 when synchronisation occurs (Figure 5-3 purple marker).

Starting from sample zero, the magnetron tuner servo (plotted in green) is driving the tuner to the operating frequency ( $F_0$ ) of the accelerating waveguide until just after sample 70 where the tuner servo error is less than 1 unit. This triggers a transition in the gun filament current (plotted in red) from standby to aiming level. The magnetron tuner then follows the  $F_0$  of the waveguide as the magnetron anode assembly warms up to its operating temperature.

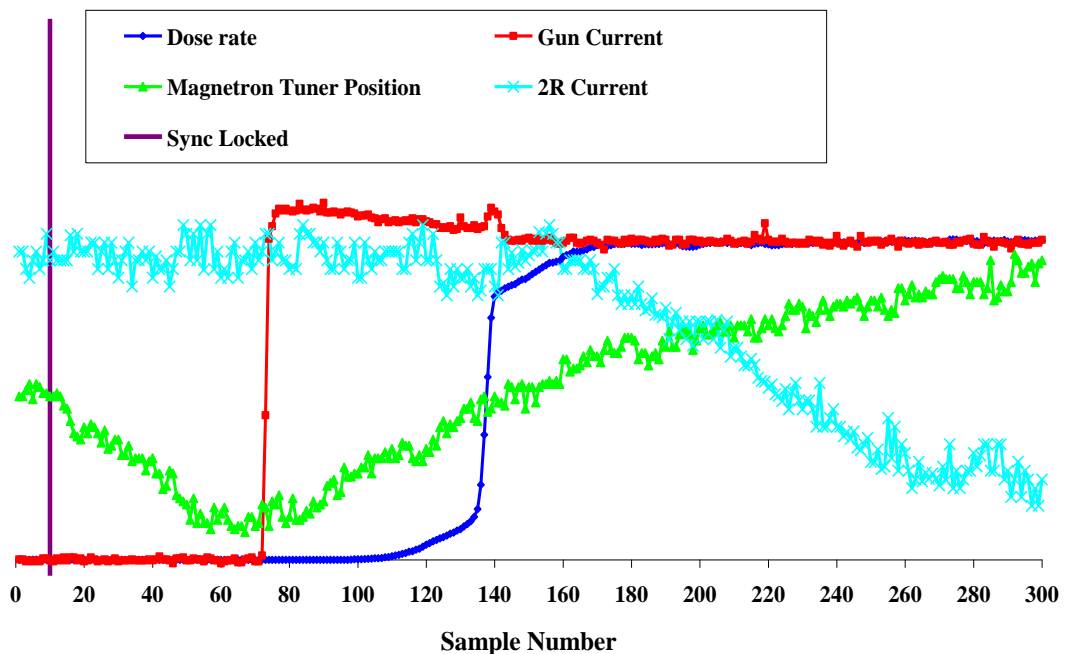


*Figure 5-3: Typical signal timing during the beam start-up phase. All the signals have been scaled to fit the vertical axis to show the sequence of events. The acquisition control system in the ‘Beam Scope’ was ‘sync locked’ by sample 10, shown in purple. Each sample is a 15 ms period.*

At sample 135 a small 'kick' can be observed in the gun filament current where the gun control system switches to servo mode, the doserate (dark blue) rises and the 2R servo (Lt blue) takes control of the radial steering current.

The data is presented in the time domain using the beam start sample as a reference point. Control system activity is at its greatest at the beam on and it is vital to ensure that this point is accurately established.

The acquisition logic used in the 'Beam Scope' system to determine the 'Beam Start' sample follows a logical sequence to satisfy a progression from an initial, to a programmed threshold to establish 'beam on' status to avoid false detection. If the correct sequence is not followed then the application displays a warning error box to the user.

Values were carefully chosen for the programmed thresholds. After over 300 beams measured the start detect error message warning has not been activated, demonstrating good performance of the beam detection algorithm.

At the 50 raw unit threshold point, 310 raw ADC units of dose were delivered in the test data file shown in Figure 5-2. Based on a nominal dose calibration factor of  $9.62 \times 10^{-05}$  cGy calculated as described in Section 5.1.2, a value of 310 raw units equates to 0.03 cGy or 0.03 % of the total beam (100 cGy) of lost dose in the start detector algorithm, which is an insignificant amount.

#### **5.1.4.2 Beam End Detection**

When the set dose is completed, the PRF signal to the modulator is inhibited by the dosimetry system in the machine and the 3 phase power supply is switched off to the modulator and HT generator. The PRF signal is also linked to the charge command sent to the HT generator and so PFN charging also ceases. Since radiation pulses are initiated by PFN discharge, which cannot be stopped once activated,

radiation, will always end on a whole pulse. Experimental data from a range of measurement sessions was used to confirm this.

Twenty beams of 100 cGy acquired at a PRF of 400 PPS and a sample time of 15 ms, resulting in 6 radiation pulses per sample being analysed. A mean of the signal over the last 75 % of each beam was calculated (the first 25 % was not used to limit spread due to doserate warm up). The expected signal per sample was calculated for each beam by dividing each mean by 6 (the number of radiation pulses per sample). A table of the expected signal for 1 to 6 pulses in a sample was calculated. The value of the penultimate sample, at ‘beam off’, before the signal level dropped to less than 5 units (background noise) was noted, and the sample it was closest to in the table was identified for each of the 20 beams. It was then possible to determine in which pulse in the sample radiation had ceased. The percentage difference between the expected value in the table and the penultimate sample is shown in Figure 5-4.

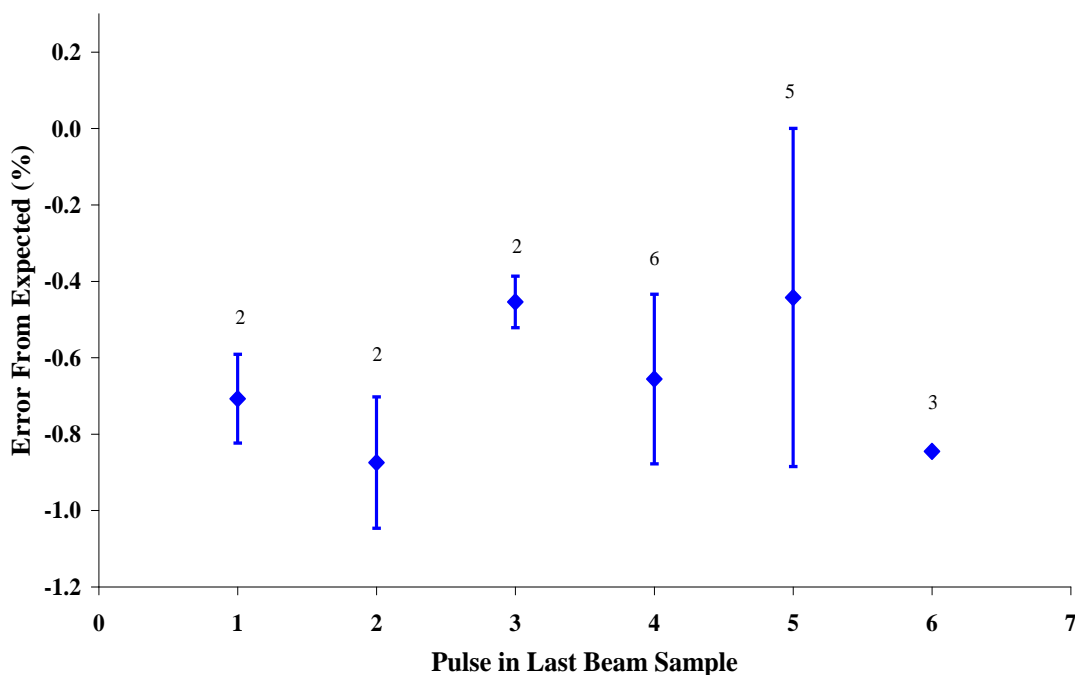


*Figure 5-4: Error from the expected value in the last beam sample of the signal at secession of radiation. The value above the error bar is the number of beams found with the pulses in the x axis (total of 20).*

The plotted errors are all within 1 % of the expected value for each of the possible radiation pulses in the penultimate sample. This shows that radiation does not cease within a pulse period and completed pulses are always delivered. Therefore to detect the beam off sample, the beam status detection routine in the analysis code simply monitors the signal level during beam on, and determines beam off when the level drops below a set threshold. The threshold is set higher than the random signal noise for beam off (5 units) and lower than the signal for one radiation pulse (approximately 200 units, dependent on of the signal per pulse of the array due to calibration drift, local temperature and pressure).

## **5.2 Data Pre-processing**

When reference and experiment data sets have been saved, it is necessary to pre-process all the files (See Pre-process Figure 5-1). This allows the user to confirm or change the machine configuration data and also applies the chamber matching calibration (See Section 4.3.6). A set of fully calibrated reference and experiment data sets are then available for analysis.

## **5.3 Analysis**

A fundamental requirement is that experimental results should be presented in a common domain. As mentioned in the previous Section, each of the data files is acquired in the time domain at a fixed sample rate. Although each beam data file contains useful information in its own right, not much useful information can be gained by combined analysis of beam data sets in the time domain since the dose rate of the accelerator is not fixed. Therefore one of the major functions of the analysis is to enable the data files to be plotted in the cumulative dose domain. The dosimetric calibration factor generated from the reference files in Section 5.1.2 is used to calculate and then accumulate the dose value in cGy.

To analyse each data file individually, to explore the results of an experiment would be a cumbersome and time-consuming process. A simple software function named Multi-File Analysis (MFA) has been created to aid this process taking advantage of the common cumulative dose domain described above. The data file details are grouped into a single MFA data file that holds the names and path details of the definitive, reference, experimental data files and all the user analysis options. The user simply sets the analysis options required and selects the 'Execute' function. The program then runs the analysis and compiles the data in two sets of output files. The first type has the extension .CSV (Comma Separated Variable) for import in Microsoft Excel™ or Mathworks Matlab™ for further processing or graphing. The second directly imports the results into a further 'Beam Scope' application known as the 'Beam Scope Viewer' to present the results in a graphical format.

### **5.3.1 Data Filtration**

Accurate extraction of the underlying process from noise and unwanted signals, without misrepresentation is a prime requirement which allows the properties of the underlying process to be meaningfully observed and measured (Smith S W, 2003b). This is achieved by filtering the data to suppress or completely remove unwanted components or features of the signal under investigation. Because of their good performance in both the frequency and time domains, digital filters were used in the 'Beam Scope' analysis application to eliminate or suppress some aspect of the signal to help reveal underlying processes.

A simple moving average filter was chosen to remove random noise while retaining a sharp step response, since it is the optimal filter to remove noise in time domain encoded signals (Smith S W, 2003a). To filter periodic waveforms, the Finite Impulse Response (FIR) filter based on the 'sinc' function was chosen. This type of filter is very stable and offers a high level of performance compared to its counterpart, the Infinite Impulse Response (IIR) filter. The IIR filter requires careful consideration

of phase response and stability, and was therefore not chosen for this application. The overriding advantage of IIR type filters is execution speed and they find their niche in applications requiring real time processing. FIR filters are implemented by convolving the digitised signal with a filter kernel that is configured to produce the required filter parameters. A series of low-pass filter kernels with a range of cut off frequencies and stop bands were produced using the 'Signal Processing Toolbox' in MatLab™ for use in data analysis.

Shift invariance is a key property of any filter to be used in an application where data sets are compared to characterise a process. Any unwanted modification by the filtration process will result in the misrepresentation of experimental results, be it in the x axis in time or frequency domains, or in the y axis as a shift in the DC level or gain of the signal. Therefore it is vital to confirm the implementation of the filter software by checking their transfer functions for shift-invariance.

### **5.3.1.1 Moving Average Filter**

The moving average filter works by taking the average of a number of samples from the input signal to produce a 'smoothed' value in the output. As described above, this filter was chosen to allow the user to optimally remove noise from the signal. This filter type is sample shift invariant by design as long as the range of samples chosen from the input signal is symmetrical about the output sample and the number averaged is an odd number (Smith S W, 2003a). To ensure this, the application checks that the user inputs an odd number of averages for data analysis. The MFA mode described above was used to demonstrate shift invariance in the moving average programming code taken from the routines made available in the 'The Scientist and Engineer's Guide to Digital Signal Processing by Steven W. Smith' as described above, incorporated in the analysis application. The same beam reference data set was analysed over 2 averaging values and plotted (Figure 5-5).

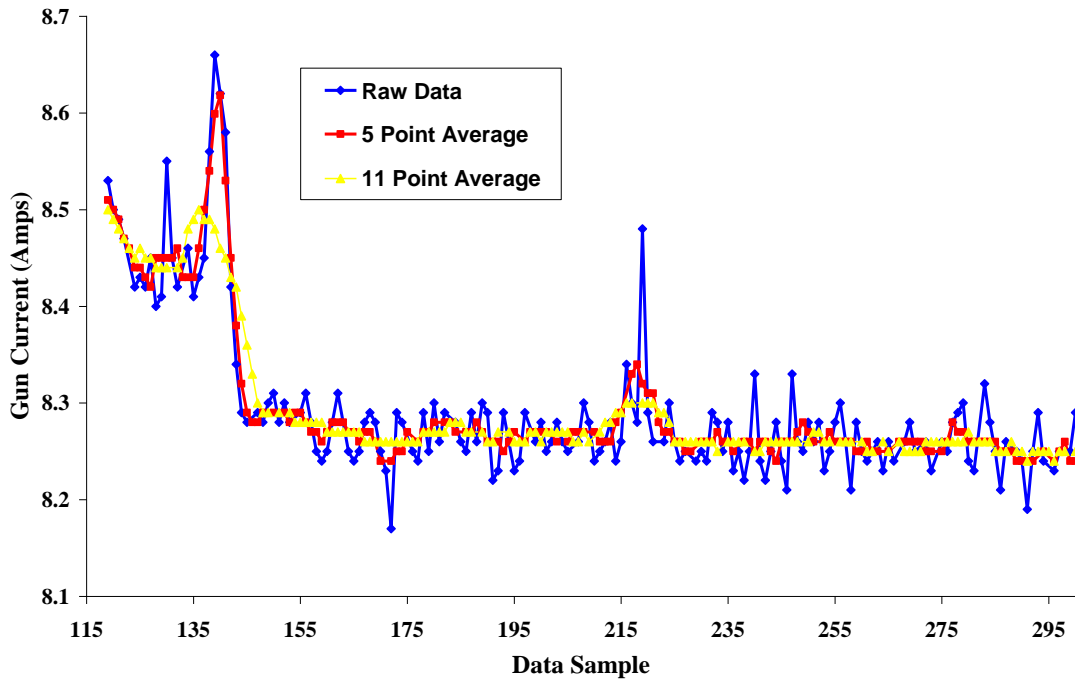


*Figure 5-5: Electron gun filament current at start-up as raw data and filter with a 5 and 11 point moving average filter.*

Visually, the filtered results show good shift invariance with the exception of the large transition just past sample 135 using the 11 point average, a small amount of ‘blurring’ in the time domain is inevitable with an averaging filter.

This filter type is optimal for the reduction of random noise, but the step response will suffer as the number of averages increases, as seen in Figure 5-5 starting at sample 135. This is due to the requirement that to optimally remove noise, as each sample is as noisy as the next, every sample in the progression must be treated the same. Since it is not possible to weight samples as they move away from the central value, signal edge response suffers (Smith S W, 2003a). Therefore if this filter type is chosen for data analysis, the user should carefully choose the number of points to be averaged, by visually comparing the raw data with the averaged to ensure points of interest in the signal are not lost. A compromise is then made between the smoothness of the data and the sharpness of the edge response.

### 5.3.1.2 Low Pass FIR Filter

The windowed ‘sinc’ function (Figure 5-6) produces the optimal low-pass filter when convolved with the input signal (Smith S W, 2003c). Note that the function is symmetrical about the centre and contains an odd number of points, which results in a type 1 FIR filter kernel. Since this is most common design mode for this filter type and has linear phase and good time invariance properties, it was chosen for inclusion in the ‘Beam Scope’ analysis application. Other inferior FIR filter types are available but will not be discussed here. The mathematical application of the ‘sinc’ function results in an infinite number of points either side of the central value. To enable this to be used in the FIR filter, as the title describes, it must be reduced to a ‘finite’ number of points. Truncating the function results in poor filter response due to discontinuities left behind by the truncation process.

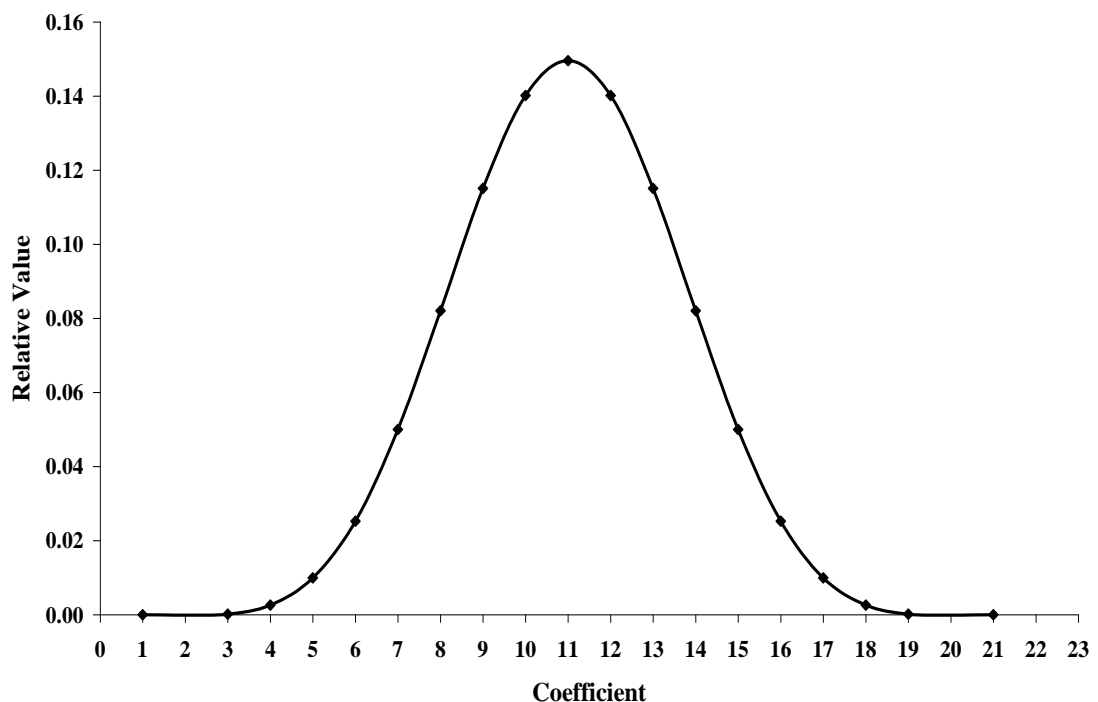


*Figure 5-6: Example of a 21 point filter kernel using a ‘Blackman window’ designed to produce a 4 Hz cut-off from a sample rate of 66 Hz (15 ms) and > -80 dB of bandstop available for use in the ‘Beam Scope’ acquisition (created using the MatLab™ signal processing toolbox).*

To eliminate this problem the function is 'windowed' to smoothly bring the ends of the kernel to zero. The example in Figure 5-6 shows a kernel produced with a 'Blackman- Harris' window which reduces the end values of the kernel to less than  $3.4 \times 10^{-19}$  units, a ratio of  $4.44 \times 10^{17}$  from the central value. This will realise  $>-70$  dB band stop attenuation in a low pass filter implemented using this kernel. To gain any benefit though from this range the convolution process to apply the low pass filter must be implemented using double precision arithmetic in the program code (Smith S W, 2003c).

The Blackman and Hamming are the most popular choices of window, and both have trade-offs in filter performance such as roll-off, stop band attenuation and pass band ripple (Smith S W, 2003c). In comparison the Blackman window has only 0.02 % ripple in the pass band (0.2 % for the Hamming) and a superior stop band attenuation of -74 dB, (-54 dB for the Hamming). The drawback of the Blackman filter is the slower roll off which can be compensated for by using a 20 % longer length filter kernel, this though results in 20 % longer computational time during convolution. Since the data analysis is performed 'off-line' for this project, this minor compromise is acceptable, making the Blackman window the preferred choice.

The same data as in Figure 5-5 for the moving average filter test were filtered using the 4 Hz FIR 21 point kernel, shown in Figure 5-6, and also a 61 point version for comparison. This was again achieved using code adapted from the routines made available in the 'The Scientist and Engineer's Guide to Digital Signal Processing by Steven W. Smith' as described above, built-in to the analysis application. Again good shift invariance over the whole of the plot is demonstrated where the filtered peaks and troughs line up with those in the raw data (Figure 5-7).

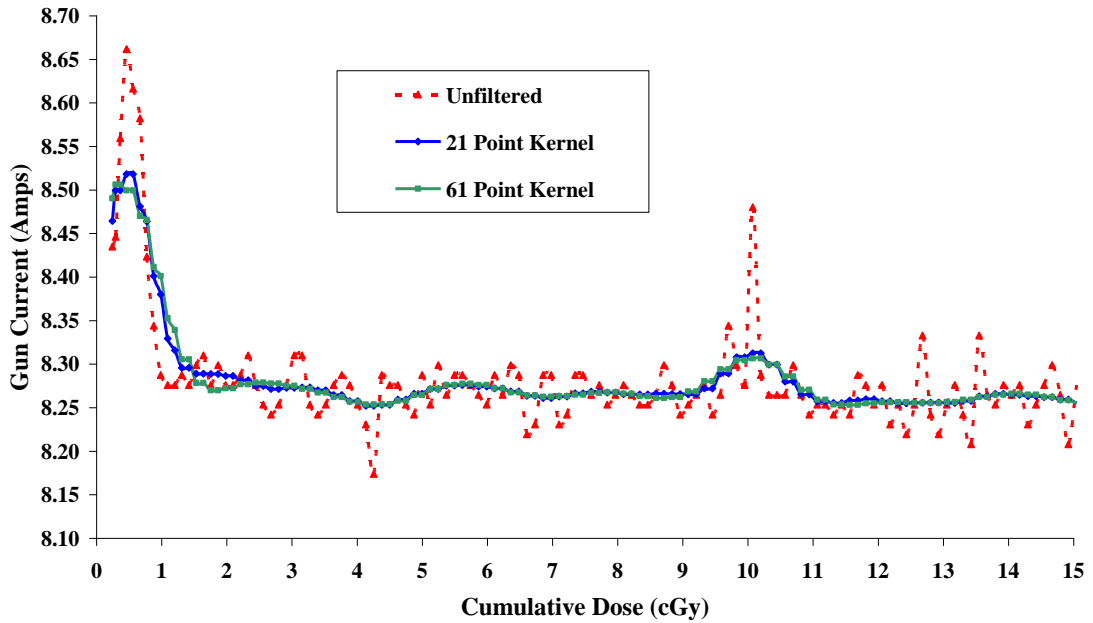


*Figure 5-7: Electron gun filament current at start-up as raw data and filtered with a 4 Hz FIR filter. Kernels of 21 and 61 coefficients are plotted.*

The DC characteristics of the filter can also be seen where the filtered signals take a mean path through the unfiltered data. DC gain was also confirmed by ensuring the coefficients in the filter kernels added up to unity, which is a requirement for unity DC gain (Smith S W, 2003c).

### 5.3.1.3 Confirmation of FIR Filter Implementation

The moving average filter is simple and easy to realise in practice compared with FIR filter implementation by convolution. The performance of the FIR filter was evaluated (Figure 5-7) with data measured from a machine at beam start-up. To be sure that the programming code used was correctly implemented, a second test was performed. The filter kernels used in the above FIR filter example were created in the ‘Signal Processing Toolbox’ in MatLab™ as described above. Frequency response plots of the filters were available at filter design time and were exported along with the two filter kernels.

The principle of the test was to generate two filtered data sets using a suitable linear ‘up-chirp’ signal for both filters used in Figure 5-7 and compare the results with

the exported frequency response saved from MatLab™. In an 'up-chirp' the frequency increases and conversely in a 'down-chirp', decreases. A linear chirp is a signal whose frequency changes linearly with time from one frequency to another (Equation 6). Thus, you can use chirp signals to characterise instrumentation systems such as amplifiers and filters. For example, by inputting a chirp signal into a low-pass filter, you can characterise the filter's frequency response.

Linear Chirp in the frequency domain

$$f(t) = f_0 + kt \quad \text{Equation 6}$$

where  $f_0$  is the start frequency (at time  $t = 0$ ) and  $k$  is the chirp rate (rate for increase/decrease in frequency) and is a constant for a linear chirp.

The formula for a linear chirp in the time domain (Equation 7) was implemented in software to fill a one dimensional array starting from  $t = 0$ , to create a chirp signal from 0.5 Hz to 12 Hz (Figure 5-8), resulting in 401 values in the array. Although some aliasing is evident in the figure at the 12 Hz end of the chirp, there are only 4 points present in last cycle of the waveform. Since this is the bandwidth limit for the chirp and therefore the highest frequency present (12 Hz), the Nyquist criteria for the minimum of 2 samples, are satisfied. The resulting chirp was used to test the frequency response of the 4 Hz filter with the 21 and 61 point filter kernels used in the example in Figure 5-7.

Linear Chirp in the time domain

$$y(t) = \sin \left[ 2\pi \left( f_0 + \frac{k}{2} t \right) t \right] \quad \text{Equation 7}$$

where  $f_0$  is the start frequency (at time  $t = 0$ ) and  $k$  is the chirp rate (rate for increase/decrease in frequency).

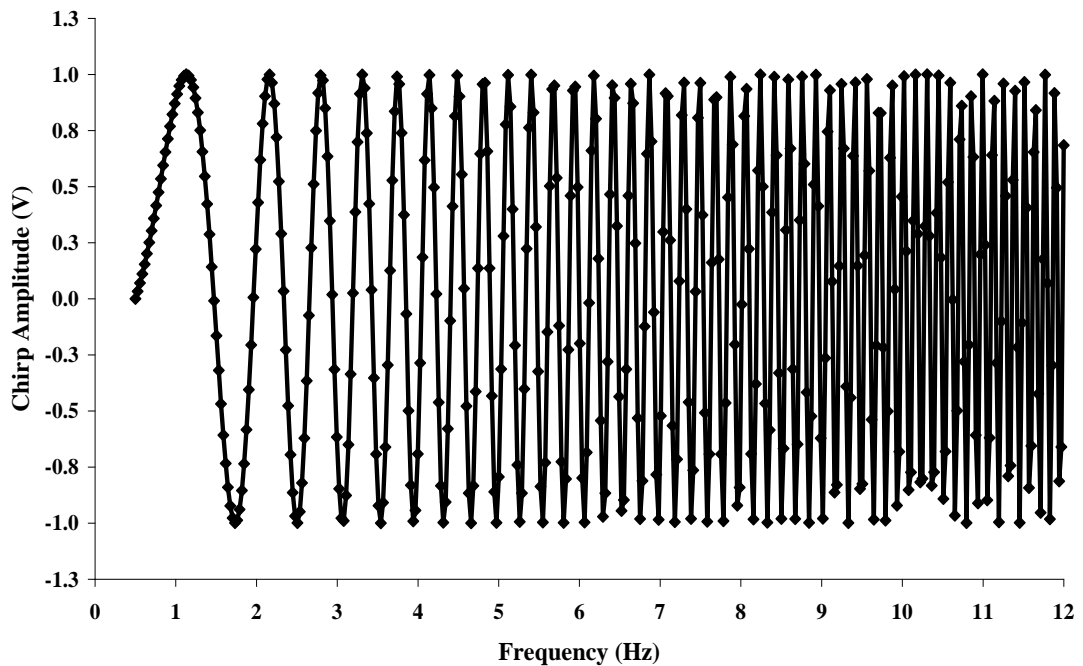


*Figure 5-8: Test chirp signal generated in software from 0.5 to 12 Hz.*

The chirp was filtered by both the 21 and 61 point filter kernel and then peak detected, using a simple algorithm to find the peaks using turning point detection. An example of the peak detection process using the filter produced by the 61 point kernel is shown in Figure 5-9.

The -3 dB marker point identified in Figure 5-9 is coincident with the design cut-off frequency marker at 4 Hz. The two peak-detected results were then plotted (Figure 5-10) along with the frequency responses saved at the filter design stage. In Figure 5-10 the filter response derived from the 61 point kernel shows some divergence from the cut-off frequency, but is only 0.3 Hz worst case at  $>-60$  dB from the peak. The plot from the filter derived from the 21 point kernel stops at the end of the chirp at 12 Hz at -60 dB.

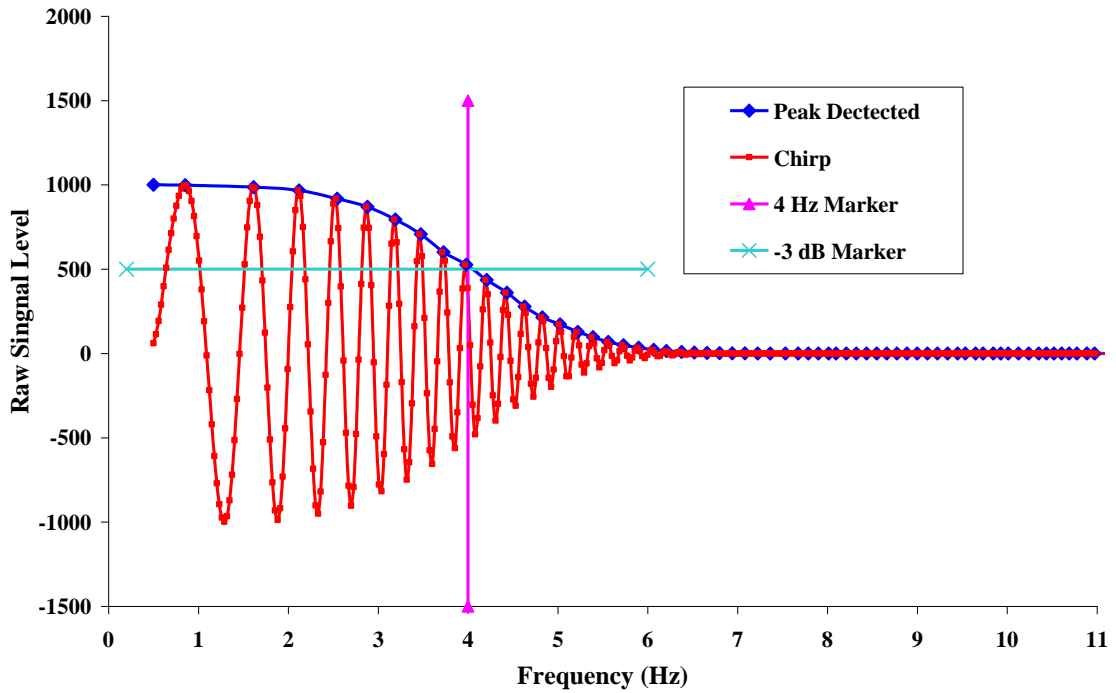


*Figure 5-9: Generated ‘up-chirp’ signal of 401 points from 0.5 to 12Hz, low pass filtered with the 61 point kernel. The result of the peak detection is also plotted (Blue series). The markers show the cut-off frequency (4 Hz) and the -3 dB point (500 units of the 1000 units of raw signal of the filter).*

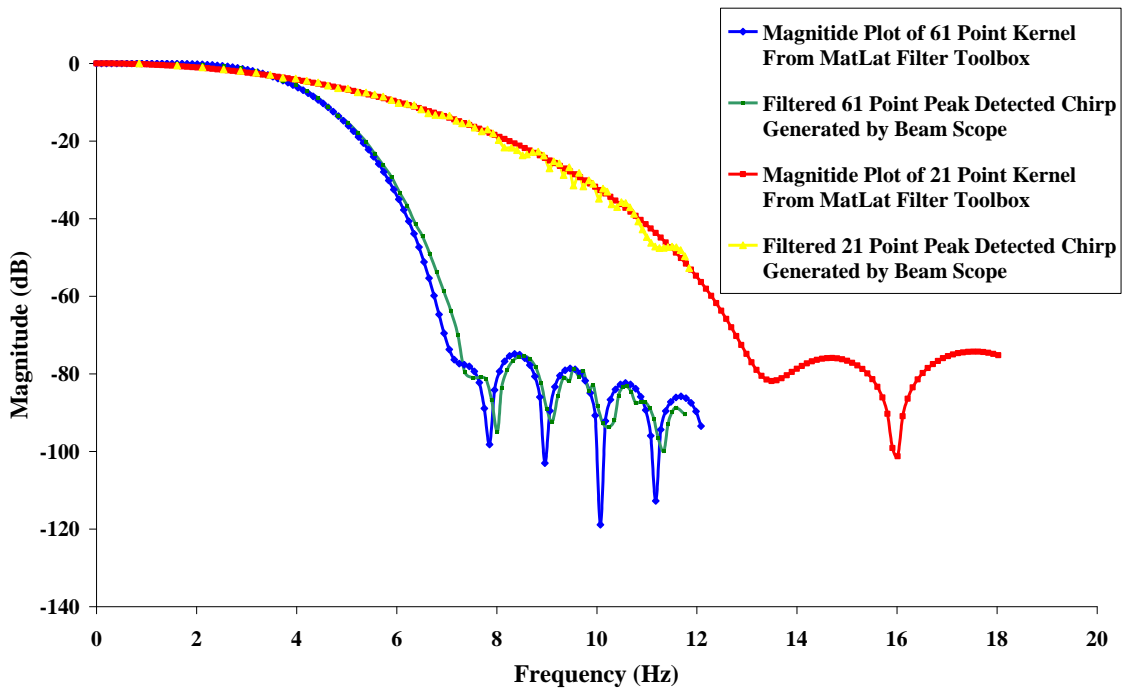


*Figure 5-10: Exported frequency response and peak-detected up-chirps produced from the ‘Beam Scope’ application plotted for the FIR filters created from the 21 and 61 point kernels.*

The correspondence is not as good as for the filter with the 61 point kernel. Some errors can be expected at small signal amplitude owing to signal aliasing due to

the simple nature of the peak-detector algorithm used in the experiment. The close match between the filtered chirps and the magnitude plots for the 2 filter kernels demonstrate the implementation of the FIR filter in the 'Beam Scope' application performs satisfactorily.

## **5.4 Conclusion**

This chapter demonstrates the processes involved in the measurement and processing of a radiation beam and its electron gun filament current signal from a clinical accelerator. Calibration, 'beam' detection and data filtration were presented with the aim of producing a visual representation of the processes involved the radiation beam start-up on a single data set. The next chapter will continue on the theme, utilising the MFA processing mode to present multiple radiation beams to demonstrate the effect of changing electron gun control parameters on the behaviour of the radiation field.

## Chapter 6. Electron Gun Behaviour at Beam Start

### 6.1 Introduction

This chapter focuses on the use of the ‘Beam Scope’ system to perform measurements in the first few cGy of ‘beam on’, as this is pertinent to the delivery of step and shoot IMRT radiotherapy. A method is described to characterise the performance of the electron gun and energy servo control system with both optimal and incorrectly adjusted electron gun filament aiming levels during:-

The beam start-up phase only, up to the first 5 cGy of beam on. (Experiment 1)

The delivery of complete beams of 2, 3, 4, 5, 10, 20, 50, and 100 cGy.  
(Experiment 2)

Although other control systems in the accelerator are active during this period, the electron gun filament aiming level parameter in the electron gun control servo was specifically chosen as a variable in the experiment since its value needs to be manually reduced over time to compensate for the ageing characteristics of the filament. Therefore the dynamic nature of the aiming value requires it to be adjusted at regular intervals to maintain machine performance.

A paper by Haas O *et al*, 2000 reports the significance of monitoring the electron gun aiming level at beam start-up on the Philips SL25 series accelerator to ensure adequate start-up performance. The work though, does not link the results to any dosimetric effects, and there is also no description of the energy discrimination system used on the accelerator (both the ‘Energy Slit’ and ‘Ion Chamber Plate’ systems were available at the time of writing (Buchgeistera M & Nusslin F, 1998)).

The term ‘Servo’ used in this chapter requires clarification: it has been included in the text since it is in general use in the description of the accelerator used in the experiments. The energy control system incorporating the electron gun control

electronics is commonly known as the ‘Gun Servo’. The word servo is a shortened term for servomechanism which implies some mechanical element. There are no moving mechanical parts in the gun control system of the machine, but the word has been adopted by the manufacturer to describe all ‘closed loop’ control systems on the accelerator.

### **6.1.1 Electron Gun Filament ‘Aging’**

Over time, the cross-sectional area of the filament winding reduces during high electron emission yield at radiation on, with the filament typically lasting around 4 years (for low energy X-ray beams) before a replacement is required. Over this period, the operating current of the electron gun filament required to produce a calibrated radiation beam is reduced by approximately 400 mA, starting from between 8.0 and 8.2 Amperes for a new filament.

## **6.2 Prerequisite**

The GT axis was chosen for the experiments in this chapter, since this configuration measures the electron beam in the bending plane, and therefore any achromatic effects in the beam bending system will be reflected as radial beam tilts. Although beam ‘tilt’ versus electron beam energy has not been presented in this chapter, its effects were measured during accelerator maintenance, and were well within the specification of the machine and similar to those measured during commissioning (better than  $\pm 2\%$  tilt over a range of  $\pm 50$  mA nominal electron gun operating current). This demonstrated correct operation of the beam bending system, which is a critical aspect in the quality of the measurements that were undertaken in this chapter.

### 6.3 Beam Start-up (Experiment 1)

In this experiment the behavior of the electron gun filament and its associated servo control system is investigated during the beam start-up phase. Since the required operating current of the electron gun filament falls with time (Section 6.1.1), the electron gun filament servo reference current needs to be adjusted accordingly to maintain optimal performance of the servo system. The servo reference value will be referred to as the ‘electron gun aiming level’ in the text. Optimal setting of this value to any servo system affects its performance, particularly during the initial settling time of the control loop to its steady state condition. This is pertinent to this experiment for the investigation of the start-up phase, since precise control of electron gun filament and hence electron beam current is required to maintain beam energy (Section 6.5.3). Therefore the setting of the electron gun aiming level was checked at the commencement of the experiment.

Furthermore, a test data set was measured before the commencement of the experiment to confirm the electron gun control system calibration to ensure the operation within the design specification. In this first experiment the electron gun control system behaviour in the first 5 cGy only of CAX dose was investigated and rest of the beam dose ignored.

#### 6.3.1 Materials and Methods

##### 6.3.1.1 Choice of Electron Gun Aiming Levels

It was decided to use gun servo aiming currents that differed by +/-50 and +/-100 mA from the nominal electron gun filament aiming current set for peak doserate, stability and 2.8 % ‘flatness’ level as specified in the planning system commissioning data for the accelerator used in the experiment. The overall range of +/-100 mA was based on measurements of electron gun filament current *vs.* doserate.

Figure 6-1 shows the operating point chosen on the plot for the nominal electron gun aiming level. The point is not at the exact peak doserate point, since this would be too close to the sharp rising edge of the characteristic and would result in instability should there be any slight negative drift in the operation of the gun servo working point.

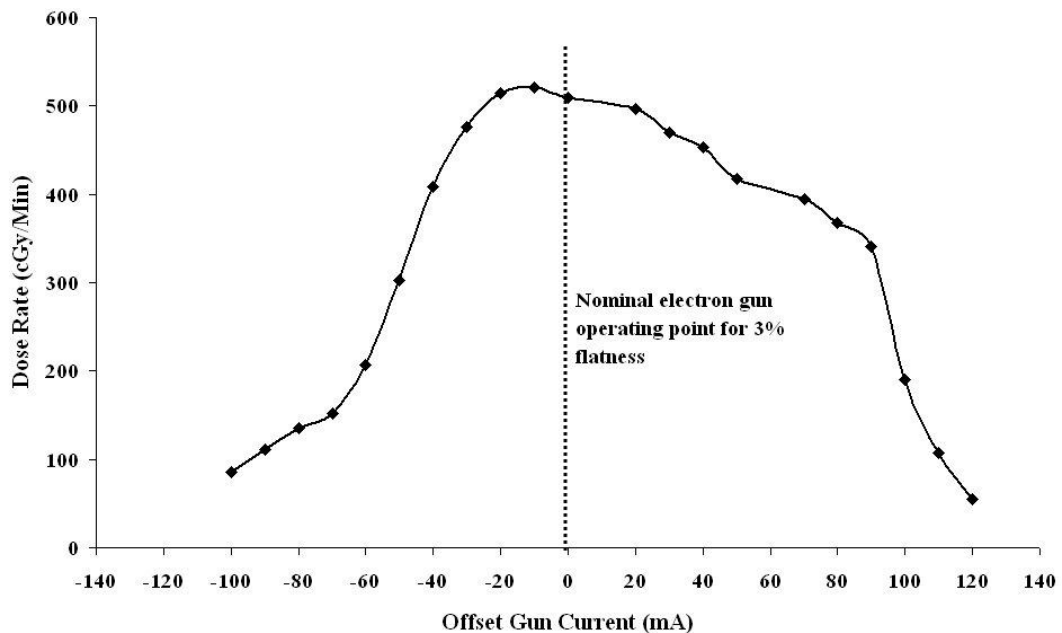


**Figure 6-1:** Doserate plotted for a range of gun filament currents either side of the nominal gun operating point, where a range of +/-100 mA offset reduces the doserate to a near zero value. Data was taken from the commissioning data set for the machine.

At the farthest points (+/-100 mA), the doserate is no more than 20 % of the peak doserate, and there is no useful data to be measured outside this range; this therefore represents the limit of the expected electron gun servo system operating range. The experiment aimed to investigate the ability of the electron gun servo system to maintain the correct electron gun operating current with the electron gun filament aiming levels set to these limit values and two points midway at +/-50 mA, and the effect on the resulting radiation beam.

### 6.3.1.2 'Beam Scope' Configuration

The operation of the gun control system was measured using the 'Beam Scope' system with the ionisation chamber array configured in the GT axis of the accelerator to measure the profile in the beam bending plane and one analogue input configured to record electron gun operating current from a test connector on the machine using the 'Standard Array Configuration'. Radiation beams were measured for each of the electron gun filament aiming levels stated above, as well as a set of reference beams for dosimetric calibration as described in Section 6.3. The data were then processed off-line; the electron gun operating current and beam data were filtered using a low pass 2 Hz windowed sinc filter with a 12.6 Hz cut-off frequency to filter unwanted higher frequency sinusoidal components in conjunction with a 5 point moving average filter to reduce random noise. The results are plotted in Figure 6-2.

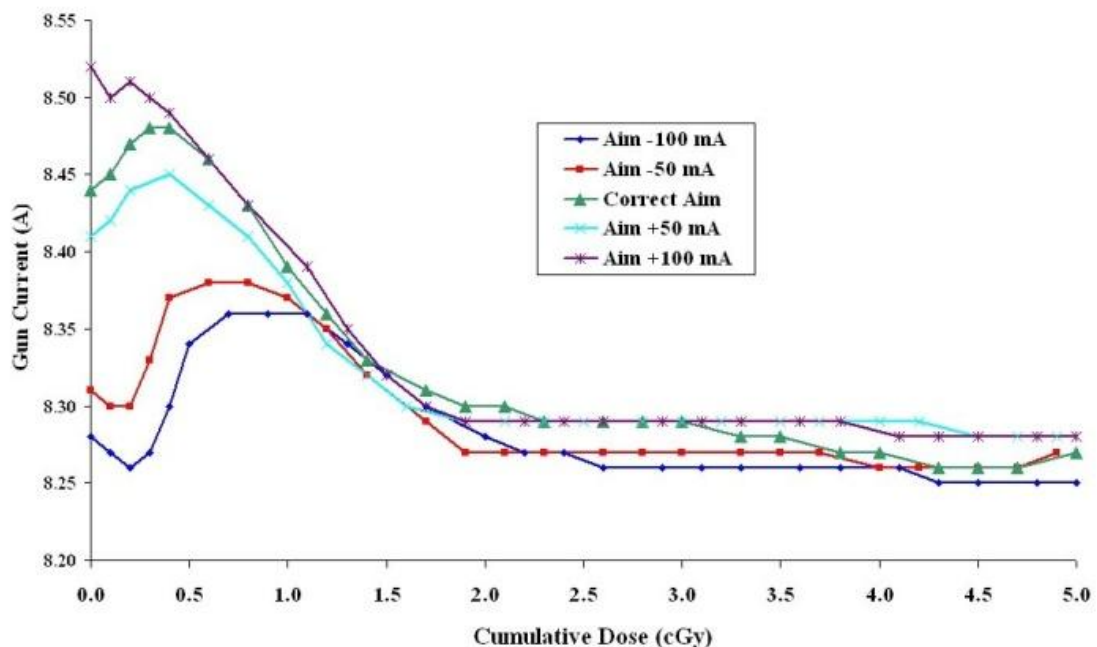


**Figure 6-2:** Electron gun operating current plotted for +/-50 mA, +/-100 mA and the nominal electron gun filament aiming levels. The plot shows that the nominal operating current does not match the electron gun aiming level at the start of the beam.

The electron gun operating current at beam start-up is plotted in Figure 6-2 in green. The electron gun operating current at zero cumulative dose is 8.44 Amperes,

but should be the same as the electron gun aiming level set in the machine control software (8.24 Amperes). The experiment shows a discrepancy of approximately 200 mA between the electron gun filament aiming current set in the machine control software and the actual current presented to the electron gun servo control hardware at 'Beam on'. Furthermore, the operating electron gun filament current can be seen to be settling at the 2 cGy cumulative dose point to a value just greater than 8.25 Amperes, demonstrating that the electron gun aiming current was correctly set in the machine control software. Based on these findings, the electron gun filament aiming current with an offset of -100 mA (plotted in blue) is actually closer to the ideal electron gun aiming level setting for the electron gun servo system. With this error in the electron gun start-up control it was not possible to characterise the machine performance accurately until the problem was located and corrected. A software calibration error in both the 'read back' of the electron gun operating current and the analogue output of the electron gun filament aiming level were found on the machine. The calibration of the gun control system instrumentation is not part of the manufacturer's standard schedule. On the linac used this would normally only be checked during an electron gun replacement or during supplemental in-house planned maintenance checks, performed yearly. A re-calibration of the gun servo instrumentation was performed according to the manufacturer's instructions and the data re-measured using the same configuration and processed as previously. The results are plotted in Figure 6-3.

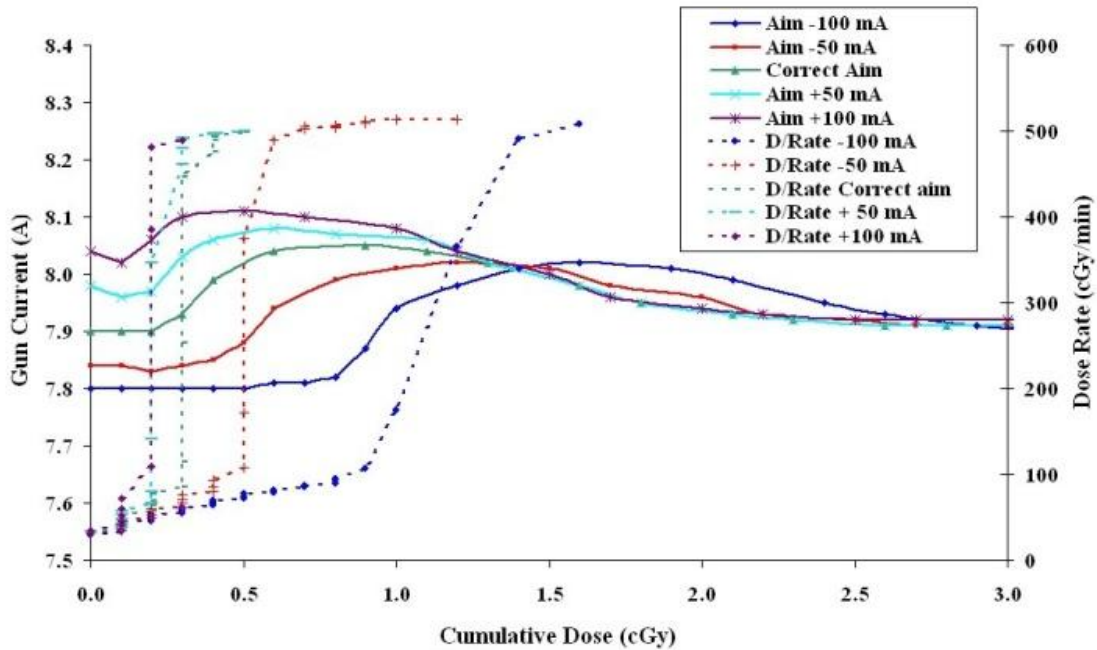


**Figure 6-3: Electron gun operating current plotted for +/-50 mA, +/-100 mA and the nominal electron gun filament aiming levels after recalibration. The plot shows that the nominal operating current now closely matches the correct electron gun filament aiming level (plotted in green) at the start of the beam. The dotted lines denote CAX doserate for each electron gun filament aiming level.**

The nominal electron gun operating current at start-up measured at cumulative dose zero of 7.90 Amperes plotted in green now closely matches the electron gun filament aiming level of 7.92 Amperes and the running current of 7.90 Amperes at 5 cGy cumulative dose.

Before correction, the beam profile would have been sub-optimal during the first 2 cGy (Figure 6-3), since this is where the error in electron gun filament current was greatest. Moreover, since the electron gun filament current was initially too high, due to the gun servo calibration error (Figure 6-2), increased electron beam loading in the accelerator, and therefore reduced beam energy would have resulted. The consequence to the final X-ray beam would be a reduction at the CAX doserate, due to the effect of the flattening filter by the reduced beam energy, as discussed in Section 6.5.3., during the first 2 cGy of beam.

This confirms the correct dynamic operation of the electron gun servo control system, after recalibration, for the nominal electron gun filament aiming level

parameter. Having verified the calibration of the electron gun control system, the same data were used to explore the operation of the system at beam start-up.

## 6.3.2 Results

### 6.3.2.1 Gun Start-up Characteristics

With reference to Figure 6-3, the CAX doserates for each of the electron gun aiming currents have been added to the plot to indicate the initiation of radiation. A shortcoming in the data presented in Figure 6-3 is that the signals are in the dose domain, since this best describes the electron gun start-up characteristics from a dosimetric point of view. This is of most interest when analysing the dosimetric aspects of beam start-up for short segment beams for IMRT step and shoot. However, preceding the radiation start point, where the doserate is zero, there is still valuable control system data to be observed. The 'Beam Scope' measurement system also allows data to be presented in the time domain (Section 5.1.4) which in this case allows the transition of the electron gun filament current from the 'standby level' (4.5 Amperes) to the aiming level to be observed before radiation commences (Figure 6-4). The time domain data is unfiltered to present the gun transition at the highest temporal resolution, since there are only a small number of data samples in the signal at the transition point, which is close to the sampling rate limit of the 'Beam Scope' system.

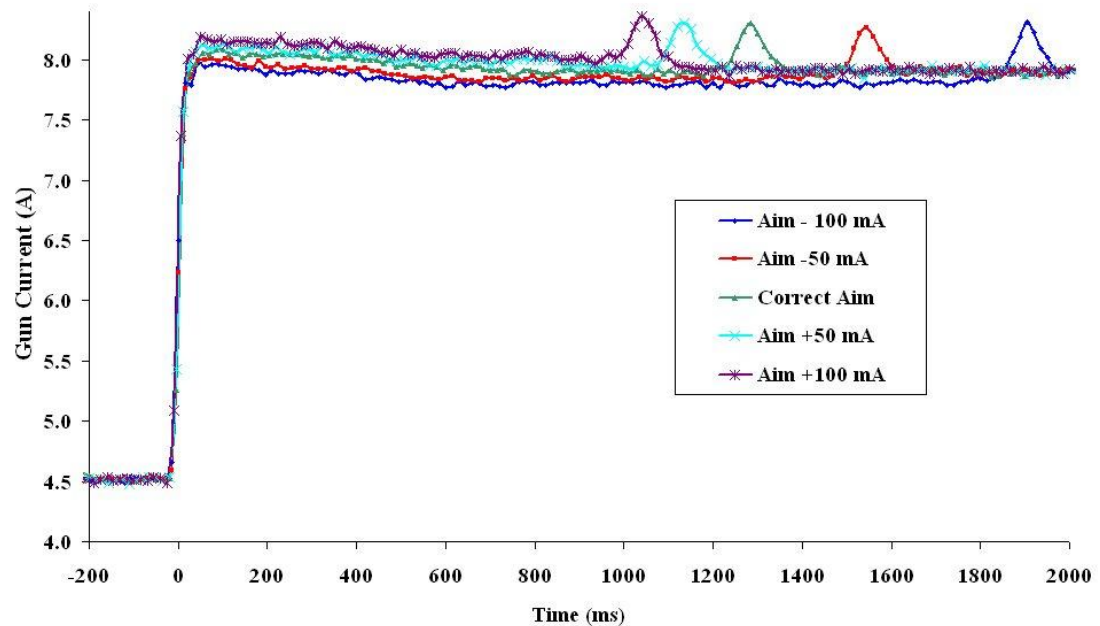


*Figure 6-4: Electron gun start-up presented in the time domain for  $\pm 50$  mA,  $\pm 100$  mA and the nominal electron gun aiming levels. The peaks at the far right of the plot are the points where the electron gun servo takes control of the beam energy and where the transition to peak dose rate commences. The data sets have been aligned along the x axis to the electron gun transition from the standby state.*

If the electron gun operating currents in Figure 6-4 are examined there are the two properties that are prominent:-

Immediately after the transition from the standby value all of the plots, irrespective of the aiming value, overshoot the expected current

There is a time delay in the peaks where the electron gun servo takes control of the beam energy that is dependent on the aiming value set.

Since electron gun filament current overshoots the expected value, the consequences to the final X-ray beam profile would be the same as those discussed at end of Section 6.3.1.2.

### 6.3.2.2 Overshoot

A rescaled version of Figure 6-4 is shown in Figure 6-5, clearly showing the overshoot of approximately 150 mA in the electron gun operating current and the recovery to the aiming current set for each of the experimental values. This effect will be further investigated in Section 6.4.2.

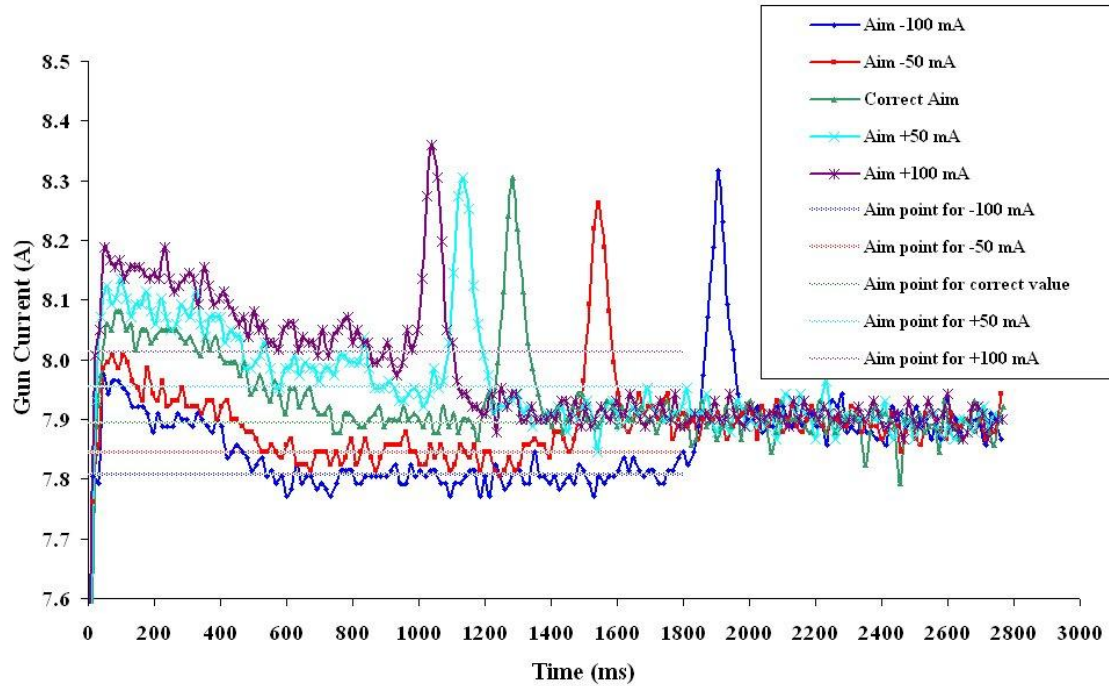


*Figure 6-5: Rescaled version of Figure 6-4 the electron gun aiming levels added based on the mean of values of the plateau just prior to the gun servo takes control of the electron beam energy. Approximately 150 mA of overshoot is evident on each of the electron gun filament aiming level settings between the transition from standby and the electron gun filament aiming level plateau. The data sets have been aligned along the x axis to the electron gun transition from the standby state.*

### 6.3.2.3 Delay

A delay in the transition of the dose rate from the initial starting level of 50-100 cGy/min to the nominal operating value that is dependent on the electron gun filament aiming level used can be seen in Figure 6-3 presented in the dose domain. In the figure, the transition point to the operating dose rate falls inside the peaks of the gun filament current at the point where the servo takes control of the electron beam energy. These peaks are reproduced in Figure 6-4 and Figure 6-5 in the time domain and again represent the transition point to the operating dose rate. There is a difference of nearly 1 second between the electron gun transition from stand-by to aim value at time  $t = 0$  in Figure 6-5 to the peak representing the initiation of the accelerator to the operating dose rate. It was expected that the optimal electron gun filament aiming level would produce the shortest delay, but this is clearly not the case. Other than the gun

filament aiming level, the only signal in the gun servo controller is the error signal generated from the electron gun servo system. Its effect with relation to the time delay will be further investigated in Section 6.4.4.

### 6.3.3 Discussion

If the correct electron gun aiming level is set, the value will be the theoretical optimal for the operation of the electron gun servo system hardware during normal beam running conditions, but not for the start-up period of the beam. This is suggested in Figure 6-5 where aim is set +100 mA above the nominal aiming value, but results in the shortest time for the electron gun servo electronics to take control of the beam energy. The consequences of this are minimal, except for multi-segment IMRT step and shoot beams, where optimisation of the start delay and beam profile is essential (Cheng C W & Das I J., 2002 Mohr P *et al*, 2007 Grigorov G N *et al*, 2006). Setting the aim current higher than the theoretical value appears to enhance operation of the gun servo at beam start-up, this effect needs to be explored in more detail.

In the author's experience, in the past it was common practice to set the electron aiming current level higher than the nominal value. This was done to force the electron gun servo to operate correctly should the machine fail to transition from the start-up state of 50-100 cGy/min to the peak dose rate state to cure a then undiagnosed problem which was eventually traced to a fault in the beam monitor chamber energy discrimination plates. The fault condition would cause the 'low dose rate' interlock to be triggered after its timeout period was exceeded. This is very similar to the delay effect noted in the experiment where the time taken for the gun servo error to reduce to zero was decreased by raising the electron gun filament aiming current level above the nominal value.

## 6.4 Further Investigation into Beam Start-up Effects

### 6.4.1 Materials and Methods – Overshoot Effect

The same experimental set-up as described in Section 6.3.1.2 was used to further investigate the ‘overshoot’ artefacts found in experiment 1. To ascertain where the overshoot was introduced in the start-up sequence, the gun filament current was again re-measured, but this time using the gun standby value to simulate the start-up transition (the accelerator in the beam off state), thus removing any gun servo control error signal from the measurement. The electron gun standby current in the accelerator service mode option was changed from the nominal 4.5 Amperes to the 7.9 Amperes (nominal electron gun aiming level), therefore measuring only the step transition, without any contribution from the gun servo system.

### 6.4.2 Results – Overshoot Effect

Using the standby value to simulate the transition of the electron gun filament current from the standby state of 4.5 Amperes to the nominal aim level produced an overshoot of only 58 mA (2 SD = 5 mA) compared with mean overshoot at beam start-up for the beam measured in Figure 6-5 of 144 mA (2 SD = 27 mA).

### 6.4.3 Discussion – Overshoot effect

The results suggest that some element of the overshoot is inherent in the physical characteristics of the electron gun filament resistance (58 mA) and the rest (86 mA) is produced by the error signal from the gun servo at beam start-up, resulting in a total of 144 mA as presented in Section 6.4.2.

An overshoot following a large step transition is expected, since the electron gun filament resistance at the standby current of 4.5 Amperes is lower than when the filament is at its operating temperature during X-ray production, which requires an operating current in the range 7.5 to 8.3 Amperes (dependent on the electron gun filament age as described in Section 6.1.1.) Typical resistance values for the Elekta

electron gun at standby and ‘beam on’ are  $0.5 \Omega$  at 11 Watts and  $0.9 \Omega$  at 60 Watts respectively (Figure 6-6)

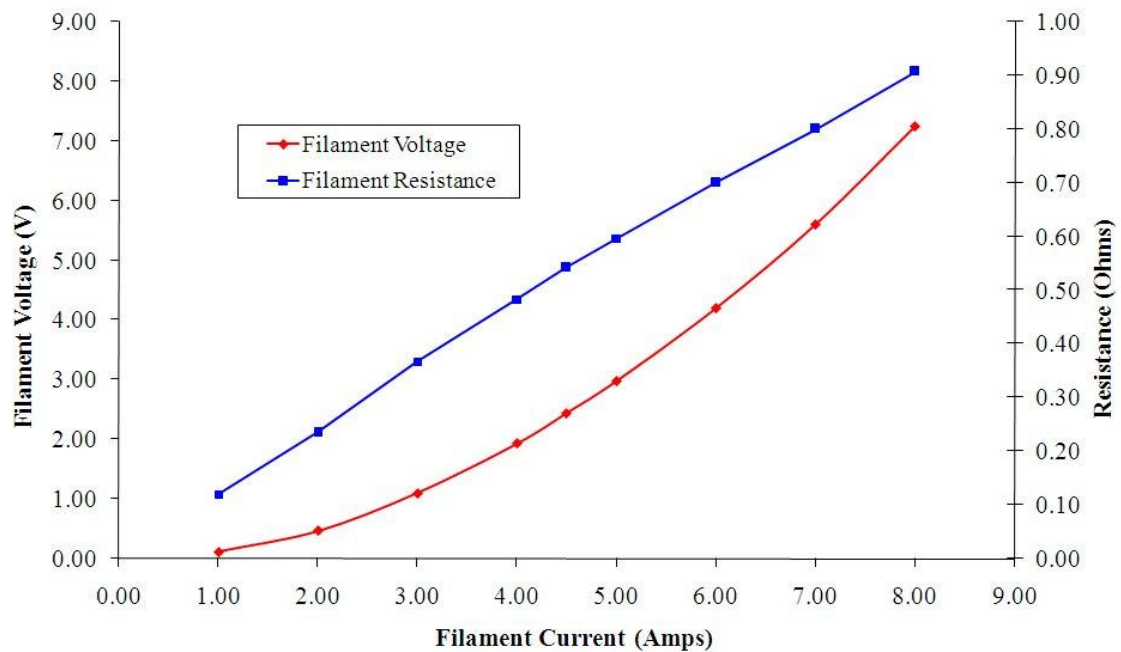


*Figure 6-6: Typical electron gun filament current/voltage characteristic and calculated resistance. The data was taken from the author’s notes on gun filament replacements (2002); the test filament was under a vacuum of approximately  $5 \times 10^{-5}$  mbar.*

At the transition from ‘standby’ to the ‘electron gun aiming level’ state, the thermal lag in the filament results in a current surge and therefore a current overshoot until the resistance settles at the final operating temperature. The reason for the additional overshoot produced by the gun servo control system is unclear, and needs further investigation; however, it may be caused by the control system compensating for any increased mean beam energy of the electrons that pass through the beam bending magnet during the electron gun start-up transition.

#### 6.4.4 Materials and Methods - Delay Effect

The delay mentioned earlier was investigated further. An experiment using the same experimental set-up as described in Section 6.3.1.2 was used to further investigate the ‘overshoot’ artefacts found in experiment 1. An additional analogue channel on the ‘Beam Scope’ was configured to measure the output signal from the

high gain error amplifier on the accelerator gun servo control PCB by means of a test point and 10:1 oscilloscope probe (See Section 3.9.1). This signal is derived from the ionisation chamber energy monitor plates in the accelerator's radiation head. The signal from this stage, after further processing, is 'summed' with the electron gun aiming level to form the final signal that sets the electron gun filament operating current. Data were measured for the correct aim current and +/-100 mA aim offset.

#### 6.4.5 Results – Delay Effect

The raw data are presented in Figure 6-7. The error control signal can be seen to follow the electron gun transition from the standby state.

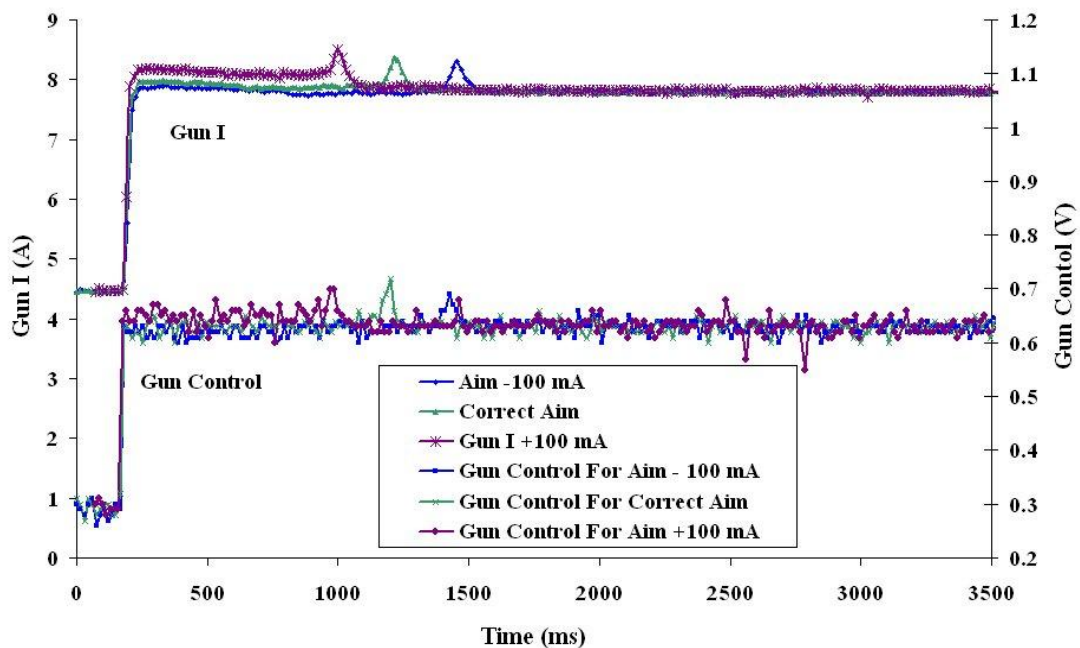


**Figure 6-7:** Raw signal from the output of the high gain error amplifier in the electron gun servo and the resulting electron gun filament current plotted for the correct aim and +/-100 mA offset. The X axis origin is arbitrary to show some pre-electron gun transition data.

The signal level changes from approximately 0.3 V for all the electron gun aiming values plotted, to values spread around 0.62 V dependent on the electron gun aiming level set. Having confirmed the progression of events in the beam start-up process, the signals were filtered and rescaled to exclude the signal prior to the electron gun transition to enable the sequence to be examined in greater detail; these

are presented in Figure 6-8. The data sets are also aligned to the transition to peak doserate from the start-up state of 50-100 cGy/min to allow direct comparison.

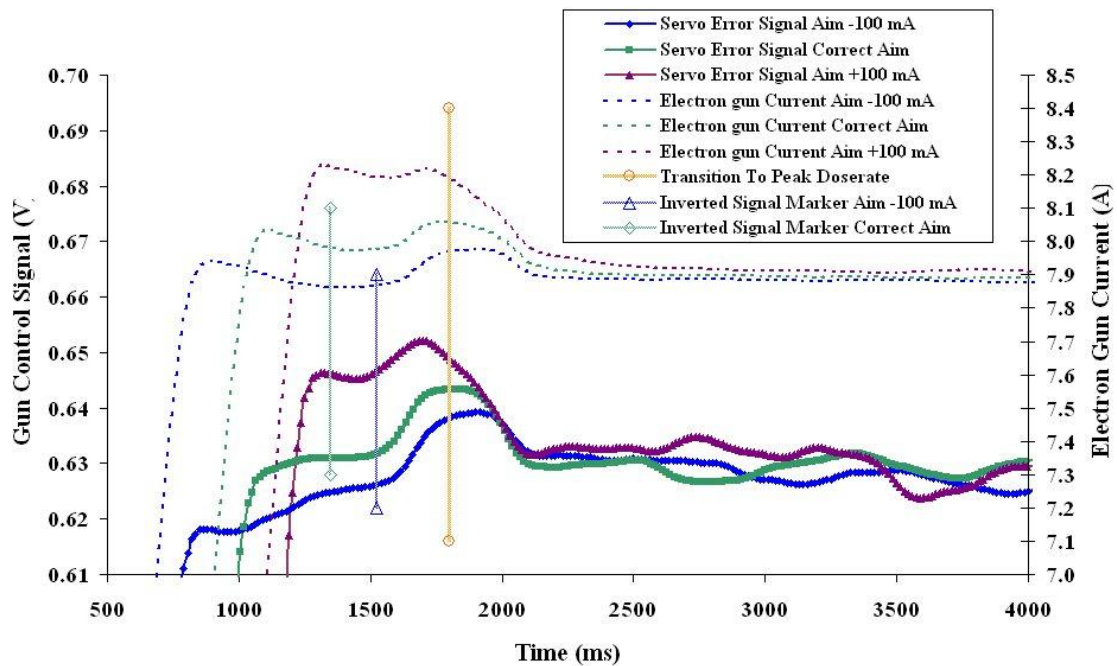


*Figure 6-8: Filtered signal from the output of the high gain error amplifier in the electron gun servo plotted for the correct aim and +/-100 mA offset. The data sets have been aligned along the x axis to the doserate transition to peak doserate from the start-up state of 50-100 cGy/min. Markers are positioned on the plots to highlight points of interest.*

#### 6.4.6 Discussion – Delay Effect

The experiment shows that with the aim set higher than the nominal value, the gun servo error signal closely follows the measured electron gun filament current, successfully compensating for start-up conditions as the electron beam energy settles. This occurs in the shortest time period of the 3 measured beams and thus demonstrates the optimal gun servo response for the experimental values. As the electron gun filament aiming value is reduced, the gun servo error signal increases causing a feedback component that opposes the expected electron gun filament current as shown in Figure 6-8 preceding the blue and green ‘inverted signal markers’ presented in the figure for the ‘nominal’ and ‘-100 mA’ electron gun filament aiming values. This results in a time lag in reducing the error in the gun servo loop to a low enough value

to produce the correct electron gun operating current for peak dose rate and beam flatness. This observed output response suggests that as the electron gun filament aiming value is reduced, the servo system intercepts the energy discrimination control response too early during the start-up condition. In the Elekta SL series accelerator, electron beam energy discrimination is achieved by producing a difference signal from a pair of concentric ionisation plates enclosed within the beam monitor chamber in the radiation head of the accelerator (Loverock L, 2007). This arrangement produces the classical 'S' characteristic curve with the gun servo operating in the central region of the response. Should the operating point intercept the curve before the 'S' curve peak, then the control function will be inverted. This appears to be the case in this experiment.

#### **6.4.7 Summary**

A disparity in the theoretical and optimal electron gun aiming level values has been identified on the accelerator under test for small segment beams. Raising the electron gun filament aiming current above the optimal value actually enhances the electron gun control system response. This effect was identified, but not explained, in the work by Hansen V N *et al*, 1998., which illustrates the purpose behind the development of the 'Beam Scope' system.

To complete the investigation, the dosimetric properties during the beam start-up phase and total set dose will be tested for comparison with literature in the field, as ultimately, it is the accuracy of patient dose that is important in short segment beams for the delivery of step and shoot IMRT radiotherapy.

### **6.5 Dosimetric Evaluation (Experiment 2)**

#### **6.5.1 Materials and Methods**

In the second experiment, the electron gun control system behaviour was considered over total accelerator set dose values of 2, 3, 4, 5, 10, 20, 50, and 100 cGy.

The effect on the total dose delivered to the CAX was measured. The same 'Beam Scope' experimental set-up as described in Section 6.3.1.2 was used.

## 6.5.2 Results

### 6.5.2.1 Using the Correct Electron Gun Aiming Value

The results for the CAX dose channel are presented in Figure 6-9 where the dosimetric error is better than 1 % for beams greater than 5 cGy, with the error increasing steeply for doses below this value. The figures closely match those reported, for the same accelerator type (Hansen V N *et al*, 1998, Moon-Sing Lee *et al*, 2004).

Electron gun filament current and flatness were also measured to assess the electron gun servo performance. Figure 6-10 shows the electron gun filament current settling to its steady-state during the first 5 cGy of cumulative dose after the initial peak.

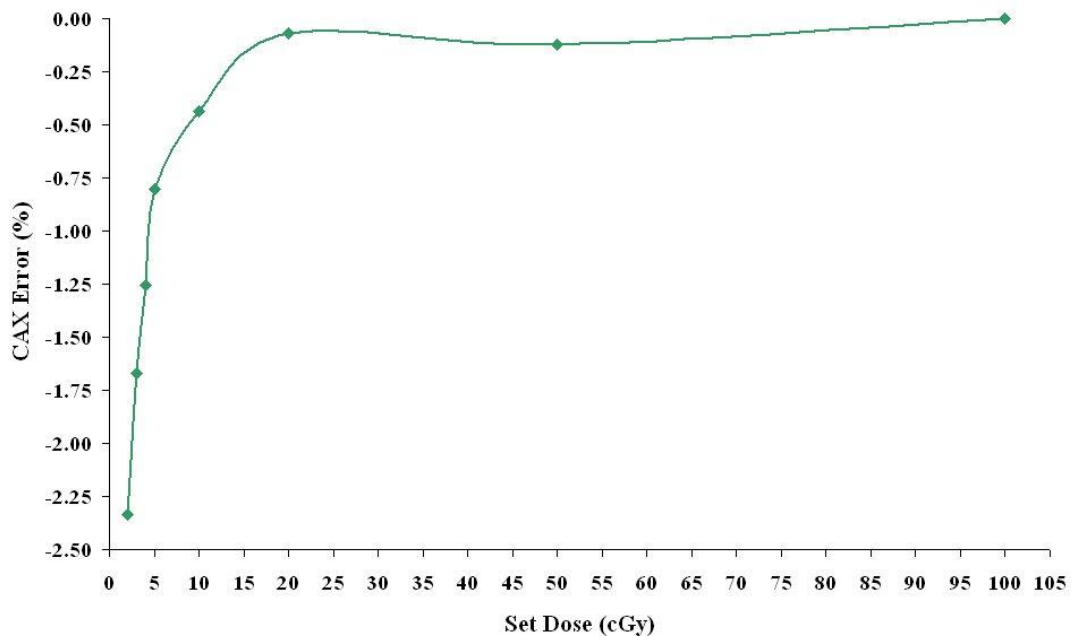


**Figure 6-9: Central Axis dose error for 2, 3, 4, 5, 10, 20, 50, and 100 cGy with the correct electron gun aiming current value.**

The initial peak results in a reduction in the mean electron beam energy, confirmed by the reduction in flatness also plotted in Figure 6-10, and thus the fall in

the dose at the central axis as shown in Figure 6-9. The peak dominates the CAX doses during first few cGy, since the electron gun servo is under high workload during this time.

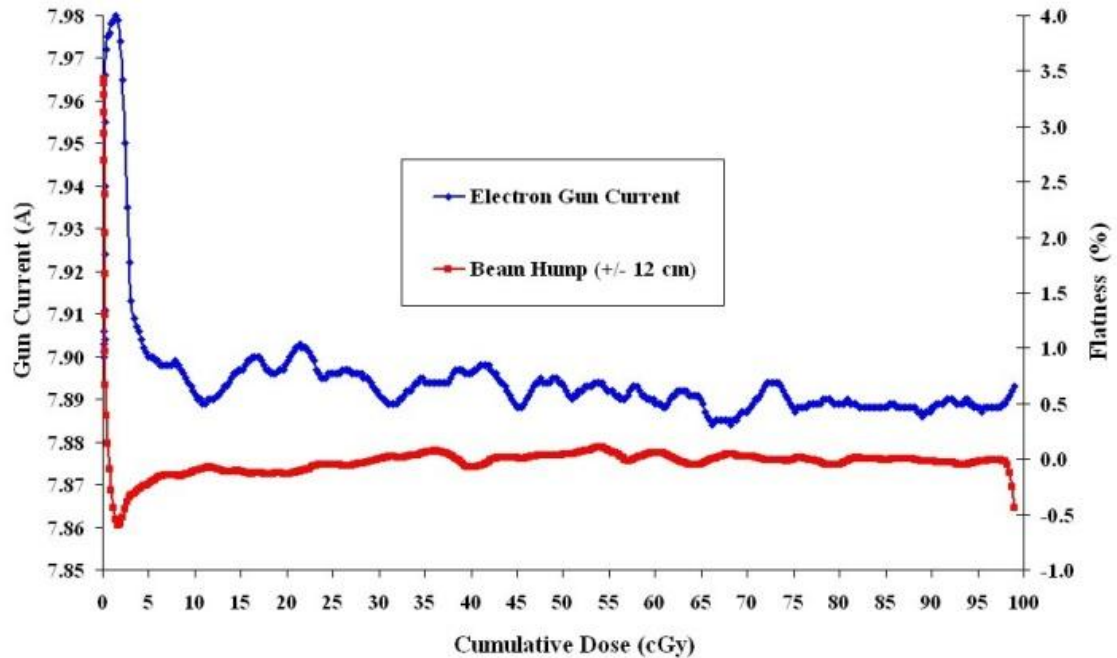


*Figure 6-10: Electron gun filament current and beam ‘Flatness’ for the correct electron gun aiming current value.*

### 6.5.2.2 Incorrect Electron Gun Aiming Values

After considering just the CAX measurements, the effect of the offset electron gun aiming level values were included (Figure 6-11) to observe how this alters the control response. As the electron gun aiming level increases from the aim of -100 mA, the dosimetric error improves. There is some correlation between the dosimetric error and the delay time depicted in Figure 6-5, and again the optimal electron gun aiming current level does not give the shortest delay time. The gun servo settling time dominates the short segment beams, particularly with the aim -100 mA electron gun aiming level setting.

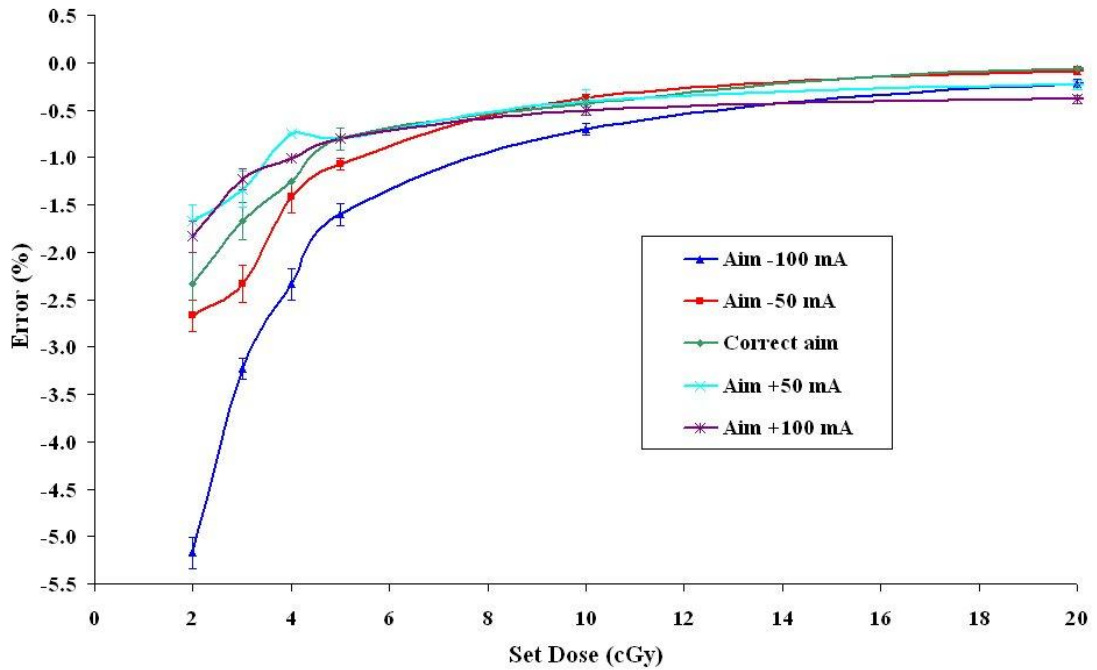


**Figure 6-11:** Central Axis dose error for 2, 3, 4, 5, 10 and 20 cGy for +/-50 mA, +/-100 mA and the nominal electron gun aiming current value.

As the electron gun filament current settles to its steady-state value, an error produced by the sub-optimal electron gun aiming current value begins to dominate the electron gun filament current (Figure 6-12, set dose of 20, 50 and 100 cGy). It might be expected that the electron gun control system would 'servo' this error to zero, and thus the CAX dose plots in Figure 6-11 would converge, but this is not the case. Although the error may eventually servo to zero if enough dose is delivered, this effect could also be due a 'steady-state' error in the gun servo response. In this case, the steady-state error is defined as the difference between the aim (required value) and the electron gun operating current (resulting value) as time tends to infinity. This inability to drive the error to zero is a known phenomenon caused by lack of gain in the integral component of a Proportional Integral Derivative (PID) control system. Proportional and integrator functions are contained within the gun servo electronics of the accelerator, and there is no obvious derivative component.

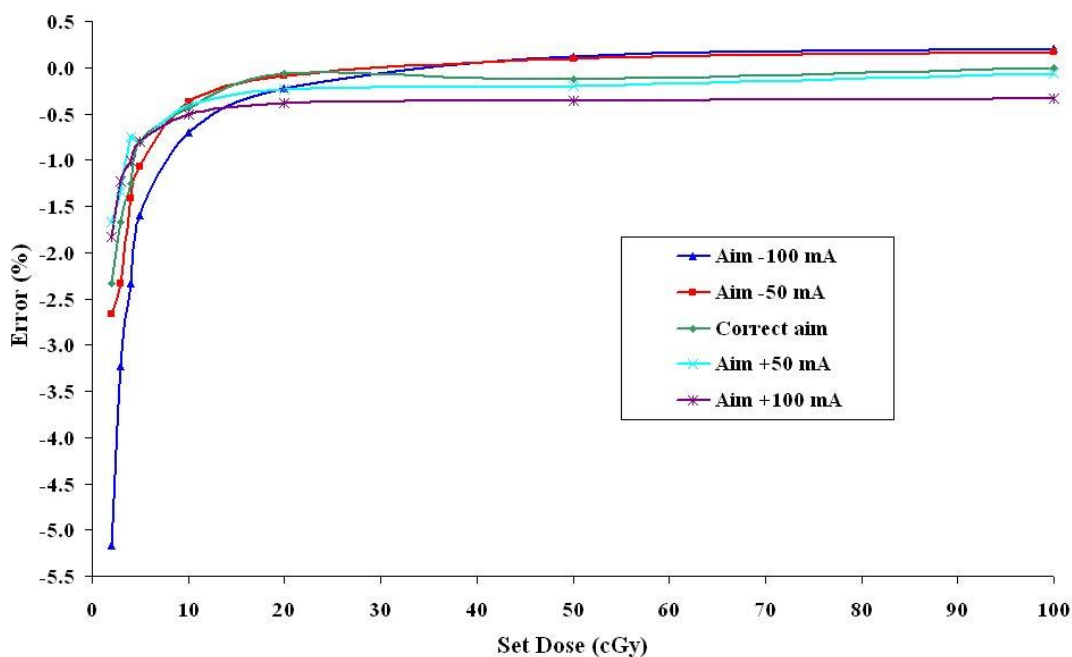


*Figure 6-12: Central Axis dose error for 2, 3, 4, 5, 10, 20 and 100 cGy for +/-50 mA, +/-100 mA and the nominal electron gun aiming current value.*

If the electron gun filament current and flatness data from the same 100 cGy beam are examined, the development of the steady-state error in the electron gun control system is made clear where the electron gun filament current (Figure 6-13) and flatness (Figure 6-14) for incorrectly set electron gun aiming levels also fail to converge.

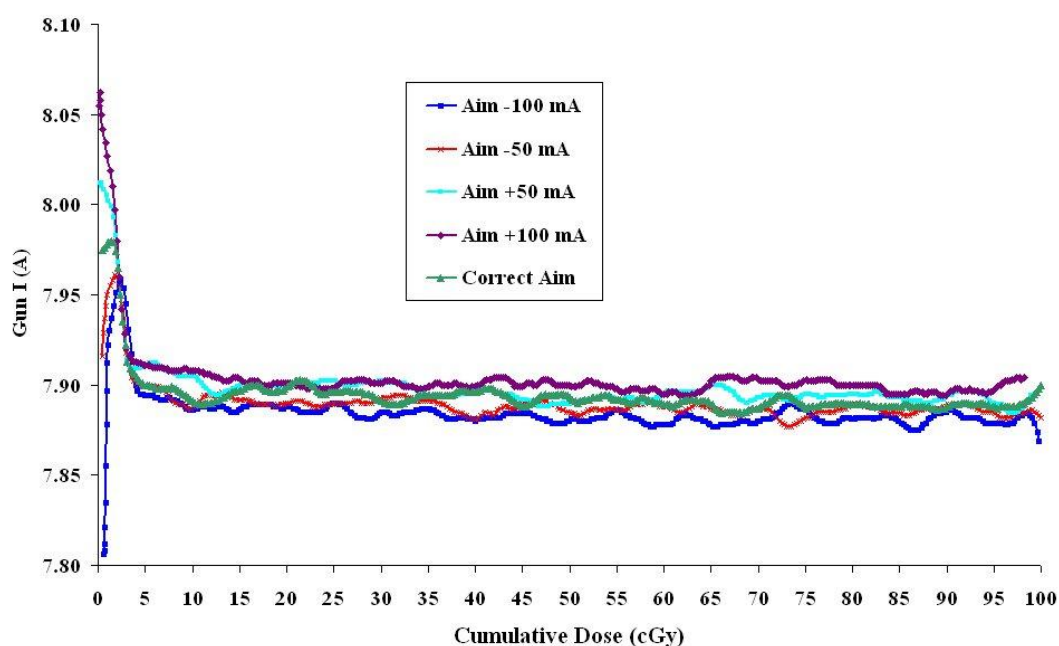


*Figure 6-13: Electron gun filament current for a 100 cGy beam showing the steady-state gun error produced by offsetting the electron aiming current.*

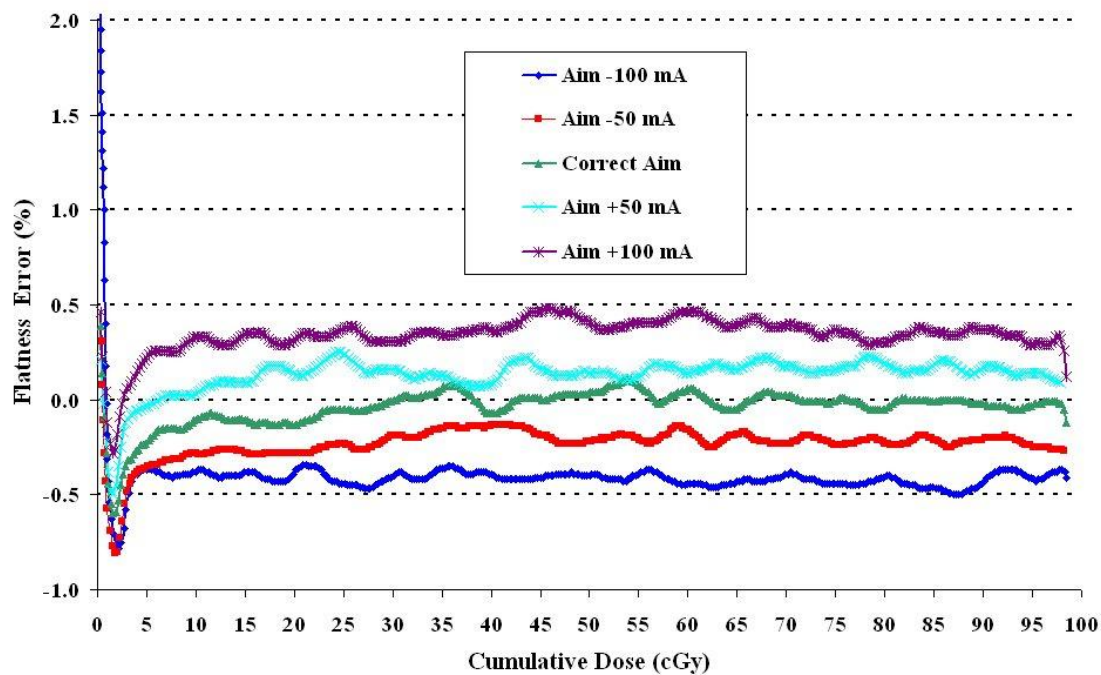


*Figure 6-14: Flatness error, from the nominal 2.8 % commissioning value, resulting from the steady-state electron gun error plotted in Figure 6-13. The Y axis grid is shown to reveal the zero flatness error for the correct electron gun aiming level (plotted in green).*

At beam termination, the result is a small dose error at the central axis depending on the electron gun aiming level set, as plotted in Figure 6-15.

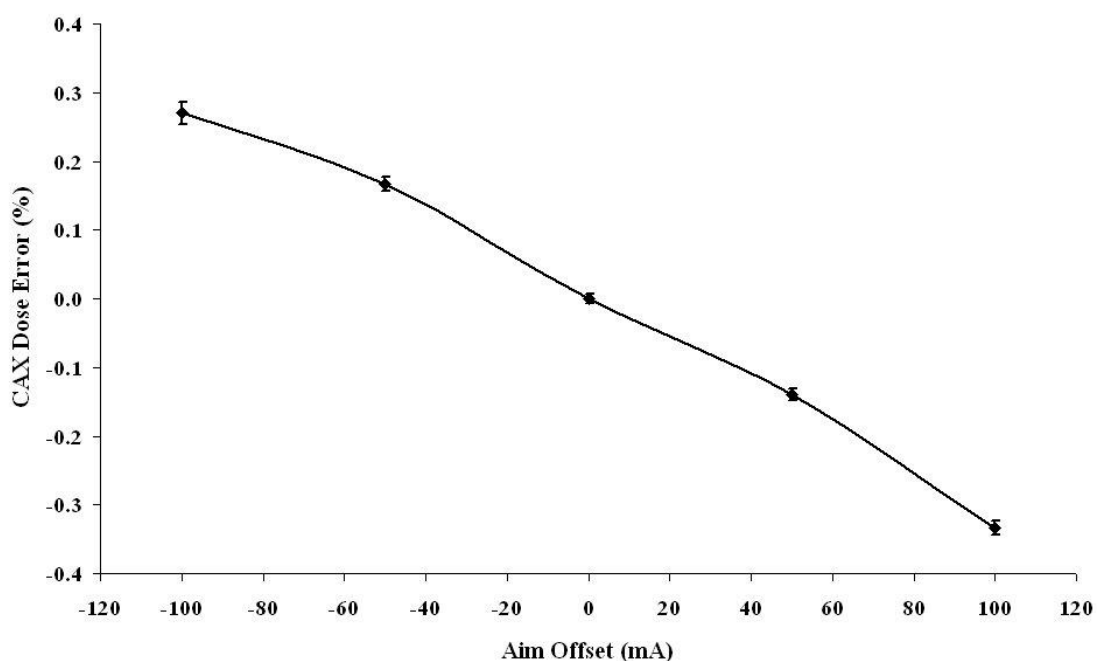


*Figure 6-15: Dosimetric error produced at the CAX of a 100 cGy beam resulting from the steady-state gun error plotted in Figure 6-13.*

Examining the case for reducing the electron gun aiming current (by -50 and -100 mA), these result in a negative steady-state error of the operating electron gun filament current, causing the mean beam energy to increase and therefore the CAX dose also to increase due the effect of the flattening filter.

### 6.5.3 Discussion

The gun filament current controls the electron emission from the gun and hence the number of electrons entering the accelerating waveguide. For a fixed microwave power flux in the waveguide, the electron gun filament current and therefore electron beam current, is the major factor that determines the final energy (Loverock L, 2007) of the electrons striking the target and consequently the distribution of the resulting X-ray beam. To produce a clinically usable beam, a cone-shaped filter is used to flatten the radiation field to a user specification. Currently, the clinical use of un-filtered beams is under investigation as the dose rate available is greater and beam energy effects caused by the filter are avoided (Cashmore J, 2008). The 'Beam Scope' would be a useful tool for investigating accelerator and control system behaviour in this field of research, although its exploration is beyond the scope of this thesis.

Attenuation by the cone filter is greatest at the central axis, resulting in greater sensitivity to energy and thus greater variation in X-ray flux at this point compared with that at the filter periphery. Any deviation from the nominal energy will result in a dosimetric change at the central axis. Since the linac monitor chamber covers the whole of the beam area, the linac dosimetry system will average out this error, resulting in the set beam dose being correctly delivered, but with non-uniformity across the beam axis.

## 6.6 Conclusions

The properties of the energy control system have been investigated at beam start-up using 'Beam Scope'. Although the data is only representative of one machine, a great deal of care was taken to ensure the accuracy, setup and calibration of all the beam control systems to avoid systematic errors in the results. Measurements were extended to longer beams of 100 cGy to reveal a steady-state error condition found in the electron gun filament operating current that resulted in a small dosimetric error at the central axis depending on the electron gun aiming level set.

The most obvious finding to emerge from the experiments was the effect that the electron gun filament response had on the start-up characteristics of the first few cGy of beam due to stabilisation effects after the initiation of the electron gun to its aiming level. The thermal time lag in the filament response appears to be a major factor in the inability of the servo to optimally drive the gun servo error to zero to produce the correct electron gun aiming conditions at beam start-up. In fact, raising the electron gun filament aiming current above the optimal value actually enhanced the response as was seen in Figure 6-2, where the mis-calibration of the gun servo instrumentation resulted in an effective high aiming level with stable dose rate and 'flatness'.

The aging of the electron gun filament requiring the aiming level current to be reduced over time (as discussed in Section 6.1.1) does at least favour the electron gun filament operating point, as the aiming value is actually higher than required. This is advantageous for short duration beams as discussed above. Taken together, these results suggest that the electron gun filament aiming current should be checked on a regular basis in the engineering PPM schedule or if beam QA consequences can be identified, when changes in beam QA might indicate it. Also, before any issues with the primary dosimetry system are investigated, the flatness profile and electron gun servo operation for both short and long segment beams should be confirmed.

The application of the 'Beam Scope' system to the measurements made in the above experiments demonstrates its usefulness in enhancing our understanding of the dynamic conditions that occur during the beam start-up sequence of an energy control system in a medical linear accelerator. The application of test instrumentation that offers the engineer a greater understanding of the properties and operational characters of a dynamic system is crucial in the development and safe operation of complex accelerator technologies in medicine.

## Chapter 7. Secondary Radial Steering During Rotation

### 7.1 Introduction

In this chapter the use of the ‘Beam Scope’ system to characterise the performance of the secondary radial steering system during gantry rotation is described. Control system behaviour is examined during clockwise and anti-clockwise rotation of the gantry, as would happen during the delivery of dynamic volumetric arc therapy beams. Measurements were made in the GT axis of the radiation beam, since the radial steering system has maximum influence on electron beam transport within the accelerator in this axis. Five experiments were performed to examine and characterise the performance of the secondary radial steering system during gantry rotation. These experiments were to:

1. Confirm the measurement system connection to the accelerator and measure the radial steering current in steps of 10 units. Verify that the machine calibration is in order, and that 1 unit change in the accelerator software results in 1 mA change in current in the radial steering coils. Show any artefacts in the machine instrumentation. (Radiation off)
2. Measure the accuracy of the radial steering system without gantry rotation. Compare the measured data to that taken at machine commissioning to demonstrate the functional performance of the ‘Beam Scope’ measurement system. (Radiation on)
3. Reveal the current look-up table values as described in Section 7.2 used by the radial control system and identify any hysteresis and artefacts that may be present during clockwise and anti-clockwise rotation. (Radiation off)
4. Measure the radial control current under servo conditions. Show the system performance under clockwise and anti-clockwise rotation of the gantry with two appropriate rates of rotation. Illustrate any artefacts in the data. (Radiation on)

5. Measure and examine one possible cause of radial displacement in the waveguide during rotation to confirm any correlation with the radial control current under servo conditions measured in experiment 4.

As mentioned in Chapter 6, the term ‘Servo’ is used in this chapter to describe the secondary radial control system, which is known in the machine dialog as the ‘2R Servo’. The word servo is a shortened term for servomechanism which implies some mechanical element. Again, there is no such function in the 2R control system of the machine, but the word has been adopted by the manufacturer to describe all ‘closed loop’ control systems on the accelerator.

### **7.1.1 Measurement Conventions**

For the Elekta SL series machine used in the experiment, all references in the text to ‘tilt’ and ‘symmetry’ refer to the difference between the G and T sides of the ‘Beam Scope’ array at the +/-12 cm points from the CAX using the ‘Standard Array Configuration’. These points will be referred to as G12 and T12. Additionally, CW rotations start from -180 degrees and ACW rotations from +180 degrees.

## **7.2 Technical Overview**

The Elekta SL series accelerator uses two pairs of electromagnets within the electron beam transport system of the accelerator for beam steering. The first coil pair (named 1R and 1T) is close to the electron gun at the injection point into the accelerator and aligns the electron field emitted from the gun to the centre of the accelerating axis. The second pair (named 2R and 2T) is positioned midway along the accelerating structure to control the beam entry into the beam bending system. The coil pairs are orthogonal to each other and provide ‘radial’ and ‘transverse’ correction to the electron beam to afford optimal transport along the accelerating axis to produce

a uniform treatment field to a known specification. The correction required is sensitive to external influences, such as the local magnetic field in the treatment room. These are considered to be constant, and are therefore stored in a lookup table to limit the workload on the beam steering system. In fact, the secondary transverse correction (2T) is provided exclusively by the lookup table. Both the 2R and 2T control systems are described as servo controlled systems in the machine documentation, but only the secondary radial system (2R) has a feedback component from the monitor ionisation chamber in the radiation head to provide dynamic correction, while the gain component of the 2T servo is set to zero. The required current at beam on is calculated in the accelerator control software by summing the aiming value, the lookup table value for the current gantry position and any error contribution from the servo control system feedback (2R only).

Six lookup tables in steps of approximately 3 degrees are provided in 3 radial/transverse pairs for low, medium and high energy beams. A lookup table is created by setting the control software for the chosen servo into ‘learn’ mode, where the table contribution to the control function is disabled. Whilst the gantry is slowly rotated one full cycle, the machine control software records the 2R value required to drive the servo error to zero into the table, in steps of approximately 3 degrees.

## **7.3 Fundamental Operation (Experiments 1 and 2)**

### **7.3.1 Materials and Methods**

To form a firm foundation for understanding the behaviour of the electron beam under the influence of secondary radial (2R) steering during gantry rotation, an experiment was performed using a static gantry position. The ‘Beam Scope’ was setup with the ionisation chamber array configured in the GT axis to measure the profile in the beam bending plane of the accelerator using the ‘Standard Array configuration’. One analogue input was connected to a test output on the machine and calibrated to record the current flowing in the 2R coils. The same 2 Hz windowed sinc filter as used

in the electron gun data (Section 6.3.1.2) with 12.6 Hz cut-off frequency and 5 point moving average filter was applied to the 2R signal to remove unwanted noise and high frequency artefacts. A set of 100 cGy reference beams was then measured for dosimetric calibration. The 2R servo control system was set to manual operation and the radiation was measured whilst manually stepping the 2R current, by means of the 2R aiming value, in 10 mA steps using the service mode application on the accelerator.

Beams were measured with the gantry initially driven to zero degrees, using the mechanical gantry scale pointer, from both clockwise and anti-clockwise directions, to assess any hysteresis in the accelerator's readout instrumentation. The start and end angles were extended by 2 degrees, such that a CW rotation would start at -182 degrees and end at +182 degrees to minimise effects from gantry acceleration and deceleration. The extended start and end angles used in the experiment guaranteed that the gantry rotation speed was constant between the angles of +/-180 degrees since the mean number of 'Beam Scope' data samples measured per degree (Table 7-1) was constant.

### **7.3.2 Results and Discussion**

#### **7.3.2.1 Experiment 1 (Artefact in the 2R Current Data)**

Examination showed an artefact in the 2R current data set. A short sample of data is presented in Figure 7-1, showing spurious short pulses randomly occurring in some of the 10 unit steps.

It was noted when the experimental data was collected that the 2R aiming level read back in the service mode software was also randomly flipping in short bursts to an undefined value as the step values were entered during the experiment. On further examination, it became clear that the presence of the artefact was present depended on the gantry rotation direction before setting it to zero degrees. A clockwise rotation

would always remove the artefact from the signal and an anti-clockwise origin would always manifest the artefact.

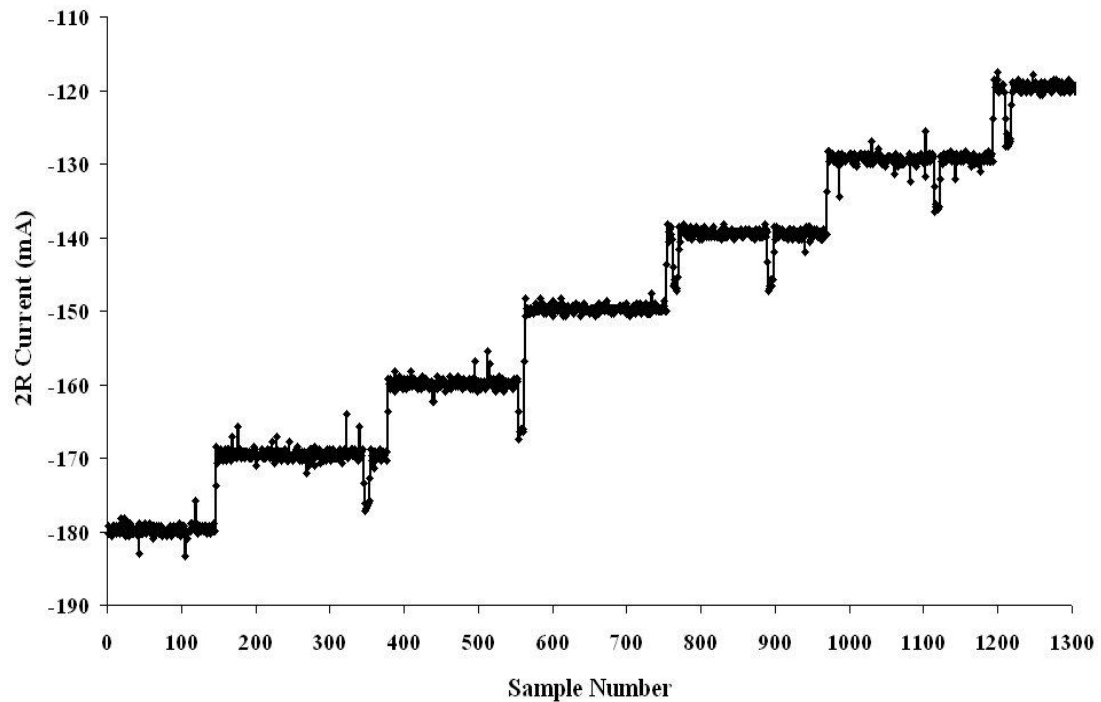


*Figure 7-1: Sample of the resulting 2R current from the 10 mA steps generated in the experiment showing the artefact noted from the anti-clockwise rotation to zero angle.*

An overall mean of the differences in the 2R current steps in Figure 7-1 of 9.99 mA (2 SD = 0.01 mA) confirms the calibration of the out-going radial control signal from the accelerator, since each step of 10 units results in 10 mA of current measured in the radial steering coils and that the ‘Beam Scope’ is correctly calibrated to the accelerator.

Although the gantry was stationary during the experiment, there is a link between the manifestation of the artefact and the origin of the gantry before it was set to zero degrees for each beam in the experiment. Gantry position and radial current are linked by the radial look-up table in the machine software. The look-up table is indexed using a digitised value from the gantry readout system on the machine to present the ‘learnt’ optimal 2R aiming value for the current gantry position to the radial servo control system.

If hysteresis were present in the gantry positioning readout system mechanical gear train between clockwise and anti-clockwise rotations, and the anti-clockwise position settled at the index pointer threshold, then a noisy signal in the generation of the radial lookup table index pointer from the gantry readout hardware on the accelerator would account for this effect. This would not be present if the gantry was initially rotated from a clockwise position. This will become clearer later in the text when the behaviour of the lookup table is investigated in more detail (see Section 7.4.3.2).

7.3.2.2 Experiment 2 (Effect on GT Tilt and CAX Doserate)

The mean of the data for each of the 10 mA steps of 2R current is plotted against their associated CAX doserates (light blue) and symmetry values (red) and is presented in Figure 7-2 as measured by the ‘Beam Scope’.

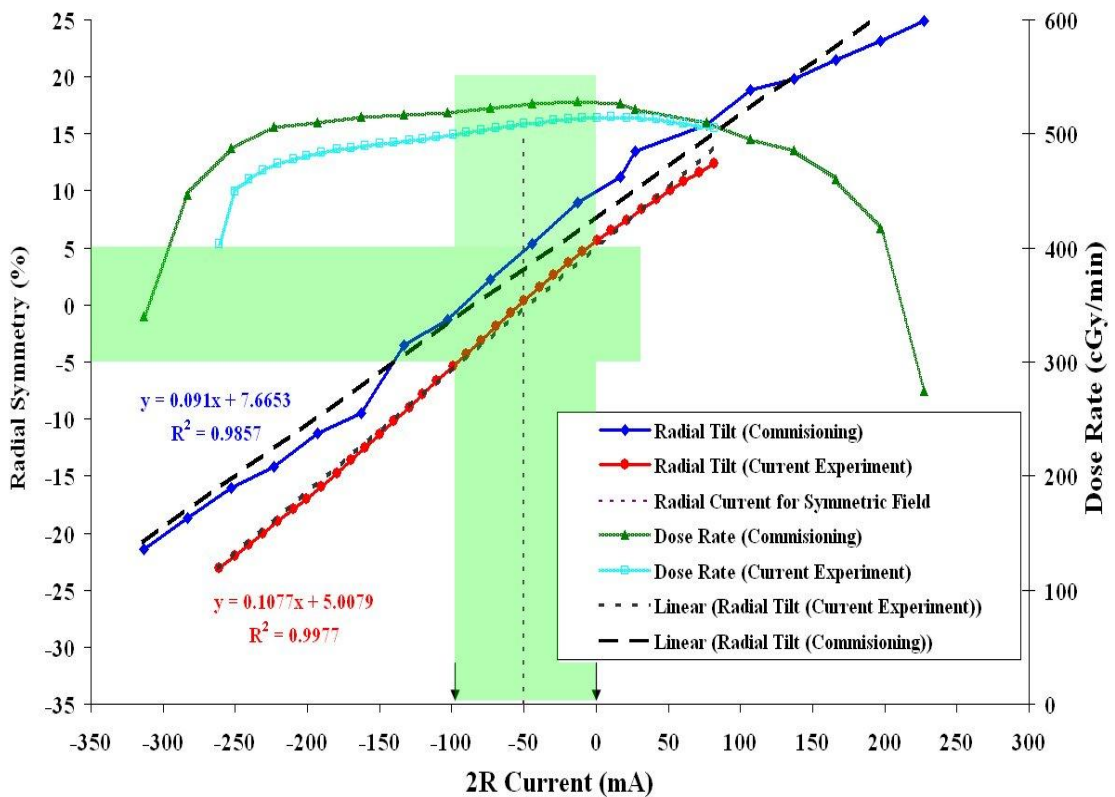


Figure 7-2: The effect of 2R current on radiation symmetry and doserate in the GT axis. The data measured by the author at machine commissioning has been included for comparison. The linear regression line is plotted for the tilt in GT symmetry for the experiment to demonstrate its close proportionality to current. The dotted vertical line shows the 2R current required for GT axis symmetry.

The values measured by the 'Beam Scope' system are similar to those taken at commissioning for the machine used in the experiment. The plot demonstrates a near linear relationship between 2R current and tilt in beam symmetry with a regression line slope of 0.9977 for the experiment and 0.9857 for the commissioning data.

A 2R current of approximately -50 mA (indicated by the dotted vertical line) results in a symmetrical beam profile that is close to the centre of the peak operating dose rate for the experimental data. The commissioning value plot, though results in a value closer to -100 mA for zero symmetry error. This change is due to an adjustment made early in the operating life of the machine. The 'trim' current in the final bending magnet, or 'bending fine' as it is known for the accelerator under examination, was adjusted to optimise the radiation light field alignment. This change resulted in a new value of radial correction current to produce a zero radial symmetry error.

The green 'in-filled' area shows the current radial symmetry operating zone protected by the +/-5 % symmetry interlock built into the accelerator. A violation of the limit results in termination of radiation. The two arrows at the x axis line show the nominal operating range for the radial control system, with the gantry position at zero degrees, to satisfy the radial symmetry interlock for the current beam transport system set-up. In this operating region, 100 mA of current tilts the radiation field by approximately 10 %; therefore the system gain is 0.1 %/mA.

This initial work forms a baseline understanding of the operation and performance characteristics of the secondary radial beam steering system on the machine.

## 7.4 Measuring the Radial Lookup Table (Experiment 3)

### 7.4.1 Materials and Methods

With reference to the 2R servo operation as stated in Section 7.2, if the gantry is rotated with the beam off, the 2R control system error contribution will be zero and thus only the table plus the 2R aiming value will be measured. The ‘Beam Scope’ system was configured as for the last experiment with the addition that the ‘Beam Scope’ hardware was placed so that the gantry was free to rotate (Figure 7-3). A further analogue channel was connected to the gantry readout potentiometer on the accelerator gantry base frame using a 10:1 oscilloscope probe (see Section 3.9.1) and calibrated to measure gantry angle.

The 2R current was then measured whilst rotating the gantry between clockwise and anti-clockwise limits in both directions and over arcs of 30 degrees with the radiation off.

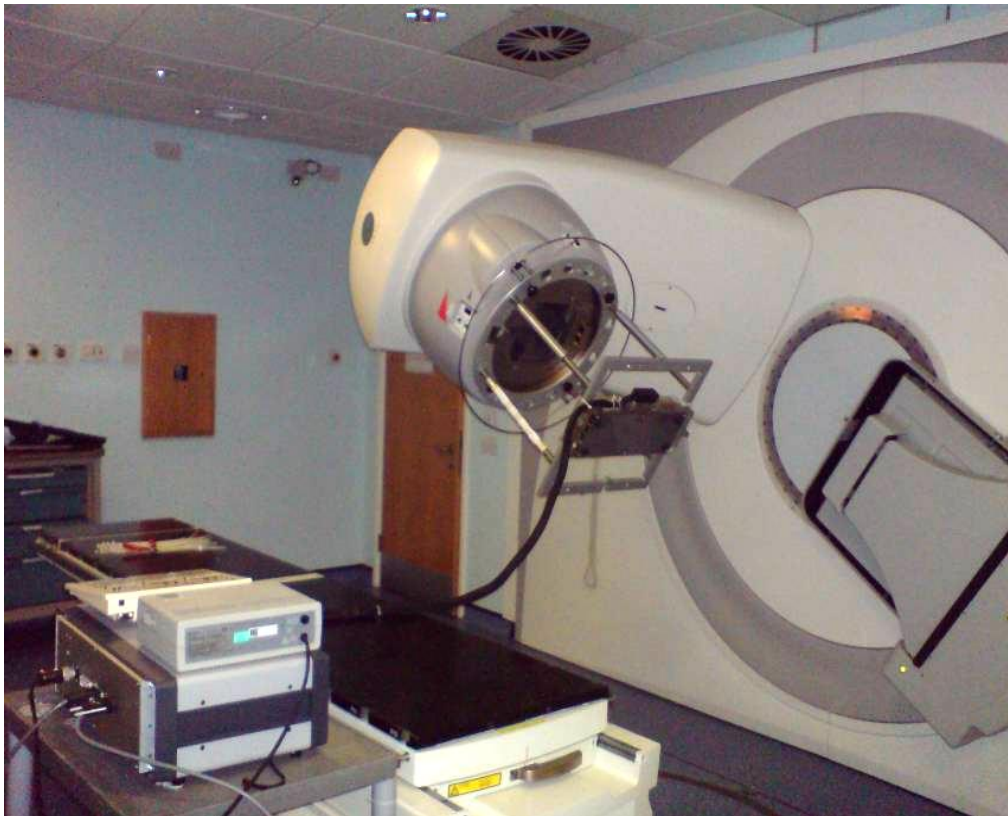


*Figure 7-3: Set-up allowing free rotation on the accelerator gantry for measurement.*

## 7.4.2 Results

The plot in Figure 7-4 shows the actual measured 2R current for one complete anticlockwise and one complete clockwise rotation.

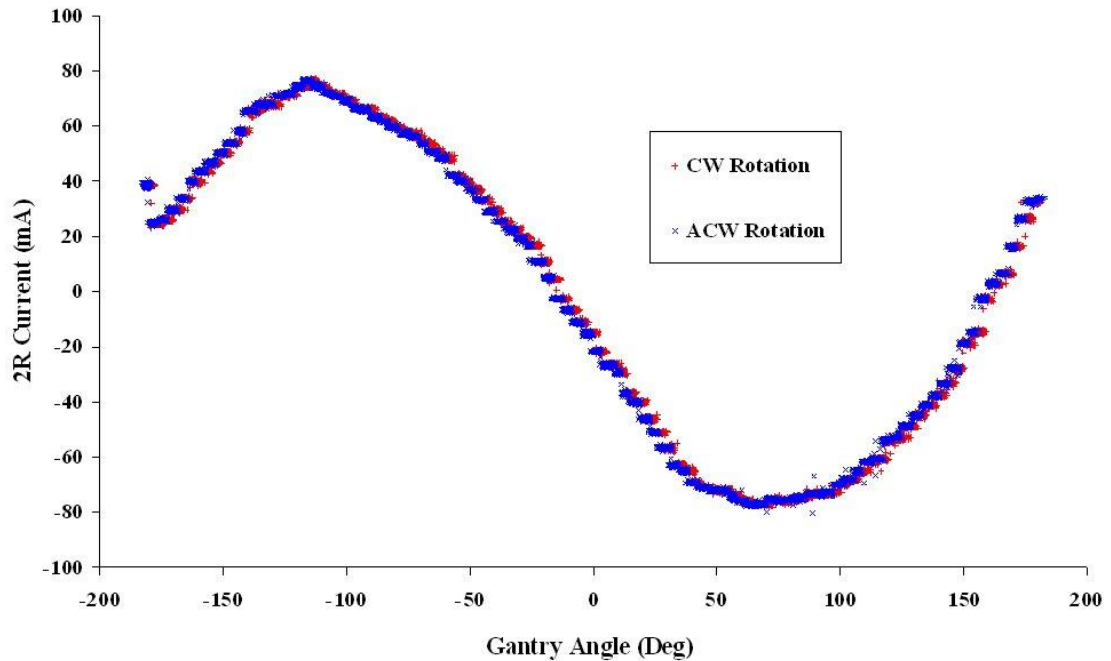


*Figure 7-4: The 2R current, as presented to the radial steering coils, measured whilst rotating the gantry between clockwise and anti-clockwise limits in both directions with the radiation off, to determine the look-up table values stored in the accelerator.*

The look-up table resolution of approximately 3 degrees, as described in Section 7.2, between the entries in the table can be seen as ‘steps’ in the plotted data. The errant point at the start of the table would not be a problem in practice, since it is less than -180 degrees, and is therefore out of the clinical range of the machine. The point was probably generated when the table was created if the point was not included in the ‘table learn’ process described in Section 7.2 above.

## 7.4.3 Discussion

### 7.4.3.1 Positional Hysteresis

As predicted from experiment 1, there is some path dependent ‘memory’ in the radial current look-up table presented in Figure 7-4, as evidenced by the phase difference between clockwise and anti-clockwise rotations. It was considered that this

hysteresis was due to backlash in the readout gear train, since the angular lead or lag depended on the rotation direction, even for small angles of rotation.

#### 7.4.3.2 Analysis of Lookup Table at Gantry Zero Degrees

The data in Figure 7-4 is presented between the gantry angles of  $\pm 7$  degrees in Figure 7-5 to investigate the artefact found in Section 7.3.2.1. The gantry angle presented on the x axis of the figure is read by the 'Beam Scope' directly from the machine gantry read-out potentiometer. The accelerator also processes the same signal to index the lookup table.

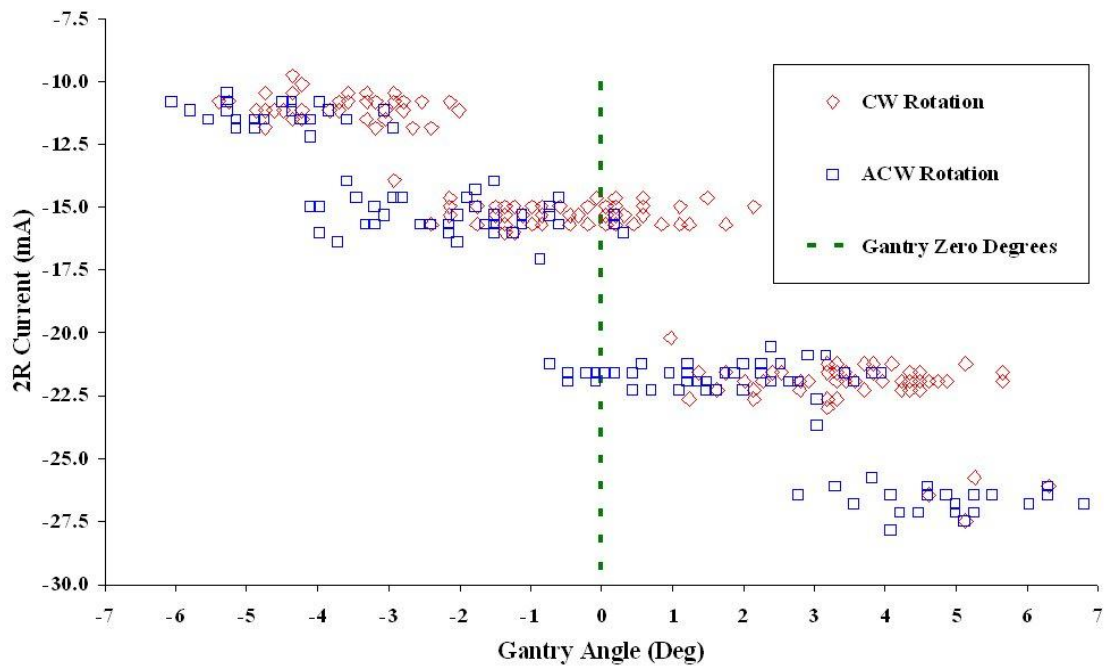


**Figure 7-5:** Data in Figure 7-4 between  $\pm 7$  degrees gantry position for clockwise and anti-clockwise rotations. The dotted line marks the gantry zero point for comparison.

With reference to Figure 7-5, anti-clockwise rotations present two possible values of the 2R current for zero gantry angle in the -22.5 mA cluster and the -15 mA cluster of points, whereas for clockwise rotations all the points are in the -15 mA cluster. The negative polarity of the artefact in Figure 7-1 suggests that the dominant value for the anti-clockwise table at zero gantry angle is the -15 mA cluster and the artefact then results in a momentary negative transition to the -22.5 mA cluster of

values. This indicates the reason the artefact only presents itself in the data set measured with the anticlockwise origin.

A raw radial symmetry data set was also generated from the beam profile data for the same beam data range as in Figure 7-1, filtered with an 11 point moving average filter (Figure 7-6). It can be seen from the figure that the artefact actually produces a real ‘tilt’ in the radiation field symmetry. The tilt produced closely matches the 0.1 %/mA figure quoted above, where the first artefact (marked in the figure by the two green arrows) is approximately 8 mA peak-to-peak in amplitude and the corresponding tilt is approximately 0.8 %.

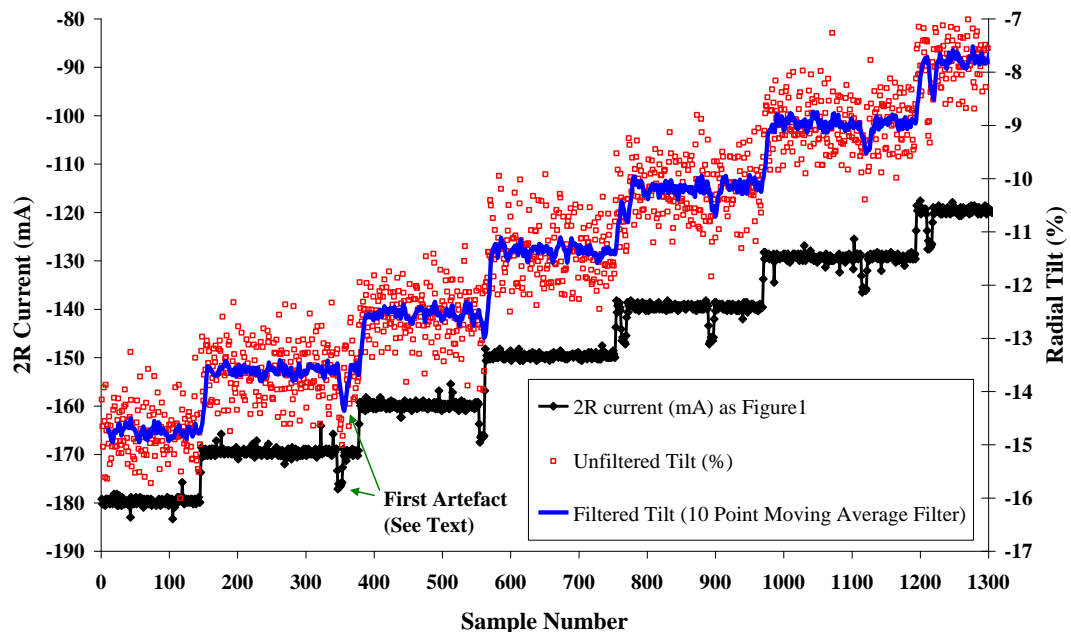


*Figure 7-6: Sample of the resulting 2R current from the 10 mA steps presented in Figure 7-1, with the raw tilt plotted from the G12 and T12 points, and an 11 point moving average filtered version of the tilt data. The first artefact in the sample is marked by the green arrows.*

This confirms that a clockwise rotation to zero gantry angle removes the artefact from the signal as predicted in Section 7.3.2.1, and that the effect is due to noise in the gantry read back system on the accelerator when the lookup table indexer is close to a 3 degree threshold point in the table. The system noise identified here should be considered when rotational beam data is analysed.

## 7.5 Results Summary for Initial Measurements

The data collected so far forms the groundwork to the measurement of rotational beams. Good linearity has been confirmed in the normal operating range of the 2R servo and a figure of 0.1 %/mA calculated for the gain of the radial control system. The radial correction current for gantry zero degrees of -50 mA closely matches the commissioning current of approximately -100 mA, bearing in mind the change to the bending fine value described in Section 7.3.2.2. An artefact was identified due to noise present at the threshold of the radial lookup table and was examined in detail for the gantry zero entry in the table as illustrated in Figure 7-1.

## 7.6 Rotation under Servo Control (Experiment 4)

The radial steering current was measured under servo conditions, during clockwise and anti-clockwise rotation of the gantry using two appropriate speed settings, with the radiation on. The aim of the experiment was to measure the gantry rotation speed for a range of beams pertinent to rotational therapy. Gantry speed is selected in the machine control software as Automatic Set-Up (ASU) units typically in the range 10 to 100 and these were measured units of deg/min.

The accelerator control system software limits gantry rotation speed based on the gantry control system operating limits and physical mass of the gantry structure to maintain radiation delivery accuracy. In order to deliver small doses per degree of rotation, the PRF is reduced by the accelerator control software. In order to produce the most stringent test of the radial control system behaviour, measurements were made at the maximum PRF of 400 PPS (approximate doserate 520 MU/min). This does not imply that greater errors would not be found at lower PRF settings, where higher stability would be expected from the beam control systems. For the same accelerator type used in the experiment, Bedford J & Warrington A, 2009 reported satisfactory beam stability down to doserates of 37 MU/min, but suggested that beams

of less than 75 MU/min should only be used in small dose segments due to sub-optimal symmetry. PRF is therefore a parameter to be considered, but the length and scope of this thesis is limited compared to the capacity of the ‘Beam Scope’ system to measure all beam parameters related to rotational therapy.

### 7.6.1 Material and Methods

The ‘Beam Scope’ system was configured as for the last experiment. Utilising the Automatic Setup (ASU) in the machine software to set gantry rotation speed, a set of rotational radiation beams was measured starting from fully clockwise (CW) to fully anti-clockwise (ACW) and back, with ASU values of 20, 30, 50 and 100 units as described Section 7.6 in order to measure the rotation speed of the gantry and the contribution to the radial steering current by the servo. The servo contribution was calculated by taking the difference between the measured radial current for each ASU gantry speed and the value measured for beam off as in Section 7.4.

### 7.6.2 Results and Discussion

The data are presented in Table 7-1; the ‘samples per degree’ value is the mean number of the data samples measured in each degree of rotation, based on a sample rate of 15 ms as described in ‘Standard Array Configuration’ used in the experiment. Data were processed by calculating the mean of all the points sampled for the dose and data channels within 0.5 degrees either side of the current gantry angle.

ASU Value	Samples per degree	Speed (deg/s)	Total time (s)
20	72	0.93	388.8
30	18.4	3.622	99.4
50	11.16	5.97	60.2
100	9.55	6.98	51.6

**Table 7-1:** *Rotational data for the measured beams based on the measurement sample time of 0.015 seconds set in the ‘Beam Scope’ configuration.*

The rotational accuracy was assessed by Bedford J & Warrington A, 2009 as part of rotational therapy commissioning tests for the same accelerator over a range of 6 deg/s at 150 MU/min dose rate to 1.5 deg/s at 600 MU/min (PRF = 400 PPS). The range in Table 7-1 therefore presents a stringent test of the radial control system under servo control at the maximum accelerator PRF.

The servo contribution for each ASU setting was measured as follows. First, the mean of the clockwise and anti-clockwise measured values for 'beam off' were calculated, as presented in Figure 7-4, to account for the read-out system hysteresis found in Section 7.4.3.1. For each of the ASU settings, the difference between this value and the clockwise and anti-clockwise rotation beam data sets was calculated (Figure 7-7).

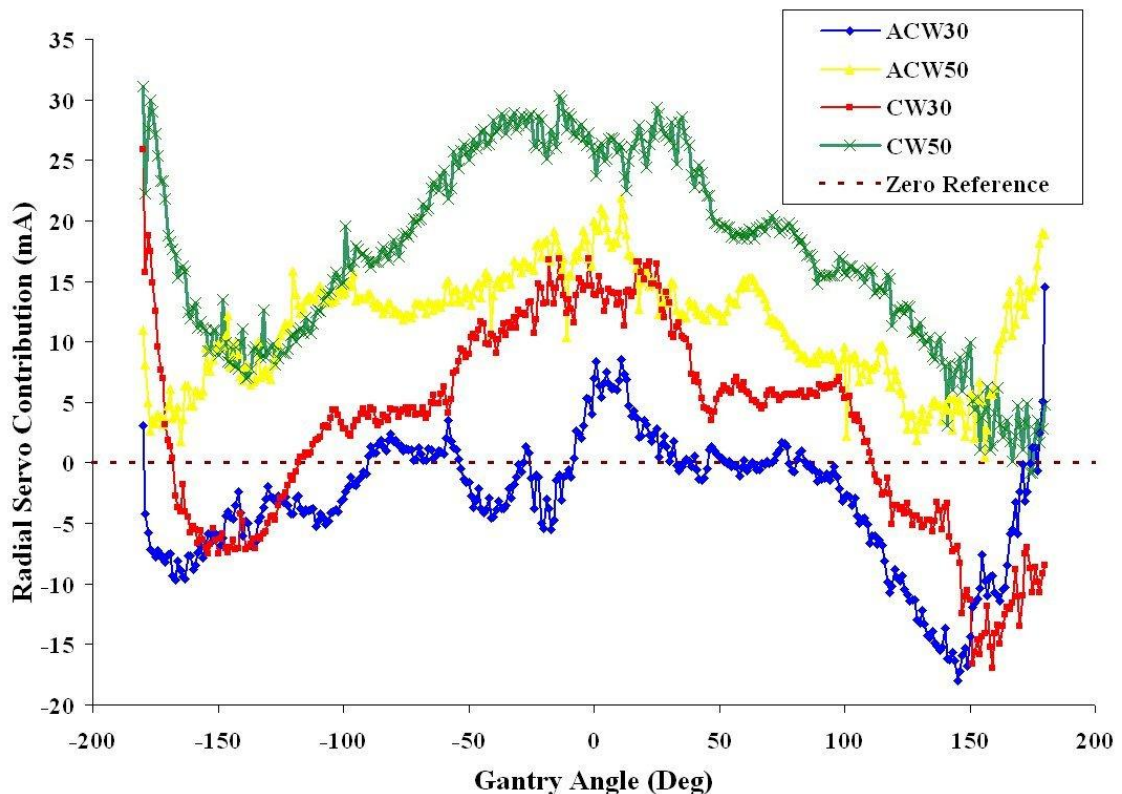


*Figure 7-7: Radial servo contribution for clockwise and anti-clockwise rotations for ASU values of 30 and 50 units, pertaining to gantry speeds of 3.62 and 5.97 deg/s respectively.*

The DC levels for the signals in Figure 7-7 were calculated using mean values of the data sets, and the AC signal content, which relates to the servo contribution, was calculated from the standard deviation of the data sets.

The DC levels appear to be randomly distributed, possibly due to the limited number of data sets measured. It is unclear why any DC shift is present, since all the beams used in the experiment had the same radial servo aiming value. This is a topic for future investigation, as this result contradicts the original design criterion for stable servo operation and may therefore be a measurement error. The mean servo contribution for a clockwise rotation was 55.3 mA (2 SD = 0.5 mA) and anti-clockwise rotation was 53.3 mA (2 SD = 1.14 mA). It could be assumed that re-learning the look-up tables in the accelerator would reduce these values to near zero, after which only the clockwise/anti-clockwise hysteresis component would still be present. It is of interest, therefore, to note that this was performed only a year ago for this machine, so based on these findings there must have been a change in the conditions affecting rotational electron beam displacement during this period.

The data in Figure 7-7, with the DC Levels removed, are plotted in Figure 7-8 to present just the AC component. The servo contribution for both the clockwise and anticlockwise rotations for ASU values of 30 and 50 are of similar amplitudes between -165 and +150 degrees of rotation. The clockwise and anti-clockwise rotations for both ASU values then diverge.

From the plot, it is clear that this divergence is dependent on the direction of rotation. This implies that there must also be an external influence that is dependent on the direction of rotation and that is not included in the look-up table profile and therefore is corrected by the radial servo system. Based on similar work performed by the author in the transverse steering plane, this effect may be due to the displacement of the gantry in the radial direction during gantry rotation.

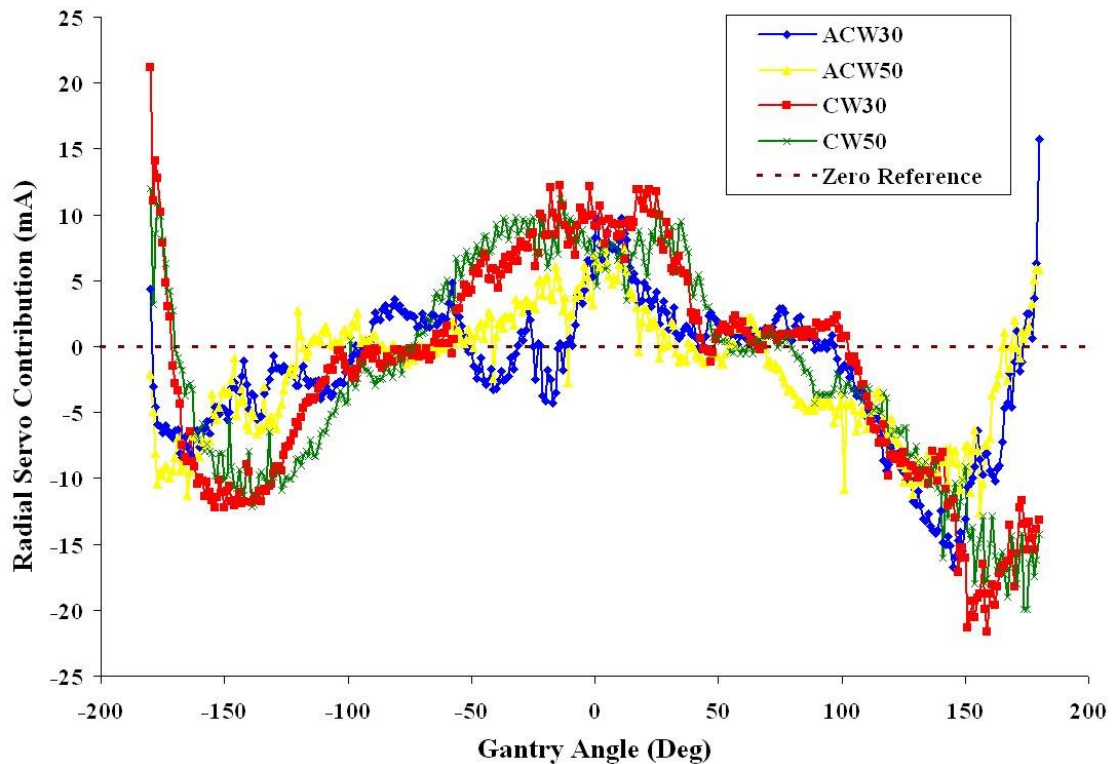


*Figure 7-8: Data from Figure 7-7 presented with the DC level subtracted for the data sets.*

## 7.7 Measurement of Radial Displacement (Experiment 5)

The measurement of radial displacement of the accelerating waveguide is a topic that is beyond the scope of this thesis, but it was decided to investigate one possible characteristic to establish whether there was any waveguide displacement evident during gantry rotation (Karzmark C J, 1984).

### 7.7.1 Materials and Methods

The accelerating waveguide in the machine under test is mounted at the distal end, and allowed to expand longitudinally to allow for change in temperature produced by power dissipation during ‘beam on’, by the use of support roller bearings along its length. This allows longitudinal freedom of movement at the electron gun end, but inevitably leads to a small amount of radial displacement during gantry rotation due to the ‘radial play’ in the support roller bearings and mounting assemblies. Any positional displacement at the electron gun end will result in a small

bend in the waveguide structure and thus an increasing deviation of the trajectory of the electron beam, along the length of the 2 m long accelerating waveguide structure. Furthermore, this will manifest as a steering error and be seen by the monitor ionisation chamber in the radiation head. In the radial beam axis this will be controlled by the 2R servo. In the transverse axis this will result in a symmetry error, since this axis uses only a lookup table value (Section 7.2). Based on the results of previous experiments in this chapter, it would be expected that some positional hysteresis would also be present between CW and ACW rotations as well just positional translation. The results will also be compared with the radial servo contribution from Figure 7-8. A measurement of radial displacement at the electron gun end of the waveguide was attempted using a Linear Differential Voltage Transformer (LVDT).

An LVDT is a displacement transducer comprising one primary and two secondary coils. The phase relationship between currents coupled between the primary and two secondaries is dependent on the position of an armature physically connected to the displacement to be measured. At the central position, the two voltages across the transducer secondaries would be equal, but since they are connected with opposing phases, the output is zero. As the armature moves away from central position, there is a positive phase shift in one of the position sensor secondaries and a negative one in the other, which results in an output voltage. These devices are generally used in conjunction with a phase discriminator that compares the phase of the excitation current presented to the primary winding of the transducer with the currents from the pair of secondary coils to produce a DC signal. This results in a transducer that is highly sensitive to position, with very low DC drift and minimal internal mechanical contact.

The device chosen (Solartron Metrology UK) shown in Figure 7-9, has an inbuilt phase discriminator, and is thus simple to employ requiring only a low current 12 V supply. The output is a signal of approximately 750 mV/mm of linear travel,

with a repeatability of better than  $0.15\ \mu\text{m}$ . The device also contains a return spring to maintain mechanical contact.

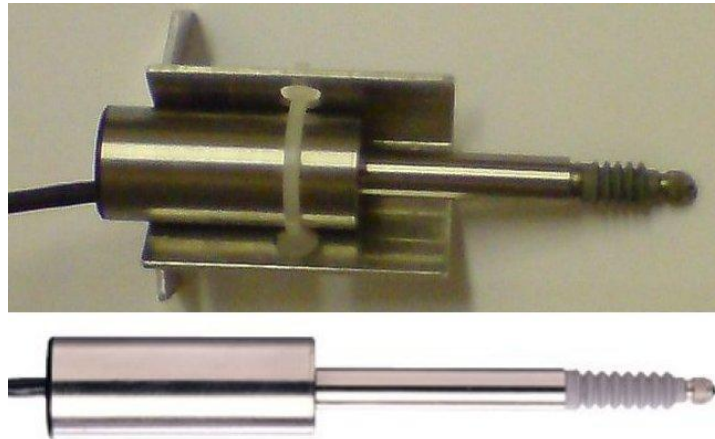


*Figure 7-9: LVDT chosen to measure radial displacement. The upper picture shows the device fitted to a mounting bracket fabricated to attach the transducer to the accelerator during the experiment.*

The device was positioned between the waveguide and its support tube (Figure 7-10) and the gantry rotated to fixed positions, again starting from the fully CW direction. The output from the LVDT was then measured using a digital multi-meter. Data were measured over two complete gantry rotations.

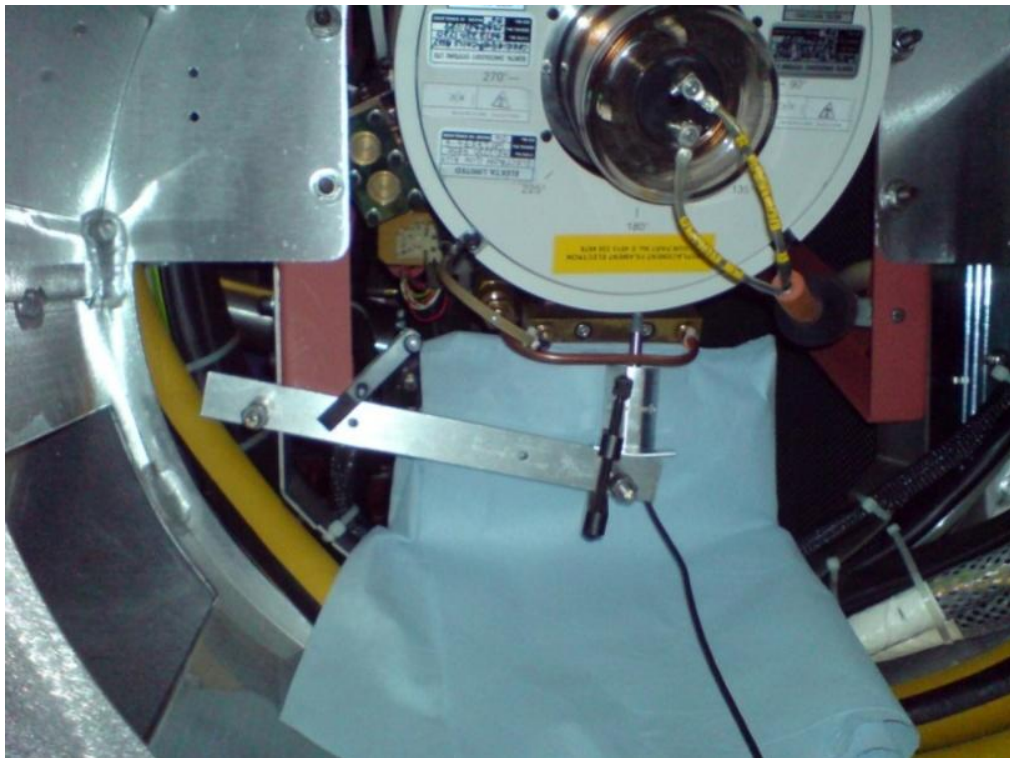


*Figure 7-10: LVDT mounted to measure radial displacement of the waveguide during gantry rotation.*

### 7.7.2 Results and Discussion

The recorded voltages were converted to displacements in millimeters using the calibration factor supplied with the LVDT and plotted for clockwise and anti-clockwise rotations (Figure 7-11).

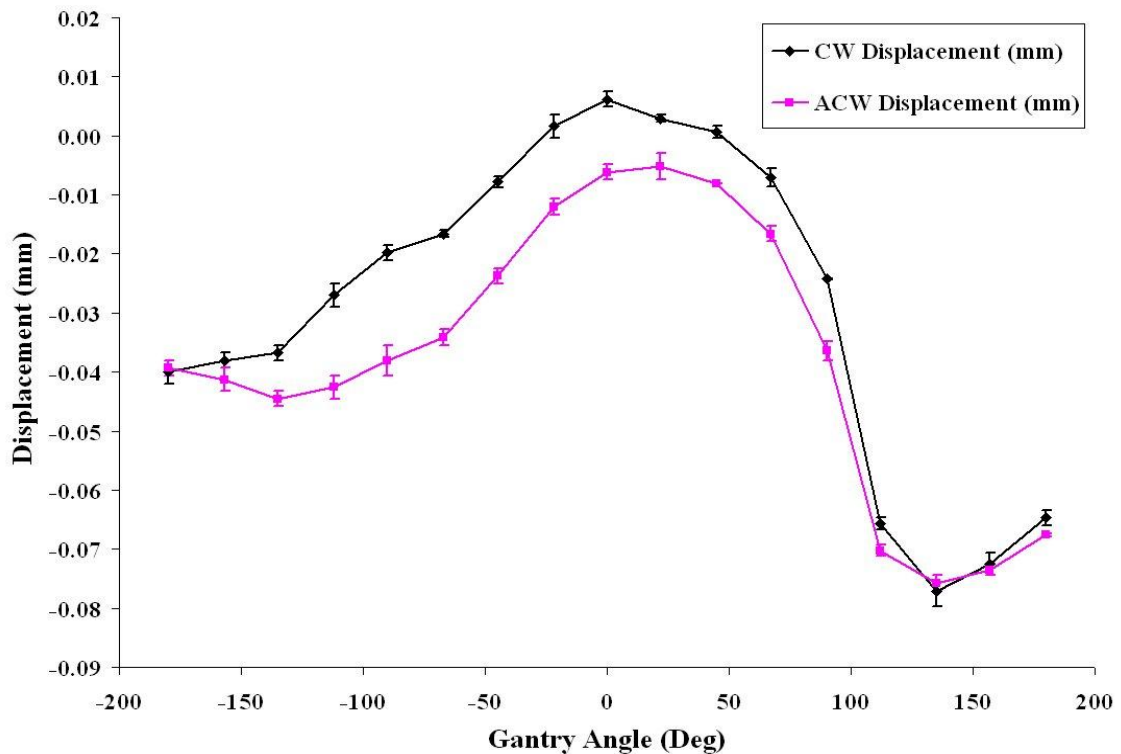


**Figure 7-11:** Radial displacement measured by the LDVT based on 2 full 360 degree rotations from -180 to +180 degrees (The error bars are 2 SD).

The displacement recorded was consistent for two consecutive rotations and also demonstrates some directional hysteresis. This information is presented in Figure 7-12 along with the servo contribution data from Figure 7-8.

In Figure 7-12, there is some correlation between the servo contribution and the measured displacement, although the impact of hysteresis is not so clear. Bearing in mind the complexity of the mechanical forces present on the masses of the gantry components during rotation, this crude measurement demonstrates that some waveguide displacement is present. However, there is insufficient evidence that a corrective servo contribution results from the displacement alone, since other parameters related to gantry rotation may also correlate.

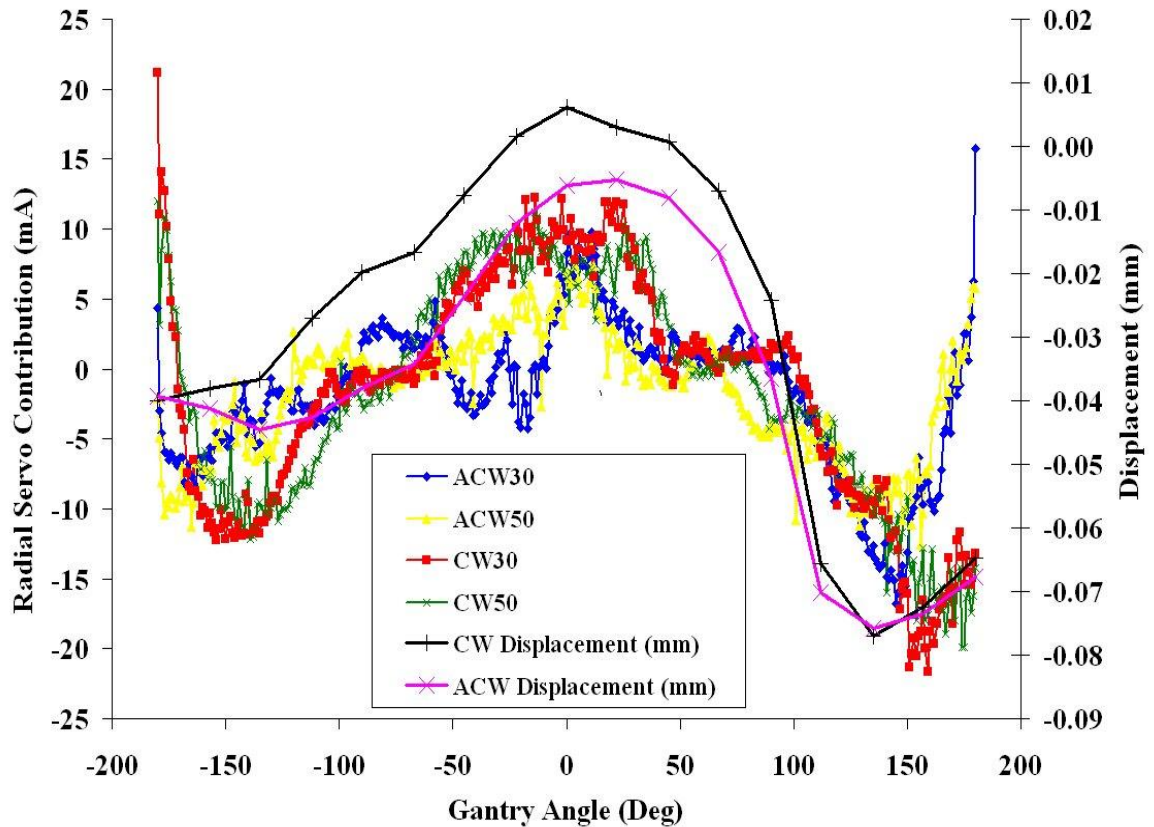


*Figure 7-12: Displacement as plotted in Figure 7-11 together with the servo contribution from Figure 7-8 for comparison.*

## 7.8 Radial Symmetry

### 7.8.1 Materials and Methods

In the previous section, the performance of the radial beam control system during gantry rotation on a clinical machine was investigated by presenting the radial servo contribution to its look-up table value. In this section, the resulting radiation profiles and radial symmetry based on the G12 and T12 points were calculated from the same beam data sets (Section 7.6.1) for all of the 19 ionisation chambers along the GT isocentric axis line for each degree of rotation. The measurements were made in two segments starting from fully CW rotation. In the first segment, the gantry rotates to the ACW limit, then stops, and rotates back to the start angle. Also, subtracting the CW profiles from the ACW profiles for each point in the rotation shows any difference in the servo control system with direction.

## 7.8.2 Results and Discussion

The radial symmetry for ASU values of 20, 30, 50 and 100 units (Table 7-1) for CW and ACW rotations are presented in Figures 8-1, 8-2, 8-3 and 8-4. There are short beam segments in the measurements not included in the plots prior to the start, and after end of rotation where the gantry was accelerating or decelerating (Section 7.3.1.). There is a spike artefact on all four of the plots at around the zero degrees region of gantry rotation. This was due to a faulty ion-sputter pump on the accelerator, resulting in an intermittent vacuum interlock and thus a momentary loss of radiation at that angle.

### 7.8.2.1 Error in Clockwise Rotation

It is immediately evident that, close to the rotation limit of -180 degrees there is errant peak of asymmetry at the start of the CW segment of the rotation for all of the 4 beams measured in figures 8-4, 8-5, 8-6 and 8-7. Other than this, the radial control servo maintains symmetry within  $\pm 1\%$  of the 2.8 % levels at the 12 cm points defined by the commissioning data, for the majority of the beam measured.

There is a high rate of change in the servo contribution evident at the end of the ACW segment of rotation in Figure 7-8, at the far left of the plot at 180 degrees. The radial servo is slow in correcting this error at the initiation of the CW rotational segment, leading to the peak in asymmetry. The error is not found at the opposite end of the range where both CW and ACW rotations are within  $\pm 1\%$  symmetry.

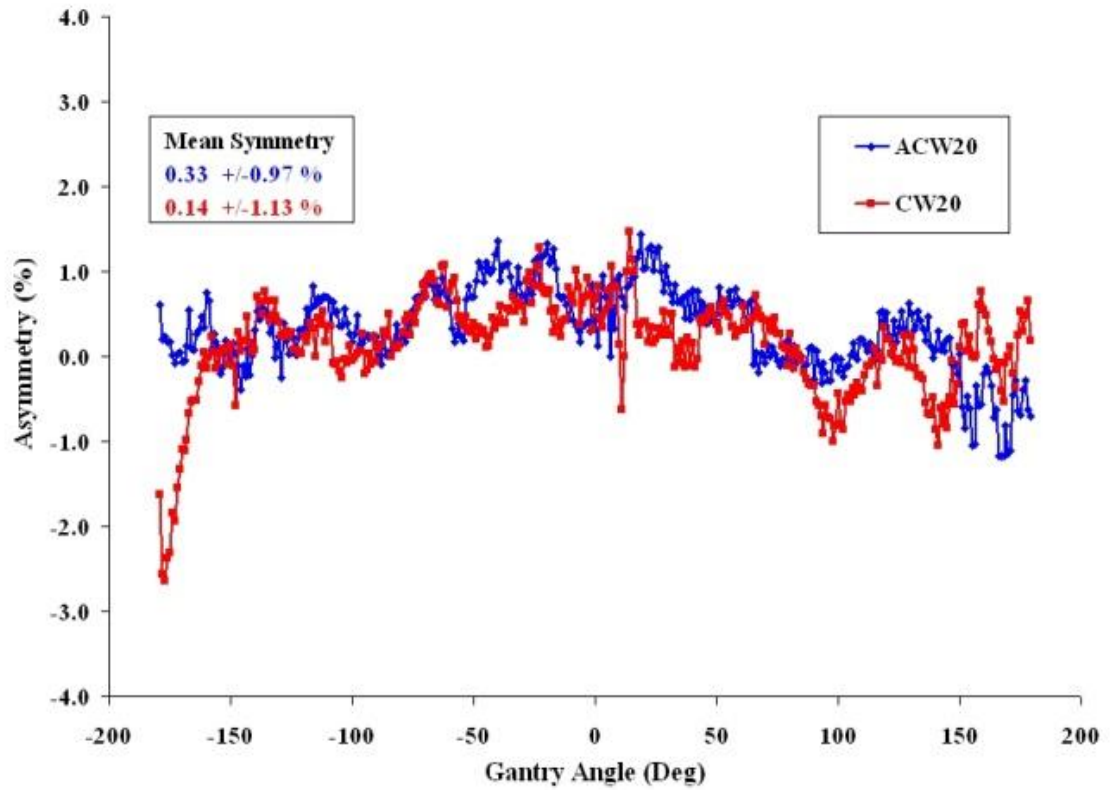


Figure 7-13: Radial asymmetry for full clockwise and anti-clockwise rotations for ASU value of 20 units.

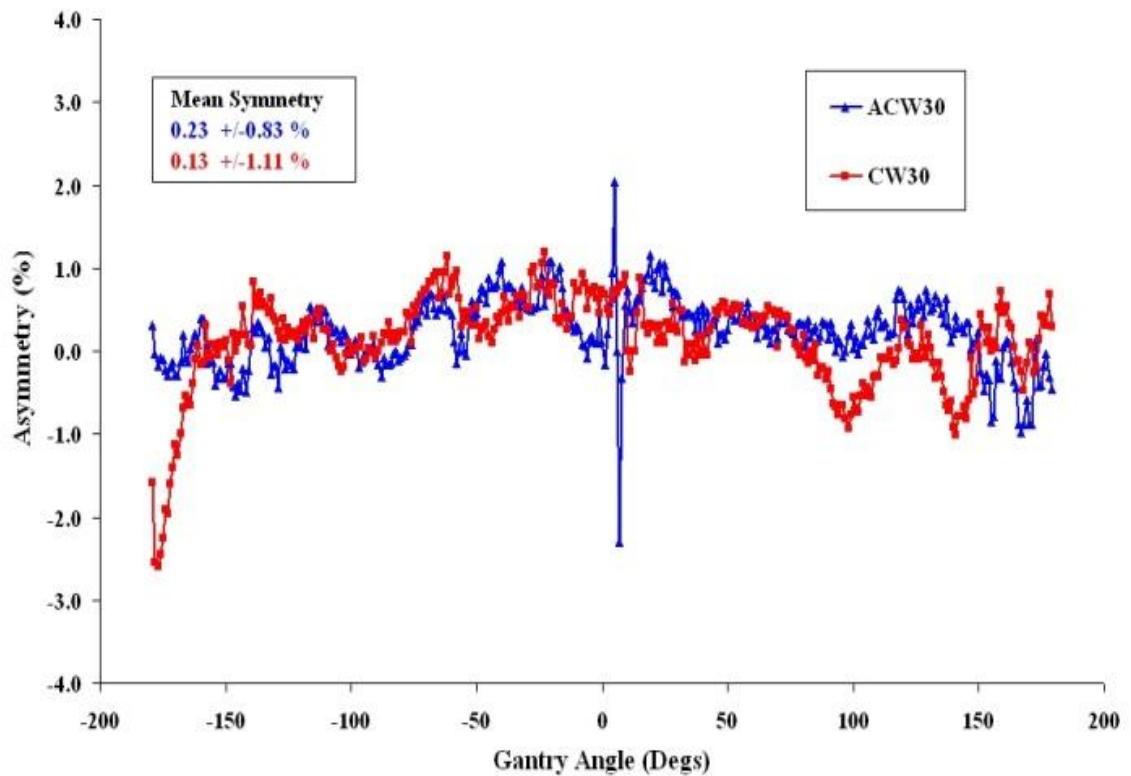


Figure 7-14: Radial asymmetry for full clockwise and anti-clockwise rotations for ASU value of 30 units.

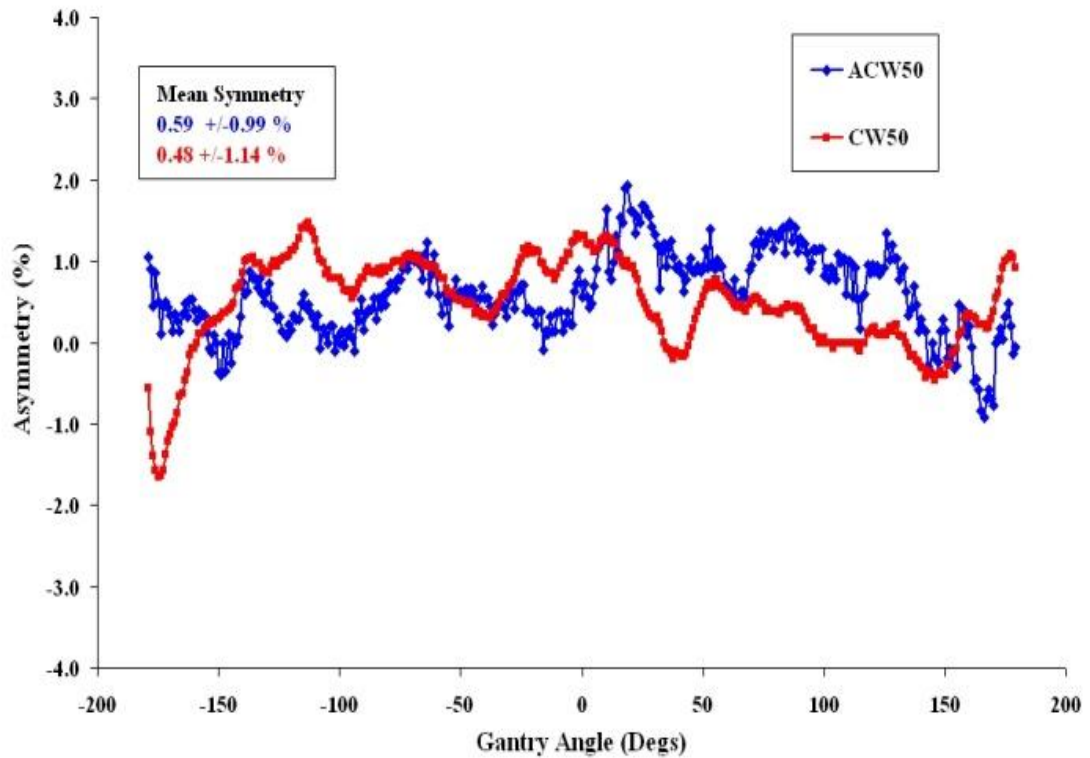


Figure 7-15: Radial asymmetry for full clockwise and anti-clockwise rotations for ASU value of 50 units.

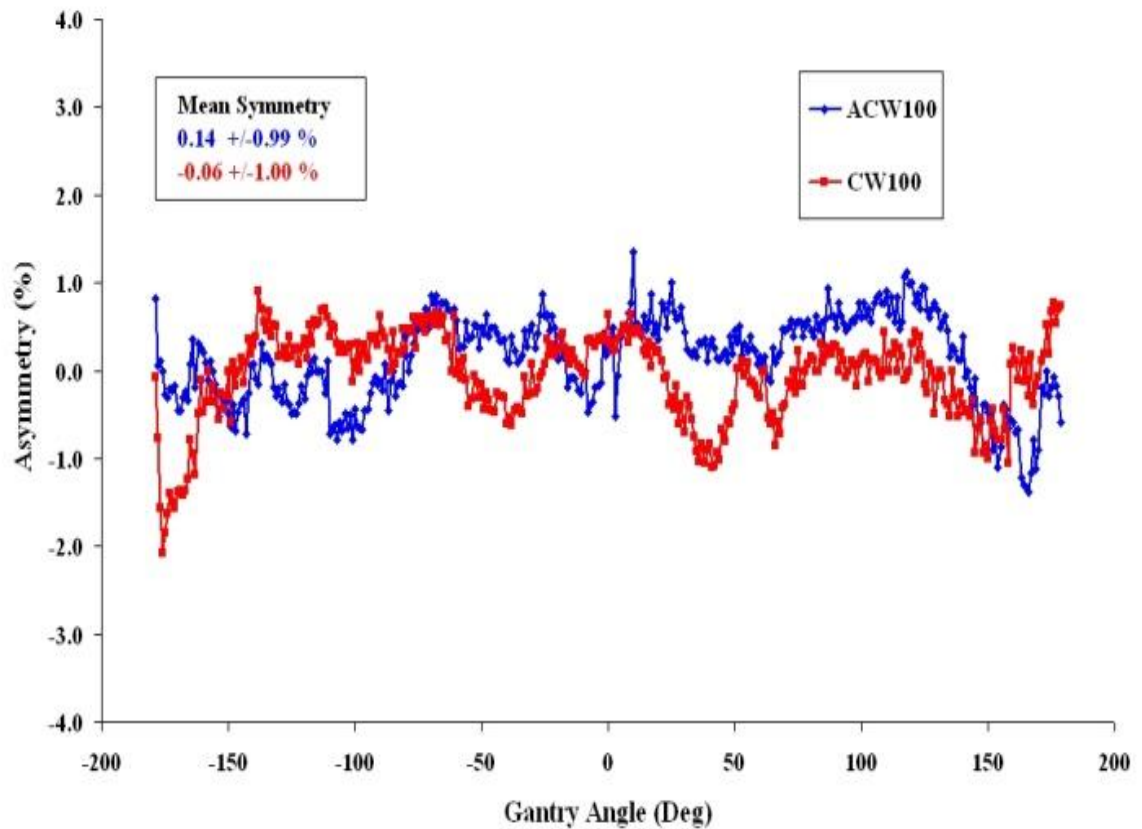
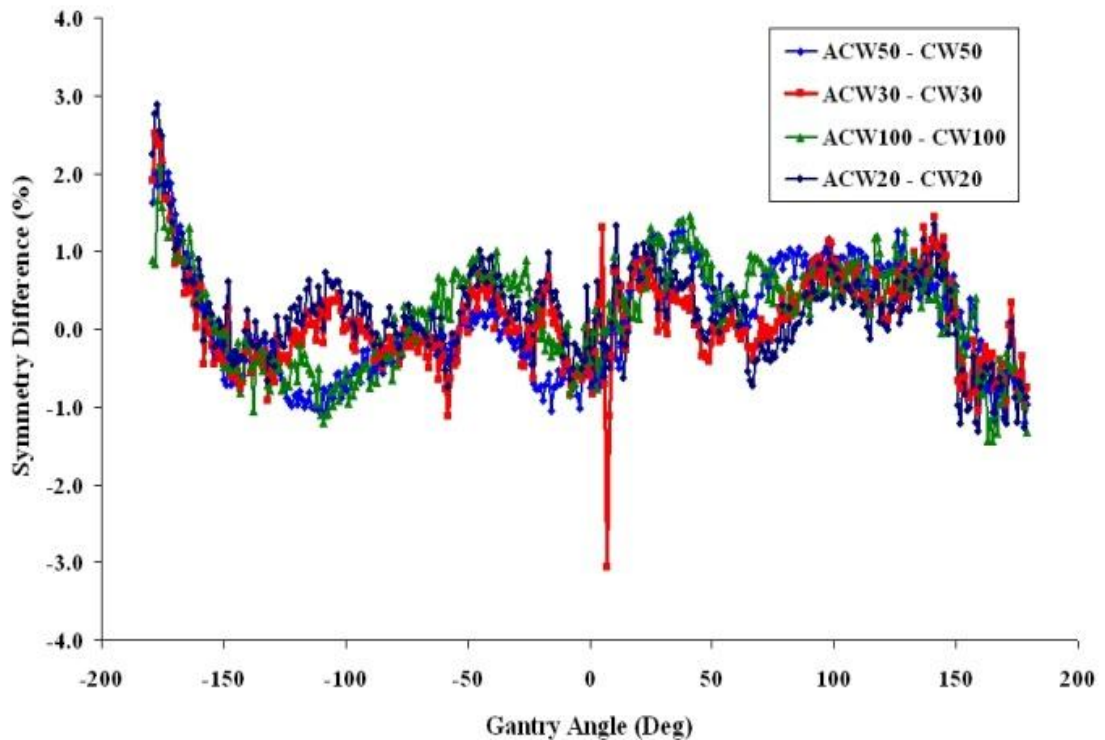


Figure 7-16: Radial asymmetry for full clockwise and anti-clockwise rotations for ASU value of 100 units.

Since the gantry speed has been established to be constant to the end of the ACW rotation and after the commencement of CW rotation (Section 7.3.1), effect of gantry deceleration should not be present in ACW measurements at gantry angles less than -180 degrees. However, it is possible for any effect produced during the transition from ACW to CW motion, for example due to the movement of masses as suggested in (Section 7.7), to present itself as an error at the initiation of the CW segment.

Plots of the differences in asymmetry for the CW and ACW rotations are shown in Figure 7-17, where the hysteresis created by the direction of rotation is evident. If no hysteresis were present, then the radial symmetry would be the same irrespective of rotation direction, and therefore both the CW and ACW plots would be a zero for all gantry angles.



**Figure 7-17:** *Difference in radial symmetry between CW and ACW rotations for the 4 values of ASU used in the experiment (The red spike is discussed in Section 7.8.2).*

This demonstrates an inability in the radial servo to zero the symmetry error using the radial current value learnt and stored in its look-up table, plus any servo error signal generated by the internal monitor ionisation chamber in the radiation head

of the machine. It is conceivable that the error is not measured by the radial servo plates in the beam monitor ionisation chamber, due to an error in radiation beam geometry at the monitor chamber location in the beam path, and hence no servo error is produced, but this would require further investigation to clarify.

### **7.8.3 Conclusion for Error in CW Rotation**

An error was identified in the radial symmetry at the initiation of CW rotations for all of the 4 beams measured at gantry -180 degrees; other than this the symmetry measured was within the manufacturer's specified range of +/-1 %. As was expected from experimental results found in the previous chapter, hysteresis noted in the radial steering current in the previous chapter are also evident in the radial symmetry data.

## **7.9 Conclusion**

The properties of the secondary radial steering system during gantry rotation have been investigated using the 'Beam Scope' system. As for the previous chapter, the data is only representative of one machine and care was taken to ensure the accurate setup and calibration of all the beam control systems involved to avoid systematic errors.

The initial experiments demonstrate the use of the 'Beam Scope' to describe control system behavior at a fundamental level, its consequence for radiation beam profile, and its use as a development tool in the design and testing of linear accelerators.

Some rotational hysteresis was identified based on full clockwise and anti-clockwise rotations. A similar effect has been noted by the author during machine installation in the transverse plane, which was reduced by taking a mean value for each point in the look-up table data sets learnt from clockwise and anti-clockwise rotations, then manually entering the result into the look-up table.

It was interesting to discover the contribution required by the radial control system, considering that both the radial and transverse look-up tables were generated approximately a year before the current measurements. Measurement of the mechanical displacement of the accelerating waveguide at the electron gun was undertaken, showing some mechanical hysteresis and positional translation during CW and ACW rotations. However, there is insufficient evidence that any corrective servo contribution results from accelerating waveguide displacement alone, since other parameters related to gantry rotation may also correlate.

Periodic oscillations and errors in symmetry were in the main within the manufacturer's specified range of  $\pm 1\%$ , with the exception of CW rotation at  $-180$  degrees. This is fine, for an engineering evaluation of radial steering system behaviour, where the 'Beam Scope' is a valuable tool in the measurement of control system performance and its effect of radiation beam profile. However, the question of whether there is significance in these results for patient dose will be explored in the following chapter.

## Chapter 8. Consequences for Patient Dose

### 8.1 Introduction

The purpose of this chapter is to demonstrate the relevance to patient dose of the parameters that are measurable by the ‘Beam Scope’ system. The author makes no claims for the ‘Beam Scope’ as a patient dosimetry system for dynamic therapy: other, more sophisticated dosimetry equipment is available (e.g., Delta 4, ScandiDos AB and the ArcCheck, SunNuclear Corp., See Chapter 2) to validate the delivery of a planned therapeutic dose with the accelerator in the clinical mode, using the manufacturer’s bespoke dynamic therapy software to deliver the treatment. On the other hand, the consequences for patient dose of factors that can be measured by the ‘Beam Scope’ should be considered, and as a demonstration the effect of a change in radial servo gain on the dose in a 3D volume is presented.

#### 8.1.1 Quality Control

Effective quality control in radiotherapy is essential to ensure consistency in the delivery of the prescribed treatment. This is achieved by a multi-disciplinary approach, including dosimetry physics, treatment planning and machine engineering to limit uncertainties in the treatment process (Mayles P & Thwaites D I, 2007, Thwaites D I *et al*, 2005). Veracity in the whole process is achieved by limiting systematic and random errors in all stages of the dosimetry chain to attain doses as close to the ‘target value’ as possible.

##### 8.1.1.1 Accuracy and Precision

Errors in measurements can be described by two factors, these being accuracy and precision (Smith S W, 2003b). Accuracy is a measure of the degree to which the mean of the measurements deviates from the ‘true value’ of the underlying process as a result of ‘systematic error’ or ‘systematic uncertainty’. Precision is the spread in the

results of individual measurements resulting from ‘random error’ or ‘random uncertainty’. This is illustrated in Figure 8-1.

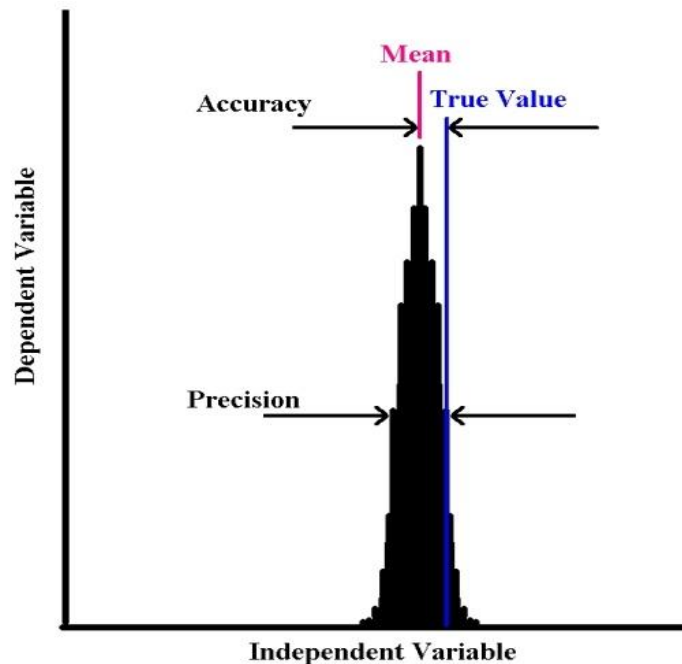


**Figure 8-1: Accuracy and Precision.** The accuracy is the difference between the ‘True Value’ and the mean value of the measured process, whereas the precision is the spread of the measured values, and is specified by the standard deviation.

In relation to radiotherapy, uncertainty due to random effects can be evaluated by measuring the standard deviation of repeated measurements. The true distribution of the underlying process is generally unknown, but is usually assumed to approximate a normal distribution where the uncertainty can be measured as 2 standard deviations or the 95% confidence level. The assessment of systematic error requires careful analysis of the processes used in each stage of the dosimetric chain. Traceable calibration and comparison of different pieces of equipment and measurement methods are possible ways of limiting these errors.

These uncertainties can be added in quadrature (Mayles P & Thwaites D I, 2007 Thwaites D I *et al*, 2005) to estimate an overall value. However generally, systematic errors would normally be added together arithmetically.

Uncertainties in the delivery chain, both systematic and random, can be expressed either dosimetrically or geometrically. A 3 dimensional fluence map in a

phantom can be compared with the expected fluence from the planning stage using Gamma analysis for confirmation of dosimetric and geometric accuracy (Low et al, 1998). Whilst not described in full here, the Gamma concept involves combining dosimetric and geometric error into a single quality metric by comparison to set criteria. The conclusion of a recent national dosimetry audit (Clark C *et al*, 2009) that compared IMRT to conventional radiotherapy proposed Gamma criteria of 3% or 3 mm (Figure 8-2) on individual fields and 4% or 3 mm for combined fields in multi-centre head and neck IMRT trials.

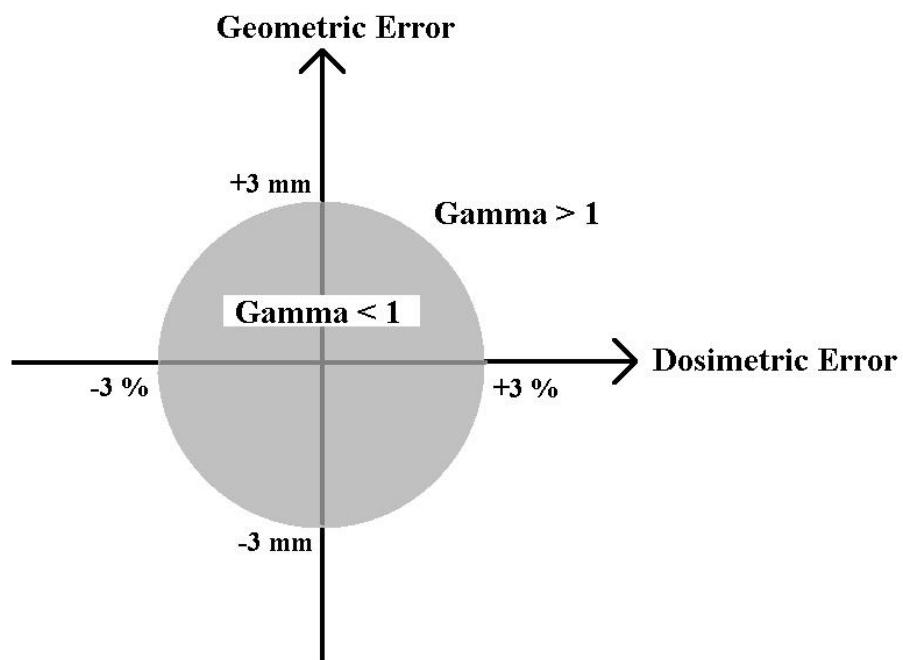


**Figure 8-2:** Example diagram of Gamma criteria. A positive outcome within the grey circle results in a Gamma value of less than one.

Accuracy in any measurement can be achieved by keeping systematic errors in all stages of the process to a minimum. The precision can be characterised by making repeated measurements in order to estimate the variabilities inherent in the system. A comprehensive description of the requirements for delivery accuracy and precision in radiotherapy is presented by Mayles P & Thwaites D I, 2007 and also IPEM Report 81 (Thwaites D I, 1999).

### 8.1.1.2 Therapeutic Consequences

As discussed in Section 1.3, the probability of tumour control and sparing of healthy tissue is characterised by two sigmoid curves, with the aim of radiotherapy being to maximise tumour control with minimal normal tissue complications. It is the aim of Radiotherapy Treatment planning to optimise the gap between the TCP and the NTCP curves, and hence enhance the therapeutic ratio. Furthermore, a prerequisite is that the completed plan should be delivered on a treatment unit with stable beam operating conditions and hence consistent beam symmetry. Consequently, what will actually be delivered, should match the planned and therefore optimised dose distribution, to within acceptable limits.

The consequence of asymmetry due to an inaccurately generated beam is a variation in the delivered dose distribution, producing ‘hot spots’ and ‘cold spots’ of dose both inside, and outside the Planning Tumour Volume (PTV) compared with that planned. In a non-uniformly irradiated tumour the TCP will be limited by the segment of tumour that receives the lowest dose, regardless of what is received by the segment of tumour that receives the highest dose. Similarly, the adverse effect on many normal tissues will be dominated by the segment of tissue that receives the highest dose, although there are some normal tissues where it is the average dose that is more important which will generally be unaffected by changes in uniformity.

### 8.1.1.3 Simplified Example

The consequence of beam asymmetry error is illustrated for an idealised treatment of a modelled prostate tumour.

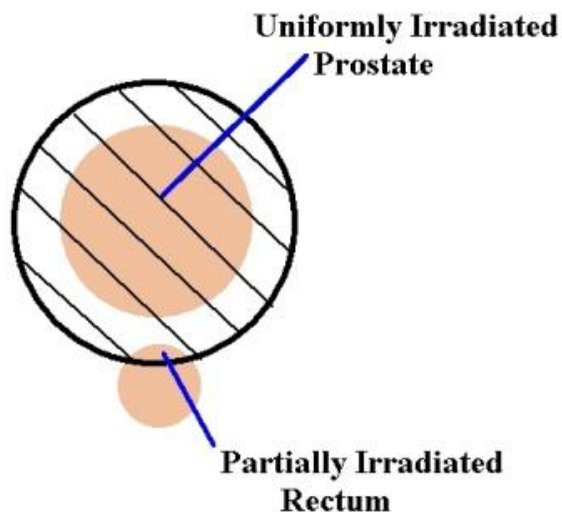


*Figure 8-3: Simplified schematic of a prostate treatment.*

With reference to Figure 8-3, the planned uniform dose distribution across the prostate results in a partial dose to the rectum. In Figure 8-4 a prescribed dose of 'PD' results in a high TCP to the prostate, shown in curve (a) and a relatively low NTCP on curve (d) for the partially irradiated rectum.

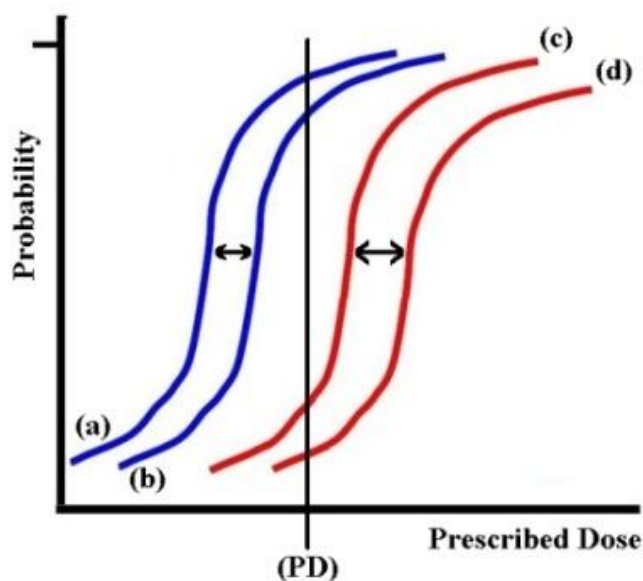


*Figure 8-4: Simplified illustration of dose response curves showing the NTCP and TCP for errors in beam delivery. The TCP curves are plotted in blue and NTCP curves in red.*

Asymmetry in the beam delivery profile results in a possible reduction in TCP, since there is the likelihood of ‘cold spots’ in the dose delivered to the target volume. This will cause curve (a) to move to the right as in curve (b) since for any given Prescribed Dose (PD) the minimum dose delivered to the tumour and hence the TCP will be reduced. Conversely an asymmetric profile increases the risk of hot spots in the rectum, shifting curve (d) left, as in curve (c) since the likely maximum dose to the rectum and hence the NTCP will be increased for a given prescribed dose. Both these effects cause the TCP and NTCP curves to move closer, reducing the therapeutic ratio.

## 8.2 Materials and Methods

There are several possible control system setting errors with potential consequences for the patient dose in rotational therapy. Incorrect values in steering servo ‘lookup tables’, ‘gain’ and ‘bandwidth’ are 3 examples. Servo gain was chosen for this investigation since any periodic oscillations in the radial servo signal would be averaged over the treatment volume during rotation, making an interesting case for which to model the 3D dose map. An ‘out of service’ linac was used for the experiments in this chapter, specifically to allow freedom to set up non-optimised parameters.

The ‘Beam Scope’ ionisation chamber array was fitted to the holding device and attached to the radiation head to measure beams during rotation. The ‘Standard Array configuration’ was used, together with the same analogue measurement setup as in the previous chapter to measure the gantry angle and radial steering current. The array was then pre-irradiated and a calibration factor obtained for the array as described in previous chapters. The start and end gantry angles were also extended by 2 degrees to minimise effects from gantry acceleration and deceleration, (Section 7.3.1). Rotational profiles and control data were measured with the ionisation chamber array in both the GT and AB axis for a ‘normal’ beam and also for a beam with the radial servo gain changed on the linac from 120 to 320 units to produce

under-damping in the servo feedback loop. A 'beam off' control signal data set was also recorded for the radial axis servo to capture the lookup table values. This allowed the actual servo contribution to the steering current to be calculated by taking the difference from the radial control data recorded at beam on.

Confirmation that the gain change resulted in beam profile oscillations was made first, by visual comparison of the shape and magnitude of the servo contribution to the steering current between the 'normal' and 'high gain' beams. Then, comparison and correlation of the resulting radial current and measured intensity of the beam at the 12 cm points for the 'normal' and 'high gain servo' beam data sets were performed, to confirm that the resulting symmetry error was in fact caused by the change in steering current.

To fully represent the dosimetric error in a 3D dose map would be beyond the scope of the thesis, due to the complexity of modelling the beam divergence and depth characteristics. In this elementary demonstration of the effect on patient dose, these effects were ignored. Furthermore, due to the limitation of the 1D array, it was assumed that off-axis profiles were the same as the measured CAX profile for the both the GT and AB planes. With these limitations in mind, a 3D dose map was produced in a cylinder 19 cm long and of diameter 19 cm at the linac isocentre based on a rotational step of 0.5 degrees.

A data set from gantry zero degrees was used as a known good reference, since this was the profile accepted during machine quality assurance, and also the profile that would be expected for all other gantry angles. To produce the dosimetric error for each of the 0.5 degree angles in the data set, the percentage error between each angle and the profile for gantry zero degrees was calculated with the data normalised to the CAX dose.

### 8.2.1 Processing to produce the 3D Dose Map

To produce the 3D dose map, an application was written in Visual Basic™ to combine the measured data sets and produce a 3D dose map between any user selected arc start and arc stop angles. The dosimetric errors in the rotational data sets for both the GT and AB axis were added and mapped to points in 2D arrays to produce coronal planes at gantry 0 and 180 degrees, sagittal planes at gantry +/-90 degrees and planes at all other 0.5 degree steps (720 planes in total for a whole rotation).

For each of the 2D planes, between the required arc start and stop angles, each point was ray traced from the 2D plane, into all corresponding points, inside the cylinder of the 3D dose map and the resulting doses summed over all angles. Each cell in the 3D dose map was then divided by the number of planes processed to form the average dosimetric error.

During processing, the program displayed a representation of a single slice to aid debugging; in Figure 8-5, a 'screen shot' of one gantry angle is presented as an example, to support the description above. With reference to the figure, the CAX transverse plane of the dose map is outlined in (a) and the boundary of the points to be processed in (b), the detector (c) shown in the AB axis. The outer non-diverging rays lines are indicated in (e) from the linac radiation head (f).

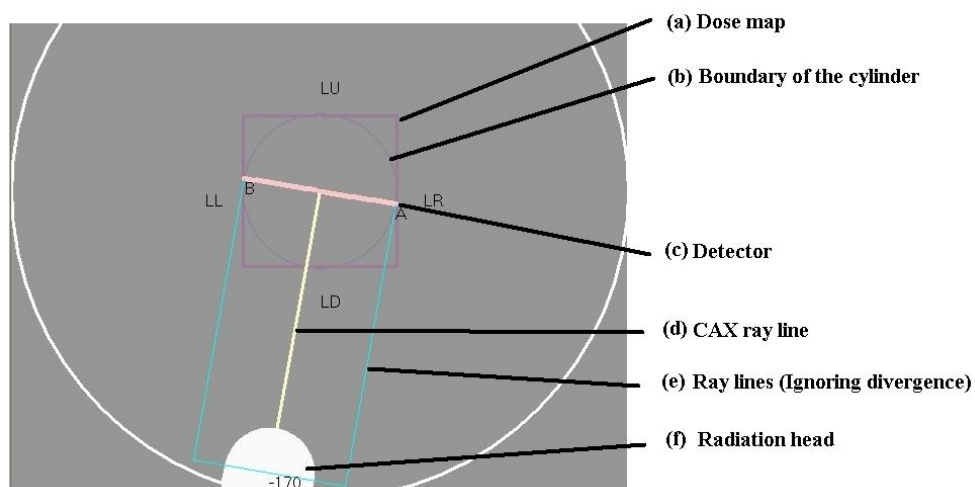


**Figure 8-5: Central axis slice visualisation 'screen shot' taken from the program during data processing (for gantry angle of -170 degrees).**

Using this technique, doses were calculated for whole CW rotations and for CW segments of rotation for both of the beam data sets in the experiment.

## 8.3 Results

### 8.3.1 Confirmation of Under-damping

The ‘normal’, ‘high servo gain’ and ‘lookup table’ data sets for one whole CW rotational measurement were used to calculate the radial/2R servo contributions, which are plotted in Figure 8-6. The plot shows larger amplitude oscillations on the radial servo contribution with the gain set to 320 units and thus demonstrates a reduced damping factor for the servo. Note the phase shift due to the 10 point averaging from Excel™ used for the plotted raw data; for comparability, the same method of averaging was used for all the raw data plotted in this chapter. Likewise, the measured radial symmetry for the ‘normal’ and ‘high servo gain’ data sets is presented in Figure 8-7.

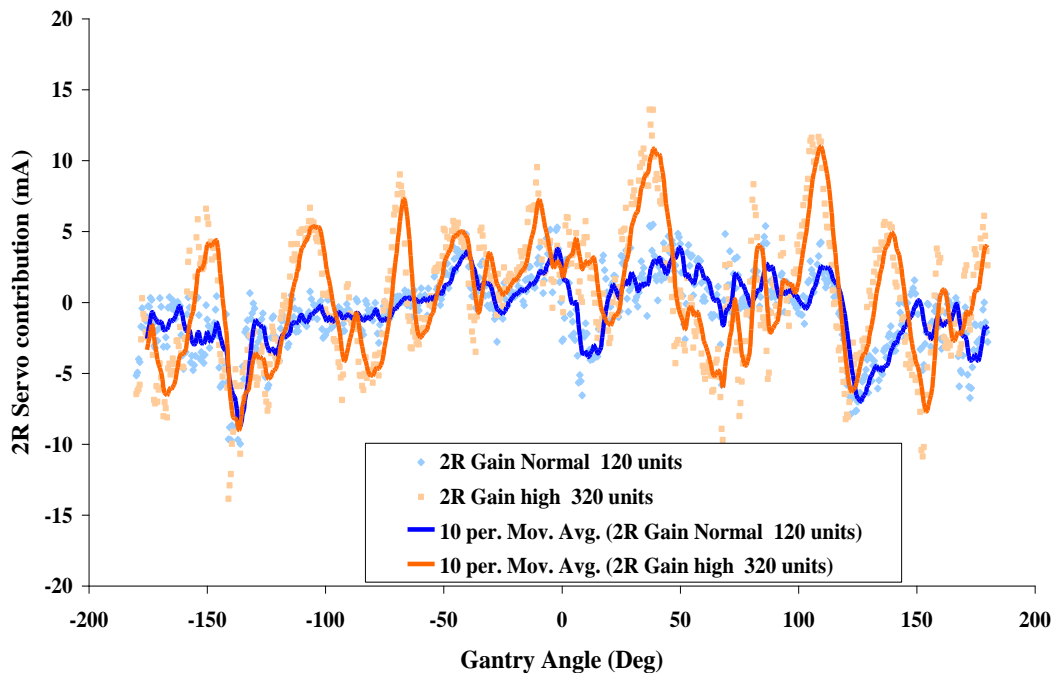


*Figure 8-6: Radial (2R) contribution from the lookup table for the ‘normal beam’ and the beam with the servo gain set to 320 units for one whole CW rotation. A 10 point moving average was used to reduce noise in the plotted data.*

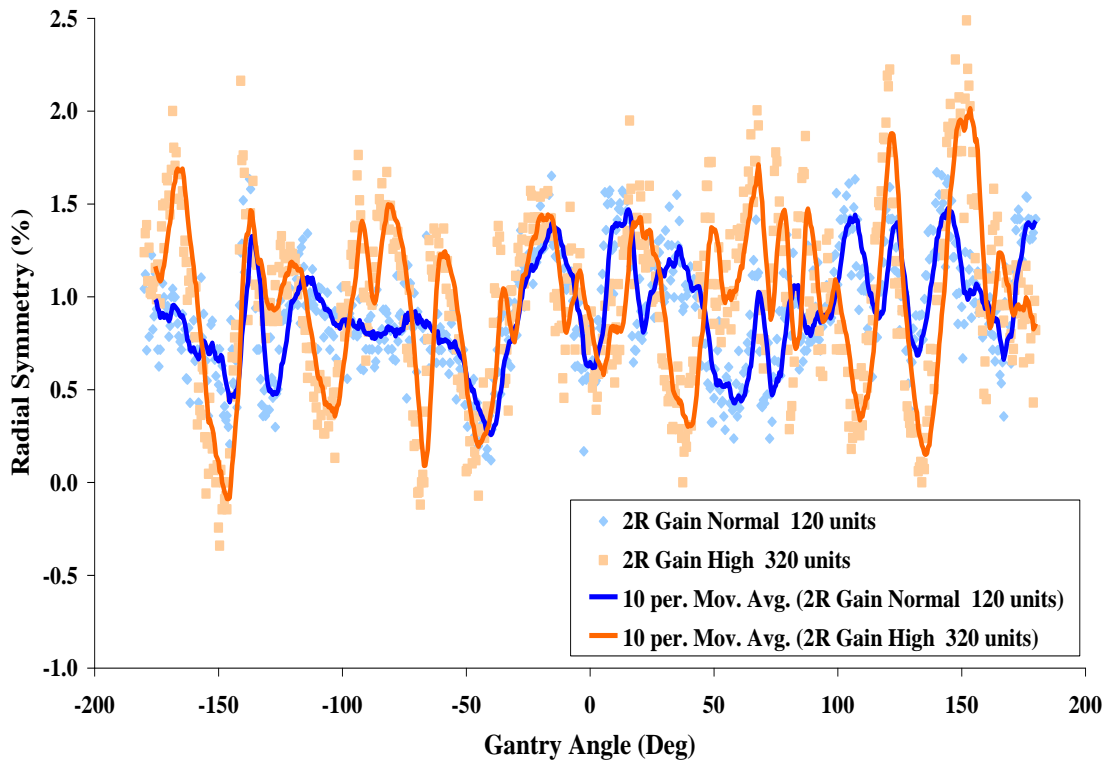


*Figure 8-7: Radial symmetry measured at the 12 cm points for the ‘normal beam’ and the beam with the servo gain set to 320 units for one whole CW rotation. A 10 point moving average was used to reduce noise in the plotted data.*

If the difference between actual servo contributions and beam profiles is plotted for the two cases (Figure 8-8), it is clear that the variation of the beam profile is a direct result of the change in radial/2R current due to the oscillation within the radial servo control loop produced by the increase in gain. Indeed, a correlation coefficient of -0.94 was calculated for the raw data used in Figure 8-8.

### 8.3.2 Dosimetric Effect on Whole Rotations

Having confirmed that the change in radial servo gain resulted in an underdamping in the control loop and subsequent oscillation of the radial beam profile, data for one whole rotation of a ‘normal beam’ was processed, as described (Section 8.2.1) to explore the dose distribution.

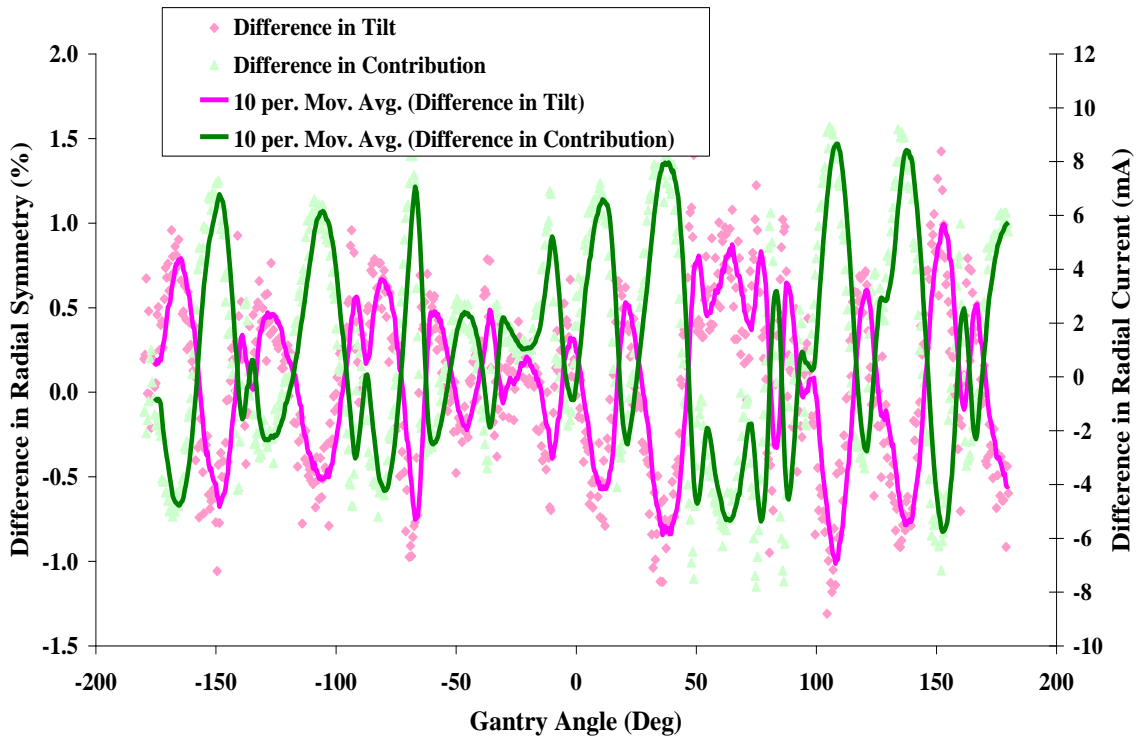


Figure 8-8: Difference between radial servo contributions and beam symmetry for the normal and high servo gain beams. A 10 point moving average was used to reduce noise on the plotted data.

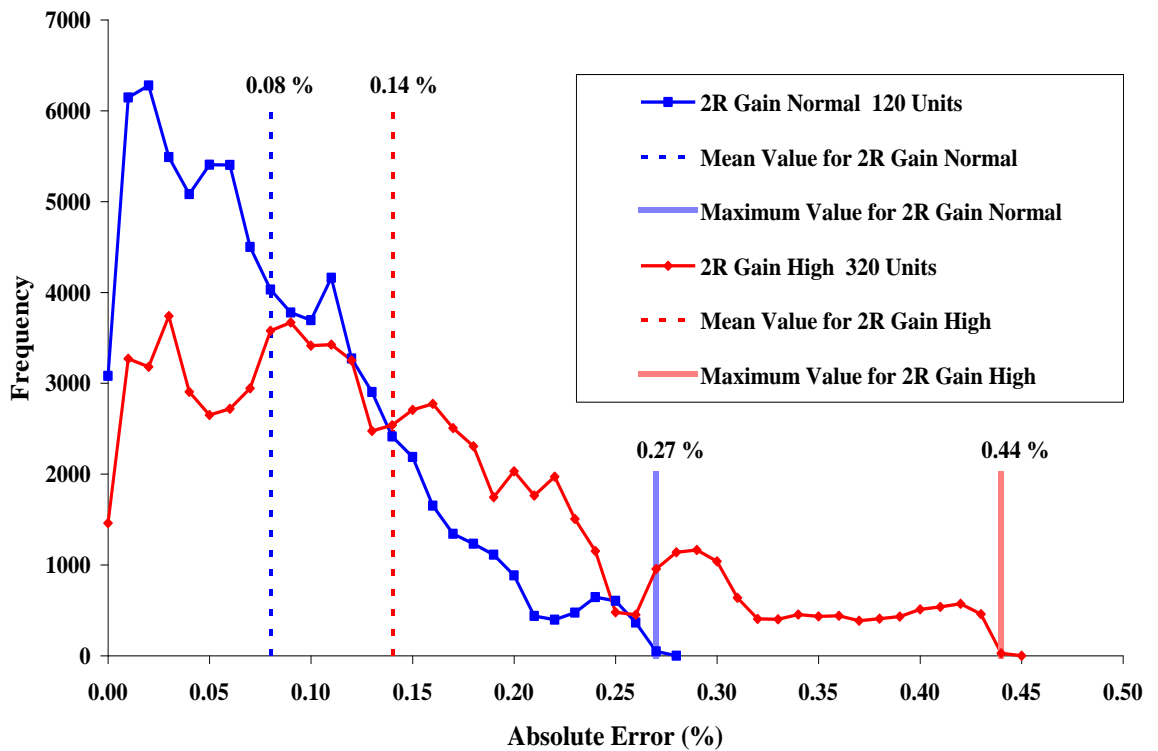


Figure 8-9: Frequency plot of the absolute error in all 77007 points processed within the dose cylinder for the two data sets.

Dosimetric error is calculated as an absolute value in this section, since any deviation is taken as an error whether it is positive or negative, and is therefore not normally distributed. Consequently, the data were binned to produce a frequency plot (Figure 8-9), and to present the dosimetric error results as mean and maximum value with a frequency plot available to show the distribution.

### 8.3.2.1 Dosimetric Error for the Normal Beam

Transverse planes are presented in Figure 8-10 at G12, CAX and T12 with a common absolute dosimetric error scale range of 0 to 0.17 % to allow comparison, and a coronal plane absolute dosimetric error scaled at 0 to 0.27 % allowing for high points at the TA side of the beam edge. The calculated mean absolute dosimetric error for all points within the cylinder was 0.08 % (Max = 0.27 %).

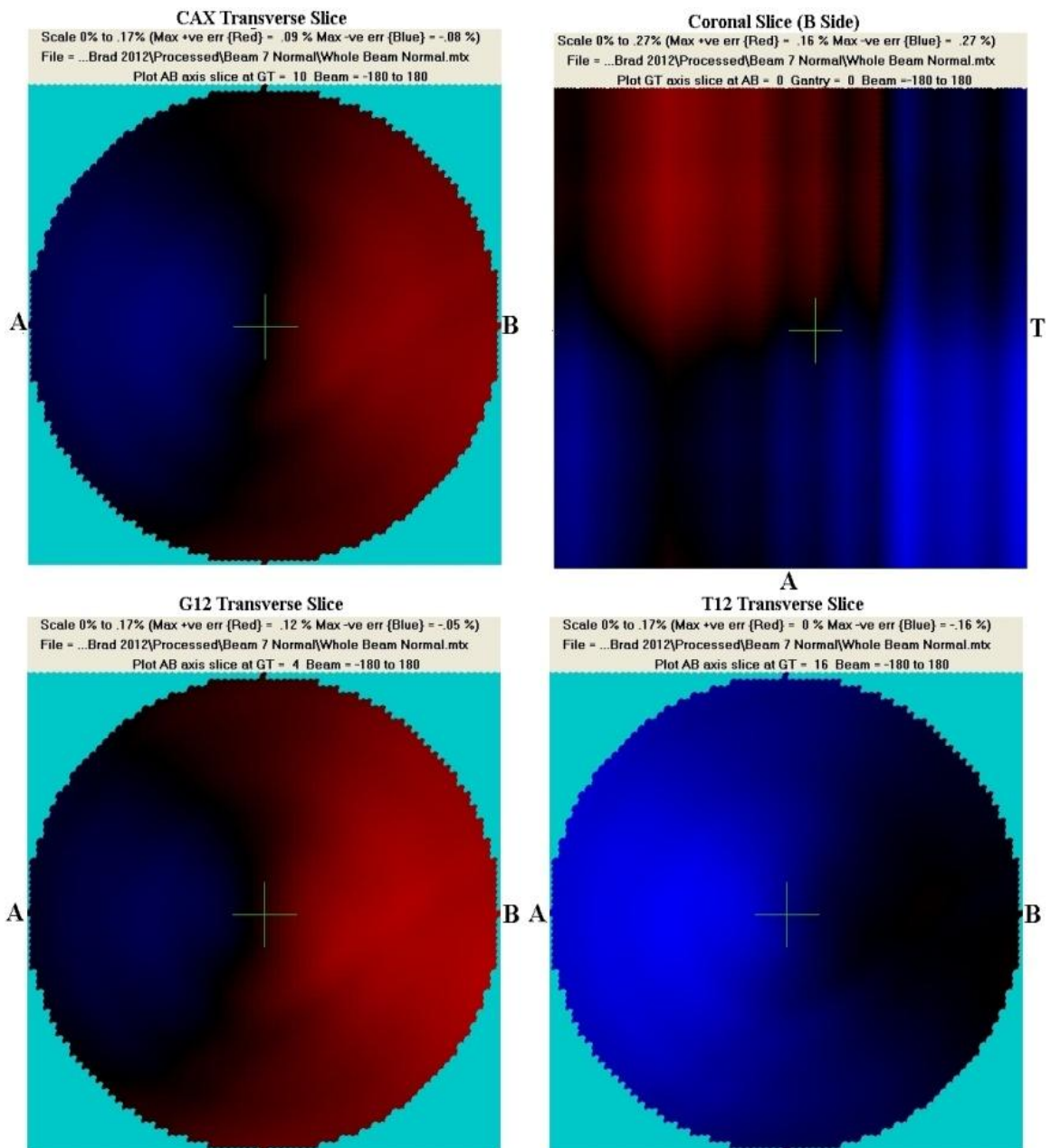
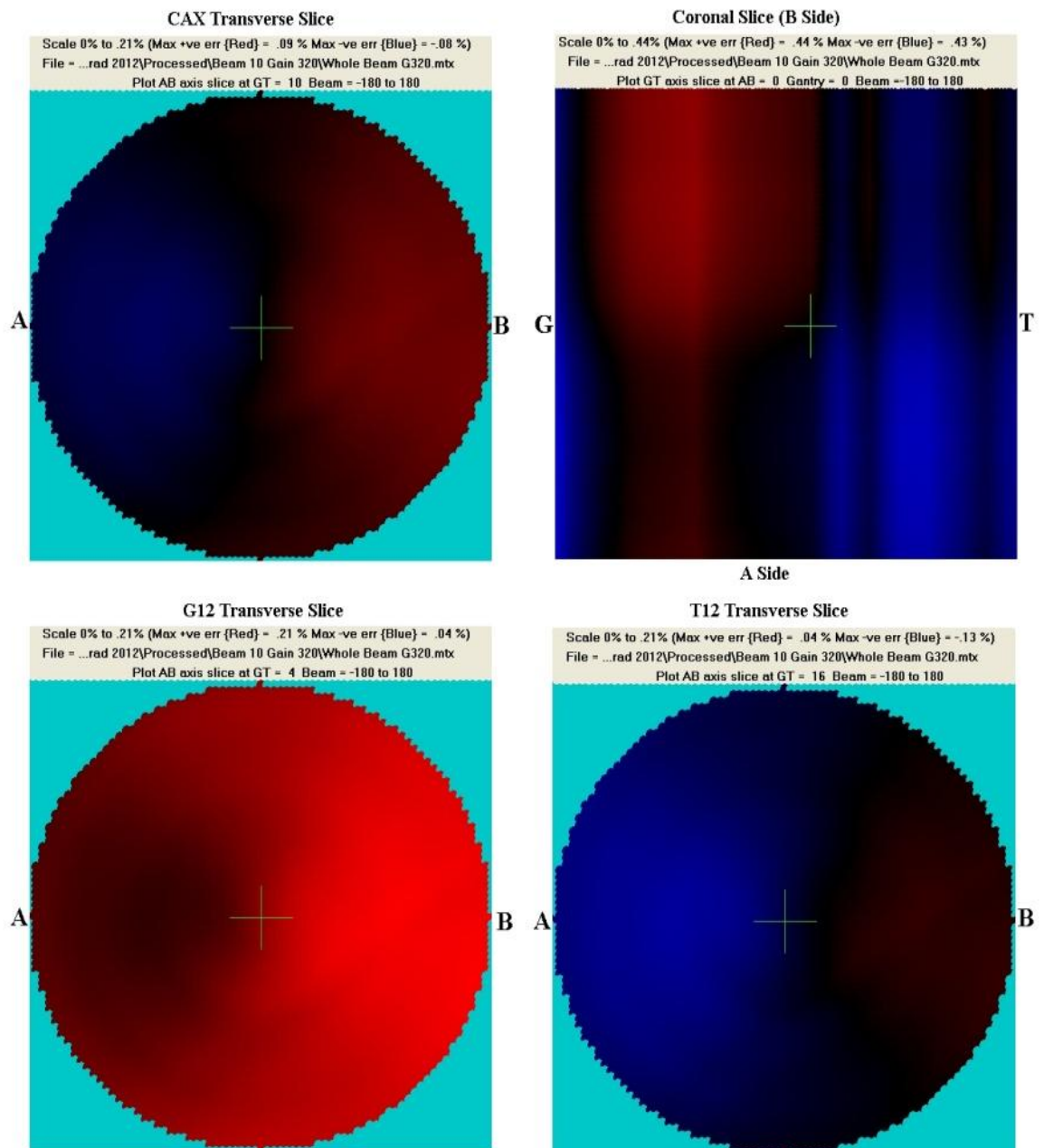


Figure 8-10: Transverse and coronal slices through the dose error map for the 'normal' beam.

### 8.3.2.2 Dosimetric Error for the High Gain Beam

For the case with the high radial servo gain, transverse planes are again presented at G12, CAX and T12 with a common absolute dosimetric error scale range of 0 to 0.21 % and a coronal plane absolute error scaled at 0 to 0.44 % allowing for high points at the TA side of the beam edge (Figure 8-11). The calculated mean absolute dosimetric error for all points within the cylinder was 0.14 % (Max = 0.44 %)



*Figure 8-11: Transverse and coronal slices through the dose error map with the high radial servo gain.*

### 8.3.3 Dosimetric Effects of Segments of Rotation

Using the same source data sets, small sequential arcs of 20 degrees were processed to investigate the ‘averaging effect’ on the dosimetric error over a whole rotation. The absolute dosimetric errors for each segment are plotted in Figure 8-12.

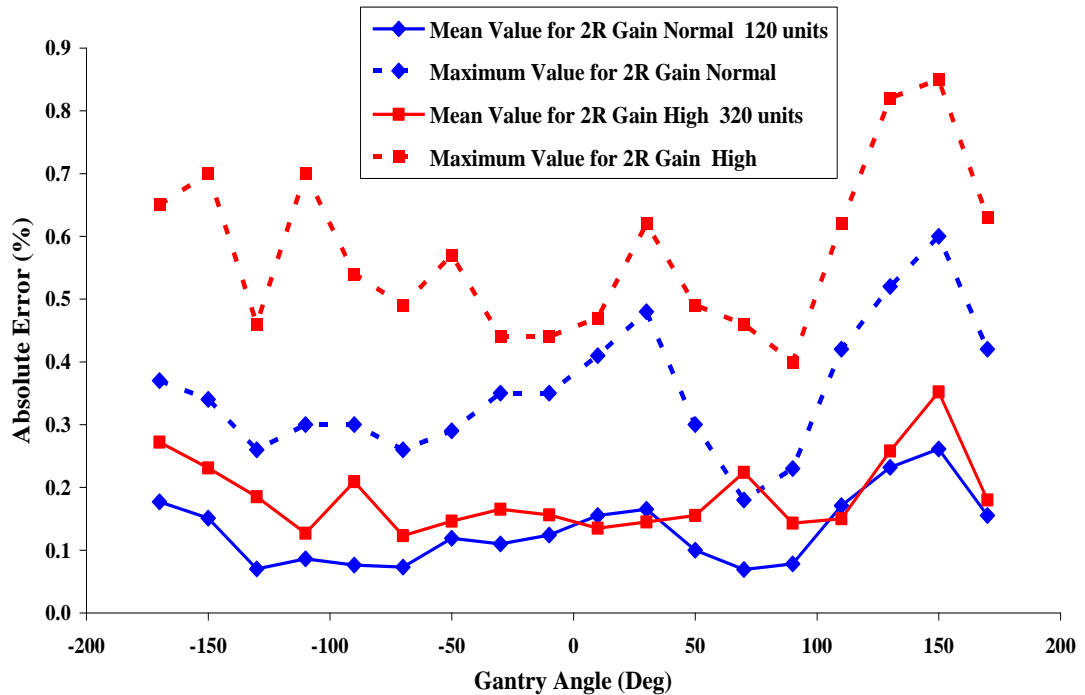


*Figure 8-12: Processed sequential arcs, each of 20 degrees, for both the ‘Normal’ and ‘High’ gain radial servo settings.*

Frequency plots are presented for two 20 degree beam segments for the worst case dosimetric error on the central angle of 150 degrees (Figure 8-14) and at a 10 degree central angle (Figure 8-13) where the error is small. The choice of these two angles assumes that the spread in the data and the extent of the data tail up to the maximum value in the frequency plots signifies the level of oscillation found in the processed data. The mean absolute dose error for all the points in the segment at 10 degrees central angle for the ‘Normal’ and ‘High’ gain beam were 0.16 % (Max = 0.41 %) and 0.14 % (Max = 0.47 %) respectively. The results for the segment at 150 degrees central angle for the ‘Normal’ and ‘High’ gain beam were 0.26 % (Max = 0.6 %) and 0.35 % (Max = 0.85 %) respectively.

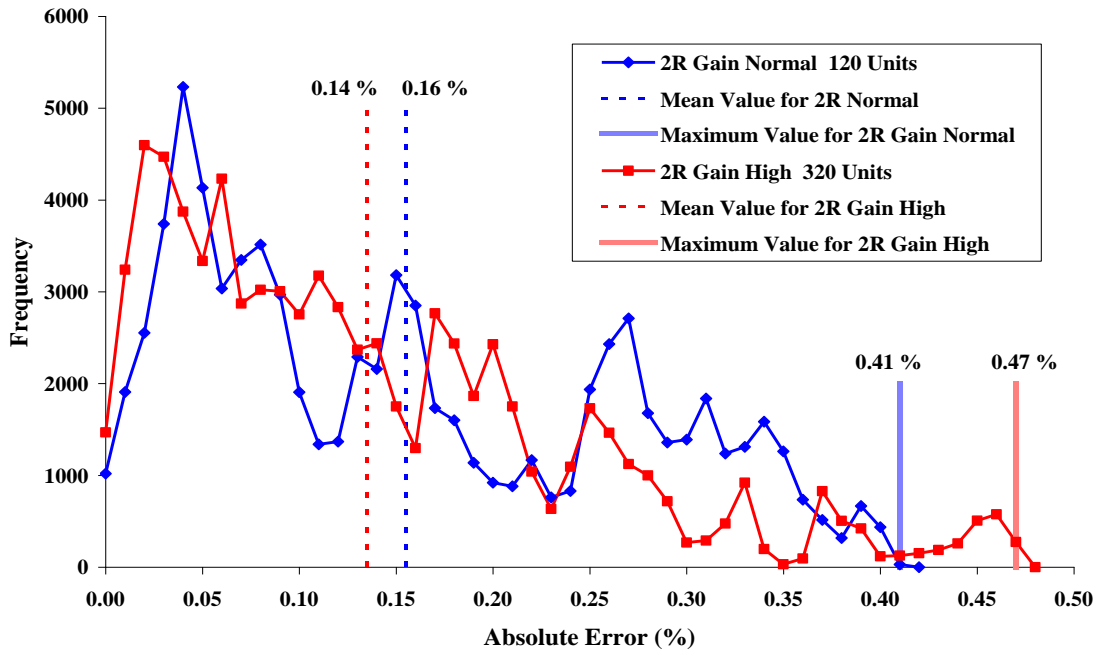


Figure 8-13:: Frequency plot of absolute error in all 70077 points processed within the dose cylinder for a 20 degree beam segment at the central angle of 10 degrees.

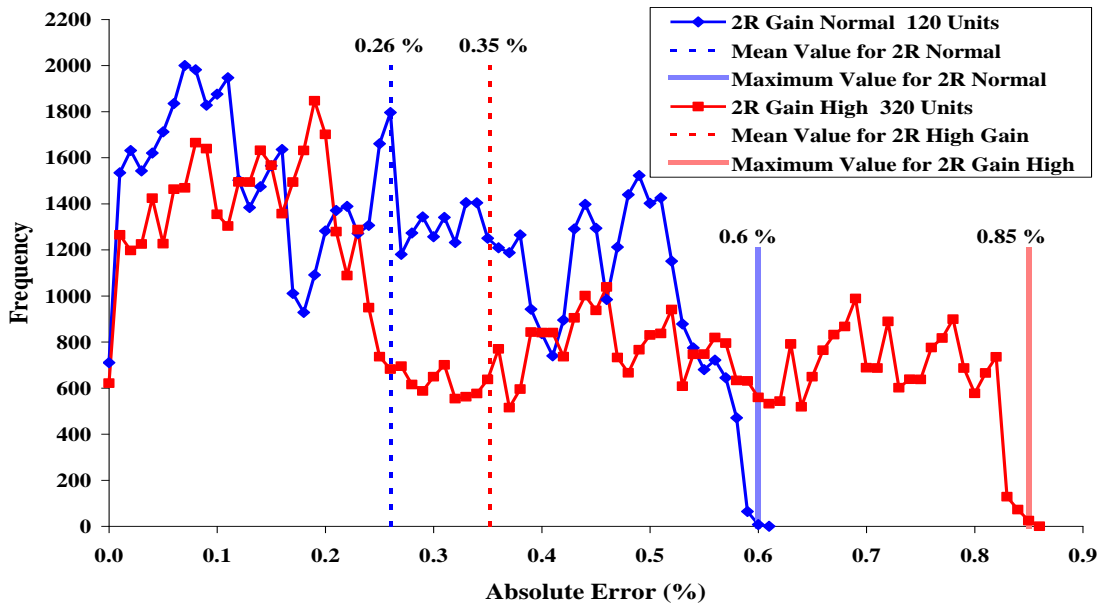
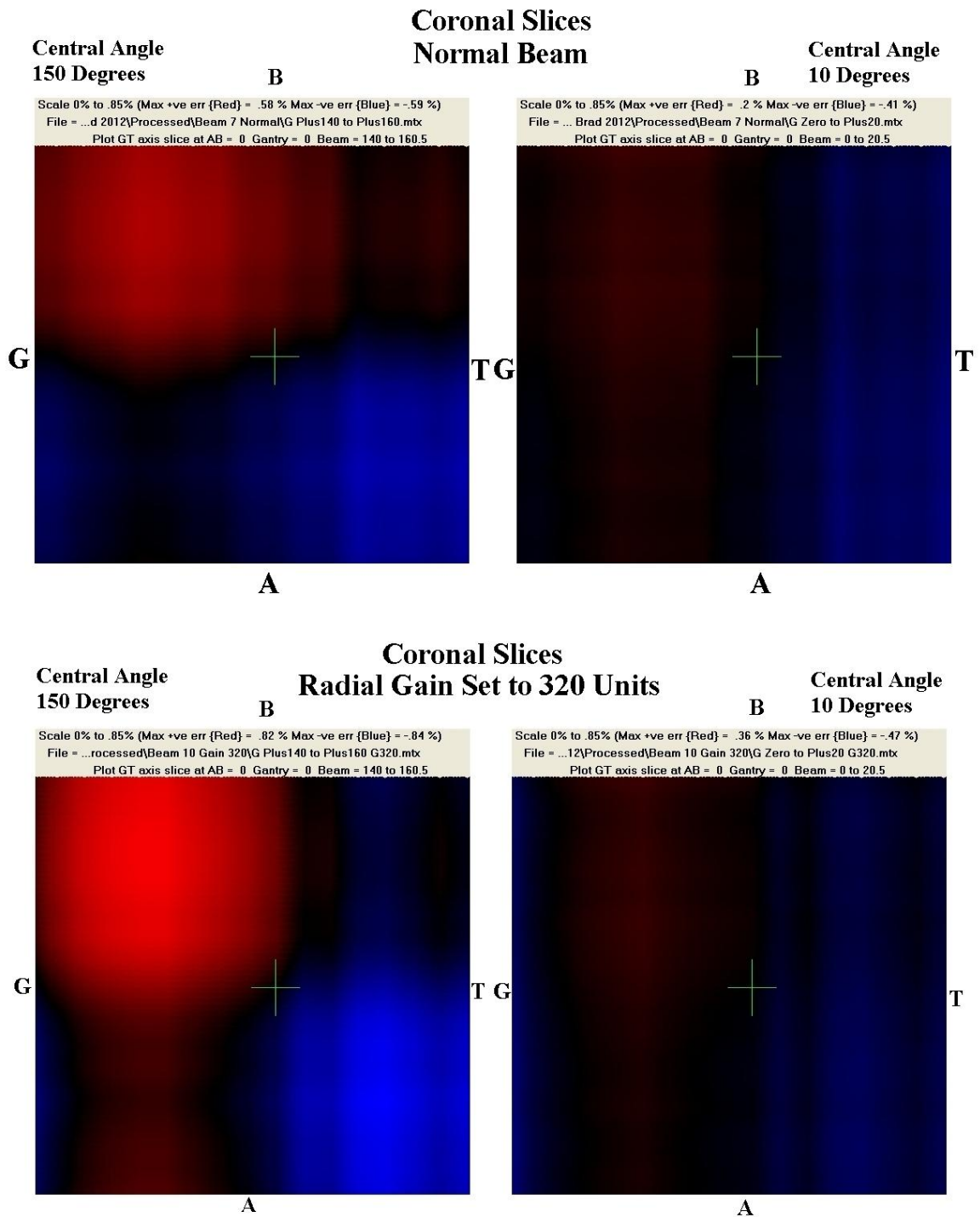


Figure 8-14: Frequency plot of absolute error in all 70077 point processed within the dose cylinder for the worst case 20 degree segment at the central angle of 150 degrees.

Coronal slices are also presented for the same data in Figure 8-13 (central angle = 10 degrees) and Figure 8-14 (central angle = 150 degrees). These are plotted on a common scale range of 0 to 0.85 % absolute error.



*Figure 8-15: Coronal slices for a 20 degree segment for the worse case central angle of 150 degrees and the reference angle of 10 degrees, for both the 'Normal' and the 'High' gain radial servo settings.*

### 8.4 Discussion

Confirmation that the change in radial servo gain resulted in an under-damping of the control loop and subsequent oscillation of the radial beam profile was considered to be important in the design of this experiment. With reference to Figure 8-7, it can be seen that oscillations in the beam profile were of larger amplitude with

the high radial servo gain. The servo maintained radial symmetry over the whole rotation to within 1.3% for the normal beam and 2% with the radial servo gain set to 320 units. However, when processing this data into a 3D dose map, averaging occurs, since all points in the volume are irradiated throughout the 360 degree rotation. This averaging effect resulted in a relatively small dose error for both the cases investigated, with an absolute value of 0.08 % (Max = 0.27 %) for the normal beam, and 0.14 % (Max = 0.44 %) for the beam with the high radial servo gain.

Furthermore, a full 40 x 40 cm field that is rotating at a uniform rate over 360 degrees produces a high level of averaging compared to a small field, using complex MLC shapes, since asymmetries are more likely to cancel. Additionally, the limitation in the modelling with regard to depth dose variation (Section 8.2) means that doses are even more likely to cancel over a complete rotation. For actual rotational therapy, different segments use varying gantry speeds and dose rates and therefore produce different dose distributions. Some points will therefore be more prone to errors than others, compared to the simple situation modeled here, where each point is irradiated from all angles. This is corroborated by the data for small segments in Figure 8-12, where the reduced averaging results in a larger spread in the data for the beam with the greater oscillation in the radial symmetry (gain = 320 units).

Using the 'Beam Scope', it is not possible to assess the geometric component of the 3mm / 3% error requirement (Section 8.1.1.1) due to the low spatial resolution of the ion chamber array. However, the dose error found can be compared to the 3% value, bearing in mind that the errors due to the radial steering system were normalised to the CAX and that other errors are also present. If the small dosimetric errors estimated in the simulations were added in quadrature (Section 8.1.1.1) to other errors of much greater magnitude, where attention for their correction would result in reduction, then the error component due to radial steering defects would be

insignificant in this example. However, should systematic errors be identified in the chain, and are correctable, then this is beneficial to the overall reduction of uncertainty.

This example is one possible area where the 'Beam Scope' system could be used to identify the source of oscillatory components by simultaneous measurement of control signal values and beam profile. The magnitude, frequency and phase relationship of these oscillations could be evaluated and used to improve dose delivery performance. Where oscillations in the beam generation system occur at frequencies closer to the frequency of rotation, it is likely that there would be less averaging over the rotation and therefore greater dosimetric error.

## 8.5 Conclusions

This chapter used data generated by the 'Beam Scope' to estimate the consequences for radiation dose of mis-setting of the accelerator's control system, and demonstrates the potential of the 'Beam Scope' system for performance characterisation. A dosimetric comparison with a commercial device would be a further step in validating this measurement mode and would be a topic for further work (Chapter 9).

In the case presented, the results were not significant for patient dose, which is as expected, since the type of linac evaluated is in use in many radiotherapy centres throughout the world. However, it should not automatically be assumed that this would be the case for other scenarios, for example for lower periodic frequency oscillations, smaller fields with complex delivery structures, or dynamic changes in gantry rotational speed and dose rate. These more complex scenarios are beyond the scope of this chapter.

Given that there are commercial dosimeters available for patient plan verification, it is envisaged that the 'Beam Scope' would prove to be of most value in

the development of linear accelerators. It would have a role in system designs for new machines, or functional upgrades to control systems in existing equipment, for the purpose of identification, characterisation and reduction of systematic errors, more than as a general QA tool. However, this does demonstrate its usage to gain a deeper understanding of the behaviour of accelerator beam transport and generation control systems during dynamic operating conditions in relation to patient dose.

## Chapter 9. Conclusions and Further Work

### 9.1 Conclusions

The introduction of dynamic therapy has brought many challenges to an array of scientific disciplines in radiotherapy. From an engineering perspective, continual development of medical linear accelerators has resulted in highly sophisticated treatment delivery platforms, where greater demands are placed on electron beam transport systems, compared with conventional radiotherapy.

A novel test instrument has been developed that is capable of simultaneously measuring the radiation profile and four associated accelerator control signals in a single pulse of radiation, fully synchronised to the beam generation system of the accelerator. The design and use of an ionisation chamber array capable of measuring the dose delivered during a single radiation pulse was explored in detail. Great care was taken in the development (Chapter 3) and validation phases (Chapter 4) of the design, in order to produce a working system with properties that were well matched to the need for high temporal resolution measurements. Since commercial confidentiality by manufacturers restricted engineering development information about similar equipment from reaching the public domain, extensive testing and validation were undertaken. The result was a design that could be used with a high level of confidence, since stability and performance were confirmed by automated diagnostic testing, logged to a computer file for each measurement session.

Software was developed that enabled results to be viewed off-line and presented graphically. Processing tools were also developed, allowing signals to be filtered to reduce noise and ‘limited’ to remove out of range extraneous signals (clipped). This proved to be an essential feature, since aiding the user to visualise the processes taking place in the control system signals, enhanced the interpretation of the

measured data. Furthermore, dosimetric calibration of the system enabled the results of experiments to be put in the context of dynamic therapy patient dose delivery.

The PIC processor used in the ‘treatment room control box’ proved crucial to the success of the hardware, due to the extensive internal features available to the programmer and its ability to be easily re-programmed, even in-situ while connected to an accelerator.

The system proved to be extremely reliable and easy to configure when used for measurements. This was an essential requirement, since there is significant workload involved in setting up an experiment on an accelerator. Poor physical set-up, incorrect calibration and missing data are not observable until the measured data are processed in an off-line measurement system design. The system does show live data to provide user confidence, but this is only at low temporal resolution. Therefore, access to display and processing tools during the data acquisition phase would be a major enhancement, rather than processing all data off-line away from the accelerator.

In hindsight, a shortfall in the validation process was that when dosimetric calibration beams were measured during a session, the local temperature and pressure should have been recorded. It would have been of interest to note the correlation between the ‘dosimetric calibration factor’ calculated for the measurement session and the air density. This would confirm that the ‘dosimetric calibration factor’ was only correcting for local air density, and did not include an additional errant factor intrinsic to the ionisation chamber design.

While there is a huge range of possible measurements that could have been undertaken, there was limited time available on the accelerator. Furthermore, experiments that were beyond the scope of this thesis had to be curtailed, limiting the number of processes and parameters measured. One of these omissions was the effect that PRF had on the results of the experiments. On reflection, this was a major

limitation, since it would have been most pertinent to the delivery of dynamic therapy. Furthermore, data were only measured in the GT axis.

A longstanding concern of the author during the formation of radial and transverse steering lookup tables (Section 7.2) during machine commissioning and when resolving problems found during machine quality assurance, has been errors in the steering control system reference level with gantry rotational direction. This was investigated in Chapter 7 for the radial steering system, where hysteresis was found in the control system contribution to radial steering error and linked to the direction of gantry rotation. A suspected shifting of masses in the gantry and accelerating waveguide structures (Karzmark C J, 1984, Padikal T N *et al*, 1981) during rotation was explored using an LVDT transducer to measure waveguide displacement, but required further investigation. This was a useful test though, as it demonstrated the ease with which the LVDT transducer could be connected and calibrated to one of the analogue input channels of the 'Beam Scope'. Furthermore, some periodic oscillations and errors in symmetry were noted during rotations and their significance to patient dose was explored in chapter 8, where the errors found would have had little impact on patient dose.

An Elekta SLi series accelerator (M/c 1188) at Leicester Royal Infirmary was used in the majority of experiments. While this machine is not currently in use for the delivery of dynamic therapy, and therefore not strictly maintained or quality assured for this treatment regime, it proved to be more than satisfactory for the delivery of dynamic beams in the experiments that were undertaken. A move to dynamic therapy would simply require the appropriate quality assurance to be in place. In the work presented in Chapter 6, with electron gun filament aiming level set to the correct value, there was a CAX error for a 2 MU beam of 2.4%. When the aiming level was reduced by 50 mA, then the error increased to 2.7%; conversely when the aiming level was increased by 50 mA the error was reduced to 1.7%. Since aging of the electron

gun filament requires the aiming level current to be reduced over time (as discussed in Section 6.1.1) this is favorable for the electron gun filament operating point, since the aiming value is actually higher than the optimum (Section 6.6). Based on the measurements in Chapter 6, a minimum of 4 MU per segment, an electron gun aiming error window of +100 and -50 mA, the delivery error would be less than 1.5% (Figure 6-11).

Beam start-up measurements were undertaken on a Varian 'C' Series iX machine with good results. However, triggering problems were encountered due to the doserate control method employed by this type of accelerator, and again lack of time prevented further investigation. With modest modification to the trigger control software on the 'Beam Scope' treatment room control box (Section 3.9.2) the problem could have been resolved.

The ability of the instrument to observe the relationship between radiation beam profile and control system events concurrently with the radiation pulses at high temporal resolution was confirmed. This was crucial in characterising control system performance and also identifying the source of and possible cure for unexpected system behaviour found in the work presented in the thesis.

## 9.2 Future Developments

As described in the previous section, there were limitations placed on what could be measured in the time available. Developing the 'Beam Scope' system so that it can make measurements on the Varian accelerator is a primary goal, since these new machines are now available on site for system testing, development and measurement. Furthermore, these are currently treating patients using dynamic therapy regimes.

Repeating the experiments presented in the thesis over a range of PRF/doserates is also needed in order to fully understand the processes involved in machine control system behaviour for delivery of dynamic radiotherapy beams with the Elekta accelerator.

It would be useful to develop a further array arranged to simultaneously measure both the radial and transverse axis. This would include salient points at the CAX, 4 cm and 12 cm. The remainder of the spare channels would be used at 8 and 16 cm, resulting in a more comprehensive assessment of the radiation beam profile behaviour.

The software applications for the processing and display of measured data require further development, in the light of what was learnt during the experiments detailed in the thesis. Access to software processing and display tools during data capture would enhance user confidence in data collection. Also, the automated processing of multi-parameter data sets (Section 5.3) would benefit from further development.

The configuration and calibration of the analogue inputs was, in the main, easy to establish, but would benefit from further integration into the software; this would also be a consideration for future development.

Finally, comparison with an appropriate commercial system would be a further step in validating the dosimetric measurement mode. A first task would be to compare the 'Beam Scope' system with one of the commercial systems reviewed in Chapter 2.

The 'Beam Scope' test tool has opened up an array of new measurement possibilities, enabling the engineer to simultaneously view radiation beam profile and control system activity. The author will continue to explore this field to further integrate 'machine engineering' and 'radiation physics' disciplines.

## Chapter 10. Appendices

### 10.1 Appendix 1 - Standard Array Configuration

Most of the linear accelerator measurements undertaken in this thesis use a common configuration, therefore to avoid repetition in the text, the standard configuration will be named 'Standard Array Configuration'. Unless stated otherwise in the text, measurements with the 'Standard Array Configuration' consist of the following:

- Modality X-rays, beam energy 6 MV.
- Servo beam control systems in 'Auto Mode'.
- Collimator angle zero degrees.
- 40 x 40 field size.
- Gantry at zero degrees for static beams.
- Gantry angle defined in the text for rotational beams.
- Accelerator Pulse Repetition Frequency (PRF) of 400
- 100 cm Source Detector Distance (SDD).
- 5 cm deep in Perspex.
- Gun/Target (GT) axis.
- Measurement system warm-up > 15 minutes.
- Electrometer and ion chamber offsets set to zero.
- Ion chamber array high tension supply set to -420 V.
- Ion chamber array centre chamber (No. 10) at the isocentre.
- Ion chamber array pre-irradiated to 12 Gy to eliminate charge buildup.
- Ion transit delay set to 1ms.
- 15 ms sample rate.

## 10.2 Appendix 2 – Details of the Test Ionisation Chamber Array

The test chamber array was designed by the author for a previous project (Figure 10-1). The array was mounted diagonally across an accelerator accessory tray mounting plate (Figure 10-3). Therefore, to measure a major beam axis, the collimator needed to be set diagonally.

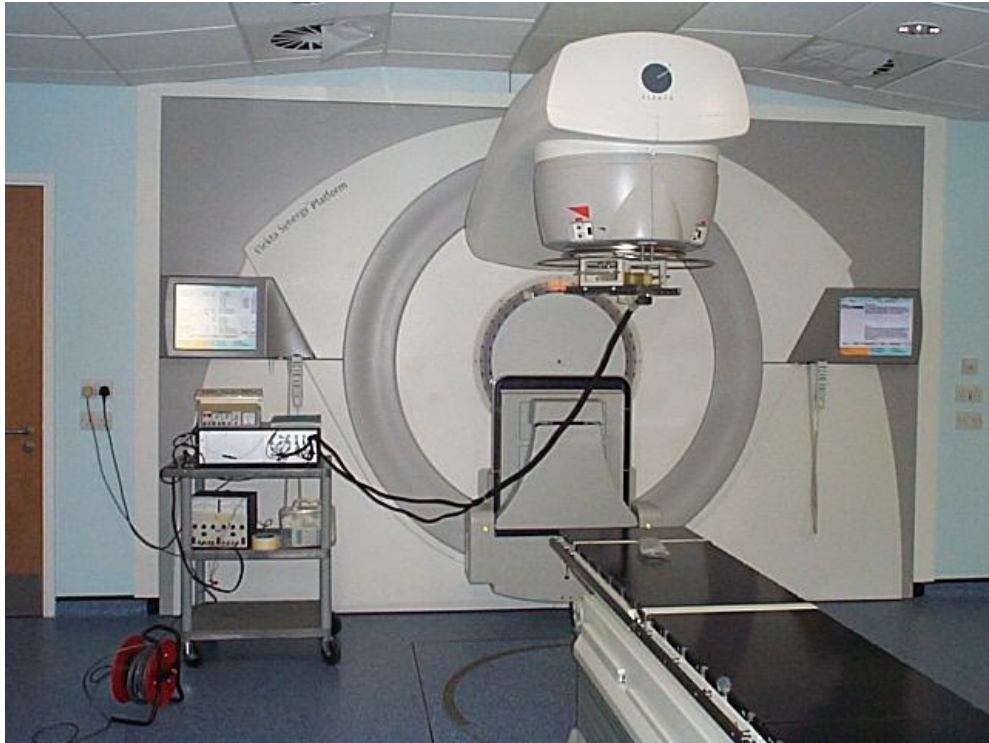


*Figure 10-1: Test ionisation chamber array located in the accelerator accessory tray during 'Beam Scope' system testing (Section 3.5.4.5).*

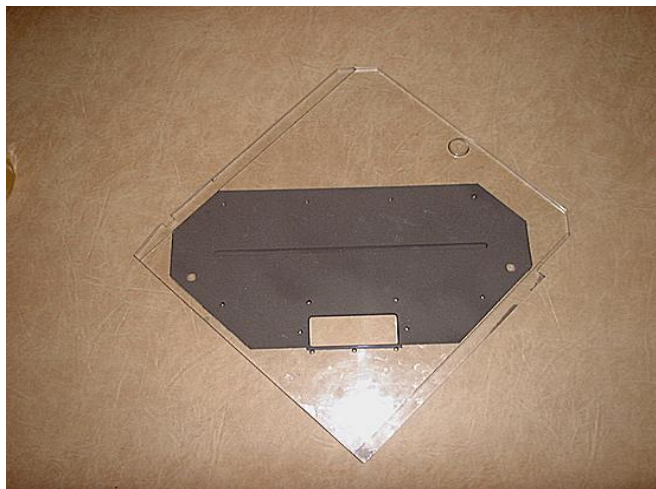


*Figure 10-2: Accelerator accessory tray mounting plate modified to secure the array components. The area designated for the array is painted in electrically conductive paint to form an electrical EMI shield.*

Specification of the test ionisation chamber array:

20 air vented ionisation chambers, spaced 14 mm between centres.

Overall length: 34.8 cm

Overall Width: 14.1 cm

Length of active collecting volume: 31.5 cm

Width of active collecting volume: 4 cm

Collecting plate width: 5 mm

Collecting plate depth: 13.5 mm

Plate separation: 5 mm.

Collecting plate area:  $0.675 \text{ cm}^2$ .

Collecting volume: 0.34 cc.

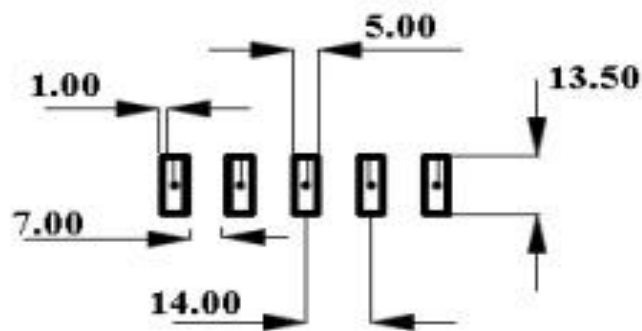
Collecting plate insulation gap: 1 mm

Zero volt guard between collecting plates: 7 mm

High tension supply: -300 V DC.

Ion transit time:  $830 \mu\text{s}$  @ -300 V high tension supply.

- Measuring point 63 cm from the source to the midpoint of the collecting volume. To be fitted in the accessory tray of an Elekta SL series accelerator.



*Detail of the collecting plates for the test array (dimensions are in mm).*

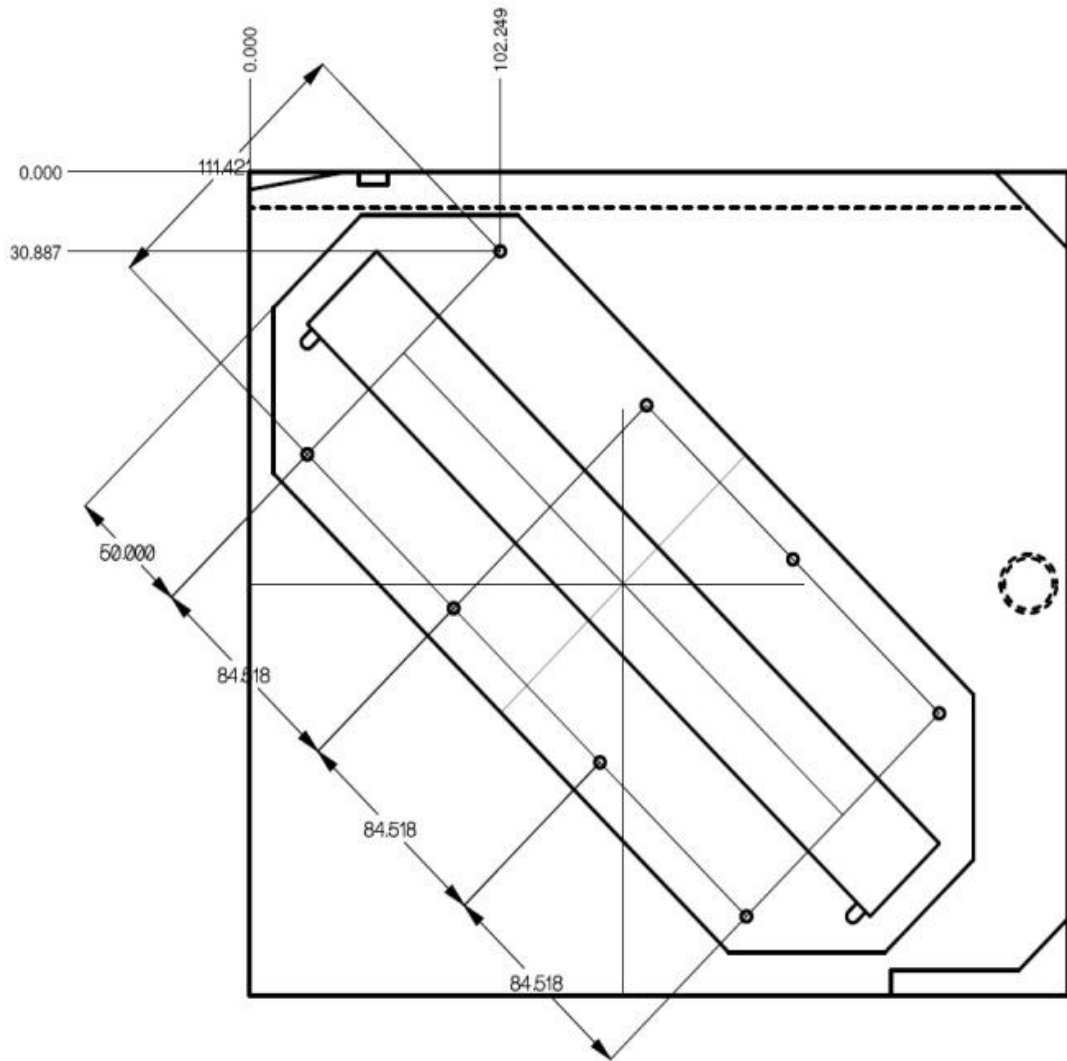


**Figure 10-3: Engineering drawing showing the completed array mounted on the accessory plate (all dimensions are in mm).**

The high tension supply is routed to the spacer plate using a small piece of electrically conductive foam pad that touches the upper part of the insert that is milled out to form the collecting volume in the spacer. This area is sprayed with electrically conductive paint to create the high tension plate of the chamber.

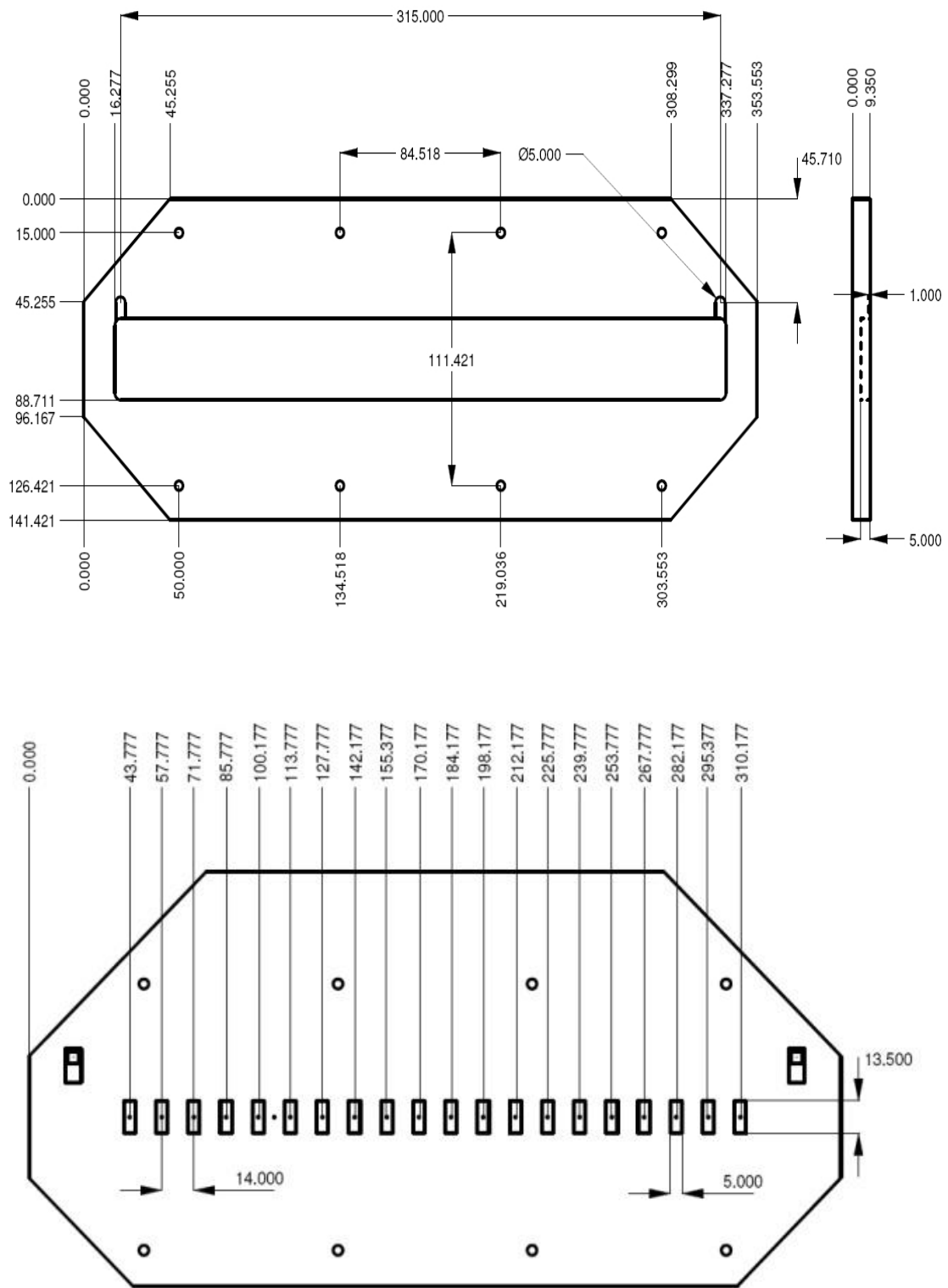


*Figure 10-4: Engineering drawings of the collecting volume, with the high-tension plate created by spraying electrically conductive paint on to the collecting volume, inset in the spacer (top drawing). The details of the 20 collecting plates are shown (bottom drawing) (all dimensions are in mm).*

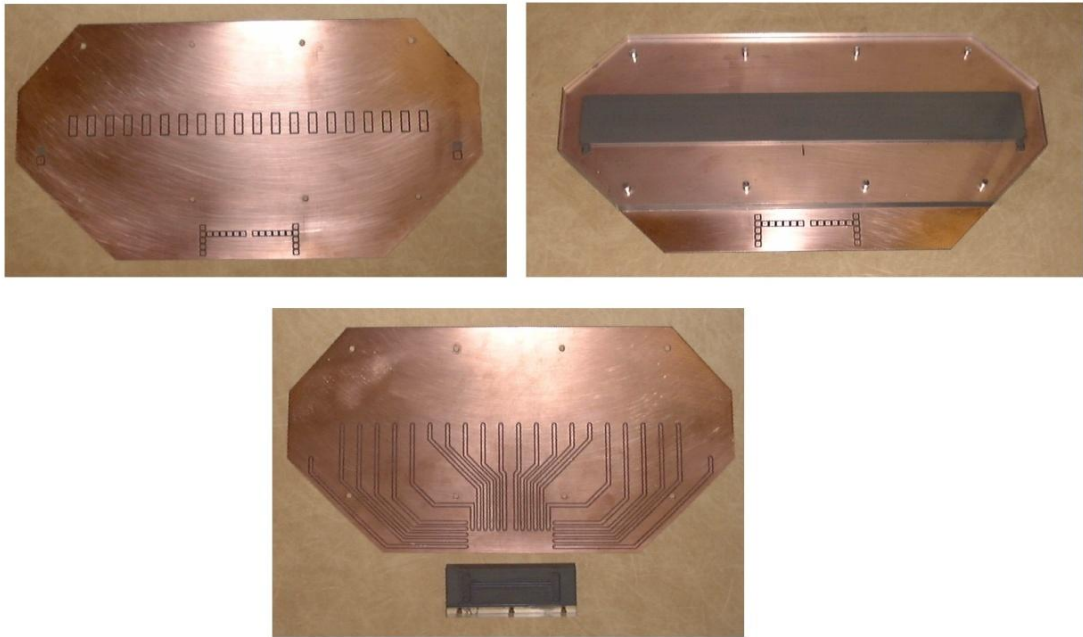


**Figure 10-5:** Photographs of the test chamber during fabrication. Top left shows the collecting plates milled into the copper sheet and top right with the spacer forming the collecting volume and high tension plate. The lower photo shows the underside of the collecting plates and the signal tracks.

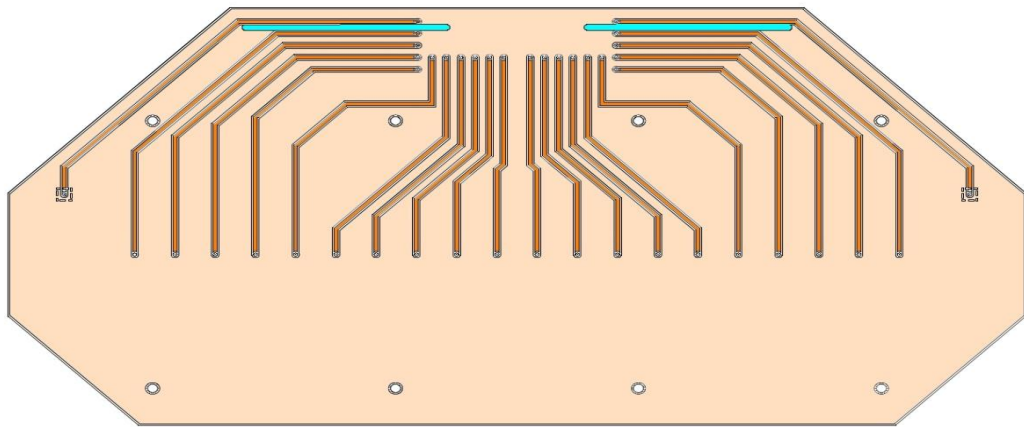


**Figure 10-6:** Diagram of the signal tracks (dark orange) on the underside of the collecting plates. The rest of the copper area (light orange) is connected to signal zero volts. The light blue zone is a cutout in the board to electrically isolate the high-tension supply from the signal tracks, since during testing, surface and substrate leakage was found to be a problem in this area.

The spacers were all made from Perspex sheet and the signal track and charge collecting areas were CNC milled into double-sided copper clad circuit board. Connection to the electrometers and high tension supply was made via a 25 way ‘D type’ connector.

## 10.3 Appendix 3 – Dose Simulator

### 10.3.1 Conception

The problem identified with the reset pulse width and cable capacitance, identified the need to methodically bench test the prototype system during the development phase using a pulse train similar to that found during live testing on a linear accelerator. The pulse train would be a precision pulse generator with settable repetition rate, pulse width and pulse height. Pulsed and fixed level outputs would be required in voltage and current modes, with a range suitable for testing the proposed measurement system.

A radiation beam measurement system was proposed using the PIC18 series microcontroller family (Microchip Technology Inc Arizona USA, 2005) as discussed in Section 3.6.2. The device was to be used in both the simulator and measurement system, with the former providing a valuable introduction and insight in hardware and software of the PIC18 series microcontrollers. A high specification device was chosen from this series, type 18F4520 (18F45 Series devices, Microchip Technology Inc Arizona USA, 2002) based on the RISC architecture. Most instructions are single word and are executed in a single instruction cycle, while each instruction cycle takes 4 system clock periods. Utilising the maximum permissible system clock frequency of 40 MHz (25 ns period) the nominal instruction cycle time is 100 ns resulting in a 10 Million Instructions Per Second (MIPS) execution rate. Due to software limitations in the current development package, a final system clock of 20 MHz was used. (The maximum 40 MHz clock was available for the measurement system project after an upgrade of the development system software).

A host of peripherals is contained within the 18F4520 controller chip including a Universal Asynchronous Receiver Transmitter (UART), various timers, analogue inputs and digital input/output ports. Since the pin out of the device is limited, the

external interfaces to these peripherals are shared on the physical device and not all the internal connections are available to the 'outside world' at the same time. Thus, careful consideration was required of the allocation of external connectivity to the internal components of the PIC controller, to make required signals available to the external hardware of the system under development.

The 18F4520 contains flash memory allowing the program to be erased and re-entered, enabling verification of the compiled code, running on the actual system hardware under development. This substantially reduces the time taken to write and test the target program. Using this system, it is also easy to update the target program in the field should the need arise.

A PC program development environment 'Microcode Studio' (Microengineering Labs Ltd, 2004) is available for the range of PIC devices produced by 'Microchip' and was acquired for the project. An application within the program suite enables a machine code 'Loader' to be programmed into a blank PIC device using custom hardware supplied with the development package. Once programmed with the loader, user developed software can be easily transferred to the PIC program flash memory using a standard serial data link.

To enable the calibration and range of the simulator to be confirmed, the output was designed to interface to a range of commercial dosimeters. Since most of these can be configured to use 'Thimble' or 'Parallel Plate' type ionisation chambers Butler D, 2005, the output interface of the simulator was made compatible with both.

Interface to 'Parallel Plate' chambers (Figure 10-7) is achieved by connecting the collecting plate of the chamber to the input stage of the dosimeter that is referenced to the zero volt line. The other plate of the chamber is connected to the dosimeter high tension power supply.

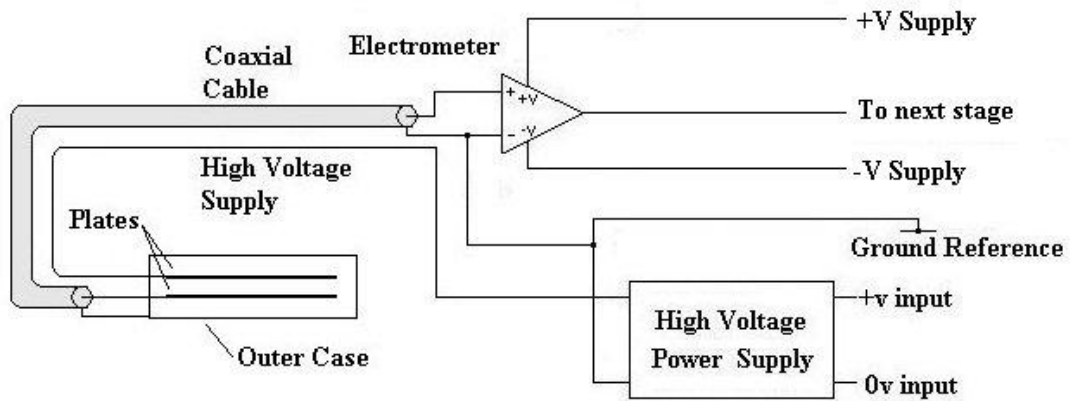


**Figure 10-7:** Dosimeter input stage configuration for a parallel plate ionisation chamber.

Connection to ‘Thimble’ type chambers (Figure 10-8) is more complex, as the outer cap of the chamber is the source of the electric field. This would be connected to the high tension supply in the case of the parallel plate chamber, but must be at ground potential in the ‘Thimble’ type to avoid short circuiting the supply to other equipments and to avoid the danger of electric shock to the user. To overcome this problem, it is common practice to connect the outer cap of the thimble chamber to ground and then ‘float’ the input stage of the dosimeter.

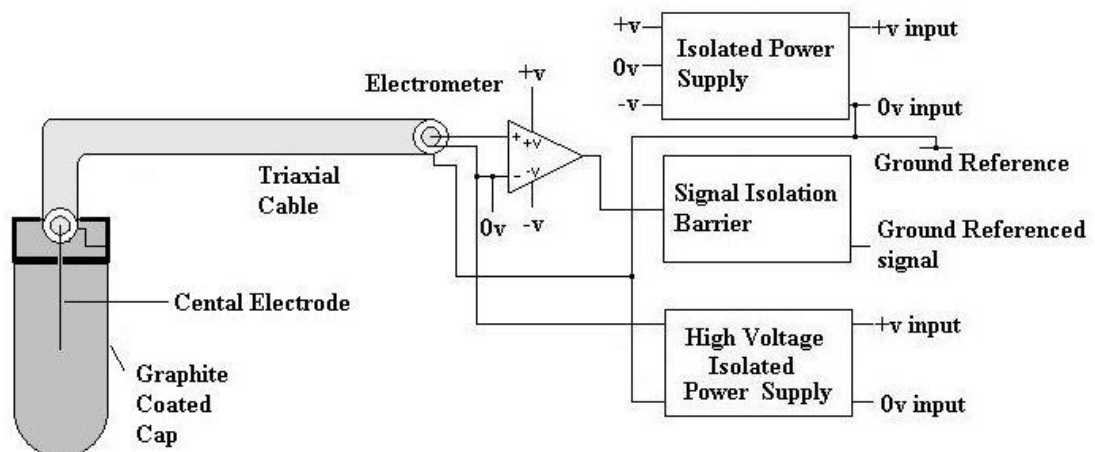


**Figure 10-8:** Dosimeter input stage configuration for a ‘Thimble Ionisation Chamber’.

Connecting the ‘floating’ input stage to the high tension power supply completes the measurement circuit. To achieve this precision electrical isolation of the

input stage from the rest of the dosimeter, carefully designed electronics is required, as detailed in Figure 10-8.

### 10.3.2 Design

A design was developed using an 18F4520 PIC as a user interface and pulse generator with an isolated output interface (Figure 10-9). Digital signal isolation was achieved using opto-couplers, as this overcomes the problem of isolating analogue signals of variable amplitude and pulse width. After digital isolation, the analogue signal is produced by a digital to analogue converter (DAC) on the isolated side of the system.

In DC output mode, the analogue signal is presented to a high value resistor (10 G $\Omega$ ) to act as a voltage to current converter and then routed to the output connector. In pulse mode the analogue signal is used to set the supply voltage to a pulse amplifier which is driven by an optically isolated logic pulse derived from the pulse generator under the control of the PIC. This enables a variable pulse height signal to be generated. This signal is then presented to a high value resistor (200 M $\Omega$ ) in the same way as the DC mode.

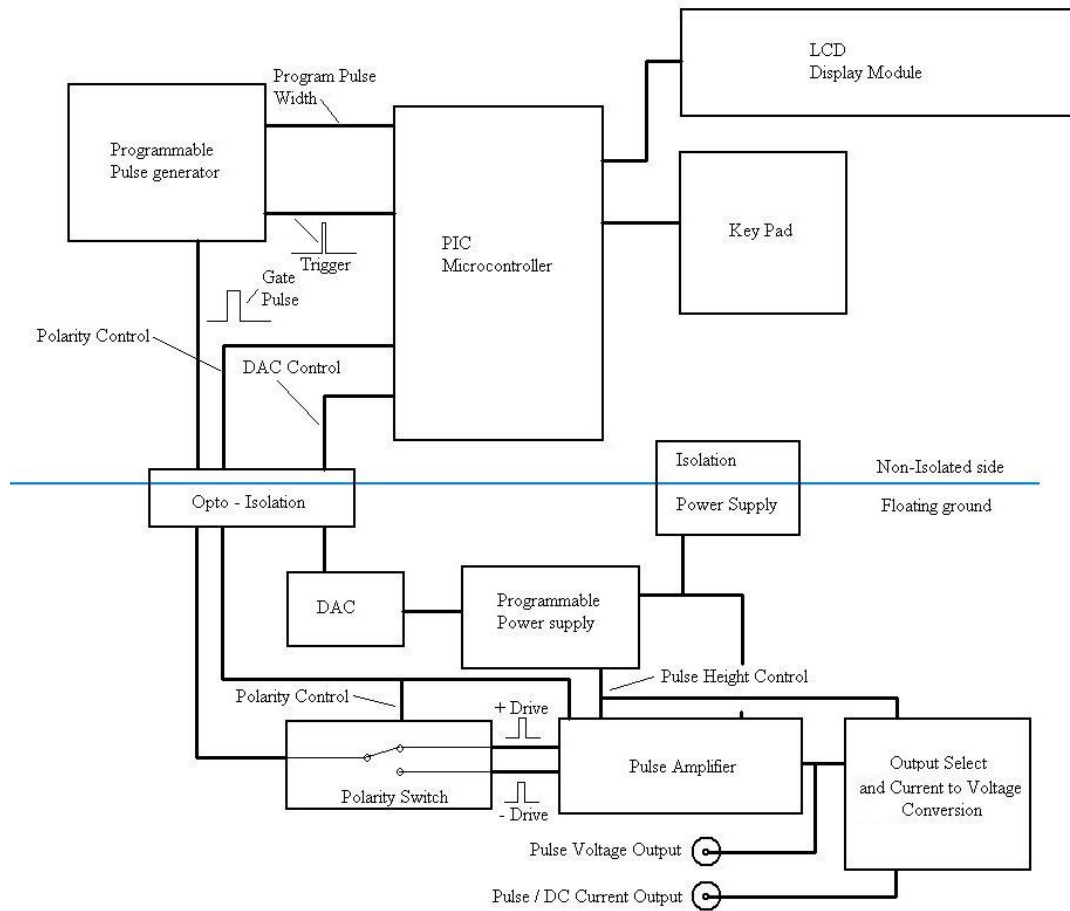


**Figure 10-9: Block diagram of the proposed simulator.**

### 10.3.2.1 Pulse Generation

The proposed design was prototyped and tested on the bench using minimal software to program two of the PIC's internal timers to produce a pulse with settable interval and repetition rate. The pulse interval was set to  $3.2 \mu\text{s}$  and the repetition time to  $2.5 \text{ ms}$ , to simulate a PRF of 400 PPS. The resulting output pulse was sent to an output pin on the PIC and measured using a timer/counter.

### 10.3.2.2 Isolated Interface

An isolated interface for the digital to analogue converter (DAC) and the pulse generator was added to the prototype using opto-couplers for isolation as described earlier. Power for the isolated side of the system was derived from a commercial 'switch mode' device designed for ground isolated supplies, with a guaranteed

isolation barrier of 2500 Volts DC. A DAC with a serial interface was chosen to reduce the number of isolated digital lines required to interface with the PIC. The output of the DAC was filtered to remove any noise induced by the PIC, digital logic and isolation power supply.

**10.3.2.3 Output Interface**

The output interface is floating with no reference to true earth potential. Figure 10-10 shows an outline of the component parts of the interface. The DAC sets the amplitude of the output current in both the DC and pulse modes. The current output modes, positive or negative polarity, are selected by high voltage isolation relays with the coils referenced to true earth potential. This fulfills the requirement for the operator to select the mode using the PIC processor software whilst still maintaining the output isolation.

For DC mode, the output of the programmable power supply is simply connected to a 5 GΩ resistor, as a voltage to current converter, via its selection relay. In pulse mode a logic signal is exclusively connected to a V-groove Metal Oxide (Vmos) power FET driving a step up ratio pulse transformer. This produces a high voltage pulse (range 0 to 400 Volts) which is selected by a relay as in the DC mode and routed to a 200 MΩ resistor, as a voltage to current converter to the output connector.

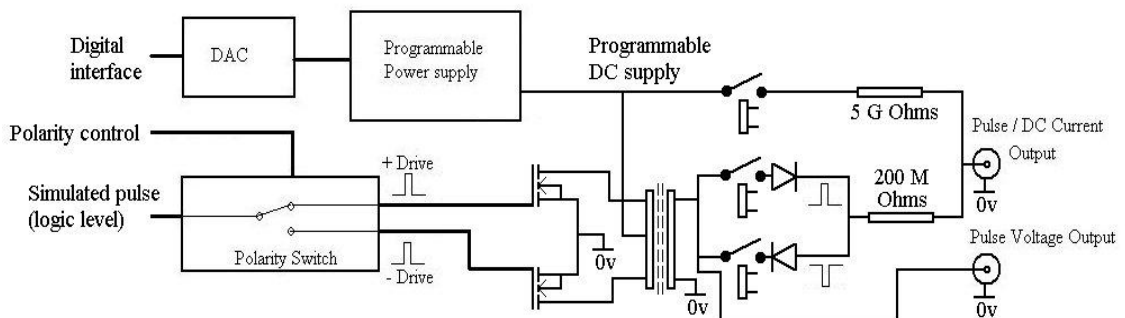


*Figure 10-10: 'Dose Simulator' output interface.*

To produce a programmed quantity of charge the output is activated for a given current over a set period. In DC mode, the DAC output is programmed to zero then the output relay is closed and the DAC is then programmed to the desired level during the simulation period. The DAC is then set to zero and the relay opened. For pulse mode operation the DAC is programmed for the desired pulse amplitude. The appropriate output relay (positive or negative polarity) is closed, and then the pulse generator is activated. The correct number of pulses is delivered during the simulation and when the simulation is complete the output relay is opened.

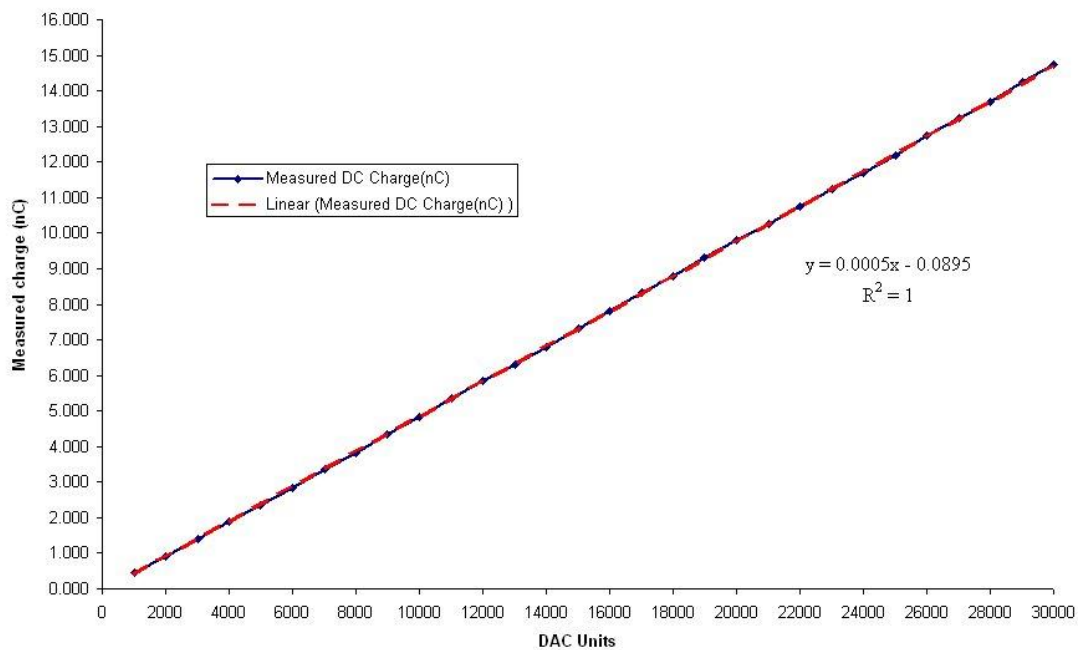
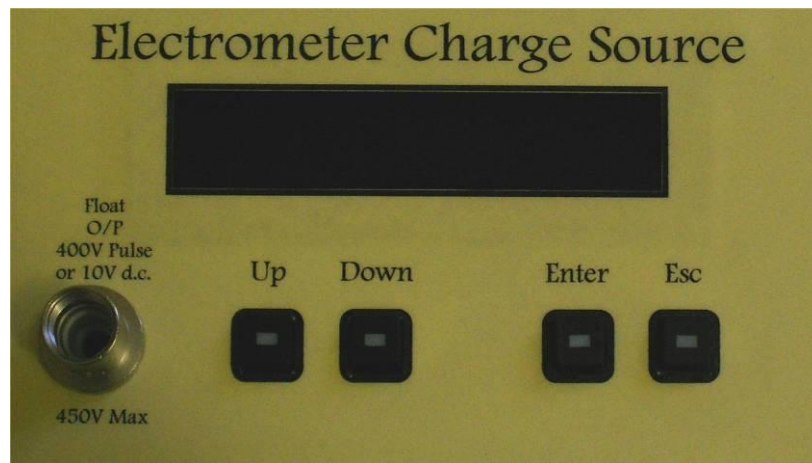


Figure 10-11: DC mode output measured over a range of DAC values. The regression line is also plotted.

### 10.3.2.4 Display and User Keypad

A keypad of 4 push buttons and an intelligent Liquid Crystal Display (LCD) are connected to the PIC (Figure 10-12). Using software, a menu driven user interface enables commands to be executed for data entry, calibration, configuration and execution of charge delivery schemes.



*Figure 10-12: Front panel of electrometer ‘Dose Simulator’ showing the display and keypad.*

### 10.3.3 Construction

Since the ‘Charge Source’ is a one off instrument, it was more practical to fabricate the electronics on copper strip board. This made modifications easier to implement compared with a bespoke PCB. The only area to require special attention was the output interface voltage to current converter resistors. Based on the knowledge gained from the integrating electrometer construction, a PTFE spacer was used to adequately insulate these components from the strip board substrate. Before populating the output interface strip board, a slot was milled across the centre from edge to edge. The isolated output interface was built on one side of the slot and the connection to the PIC on the other. This enabled the isolation components to be mounted across the slot, thus providing a satisfactory electrical barrier between the PIC and the output interface. A metal enclosure was chosen to screen the internal circuits from electromagnetic interference (EMC) and also present a constant leakage capacitance around the pulse transformer. During initial design tests, the transfer characteristics of the pulse transformer were found to be affected by stray capacitance. Inconsistency of the stray capacitance would lead to instability in the calibration of the instrument; this was resolved using a metal enclosure.

#### 10.3.4 Conclusion

A current pulse generator with a settable time period to generate a known charge was constructed and tested. The output was designed to simulate a current pulse train, similar to that generated by a standard ionisation chamber, during X-ray output calibration, of a linear accelerator.

The charge can be preset for a range of ionisation chamber types. The instrument was tested for short term stability and consistency of performance. The purpose of the instrument is to aid the development of a multi-channel electrometer array to measure the radiation beam profile of a linear accelerator at high temporal resolution.

## 10.4 Appendix 4 - System Specification

### Ionisation Chamber Array

- Chambers: 19 (Chamber 10 at the central axis)
- Plate centres: 2 cm
- Plate width: 10 mm
- Plate depth: 20 mm
- Collecting plate insulation gap: 1 mm
- Zero volt guard between collecting plates: 8 mm
- Collecting volume: 1 cc
- Plate separation: 5 mm
- High tension supply: - 420 V
- Charge per pulse: <sup>1</sup>7 pC
- Ion transit time: (420 volt supply) <sub>1</sub>  $\approx$  600  $\mu$ s

### Electrometer and Data Acquisition

- Electrometer channels: 20
- Analogue channels: 4
- Maximum design PRF: 500 Hz (2 ms)
- Electrometer output per pulse: 148 mV <sup>1</sup>
- ADC resolution: 12 bits
- Data acquisition system resolution: 1mV
- Charge resolution 48 fC per ADC step <sup>1</sup>
- 7 pC pulse resolution in 156 ADC steps <sup>1</sup>
- 1.52  $\mu$ Gy resolution per ADC step <sup>1</sup>
- Maximum pulses per sample: 14 (35 ms maximum sample rate at 400 PPS) <sup>1</sup>
- Acquisition time for all input channels:  $\approx$  600  $\mu$ s
- Baseline noise worst case mean of 1.55 +/-0.533 raw ADC units

1. Measurements based on a dose per pulse of 0.0255 cGy, CAX, 5 cm deep in Perspex

## Chapter 11. References

### Reference List

- Allen D, 'Engineering for the market', *IEE Proceedings Part A*, 133 (1986).
- Allibone T E, Bancroft F E, Innnes G S, 'The St. Bartholomew's Hospital X-ray Tube for One Million Volts', *IEE Journal* (IEE, 1939), 657-73.
- Althof V, de Boer J, Huizenga H, Stroom J, Visser A, Swanenburg B, 'Physical characteristics of a commercial electronic portal imaging device', *Med.Phy.*, 23 (1996), 1845-55.
- Analog Devices Ltd, 'Operational Integrators AN537', Stata R, *Application Note* (Analog Devices, 1967).
- Analog Devices Ltd, 'Op Amps as Electrometers - The world of fA', *Periodical, Analog Dialogue* (Analog Devices, 1971).
- Analog Devices Ltd, 'AD 549 Ultra low input bias operational amplifier', *AD 549 Data Sheet* (Analog Devices, 2007), 1-20.
- Andreo P, Nahum A, Thwaites D I, 'Ionisation Chambers', *Handbook of Radiotherapy Physics Theory and Practice* (Taylor and Francis, London, UK, 2007), 279-301.
- Aspradakis M, Walker C, Steele A, Lambert G, 'Radiotherapy Physics - Accelerator Commissioning for IMRT: Small MU Segments and Small Fields', *IPEM 8th Annual Scientific meeting 2002*, 73-4.
- Barish R, Fleischman R, Pipman Y, 'Teletherapy Beam Characteristics', *Med.Phy.*, 14 (1987), 657-61.
- Bates A, Allen J, Weatherup C, McGreevy J, 'Minutes of the EEV and Philips Linac User Group Meeting (EEV Ltd Chelmsford, Essex and Philips Medical Systems (Accelerator Division, Manor royal Crawley UK)', 1996), 1-24.
- Bedford J, Warrington A, 'Commissioning of volumetric modulated arc therapy (VMAT) ', *International journal of radiation oncology, biology, physics*, (2009).

- Bedford J, Webb S, 'Direct-aperture optimization applied to selection of beam orientations in intensity-modulated radiation therapy', *Physics in medicine and biology*, 52 (2007), 479-98.
- Blad B, Jacobsson L, Wendel P, 'The Influence of the magnetron frequency, the servo settings and the gantry angle on the flatness and the dose calibration of a linear accelerator', *Journal of Medical Engineering & Technology*, 22 (1998), 185-8.
- Boag J, 'Ionization Measurements at Very High Intensities Part I', *The British Journal of Radiology*, 23 (1950), 601-11.
- Boag J, 'Space Charge Distortion of the Electric Field in a Plane-Parallel Ionization Chamber', *Physics in medicine and biology*, 8 (1963), 461-7.
- Boag J, 'Distortion of the Electric Field in an Ionization Chamber due to a Difference in Potential between Guard Ring and Collector', *Physics in medicine and biology*, 9 (1964), 25-32.
- Boag J, 'Ionization Chambers', Frank, Roesgh, Tochlin, *Radiation Dosimetry* (Academic Press, 1966), 1-71.
- Boag J, T. Wilson, 'The saturation curve at high ionisation intensity', *British Journ.Applied Physics*, 3 (1952), 222-9.
- Boot H, Randall J, 'Historical notes on the cavity magnetron', *Electron Devices, IEEE Transactions on*, 23 (1976), 724-9.
- Botman J, Bates T, Hagedoorn H, 'A Double Focusing Magnet System for a Medical Linear Electron Accelerator', *Nuclear Instruments and Methods in Physics Research*, B10/11 (1985), 796-8.
- Boyer A, 'A Linear Accelerator Beam Profile Scanner', *Int.J.Radiation Oncology Biol.Phys.*, 6 (1980), 375-7.
- Buchgeistera M, Nusslin F, 'Startup performance of the travelling wave versus standing wave linear accelerator', *Med.Phy.*, 25 (1998), 493-5.
- Budgell G, Martens C, Claus F, 'Improved delivery efficiency for step and shoot intensity modulated radiotherapy using a fast-tuning magnetron', *Physics in medicine and biology*, 46 (2001), N253-N261.
- Butler D, 'Specifying the polarity of the polarizing voltage of an ionisation chamber', *Fact Sheet* (Australian Radiation Protection and Nuclear Safety Agency (ARPANSA), 2005).

- Casebow M, Mayles P, '(Report 81) Megavoltage Equipment (Beam energy. Section 5.2.13)', Mayles P, *Physics Aspects of Quality Control in Radiotherapy* 1999a), 116. ISBN: 0 904181 91 X
- Casebow M, Mayles P, '(Report 81) Megavoltage Equipment (Flatness and symmetry. Section 5.2.11)', Mayles P, *Physics Aspects of Quality Control in Radiotherapy* 1999b), 111-2. ISBN: 0 904181 91 X
- Cashmore J, 'The characterization of unflattened photon beams from a 6 MV linear accelerator', *Physics in medicine and biology*, 53 (2008), 1933-46.
- Cheng C W, Das I J., 'Comparison of beam characteristics in intensity modulated radiation therapy (IMRT) and those under normal treatment condition', *Medical Physics*, 29 (2002), 226-30.
- Chen S. Chui, Spiridon Spirou, Thomas LoSasso, 'Testing of dynamic multileaf collimation', *Medical Physics*, 23 (1996), 635-41.
- Clark C, Hansen V N, Chantler H, Edwards C, James H, Webster G, Miles G, Urbano M, Bhide S, Bidmead A, Nutting C M, 'Dosimetry audit for a multi-centre IMRT head and neck trial', *Radiotherapy and Oncology*, (2009), 102-8.
- Clayton G and Winder S, *Operational Amplifiers* (Fifth Edition, Newnes, 2003).
- Cockcroft J D, Walton E T S, 'Experiments with High Velocity Positive Ions', *Radiation Physics and Chemistry*, 129 (1930), 477-87.
- Collins G B, Clogston A M, Buck J G, Feldmeier J R, Herlin M A, Kroll N M, Millman S, Rieke F F, Smith A G, Smith V W, and Walker L R, *Microwave Magnetrons*, McGraw-Hill Book Company, Ltd., 1948).
- Constantinou C, Sternick E S, 'Reduction of the "horns" observed on the beam profiles of a 6-MV linear accelerator', *Medical Physics*, 11 (1984), 840-2.
- Convery D, Rosenbloom M E, 'The generation of intensity-modulated fields for conformal radiotherapy by dynamic collimation', *Physics in medicine and biology*, 37 (1992), 1359-74.
- Dam J, Merinello G, 'Methods for In Vivo Dosimetry in External Radiotherapy', *Estro Report* (Estro, Mounierlaan 83/12 - 1200 Brussels (Belgium), 2006).
- Das I J, Cheng C W, Watts R, Ahnesjo a, Gibbons J, li X Allen, Lowenstein J, Mitra R, Simon W, Zhu T, 'Accelerator beam data commissioning equipment and procedures: Report of the TG-106 of the Therapy Physics Committee of the AAPM', *Med.Phys.*, 35 (2008), 4186-215.

Das I J., Kase K R, Tello V M, 'Dosimetric accuracy at low monitor unit settings', *The British Journal of Radiology*, 64 (1991), 808-11.

Dearnaley G, 'Nuclear radiation detection by solid state devices', *Journal of Scientific Instrumentation*, 43 (1966), 869-788.

Dupen W D, 'Development of the electron Linear Accelerator (Slac)', *The story of Stanford's 2 mile long accelerator* (Stanford Linear Accelerator Division, 2007), 34-58.

e2v Technologies Ltd, 'MG 5028 Precision Tuned Magnetron', *Magnetron Data Sheet A1A-M5028 Issue 6* (e2v Ltd, Chelmsford UK, 2002a).

e2v Technologies Ltd, 'MG 6028 Fast Tuned Magnetron', *Magnetron Data Sheet A1A-MG6028 Issue 2* (e2v Ltd, Chelmsford UK, 2002b).

Enge H A, 'Particle accelerator provided with an adjustable 270 Degree Non-despersive magnet beam benders', US Patent, *Patent No. 3379911 (Filed 1965)* (USA, 1968).

English Electric Valve Company Ltd, 'Magnetron Preamble', *EEV Magnetron Application Data Sheet* (EEV Ltd Chelmsford UK, 1974).

Ford J C, 'The Microwave Electron Linac in the Treatment of Cancer', *Proceedings of the 2001 Particle Accelerator Conference, Chicago* (Particle Accelerator Conference, 2001), 639-41.

Fowler J F, 'Radiation-induced Conductivity in the Solid State, and Some Applications', *Physics in medicine and biology*, 3 (1959), 395-410.

Fry D W, Walkinshaw W, 'Linear Accelerators', *Linear Accelerators* (Telecommunications Research Establishment, Great Malvern, Worcs.UK, 1949), 102-32.

Gillin M, Quillin R, 'Variation in output with a fixed dose setting on a 4-MV linear accelerator', *Medical Physics*, 3 (1976), 107-8.

Glendinning A G, 'Studies of the dosimetric verification of IMRT', *PhD Thesis* (University of Leicester), 2001).

Glendinning A G, Hunt S G, Bonnett D E, 'A method for controlling image acquisition in electronic portal imaging devices', *Physics in medicine and biology*, 36 (2001a), N39-N44.

- Glendinning A G, Hunt S G, Bonnett D E, 'Measurement of the response of Gd<sub>2</sub>O<sub>2</sub>S:Tb phosphor to 6 MV X-rays', *Physics in medicine and biology*, 46 (2001b), 517-30.
- Glendinning A G, Hunt S G, Bonnett D E, 'Recording accelerator monitor units during electronic portal imaging: application to collimator position verification during IMRT', *Physics in medicine and biology*, 46 (2001c), N159-N167.
- Greene D., Williams P C, 'Basic Processes in Electron Acceleration - The Accelerating Waveguide', (*Linear Accelerators for Radiation Therapy* (Institute of Physics Publishing (IOP), 1985a), 10-24. ISBN: 0750304766
- Greene D., Williams P C, 'Control and Interlock Systems', (*Linear Accelerators for Radiation Therapy* (Institute of Physics Publishing (IOP), 1985b), 138-63. ISBN: 0750304766
- Greene D., Williams P C, 'The Electron Beam (Its Production and Transport)', (*Linear Accelerators for Radiation Therapy* (Institute of Physics Publishing (IOP), 1985c), 55-69. ISBN: 0750304766
- Greene D., Williams P C, 'The Microwave System and its High-Voltage Supplies', (*Linear Accelerators for Radiation Therapy* (Institute of Physics Publishing (IOP), 1985d), 27-45. ISBN: 0750304766
- Grigorov G N, Chow J C L, Barnett R B, 'Dosimetry limitations and a dose correction methodology for step-and-shoot IMRT', *Physics in medicine and biology*, 51 (2006), 637-52.
- Grusell E, Rikner G, 'Evaluation of temperature effects in p-type silicon detectors', *Physics in medicine and biology*, 31 (1986), 527-34.
- Guerrero Urbano M, Nutting C, 'Part 1 of 2: Clinical use of intensity-modulated radiotherapy', *The British Journal of Radiology*, 77 (2004a), 88-96.
- Guerrero Urbano M, Nutting C, 'Part 2 of 2: Clinical use of intensity-modulated radiotherapy', *The British Journal of Radiology*, 77 (2004b), 177-82.
- Haas O, Mills J, Crichton R, Shapre P, Burnham K, 'Systems Modelling Approach to Quality Control for Linear Accelerators', *Journal of Computer Simulation & Modelling in Medicine*, 1 (2000), 46-53.
- Halnan K E, 'Fifty Years of the National Health Service 1948-1998: A Personal History of Progress in the Treatment of Cancer', *Clinical Oncology*, (1999), 55-60.

- Hansen V N, Evans P M, Mott J H L, Budgell G J, Brugmans M J P, Mijnheer B J, Brown K, Wittkamper F W, 'Quality Assurance of the Dose Delivered by Small Radiation Segments', *Physics in medicine and biology*, 43 (1998), 2665-75.
- Herzen J., Todorovic M., Cremers F., Platz V, Albers D, Bartels A, Schmidt R, 'Dosimetric evaluation of a 2D pixel ionization chamber for implementation in clinical routine', *Physics in medicine and biology*, 52 (2007), 1197-208.
- Horsley R J, Price R H, Saunders J E, Dingwall P W, 'Performance of a 6 MeV Varian linear accelerator', *The British Journal of Radiology*, 41 (1968), 312-6.
- Houdayer A, Lebel C, Leroy C, Roy P, Linhart V, Pospisil S, Sopko B, Coutremanche S, Stafford M, 'Silicon planar MESA diodes as radiation detectors', *Nuclear Instruments and Methods in Physics Research Section A: Accelerators, Spectrometers, Detectors and Associated Equipment*, 476 (2002), 588-95.
- Hubner and Suhner Ltd, 'Suhner co-axial cable', *Data Sheet (G 02330 HT)* (Hubner and Suhner Ltd., 2007).
- Iida T, Kokubo Y, Sumita K, Wakayama N, Yamagishi H, 'A Fast Response Electrometer for Pulse Reactor Experiments', *Nuclear Instruments and Methods*, 152 (1978), 559-64.
- Ising G, "'Prinzip einer Methode zur Herstellung von Kanalstrahlen Hoher Voltzahl'", *Arkiv för Matematik*, 18 (1924).
- Jiang Z, Earl M, Zhang G, Yu C, Shepard D, 'An examination of the number of required apertures for step-and-shoot IMRT', *Physics in medicine and biology*, 50 (2005), 5653-63.
- Johansson B, Wickman G, 'General collection efficiency for liquid isooctane and tetramethylsilane used as sensitive media in a parallel-plate ionization chamber', *Physics in medicine and biology*, 42 (1997), 133-45.
- Johansson B, Wickman G, Bahar-Gogani J, 'General collection efficiency for liquid isooctane and tetramethylsilane in pulsed radiation', *Physics in medicine and biology*, 142 (1997), 1929-38.
- Johns H, Rawlinson J, Taylor W, 'Matrix dosimeter to study the uniformity of high energy x-ray beams', *American Journal of Roentgenology*, 120 (1974), 192-201.
- Jones A, 'The Application of Some Direct Current Properties of Silicon Junction Detectors to y-ray Dosimetry', *Physics in medicine and biology*, 8 (1963), 451-9.

- Jordan T J, Williams P C, 'The design and performance characteristics of a multileaf collimator', *Physics in medicine and biology*, 39 (1994), 231-51.
- Kallman P., Lind B., Eklof A., Brahme A., 'Shaping of arbitrary dose distributions by dynamic multileaf collimation', *Physics in medicine and biology*, 33 (1988), 1291-300.
- Sei K. Kang, Kwang H. Cheong, Taejin Hwang, Byung C. Cho, Su S. Kim, Kyoung J. Kim, Do H. Oh, Hoonsik Bae, Tae S. Suh, 'Dosimetric characteristics of linear accelerator photon beams with small monitor unit settings', *Medical Physics*, 35 (2008), 5172-8.
- Karzmark C J, 'Advances in linear accelerator design for radiotherapy', *Medical Physics*, 11 (1984), 105-28.
- Karzmark C J, Nunan C, E Tanabe, 'Accelerator Control and Interlocking', (*Medical Electron Accelerators* (McGraw-Hill, 1993a), 169-88. ISBN: 0 07 105410 3
- Karzmark C J, Nunan C, E Tanabe, 'Beam Optics of Bend Magnet Systems', (*Medical Electron Accelerators* (McGraw-Hill, 1993b), 115-36. ISBN: 0 07 105410 3
- Karzmark C J, Nunan C, E Tanabe, 'Dose Monitoring and Beam Stabilization', (*Medical Electron Accelerators* (McGraw-Hill, 1993c), 157-68. ISBN: 0 07 105410 3
- Karzmark C J, Nunan C, E Tanabe, 'Microwave Accelerating Structures', (*Medical Electron Accelerators* (McGraw-Hill, 1993d), 67-87. ISBN: 0 07 105410 3
- Karzmark C J, Nunan C, E Tanabe, 'Microwave Power Sources and Systems', (*Medical Electron Accelerators* (McGraw-Hill, 1993e), 89-104. ISBN: 0 07 105410 3
- Karzmark C J, Nunan C, E Tanabe, 'Multi-X-Ray Energy Accelerators', (*Medical Electron Accelerators* (McGraw-Hill, 1993f), 189-99. ISBN: 0 07 105410 3
- Karzmark C J, Nunan C, E Tanabe, 'Pulse Modulators and Auxiliary Systems', (*Medical Electron Accelerators* (McGraw-Hill, 1993g), 105-13. ISBN: 0 07 105410 3
- Karzmark C J, Nunan C, E Tanabe, 'The Medical Electron Accelerator', (*Medical Electron Accelerators* (McGraw-Hill, 1993h), 1-30. ISBN: 0 07 105410 3
- Karzmark C J, Nunan C, E Tanabe, 'Treatment Beam Production', (*Medical Electron Accelerators* (McGraw-Hill, 1993i), 137-56. ISBN: 0 07 105410 3

- Karzmark C J, Pering N C, 'Electron linear accelerators for radiation therapy: history, principles and contemporary developments', *Physics in medicine and biology*, 18 (1973), 321-54.
- Khan F M, 'Measurement of Ionizing Radiation', *The Physics of Radiation Therapy* (Lippincott Williams & Wilkins, 2003). ISBN: 0781788560
- Kijewski P K., Chin L M., Bjarngard B E., 'Wedge-shaped dose distributions by computer-controlled collimator motion', *Medical Physics*, 5 (1978), 426-9.
- Kirby M, Glendinning A G, 'Developments in electronic portal imaging systems', *The British Journal of Radiology*, 79 (2006), S50-S65.
- Knapp E A, Knapp B C, Potter J M, 'Standing Wave High Energy Linear Accelerator Structures', *Review of Scientific Instruments*, 39 (1968), 979-91.
- Knoll G, 'Ionization Chambers', *Radiation Detection and Measurement* (John Wiley & Sons, 2000a), 152-81. ISBN: 0-471-07338-5
- Knoll G, 'Semiconductor Diode Detectors', *Radiation Detection and Measurement* (John Wiley & Sons, 2000b), 359-85. ISBN: 0-471-07338-5
- Koschel K, Clarke H., 'An instrument for the rapid measurement of X-ray field flatness', *The British Journal of Radiology*, 36 (1963), 538-41.
- Lennox A J, 'Accelerators for cancer therapy', *Radiation Physics and Chemistry*, 61 (2001), 223-6.
- Le'tourneau D, Gulam M, Yan D, Oldham M, Wong J, 'Evaluation of a 2D diode array for IMRT quality assurance', *Radiotherapy and Oncology*, 70 (2004), 199-206.
- Li J, Dempsey J, Ding L, Liu C, Palta J, 'Validation of dynamic MLC-controller log files using a two-dimensional diode array', *Med.Phys.*, 30 (2003), 799-805.
- Li J, Wiersma R, Stepaniak C, Farrey K, Al-hallaq H, 'Improvements in dose accuracy delivered with static-MLC IMRT on an integrated linear accelerator control system.', *Med.Phys.*, 39 (2012), 2456-62.
- Li J, Yan G, Liu C, 'Comparison of two commercial detector arrays for IMRT quality assurance', *Journal of Applied Clinical Medical Physics*, 10 (2009), 62-74.
- Thomas LoSasso, Chen S. Chui, C. C. Ling, 'Physical and dosimetric aspects of a multileaf collimation system used in the dynamic mode for implementing intensity modulated radiotherapy', *Medical Physics*, 25 (1998), 1919-27.

Thomas LoSasso, Chen S. Chui, C. C. Ling, 'Comprehensive quality assurance for the delivery of intensity modulated radiotherapy with a multileaf collimator used in the dynamic mode', *Medical Physics*, 28 (2001), 2209-19.

Loverock L, 'Linear Accelerators', *Handbook of Radiotherapy Physics Theory and Practice* (Taylor and Francis, London, UK, 2007), 197-239. ISBN: 0750308605

Loyd M D., Lane R G, Laxton J, Chow C H, Rosen I I, 'Long term variation in beam symmetry as a function of gantry angle for a computer-controlled linear accelerator', *Medical Physics*, 16 (1989), 614-7.

Marconi Applied Technologies Ltd, 'Hydrogen Thyatron Preamble', *Thyatron Application Data Sheet* (Marconi Ltd Chelmsford UK, 2007).

Martens C, Budgell G J, Claus F, 'Improved delivery efficiency for step and shoot intensity-modulated radiotherapy using a fast-tuning magnetron (Poster Presentation No.241)', *Radiotherapy and Oncology*, 61 (2001a), S83.

Martens C, C De Wagter, De Neve W, 'The value of the LA48 linear ion chamber array for characterization of intensity-modulated beams', *Physics in medicine and biology*, 46 (2001b), 1131-48.

Maxim Semiconductors Ltd, 'Quad SPST Ultra low leakage CMOS Analog Switch MAX326/7', *MAX 326/MAX 327 Component Data Sheet 19-3965 Rev 2 7/96* (Maxim Semiconductor Ltd, 1996).

Maxim Semiconductors Ltd, 'Serial Output 250ksps 12 Bit ADC with T/H and Reference MAX176', *MAX 176 Component Data Sheet* (Maxim Semiconductors Ltd, 1998).

Maxim Semiconductors Ltd, 'Serial Input Voltage Output 16 Bit DAC MAX 524', *Max 524 Component Data Sheet 19-1082 Rev 2* (Maxim Semiconductors Ltd, 1999).

Mayles P, '(Report 81) Megavoltage Equipment (Multileaf collimators. Section 5.5.6)', Mayles P, *Physics Aspects of Quality Control in Radiotherapy* 1999), 137-43. ISBN: 0 904181 91 X

Mayles P, Thwaites D I, 'Rationale and Management of the Quality System', *Handbook of Radiotherapy Physics Theory and Practice* (Taylor and Francis, London, UK, 2007), 793-807. ISBN: 0750308605

McCaffrey J P, Downton B, Shen H, Niven D, McEwen M, 'Pre-irradiation effects on ionization chambers used in radiation therapy', *Physics in medicine and biology*, 50 (2005), N121-N133.

McGinty G K, 'III. Modern Trends in Accelerator Design for Therapy', *The British Journal of Radiology*, 35 (1962), 196-9.

McKerracher C, Thwaites D I, 'Assessment of new small-field detectors against standard-field detectors for practical stereotactic beam data acquisition', *Physics in medicine and biology*, 44 (1999), 2143-60.

McKerracher C, Thwaites D I, 'Notes on the construction of solid-state detectors', *Radiotherapy and Oncology*, 79 (2006), 348-51.

Meddaugh G E, 'The RF system of a typical clinical linear accelerator.', (*Microwave Symposium Digest, 1994.*, *IEEE MTT-S International 1994*), 1611-4.

Meredith W J., '40 years of development in radiotherapy', *Physics in medicine and biology*, 29 (1984), 115-20.

Microchip Technology Inc Arizona USA, '18Fxx2 PIC Data Sheet (Issue DS39564B)', (Microchip Inc, 2002).

Microchip Technology Inc Arizona USA, 'PIC 18 Microcontroller family', *PIC Series Data Sheet* (Microchip Inc, 2005).

Microengineering Labs Ltd, *PIC Basic Pro Compiler Manual* (ME Labs Inc, Colorado Springs, Co, USA, 2004).

Miller C W, 'Travelling-Wave Linear Accelerator for X-Ray Therapy', *Nature*, 171 (1953), 297-8.

Miller C W, 'Recent Development in Linear Accelerator for Therapy:- Section I. The Continuing Evolution of Linear Accelerators', *The British Journal of Radiology*, 35 (1962), 182-7.

Mohr P, Brieg S, Stahl J, Witucki G, 'Linearity of the Dose Monitor System at Low Monitor Units', *Strahlenther Onkol*, 183 (2007), 327-31.

Moon-Sing Lee, Wan-Ting Liao, Su-Hua Lo, Feng-Ling Chen, Szu-Wen Wong, Chsia-Hsi Sheng, Wen-Lin Hsu, 'Characterization of Delivery Systems for Intensity Modulated Radiation Therapy Using a Step-and-Shoot Approach', *Tzu Chi Med J*, 16 (2004), 377-88.

Mullett L B, Loach R G, 'Experimental Work on Corrugated Waveguides and Associated Components for Linear Electron Accelerators', *Research Paper, Atomic Energy Research Est.* (Atomic Energy Research Est. Harwell, 1948), 271-84.

- Naylor G P, Chiveralls K, 'The stability of the X-ray beam from an 8 MV linear accelerator designed for radiotherapy', *The British Journal of Radiology*, 43 (1970), 414-9.
- Naylor G P, Williams P C, 'An instrument for measuring small differences in dose rate at points in a radiation beam', *Physics in medicine and biology*, 16 (1971), 525-8.
- Nepal N, Kim Y, Bae Y, Ko I, Cho M, NamKug K, 'Design study on standing-wave linear accelerator', *2001 Partical Accelerator Conference*, (2001), 2802-4.
- Nutting C M, Dearnaley D P., Webb S, 'Intensity modulated radiation therapy: a clinical review', *The British Journal of Radiology*, 73 (2000), 459-69.
- Otto K, 'Volumetric modulated arc therapy: IMRT in a single gantry arc', *Medical Physics*, 35 (2008), 310-7.
- Padikal T N, Born C., Roberson P L, 'The stability of teletherapy-beam symmetry with gantry angle', *Radiology*, 139 (1981), 501-3.
- Pardo J, Franco L, Gomez F, Iglesias A, Pazos A, Pena J, Lobato R, Mosquera J, Pombar M, Sendon J, 'Development and operation of a pixel segmented liquid-filled linear array for radiotherapy quality assurance', *Physics in medicine and biology*, 50 (2005), 1703-16.
- Pirrie C A, Menown H, 'The Evolution of the Hydrogen Thyatron (Marconi Applied Technologies Ltd)', *Power Modulator Symposium, 2000. Record of the Twenty Fourth International Conference 2000*, 9-16.
- Podgorsak E B, 'Treatment Machines for External Beam Radiotherapy', Podgorsak E B, *Radiation Oncology Physics: A handbook for teachers and students* (International Atomic Energy Agency (IAEA), 2005), 123-60. ISBN: 92-0-107304-6
- Procter N, 'A device for rapidly checking X-ray beam uniformity', *The British Journal of Radiology*, 42 (1969), 860-2.
- PTW Freiburg GmbH, 'LA48 Linear Array for the analysis of dynamic fields', *Technical Data Sheet Issue ISR D168.139.0/1* (PTW Freiburg GmbH, 1997).
- PTW Freiburg GmbH, 'Electrometer with Built-in Automatic Leakage Compensation (ALC) are Typically not Suitable for IMRT Measurements', *Company Technical Note Issue D776.200.0/0* (PTW Freiburg GmbH, 2005).
- Purdy J A., D A. Goer, 'Dual energy X-ray beam accelerators in radiation therapy: An overview', *Nuclear Instruments and Methods in Physics Research Section B: Beam Interactions with Materials and Atoms*, 10-11 (1985), 1090-5.

- Rajapakshe R, Shalev S, 'Output stability of a linear accelerator during the first three seconds', *Med.Phy.*, 23 (1996), 517-9.
- Ramírez-Jiménez F, Mondragon-Contreras L, Cruz-Estrada P, 'Application of PIN diodes in Physics Research ', *Instituto Nacional de Investigaciones Nucleares*, (2006), 1-12.
- Manickam Ravikumar, Mohammed Al Asmary, A. S. alla, Hassna Al Ghamdi, 'Dose Delivery Accuracy of Therapeutic Photon and Electron Beams at Low Monitor Unit Settings', *Strahlentherapie und Onkologie*, 181 (2005), 796-9.
- Reena P, Dayananda S, Pa R, Jamema S, Gupta T, Deepak D, Rajeev S, 'Performance characterization of siemens primus linear accelerator under small monitor unit and small segments for the implementation of step-and-shoot intensity modulated radiotherapy.(Original Article Product/service evaluation)', *Journal of Medical Physics*, 31 (2006), NA.
- Rich A, 'Shielding and Guarding - How to exclude interference - Type noise - What to do and why to do it - A Rational Approach', *Analog Dialogue (Analog Devices Ltd)*, 17 (1983), 124-9.
- Rikner G, Grusell E, 'General specifications for silicon semiconductors for use in radiation dosimetry', *Physics in medicine and biology*, 32 (1978), 1109-17.
- Rikner G, Grusell E, 'Effects of radiation damage on p-type silicon detectors', *Physics in medicine and biology*, 28 (1983), 1261-7.
- Roddy D, 'Transmission Lines', *Microwave Technology* (Prentice-hall, 1986), 54. ISBN: 0-8359-4390-9
- Rosenfeld A, 'Radiotherapy and Related Applications ', *Semiconductors Detectors in Radiation Therapy* 2008). ISBN: 904810985X
- Saini A, Zhu T, 'Dose rate and SDD dependence of commercially available diode detectors', *Med.Phy.*, 31 (2004), 914-24.
- Saminathan S, Manickam R, Chandraraj V, Supe S, 'Dosimetric study of 2D ion chamber array matrix for the modern radiotherapy treatment verification', *Journal of Applied Medical Physics*, 11 (2010).
- Saw C, Li S, Ayyangar K, Yoe-Sein M, Pillai S, Enke C, Celi J, 'Dose linearity and uniformity of a linear accelerator designed for implementation of multileaf collimation system-based intensity modulated radiation therapy', *Med.Phy.*, 30 (2003), 2253-6.
- Saxon G, 'Theory of Electron Beam Loading in Linear Accelerators', 1954), 705-16.

Schmidt W, Nedelik A, Binder W, Schoeberl E, 'A Multi-diode System for Quality Assurance in Radiation Therapy', *Radiation Detection Dosimetry*, 34 (1990), 253-6.

Sharpe M B, Miller B M, Yan D., Wong J W, 'Monitor unit settings for intensity modulated beams delivered using a step-and-shoot approach', *Medical Physics*, 27 (2000), 2719-25.

Shepard D, Earl M, Li X, Naqvi S, Yu C, 'Direct aperture optimization: A turnkey solution for step-and-shoot IMRT', *Med.Phy.*, 29 (2001), 1007-18.

Smith S W, 'Moving Average Filters', *Digital Signal Processing - A Practical Guide for Engineers and Scientists* (Elsevier, Newnes, Burlington MA. USA, 2003a), 277-84. ISBN: 075067444X, 9780750674447

Smith S W, 'Statistics Probability and Noise', *Digital Signal Processing - A Practical Guide for Engineers and Scientists* (Elsevier, Newnes, Burlington MA. USA, 2003b), 11-34. ISBN: 075067444X, 9780750674447

Smith S W, 'Windowed-Sinc Filters', *Digital Signal Processing - A Practical Guide for Engineers and Scientists* (Elsevier, Newnes, Burlington MA. USA, 2003c), 285-96. ISBN: 075067444X, 9780750674447

Sutherland W H, 'Stability of a linear accelerator with "achromatic" electron beam bending', *The British Journal of Radiology*, 49 (1976), 262-6.

E Tanabe, Robert W. Hamm, 'Compact multi-energy electron linear accelerators', *Nuclear Instruments and Methods in Physics Research Section B: Beam Interactions with Materials and Atoms*, 10-11 (1985), 871-6.

Tektronix Inc, 'Sampling Oscilloscopes Techniques', *Technique Primer (47W-7207)* (Tektronix Inc PO Box 500 Beaverton, 1989), 1-4.

Thwaites D I, '(Report 81) Quality Assurance and its Conceptual Framework (Accuracy in radiotherapy as the basis for Quality Assurance standards. Section 1.2)', Mayles P, *Physics Aspects of Quality Control in Radiotherapy* 1999), 7-11. ISBN: 0 904181 91 X

Thwaites D I, Mijnheer B J, Mills J A, 'Quality Assurance of External Beam Radiotherapy', Podgorsak E B, *Radiation Oncology Physics: A handbook for teachers and students* (International Atomic Energy Agency (IAEA), 2005), 407-40. ISBN: 92-0-107304-6

Thwaites D I, Tuohy J B, 'Back to the future: the history and development of the clinical linear accelerator', *Physics in medicine and biology*, 51 (2006), 343-62.

Varian R H., Varian S F., 'A High Frequency Oscillator and Amplifier', *Journal of Applied Physics*, 10 (1939), 321-7.

Voss G A, 'Rolf Wideröe', (Physics Today, American Institute of Physics Publishing, Melville, New York, USA, 1997), 78-9.

Wagner D, Vorwerk H, 'Two years experience with quality assurance protocol for patient related Rapid Arc treatment plan verification using a two dimensional ionization chamber array', *Radiation Oncology*, 6 (2011), 1-8.

Webb S, 'Three-Dimensional Radiotherapy Treatment Planning', (*The Physics of Three-Dimensional Radiation Therapy (Conformal Radiotherapy, Radiosurgery and Treatment Planning*, (Institute of Physics Publishing (IOP), 1993), 1-7. ISBN: 0750302542, 978-0750302548

Webb S, 'Features of MLC delivery of IMRT (Section 3.4.4 Stability of accelerator and delivery of a small number of MUs and small fieldsizes)', *Contemporary IMRT: Developing Physics and Clinical Implementation* (Institute of Physics Publishing (IOP), 2005a), 81-4. ISBN: 0 7503 1004 9

Webb S, 'Intensity-modulated radiation therapy (IMRT): a clinical reality for cancer treatment, "any fool can understand this": The 2004 Silvanus Thompson Memorial Lecture', *The British Journal of Radiology*, 78 (2005b), S64-S72.

Welwyn Ltd, 'Glass Resistors with Guard Band (Type 3810)', *Application Note A 01 04* (Welwyn Components Ltd. Northumberland UK., 2004).

Whitham K, 'Standing wave linear accelerator having non-resonant side cavity', Inc. P. A. C. Varian Associates, (US Patent, 1986), 1-2.

Wickman G, Nystrom H, 'The use of liquids in ionization chambers for high precision radiotherapy dosimetry', *Physics in medicine and biology*, 37 (1992), 1789-812.

Wideroe R, 'Über ein neues Prinzip zur Herstellung hoher Spannungen', *Electrical Engineering (Archiv fur Elektrotechnik)*, 21 (1928), 387-406.

William S E., Jie S, Craig I A, 'Wide field calibration of a multi-sensor array', *US Patent (App. No. 09/058639)* (USA, 2000).

Williams P C, 'IMRT: delivery techniques and quality assurance', *The British Journal of Radiology*, 76 (2003), 766-76.

Williams T, 'Circuit Designer's Companion', (Elsevier, Newnes, Burlington MA. USA, 2005). ISBN: 0 7506 1756 X

Witte R A, 'Oscilloscopes', *Electronic Test Instruments* (Prentice Hall, New Jersey USA, 2006), 146-51. ISBN: 0-13-253147-x

Yin Z, Hugtenburg R, Beddoe A, 'Response corrections for solid-state detectors in megavoltage photon dosimetry', *Physics in medicine and biology*, 49 (2004), 3691-702.

Yu C, 'Intensity-modulated arc therapy with dynamic multi-leaf collimation: an alternative to tomotherapy', *Physics in medicine and biology*, 40 (1995), 1435-49.

Yu C, 'Intensity Modulated Arc Therapy with Dynamic Multi-leaf Collimation', US Patent, *Patent No. 5818902*, (Filed by Elekta AB Stockholm Sweden. 1 March 1996) (USA, 1998).

Yu C, Symons M, Du M, Martinez A, Wong J, 'A method for implementing dynamic photon beam intensity modulation using independent jaws and a multi-leaf collimator', *Physics in medicine and biology*, 40 (1995), 769-87.

Zetex Semiconductors Ltd, 'Precision 2.5 V Micropower Voltage Reference', *ZRef 2V5 Component Data Sheet* (Zetex Plano, Texas, USA, 2005).